INTERPRETATION OF GROUND-BASED MEASUREMENTS FROM THE SURFACE PARTICULATE MATTER NETWORK TO UNDERSTAND THE GLOBAL DISTRIBUTION OF FINE PARTICULATE MATTER

by

Crystal L. M. Weagle

Submitted in partial fulfilment of the requirements
for the degree of Doctor of Philosophy

at

Dalhousie University
Halifax, Nova Scotia
April 2018

Table of Contents

List of Tables ..... **viii**

List of Figures ..... **ix**

Abstract ..... **xi**

List of Abbreviations and Symbols Used ..... **xii**

Acknowledgements ..... **xiv**

Chapter 1 Introduction **1**

Chapter 2 Background **9**

2.1 Atmospheric Aerosol 9

2.1.1 Inorganic Aerosol *11*

2.1.2 Organic Aerosol *14*

2.1.3 Aerosol Removal Mechanisms *16*

2.1.4 Health Impacts of Fine Particulate Matter *16*

2.2 Ground-Based $PM_{2.5}$ Monitoring 19

2.3 Chemical Transport Models 22

2.4 Satellite Remote Sensing Estimates of $PM_{2.5}$ 23

Chapter 3 Global Variation in $PM_{2.5}$ Chemical Composition **26**

3.1 Introduction 26

3.2 Inferring $PM_{2.5}$ Mass and Chemical Composition 28

3.2.1 Gravimetric Analysis *30*

3.2.2 Equivalent Black Carbon *31*

3.2.3 Crustal Material *32*

3.2.4 Inorganic Species from Water-Soluble Ions *33*

3.2.5 Particle-Bound Water Associated with Inorganic Species *34*

3.2.6 Trace Elemental Oxides *35*

3.2.7 Residual Matter *35*

3.3 Sources of Uncertainty 36

3.4 Chemical Composition Results 37

3.4.1 Overview *37*

3.4.2 Literature Comparison Overview *42*

3.4.3 Individual Site Characteristics *43*

3.4.3.1 Beijing, China 43

3.4.3.2 Bandung, Indonesia 46

3.4.3.3 Manila, Philippines 47

3.4.3.4 Dhaka, Bangladesh 47

3.4.3.5 Ilorin, Nigeria 48

3.4.3.6 Kanpur, India 49

3.4.3.7 Buenos Aires, Argentina 50

3.4.3.8 Rehovot, Israel 50

3.4.3.9 Mammoth Cave National Park, USA 51

3.4.3.10 Atlanta, USA 52

3.4.3.11 Singapore, Singapore 53

3.4.3.12 Hanoi, Vietnam 53

3.4.3.13 Pretoria, South Africa 54

3.5 Conclusions 54

Chapter 4 Global Sources of Fine Particulate Matter: Interpretation of $PM_{2.5}$ Chemical Composition Observed by the Surface Particulate Matter Network using a Global Chemical Transport Model 58

4.1 Introduction 58

4.2 Methods 60

4.2.1 SPARTAN Filter Measurements and Analysis *60*

4.2.1.1 Uncertainty from Collocated Measurements 62

4.2.2 GEOS-Chem Simulation *65*

4.2.3 Constraining the Simulation with Satellite-Based $PM_{2.5}$ *68*

4.3 Sources Affecting $PM_{2.5}$ Mass and Composition 69

4.3.1 Global Distribution of $PM_{2.5}$ Chemical Composition 69

4.3.2 SPARTAN Site Characteristics 76

4.3.2.1 East Asia 77

4.3.2.2 Southeast Asia 79

4.3.2.3 South Asia 82

4.3.2.4 South America 84

4.3.2.5 Middle-East 85

4.3.2.6 Sub-Saharan Africa 86

4.3.3 Global $PM_{2.5}$ Source Categories 88

4.4 Conclusion 92

Chapter 5 Interpretation of the Relationship Between Ground Level Fine Particulate Matter and Columnar Aerosol Optical Depth using Measurements from SPARTAN 94

5.1 Introduction 94

5.2 Materials and Methods 96

5.2.1 SPARTAN Measurements 96

5.2.1.1 Filter Measurements 96

5.2.1.2 Nephelometry 97

5.2.2 Ground-Based Measurements of Aerosol Optical Depth 98

5.2.3 Global Chemical Transport Model 98

5.2.4 Statistical Terms Used 100

5.3 Results 100

5.3.1 Global variation of $PM_{2.5}$ to AOD relationship 100

5.3.2 η decomposition 104

5.4 Conclusions 108

Chapter 6 Conclusion 110

6.1 Summary 110

6.2 Future Work 113

References 117

Appendix A Author Contributions 141

Appendix B SPARTAN Standard Operating Procedures 142

B1.0 Filter Weighing Procedure 142

B1.1 General Information 142

B1.2 Maintaining the Cleanroom 143

B1.3 Microbalance Calibration 144

B1.4 Calibration Weights and Lab Blanks 145

B1.5 Weighing Sampled Filters 148

B2.0 Filter Cartridge Shipping, Receiving, and Processing 151

B2.1 Cartridge Assembly 151

B2.2 Cartridge Shipping 152

B2.3 Cartridge Receiving 153

B2.4 Converting Mass Measurements to Mass Concentrations 156

B3.0 Determining Equivalent Black Carbon 158

B3.1 General Information 158

B3.2 Smoke Stain Reflectometer Measurement Procedure 158

B4.0 Filter Analysis for Water-Soluble Ions 160

B4.1 General Information 160

B4.2 Filter Extraction Procedure and Analysis for Water-Soluble Ions 160

B4.2.1 Cutting 25 mm Filters in Half 160

B4.2.2 Water-Soluble Ion Extraction Procedure 161

B4.2.3 Preparing Standard Ion Solutions and Eluent for Ion Chromatography 162

B4.2.4 Preparing Filter Extracts for Anion and Cation Analysis 164

B4.2.5 Calculating Ion Masses for Ion Chromatography Results 165

B5.0 ICP-MS Filter Extraction & Analysis 166
B5.1 General Information *166*
B5.2 Filter Extraction Procedure for Trace Element Analysis *166*
B5.2.1 Trace Element Extraction Procedure 166
B6.0 Nephelometer Data Quality Assurance and Quality Control 168
B6.1 Purpose and Applicability *168*
B6.2 Nephelometer Performance Checks *169*
B6.2.1 Responsibilities 169
B6.2.2 Parameters for Performance Checks 170
B6.3 Nephelometer Calibration *171*
B6.3.1 Determining Calibration Frequency 171
B6.3.2 Required Equipment 173
B6.3.3 Calibration Procedure 173
B6.3.4 On-site Calibration 175
B6.3.5 Cleaning and Calibration at SPARTAN Central Lab at Dalhousie University 175
B6.4 SPARTAN Service Report *176*
B7.0 AERONET sunphotometer data 178
B7.1 General Information *178*
B7.2 Data Description *178*
B8.0 Site Selection, Installation, and Maintenance Procedures 179
B8.1 Purpose *179*
B8.2 Site Selection *179*
B8.2.1 Representative of Regional Air Quality 179
B8.2.2 Security 180
B8.2.3 Electrical Requirements *181*
B8.3 Site Installation *181*
B8.3.1 Equipment and Materials Required for Site Installation 181

B8.3.2 Pre-Installation Activities 182
B8.3.3 Instrumentation Checklist 182
B8.3.4 Installation of Filter-Based Sampler to Support Structure 183
B8.3.5 Installation of the Nephelometer to the Support Structure 184
B8.4 Sampling Procedure 184
B8.4.1 Programming the SPARTAN Filter-Based Sampler 186
B8.4.2 Programming the SPARTAN Nephelometer 188
B8.4.3 Solar Panel and Battery 188
B8.5 Installing and Changing Filter Cartridges 189
B8.5.1 Cleaning and Greasing Impactor Plates 191
B8.5.2 Measuring Flow Rates 191
B8.6 Downloading Data and Recording information 192
B8.6.1 Downloading Data from Instruments 192
B8.6.2 Recording Log Sheet Information 193
B8.7 Storage and Shipment of Filter Cartridges 194
Appendix C Copyright Agreement Letters 195

List of Tables

Table 2.1. WHO air quality guidelines and interim targets for annual mean $PM_{2.5}$ concentrations (WHO, 2006) 18

Table 3.1. Summary of speciation definitions and associated references. 31

Table 3.2. $PM_{2.5}$ chemical composition and site information for each SPARTAN sampling site. 40

Table 4.1. Summary of uncertainty for $PM_{2.5}$ and major chemical components. 63

Table 4.2. List and description of sensitivity simulation used to investigate source categories contributing to $PM_{2.5}$ mass and composition. 67

Table 4.3. Correlation coefficient from comparison between SPARTAN measurements and simulation-only (r) and simulation-satellite (r_{sat}) ground-level $PM_{2.5}$ concentrations 69

Table 4.4. $PM_{2.5}$ mass and composition at SPARTAN sites from measurements (Obs.) and GEOS-Chem simulation (GC). 71

Table 5.1. Global coincident values of measured and simulated $PM_{2.5}$, AOD, and related variables. 102

Table B.1. Ions and corresponding concentrations (Conc.) in Dionex Standard Solutions. Reference ions used for standard labels are bolded. 162

Table B.2. Method of preparation summary for anion standard solutions. 163

Table B.3. Method of preparation summary for cation standard solutions. 163

Table B.4. AERONET data description 178

List of Figures

Figure 1.1. A) geophysical satellite-based $PM_{2.5}$ estimates, and B) GWR-adjusted satellite-based $PM_{2.5}$ for 2010.. 3

Figure 1.2. Global population density for 2015 from the Socioeconomic Data and Applications Center with overlaid circles showing pre-existing collocated ground-based AOD observations and $PM_{2.5}$ measurements for 2015 (blue) and depicting SPARTAN sampling site locations to date (black)..... 5

Figure 2.1. Known monitor locations with measured PM_{10} and $PM_{2.5}$, collected from 2008-2013 for the Global Burden of Disease. 20

Figure 3.1. Diagram of AirPhoton filter assembly..... 29

Figure 3.2. $PM_{2.5}$ mass concentration (inner white circle, $\mu g\ m^{-3}$) and composition mass fractions at 13 sampling sites. 38

Figure 3.3. Comparison of SPARTAN dry (0% RH) chemical composition with 11 available collocated previous studies.. 45

Figure 4.1. Summary of daily comparisons between two collocated sampling stations located in Halifax, Toronto, and Beijing.. 65

Figure 4.2. Global simulated annual mean $PM_{2.5}$ composition..... 70

Figure 4.3. Extent of neutralization at SPARTAN sites from measurements and the GEOS-Chem simulation. 75

Figure 5.1. Annual mean simulated η (ratio of ground-level $PM_{2.5,24h}$ at 35% relative humidity to total-column, AOD_{sat})..... 103

Figure 5.2. Annual mean modeled effective scale height (ratio of total-column $AOD_{10\text{-}14h}$ to ground scatter) at satellite overpass times (1000 to 1200 and 1300 to 1500 hours local time). 104

Figure 5.3. Extinction vertical profiles at sampling sites showing the contribution of individual chemical components to total extinction. 106

Figure 5.4. Annual mean mass scattering efficiency (ratio of daily ground-level scatter to $PM_{2.5}$ mass concentration). 107

Figure 5.5. Annual mean diurnal variation (ratio of ground scatter at satellite overpass time versus 24-hour average).. 108

Figure B.1. Indicator bubble on the top of the microbalance. 144

Figure B.2. Example of filter positioned in the center of the balance pedestal 149

Figure B.3. Cartridge assembly scheme..... 152

Figure B.4. Properly completed SPARTAN sampling log sheet. 154

Figure B.5. Foreground: a disassembled SPARTAN cartridge showing the two top 2x2 blocks as well as the bottom 2x8 block. 155

Figure B.6. Raw mass data (micrograms) combined with flow rates (lpm) and sampling time determine the mass concentration during each sampling period. 157

Figure B.7. Smoke Stain Reflectometer, including display, cylindrical optical unit, circular mask, and calibration plate 158

Figure B.8. Plastic filer holder alignment.. 161

Figure B.9. Transfer of liquid extract from 20 mL pink vials to 8 mL amber vials. Amber vials are washed once with methanol, 3 times with water before use. 162

Figure B.10. Summary of trace metal extraction procedure and illustration of vial arrangement in the heating block. 168

Figure B.11: Dark PMT signal (PMT DARK) compared to the forward PMT signal at each wavelength 170

Figure B.12: Back scatter dark reference signal compared to back scatter reference signal at each wavelength 171

Figure B.13: Blank SPARTAN Service Report to be completed upon receiving a nephelometer from the field 177

Figure B.14. Illustration of SPARTAN sampler set-up 180

Figure B.15. a) Example of weather/radiation shield installed on the filter sampler, and b) Positioning of the filter sampler and nephelometer on the same pole. 183

Figure B.16. Example of using the metal bar on the back of the sampler cases to attach to a preassembled pole using the provided hose clamps. 184

Figure B.17. Example of a properly installed cartridge. 191

Figure B.18. a) Picture of where to place the vacuum grease on the impactor plates, and b) How to use the external flow adaptor to measure flow rates. 192

Abstract

Exposure to ambient fine particulate matter ($PM_{2.5}$) is increasingly recognized as the leading environmental risk factor for global burden of disease. This thesis develops the Surface PARTiculate mAtter Network (SPARTAN) to provide long-term measurements of $PM_{2.5}$ mass and chemical composition, collocated with existing aerosol optical depth (AOD) observations in highly populated, globally diverse regions. Three projects are presented that interpret SPARTAN measurements to provide insight into the spatial variation in ground-based $PM_{2.5}$ chemical composition, into the sources contributing to $PM_{2.5}$, and into the relationship between AOD and $PM_{2.5}$ used in satellite-based estimates of $PM_{2.5}$.

Analysis of SPARTAN filter samples collected across multiple continents for $PM_{2.5}$ chemical composition show that absolute concentrations of several major components vary by more than an order of magnitude across sites, and exhibit consistency with available, collocated studies. Elevated Zn:Al ratios reveal an enhanced anthropogenic dust fraction relative to natural sources, signifying the need to include this $PM_{2.5}$ source in global models and emission inventories. The developed compositional dataset provides much needed long-term chemical data for investigation of sources leading to the spatial variation of $PM_{2.5}$ mass and chemical composition.

Evaluation of the GEOS-Chem model, constrained by satellite-based estimates of $PM_{2.5}$ and informed by SPARTAN compositional measurements, shows significant spatial consistency for major chemical components. Measured $PM_{2.5}$ composition corroborate source attribution from sensitivity simulations, providing confidence in utilizing sensitivity simulations to explore the influence of source categories to global population-weighted $PM_{2.5}$. This approach of coupling observational datasets with modelling at the global scale allows for insight into the main sources determining $PM_{2.5}$ global variation, but also identification of modelled processes that require development to represent the wide range of $PM_{2.5}$ and composition observed globally.

An initial comparison between empirical and simulated relationships of $PM_{2.5}$ and columnar AOD (η) was conducted using the GEOS-Chem global chemical transport model. This comparison is the first to develop empirical, ground-based η and provide an evaluation of modelled η values widely used in satellite-based estimates. Collocated, modelled η values generally fall within a factor of two of measured values and have a mean fractional bias that is an order of magnitude lower than for either $PM_{2.5}$ or AOD alone. This lower bias in η indicates that satellite-derived $PM_{2.5}$ inferred using η is likely to have lower bias than purely simulated $PM_{2.5}$.

List of Abbreviations and Symbols Used

b_{sp}	Scattering coefficient
σ_{sp}	Mass scattering efficiency, $m^2\ g^{-1}$
AERONET	Aerosol Robotic Network
AFCID	Anthropogenic, fugitive, combustion, and industrial dust
AOD	Aerosol Optical Depth
AQG	Air Quality Guideline
AQS	Air Quality System
BC	Black carbon
CASTNET	Clean Air Status and Trends NETwork
CM	Crustal material
COPD	Chronic Obstructive Pulmonary Disease
CV	Cross-validation
CTM	Chemical Transport Model
DMS	Dimethyl sulfide
EBC	Equivalent black carbon
EDGAR	Emissions Database for Global Atmospheric Research
EEA	European Environment Agency
EMEP	European Monitoring and Evaluation Program
GBD	Global Burden of Disease
GEOS	Goddard Earth Observing System
GFED	Global Fire Emissions Database
GWR	Geographically-weighted regression
HEMCO	Harvard-NASA Emissions Component
IMPROVE	Interagency Monitoring of Protected Visual Environments
IPCC	Intergovernmental Panel on Climate Change
MISR	Multi-angle Imaging SpectroRadiometer
MODIS	MODerate resolution Imaging Spectroradiometer
NAPS	National Air Pollution Surveillance program
OA	Organic aerosol
OC	Organic carbon
OECD	Organization for Economic Cooperation and Development
OM	Organic mass
PBW	Particle-bound water
PM_{10}	Particulate matter with a mean aerodynamic diameter of 10 μm or less
$PM_{2.5}$	Particulate matter with a mean aerodynamic diameter of 2.5 μm or less

PM_{coarse}	Particulate matter with a mean aerodynamic diameter between 10 and 2.5 μm
POA	Primary organic aerosol
PTFE	Polytetrafluoroethylene (Teflon®)
RH	Relative humidity, RH
RM	Residual matter
SeaWiFS	Sea-viewing Wide Field-of-view Sensor
SEDAC	Socioeconomic Data and Applications Center
SH	Scale Height
SIA	Secondary inorganic aerosol
SOA	Secondary organic aerosol
SVOA	Semi-volatile organic aerosol
SPARTAN	Surface PARTiculate mAtter Network
STN	Speciation Trends Network
TEO	Trace element oxides
USD	United States Dollar
VOCs	Volatile organic compounds
WHO	World Health Organization

Acknowledgements

First of all, I would like to thank my supervisor Dr. Randall Martin for the opportunity to carry out research in a field that I feel so passionately about. His expertise, support, and encouragement have been continuous throughout this degree and I have no words to express how truly grateful I am to have learned from him.

I would like to acknowledge and thank the members of my supervisory committee: Dr. Rachel Chang, Dr. Alan Doucette, and Dr. Mark Gibson. Thank you all for your support and guidance over the last few years.

I have been extremely fortunate to work with an amazing group of people in the Atmospheric Composition Analysis Group. Thank you to all past and present group members. In particular, thank you to Graydon Snider, Colin Lee, Brian Boys, Aaron van Donkelaar, Sajeev Philip, Chi Li, and Melanie Hammer for the technical support, ideas, insight, and friendship. Also, a special thank you to Valerie O'Neil in the Physics Office for managing the countless SPARTAN shipments.

To all my friends and family, you have been incredibly supportive over the last few years and I can't thank you enough. I am very fortunate to have such a phenomenal support system, I could not have gotten here without you.

Last but certainly not least, I have undying gratitude for my parents (Wendy and Rodney) and wonderful husband, Talal. Mom and Dad, I have absolutely no doubt that I would not be at this point without your love and support. Talal, your love and patience have been unconditional and your support, unwavering. Thank you for celebrating all my victories no matter how small, listening to hours of presentations you didn't understand, and for being a steady voice when it all seemed a little too much to tolerate. I am who and where I am today because of each and every one of you, thank you.

Chapter 1 Introduction

Ambient fine particulate matter with an aerodynamic diameter of 2.5 μm or less ($PM_{2.5}$) is a robust indicator of increased mortality and morbidity. The size cut at 2.5 μm represents the predominant portion of particles that penetrate deep into the gas-exchange region of the respiratory tract, and ultimately into the circulatory system (Miller et al., 1979). Research on long-term exposure to $PM_{2.5}$ has documented serious adverse health impacts such as chronic cardiovascular and respiratory disease, lung cancer, stroke, and diabetes (Chen et al., 2013; Crouse et al., 2012; Laden et al., 2006; Lippmann, 2014). The burden of disease due to $PM_{2.5}$ is estimated to be substantial; the 2016 Global Burden of Disease (GBD) study attributed 4.1 million premature deaths and over 70 million years of healthy life lost to $PM_{2.5}$ exposure in 2016 (Gakidou et al., 2017). In addition, the Organisation for Economic Co-operation Development (OECD) estimates that the global welfare costs associated with $PM_{2.5}$ is expected to rise from 3 trillion USD in 2015 to 18-25 trillion USD by 2060 (OECD, 2016). Given the far-reaching implications of these estimates, additional attention is needed to improve global estimates of ambient $PM_{2.5}$ exposure.

Despite recent increases in $PM_{2.5}$ surface monitoring in some areas of the world, publically available and archived ground-level measurements of $PM_{2.5}$ are still far too sparse in terms of spatial and temporal coverage to be used directly for long-term exposure estimates. Existing monitoring networks in high-income regions, such as North America and Europe, are supplemented by PM_{10} (particulate matter with a median aerodynamic diameter of 10 μm or less) measurements (e.g. Brauer et al., 2012, 2016)

and airport visibility measurements (Husar et al., 2000; Li et al., 2016a), but only partially address monitoring needs. Direct measurement of $PM_{2.5}$ concentrations are needed in numerous densely-populated urban centers and rural areas for health impact assessments and epidemiological studies.

Satellite remote sensing, when combined with constraints from global chemical transport models (CTMs), has emerged as a powerful technique for providing estimates of ground-level $PM_{2.5}$ concentrations, especially in regions with limited ground-based $PM_{2.5}$ monitoring (van Donkelaar et al., 2010). Figure 1.1A shows the most recent geophysical satellite-based estimates of ground-level $PM_{2.5}$ concentrations (van Donkelaar et al. 2016). These estimates combine observations from multiple retrieval algorithms (Hsu et al., 2006, 2013, Levy et al., 2007, 2013, Lyapustin et al., 2011a, 2011b; Martonchik et al., 2009) and instruments (MODIS, MISR, SeaWiFs) weighted inversely by error with respect to ground-based aerosol optical depth (AOD) measurements and constrained by the simulated relationship of $PM_{2.5}$ and AOD. Figure 1.1B is based on the same satellite-based $PM_{2.5}$ estimates as shown in the top panel but includes additional statistical constraints from available ground-based $PM_{2.5}$ measurements using geographically weighted regression (GWR). Figure 1.1C and Figure 1.1D show the corresponding comparison between annual mean satellite-based estimates of $PM_{2.5}$ for the year 2010 compared to available ground-based measurements. The slope of approximately 0.8 in both the geophysical and GWR-adjusted estimates indicate a general underestimate of ground-based $PM_{2.5}$ concentrations from satellite-based methods compared to direct $PM_{2.5}$ measurements. Including statistical constraints improves agreement ($R^2 = 0.85$ vs 0.64) between satellite-based $PM_{2.5}$ estimates and direct $PM_{2.5}$

measurements as well as those inferred from PM_{10} measurements. The increased consistency of GWR-adjusted satellite-based estimates with available *in situ* observations improves quality for widespread use in global health-related studies and constraining global models. However, the improvement also highlights the need to further improve pure geophysical estimates by increasing understanding of aerosol processes and the simulated relationship between AOD and $PM_{2.5}$.

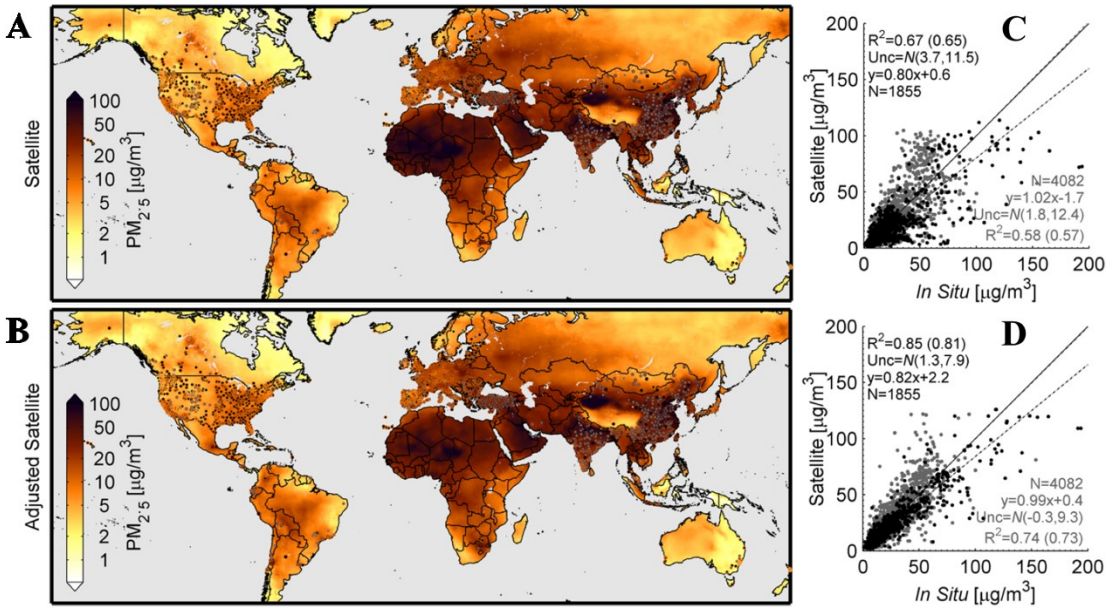

Figure 1.1. A) geophysical satellite-based $PM_{2.5}$ estimates, and B) GWR-adjusted satellite-based $PM_{2.5}$ for 2010. Overlaid circles indicate locations of available direct $PM_{2.5}$ measurements (black dots) and $PM_{2.5}$ estimated from PM_{10} measurements (grey dots). Grey denotes water. C) Comparison between annual mean geophysical satellite-based $PM_{2.5}$ estimates, and D) GWR-adjusted satellite-based $PM_{2.5}$ estimates, with available coincident *in situ* measurements, taken between 2008 and 2013. Inset text displays the coefficient of variation at all points and at cross-validation (CV) points (R^2 = all points (CV points)), normal distribution of uncertainty (N (bias,variance)), line of best fit (y) and number of points (N). Black dots/text correspond to direct $PM_{2.5}$ monitors alone. Grey dots/text indicate inclusion of $PM_{2.5}$ estimated from PM_{10} measurements. Adapted with permission from van Donkelaar, A., Martin, R. V, Brauer, M., Hsu, N. C., Kahn, R. A., Levy, R. C., Lyapustin, A., Sayer, A. M. and Winker, D. M.: Global Estimates of Fine Particulate Matter using a Combined Geophysical-Statistical Method with Information from Satellites, Models, and Monitors, Environ. Sci. Technol., 50, 3762–3772, doi:10.1021/acs.est.5b05833, 2016. Copyright 2016 American Chemical Society.

Factors that influence the relationship between satellite columnar AOD and long-term $PM_{2.5}$ concentrations include the aerosol vertical profile, the conversion of ambient

extinction by aerosols to dry $PM_{2.5}$ mass, and $PM_{2.5}$ diurnal variation. Collocated ground-based measurements of $PM_{2.5}$ and AOD are needed to evaluate simulated $PM_{2.5}$/AOD relationships and, in turn, improve estimates of ground-level $PM_{2.5}$ from satellite AOD retrievals. Measurements of $PM_{2.5}$ composition are also needed as chemical species influence mass extinction efficiency (e.g. McInniss et al., 1998; Mishra and Tripathi, 2008), which is a measure of the aerosol light extinction per mass of aerosol. Variation in $PM_{2.5}$ chemical composition has been connected to the variety of observed health outcomes from $PM_{2.5}$ exposure. For example, elevated sulfate exposure from $PM_{2.5}$ has been implicated in enhanced adverse effects from cardiovascular disease and elevated nickel, vanadium, and elemental carbon content have been linked to increased hospitalizations from respiratory and cardiovascular diseases (Lippmann, 2014). However, scarce global $PM_{2.5}$ composition measurements and uncertainty associated with simulated concentrations from global CTMs inhibit understanding of human responses to specific chemical components. Composition data also provides information for understanding formation processes (Hand et al., 2012b) and source attribution (Kong et al., 2010). Global quality assured, publically available ground-based measurements of $PM_{2.5}$ mass and composition are needed to evaluate satellite-based $PM_{2.5}$ estimates and global CTMs used to constrain satellite observations of AOD.

Observations of AOD from the Aerosol Robotic Network (AERONET) are used extensively to validate satellite observations (e.g. Levy et al., 2007; van Donkelaar et al., 2016). AERONET is a successful federation of sun photometers that provides publically available data, including long-term, time-resolved, continuous, cloud-free daytime AOD at hundreds of globally diverse sites (Holben et al., 1998). Collocation of ground-based

AOD and $PM_{2.5}$ measurements would provide an empirical estimate of the $PM_{2.5}$ to AOD relationship for validation of the simulated relationship and investigation of the factors affecting it. However, as shown in Figure 1.2 (blue circles), only 7 pre-established collocated (< 1 km) $PM_{2.5}$ and AOD measurement sites are known and are primarily located in areas with low-moderate population density.

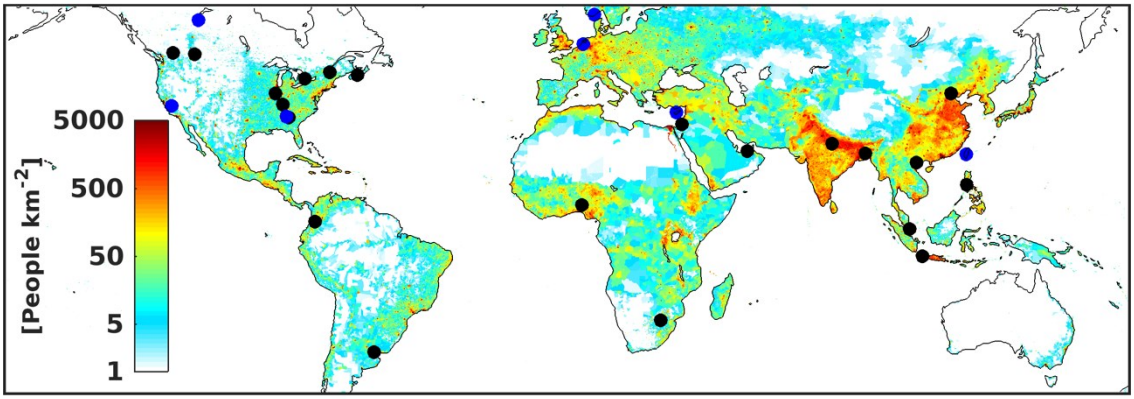

Figure 1.2. Global population density for 2015 from the Socioeconomic Data and Applications Center with overlaid circles showing pre-existing collocated ground-based AOD observations and $PM_{2.5}$ measurements for 2015 (blue) and depicting SPARTAN sampling site locations to date (black).

The Surface PARTiculate mAtter Network (SPARTAN) is a global network of ground-based $PM_{2.5}$ measurements, including integrated filter sampling and continuous monitoring through nephelometry, collocated with existing AERONET sun photometers. SPARTAN is specifically designed to evaluate and improve satellite-based estimates of ground-level $PM_{2.5}$ and to reduce uncertainties in their use for global health applications. Given the overarching objectives of SPARTAN, the following criteria are used for selecting sampling sites: (i) high population density, (ii) collocation with existing AERONET sun photometers, (iii) uncertainty in satellite-based estimates or where publically-available data are limited, and (iv) locations that span a variety of $PM_{2.5}$

concentrations and composition. Figure 1.2 (black circles) shows all SPARTAN sampling sites to date, spanning regions with low to high $PM_{2.5}$ concentrations. Site locations include regions that are influenced by significant anthropogenic activity, biomass burning, agriculture, biofuel use, monsoonal conditions, and desert dust.

The research presented in this thesis represents contributions toward the growth and development of SPARTAN sampling and filter analysis procedures to provide a comprehensive global dataset of $PM_{2.5}$ mass and compositional information for understanding the global variation of $PM_{2.5}$. Contributions toward growth of SPARTAN include extensive instrument testing, deployment of instruments to sampling sites, training of on-site operators, and maintenance of sampling sites. Development of measurement methods includes testing and standardization of filter weighing and chemical extraction procedures, and data quality assurance and control practices. In addition to developing SPARTAN measurements, this thesis also aims to use these measurements to evaluate and improve simulated $PM_{2.5}$ mass and related processes from a global chemical transport model. Chemical transport model simulations are used to further interpret SPARTAN measurements to offer additional insight into the sources and processes influencing $PM_{2.5}$ spatial variation. The outline below describes in more detail how these objectives are met.

Chapter 2 provides background information on the topics discussed in this thesis, such as aerosol processes that govern $PM_{2.5}$ formation, growth, chemical modification, and removal in the atmosphere. A summary of known $PM_{2.5}$ monitoring networks, chemical transport models, satellite-based estimates of $PM_{2.5}$, and the identified health impacts of exposure to ambient $PM_{2.5}$ are also presented.

Existing networks throughout North America and Europe use a variety of methods and assumptions to infer $PM_{2.5}$ chemical composition, however no globally consistent standard exists. Chapter 3 explains the techniques used to infer $PM_{2.5}$ chemical composition from individual filter samples. Various chemical analysis techniques were developed and refined to gather as much chemical composition information as possible from the collected, 25 mm filter samples used by SPARTAN. These analysis techniques lead to standardized procedures for determining total $PM_{2.5}$ concentration from gravimetric analysis, surface reflectance measurements for estimating black carbon content, and filter extraction for water-soluble ion and trace element analysis through ion chromatography and inductively coupled plasma – mass spectrometry, respectively. To evaluate the techniques used, results obtained from SPARTAN methods are compared to those from spatially collocated previous studies, where available. The global variation of $PM_{2.5}$ mass and chemical composition at SPARTAN sites is discussed. Measurements of chemical composition offer insight into the aerosol processes and sources that influence the spatial and temporal variation in total $PM_{2.5}$ concentrations.

Chemical transport models are employed in a variety of ways to probe the spatial and temporal variation of $PM_{2.5}$ in various regions. In Chapter 4, a global chemical transport model (GEOS-Chem) is constrained by satellite-based estimates of $PM_{2.5}$ to increase accuracy and resolution. SPARTAN measurements also inform modifications to the simulation, such as inclusion of an anthropogenic dust emission inventory and updated secondary organic aerosol formation scheme. This modified simulation is compared to $PM_{2.5}$ compositional measurements and used to interpret the globally dispersed $PM_{2.5}$ measurements from SPARTAN to provide insight into the sources and

processes that influence the global spatial variation in $PM_{2.5}$ composition through sensitivity simulations. Sensitivity simulations are also used explore the annual average influence of seven emission source categories on global population-weighted $PM_{2.5}$.

Lastly, Chapter 5 describes the initial interpretation of collocated SPARTAN measurements and AERONET AOD to examine the spatial variation in the relationship between ground-level $PM_{2.5}$ and total-column AOD. The measured $PM_{2.5}$ to AOD relationship (η) is used to evaluate potential bias in the simulated relationship from the GEOS-Chem global chemical transport model. Continuous, time-resolved aerosol scatter from nephelometer measurements and sun photometers coupled with time-integrated filter samples provides the unique ability to investigate the factors affecting η at sampling sites. Thus, measurements of ground-based scatter and AOD at satellite-overpass times (10:00 to 12:00 and 13:00 to 15:00 local time) and 24-hour averages are used along with inferred 24-hour average $PM_{2.5}$ concentrations to decompose η into three related variables. These variables, effective scale height, diurnal variation, and mass scattering efficiency, are compared to modelled values.

Overall conclusions and suggestions for future work are presented in Chapter 6.

Chapter 2 Background

2.1 Atmospheric Aerosol

Atmospheric aerosols play a significant role in visibility (Li et al., 2016a; Malm et al., 1994), climate (Bellouin et al., 2005; IPCC, 2013; Wild, 2009), and air quality (Fuzzi et al., 2015; West et al., 2016). Aerosols play a major role in visibility reduction in urban and rural areas due to their ability to scatter and absorb solar radiation (Anon, 2005; Park et al., 2006). The radiation budget is directly influenced by scattering and absorbing of solar radiation by aerosols (Pandis et al., 1995). By acting as cloud condensation nuclei, aerosols influence climate indirectly by altering the formation, lifetime, and radiative properties of clouds (Jones et al., 1994; Pandis and Cruz, 1998; Seinfeld and Pandis, 2016), however the role of aerosols is the most uncertain of known effects on climate (IPCC, 2013). Aerosols also disturb ecosystems as they are shown to influence acid deposition and delivery of nutrients such as nitrogen (Driscoll et al., 2001, 2003). Aerosols with a median aerodynamic diameter of 2.5 μm or less have been shown to be a leading risk factor for increased mortality and morbidity (Dockery et al., 1993; Forouzanfar et al., 2016; Hoek et al., 2013). A clear understanding of ground-level aerosol concentration, composition, and sources is necessary to provide insight into their extensive impacts on the atmosphere, climate, and human health.

Atmospheric aerosols are comprised of many different components that originate from both natural and anthropogenic sources and range in diameter from less than 0.01 μm to over 50 μm. Aerosols can generally be classified as primary, which are those that are emitted directly into the atmosphere as particles, or secondary, that are formed in the

atmosphere from precursor gases (Seinfeld and Pandis, 2016). Ultrafine particles are less than 0.1 μm in diameter and are made up of fresh aerosols that are formed by nucleation or primary particles from combustion sources. Coarse particles are those with a diameter larger than 2.5 μm and predominantly consist of primary aerosols that are emitted directly into the atmosphere through mechanical processes such as re-suspension of industrial dust, fly ash, suspension of soil (e.g. farming, unpaved roads, etc.), mineral dust from arid and semi-arid regions, construction, demolition, and ocean spray. Fine particles, with a diameter between 0.1 μm and 2.5 μm, can also result from primary emissions and from the growth of ultrafine particles. Although ultrafine particles have the predominant contribution to the total aerosol number, particles with a diameter exceeding 0.1 μm comprise the majority of the total aerosol mass. The mechanisms for conversion of ultrafine to fine particles are coagulation and condensation of low-volatility vapours.

Coagulation occurs when two particles collide and stick together to form a single particle. Processes that may lead to particle collisions include Brownian motion, turbulent shear, and differential settling, however Brownian motion is shown to be the dominant process (Kerminen and Wexler, 1995). Ultrafine-fine particle collisions and ultrafine-ultrafine particle collisions are most common coagulation events, leading to coagulation as the dominant loss mechanism for particle number. Though, ultrafine-fine particle collisions contribute negligibly to the growth of fine particles due to the significant size difference. Conversely, the collision of ultrafine particles with each other can lead to the generation of fine particles, although this is generally found not to be the dominant mechanism for conversion of ultrafine to fine particles (Seinfeld and Pandis, 2016). Condensation of low-volatility vapours formed by chemical reactions of precursor gases

and chemical processing of primary emissions play a vital role in particle growth and changes to chemical composition.

2.1.1 Inorganic Aerosol

Condensation of H_2SO_4 has been shown to be the dominant process for the growth of particles, especially in urban regions with high concentrations of SO_2 (Gaydos and Stanier, 2005). Sulfuric acid is primarily produced in the atmosphere by oxidation of gaseous SO_2, which can occur in both the gas- and aqueous-phase under atmospheric conditions. The majority of sulfuric acid is produced through in-cloud oxidation of SO_2 by H_2O_2. Under pH ranges of atmospheric interest, SO_2 rapidly dissociates in water to form bisulfite (HSO_3^-) as shown in reactions R1 and R2. The bisulfite ion reacts with H_2O_2 by nucleophilic displacement to produce peroxymonosulfurous acid (SO_2OOH^-) by R3, which further reacts with a proton to produce H_2SO_4 as shown in R4.

$$SO_2\,(g) + H_2O \rightleftharpoons SO_2{\bullet}H_2O \quad \textbf{(R1)}$$

$$SO_2{\bullet}H_2O \rightleftharpoons H^+\,(aq) + HSO_3^-\,(aq) \quad \textbf{(R2)}$$

$$HSO_3^-\,(aq) + H_2O_2\,(aq) \rightleftharpoons SO_2OOH^-\,(aq) + H_2O \quad \textbf{(R3)}$$

$$SO_2OOH^-\,(aq) + H^+\,(aq) \rightarrow H_2SO_4\,(aq) \quad \textbf{(R4)}$$

In the gas-phase, the dominant mechanism for oxidation of SO_2 is reaction with the hydroxyl radical that is produced as shown by R5 – R6. Sulfuric acid is then formed in the atmosphere following the R7 – R9 reaction sequence. Due to the hygroscopicity of H_2SO_4, it will absorb water even at very low relative humidity and readily condenses

under all atmospheric conditions (R10), leading to particle growth and possibility of chemical modification of the aerosol.

$$O_3\,(g) + h\nu \rightarrow O_2\,(g) + O(^1D)\,(g) \quad \textbf{(R5)}$$

$$O(^1D)\,(g) + H_2O\,(g) \rightarrow 2{\cdot}OH\,(g) \quad \textbf{(R6)}$$

$$SO_2\,(g) + {\cdot}OH\,(g) \rightarrow HOSO_2{\cdot}\,(g) \quad \textbf{(R7)}$$

$$HOSO_2{\cdot}\,(g) + O_2\,(g) \rightarrow SO_3\,(g) + HO_2{\cdot}\,(g) \quad \textbf{(R8)}$$

$$SO_3\,(g) + H_2O\,(g) \rightarrow H_2SO_4\,(g) \quad \textbf{(R9)}$$

$$H_2SO_4\,(g) \rightleftharpoons H_2SO_4\,(aq) \quad \textbf{(R10)}$$

When available, aqueous H_2SO_4 aerosol will take up gaseous ammonia, leading to the modification of the chemical composition of the aerosol. However, if the amount of NH_3 is very low, aerosols will dominantly consist of aqueous H_2SO_4. As more NH_3 becomes available, H_2SO_4 will dissociate to form HSO_4^-, allowing for the formation of NH_4HSO_4 (R11). When there is sufficient NH_3 to neutralize the H_2SO_4, the HSO_4^- will dissociate further and $(NH_4)_2SO_4$ is the preferred composition of the aerosol phase (R12). Once the available H_2SO_4 is fully neutralized, and in the absence of additional species, excess ammonia remains in the gas phase.

$$NH_4^+\,(aq) + HSO_4^-\,(aq) \rightleftharpoons NH_4HSO_4\,(s) \quad \textbf{(R11)}$$

$$2NH_4^+\,(aq) + SO_4^{2-}\,(aq) \rightleftharpoons (NH_4)_2SO_4\,(s) \quad \textbf{(R12)}$$

Although H_2SO_4 is readily produced under atmospheric conditions, measurement and model studies suggest that condensation of H_2SO_4 alone is not sufficient for particle

growth (Jung et al., 2006; Zhang et al., 2004). Condensation of other gases, such as HNO_3, as well as chemical processing (Zhang and Wexler, 2002) are additional mechanisms that promote aerosol growth.

Nitric acid has an important role in aerosol formation, growth, and chemical modification and is the primary sink for atmospheric NO_x ($NO + NO_2$). In the daytime NO_2 is oxidized to HNO_3 by the hydroxyl radical as in R13, and at night it is oxidized by O_3 as in R14 – R16 (Jacob, 2000). Nitric acid is highly soluble and rapidly dissociates once in solution to form nitrate (R17). Depending on atmospheric conditions, gaseous HNO_3 can also react with available NH_3 to produce either aqueous-phase NH_4^+ and NO_3^- (R18) or solid NH_4NO_3 (R19).

$$NO_2\,(g) + {}^{\cdot}OH\,(g) \rightarrow HNO_3\,(g) \quad \textbf{(R13)}$$

$$NO_2\,(g) + O_3\,(g) \rightarrow NO_3\,(g) + O\,(g) \quad \textbf{(R14)}$$

$$NO_3\,(g) + NO_2\,(g) \rightarrow N_2O_5\,(g) \quad \textbf{(R15)}$$

$$N_2O_5\,(g) + H_2O\,(aq) \rightarrow 2HNO_3\,(g) \quad \textbf{(R16)}$$

$$HNO_3\,(aq) \rightarrow NO_3^-\,(aq) + H^+\,(aq) \quad \textbf{(R17)}$$

$$NH_3\,(g) + HNO_3\,(g) \rightleftharpoons NH_4^+\,(aq) + NO_3^-\,(aq) \quad \textbf{(R18)}$$

$$NH_3\,(g) + HNO_3\,(g) \rightleftharpoons NH_4NO_3\,(s) \quad \textbf{(R19)}$$

Similar to an H_2SO_4 aerosol, the availability of NH_3 plays a key role in determining the extent of NH_4NO_3 formation. Since $(NH_4)_2SO_4$ is the preferred form of sulfate, in an ammonia-poor environment the available NH_3 will neutralize sulfate, and

drive nitrate into the gas phase. The remaining near-zero free ammonia also means NH_4NO_3 formation is negligible. In an ammonia-rich environment the NH_3 that does not react with sulfate will be available to react with nitrate to produce NH_4NO_3. However, in some rural regions where NH_3 is plentiful but HNO_3 levels are low, NH_4NO_3 formation is limited by the availability of HNO_3. Although the chemical mechanisms responsible for growth and chemical composition of inorganic aerosol species are complex and plentiful, condensation of organic species also play a key role in atmospheric aerosol growth and chemical modification (Kerminen et al., 2000).

2.1.2 Organic Aerosol

Similar to inorganic species, organic aerosol (OA) can be introduced into the atmosphere through formation of secondary organic aerosol (SOA) by conversion of volatile organic compounds (VOCs) to low-volatility condensable vapours or directly emitted as particles. Volatile and semi-volatile organic vapours can be functionalized by multiple oxidation pathways by the hydroxyl radical, ozone, and the nitrate radical that can lead to products that are more polar and less volatile than the parent organic compound. These reactions take place with both large VOCs (e.g. aromatics and long-chain alkanes) and relatively small compounds (e.g. isoprene) to produce functional groups such as hydroxyl, hydroperoxy, carbonyl, esters, and nitrooxy compounds. The SOA material produced from oxidation will vary depending on the oxidant that catalyzed the reaction, resulting in large variety of condensable products leading to ambient SOA consisting of hundreds of organic compounds (Griffin et al., 1999; Pandis et al., 1995).

Once in the particle phase, SOA can continue to undergo chemical modification that leads to aerosol growth. For example, dimerization creates compounds with double

the number of carbon atoms that are non-volatile, eliminating volatilization back into the gas-phase. Water-soluble SOA can undergo aqueous-phase oxidation and oligomerization that leads to highly oxidized products that remain in the aerosol if the water evaporates. In addition, heterogeneous gas-aerosol reactions can occur that further oxidize SOA once in the aerosol. The breadth of chemical reactions and parent VOC compounds that lead to SOA formation and subsequent modification means that identification and quantification of all individual components present in SOA is generally not possible.

Organic aerosols emitted directly into the atmosphere from sources, such as vehicles and biomass burning, are known as primary organic aerosol (POA). Emissions from motor vehicles include both gaseous organic compounds as well as particle phase POA and black carbon (BC). A significant fraction of POA from vehicles are semi-volatile under atmospheric conditions and comprises thousands of compounds from incomplete combustion, unburned diesel or gasoline, and unburned oil. Not all POA comes from combustion of fossil fuels, more than half of POA emissions over the United States come from wildfire, agricultural burning, and residential heating (Seinfeld and Pandis, 2016). Most of the emitted POA is found to be volatile enough to evaporate once it has been diluted from the source (Robinson et al., 2007). Once the POA has evaporated it can then react with gas phase oxidants, such as the hydroxyl radical and O_3, to form low-volatility oxidation products that can partition back into the particle phase or condense onto pre-existing particles to promote aerosol growth. The cycle of evaporation-reaction-condensation of POA leads to significant differences in chemical nature between the originally emitted POA and the POA found in aerosols. Thus, the complexity of the molecular constituency of OA coupled with numerous sources, sinks,

and chemical modification pathways, make determining the original source of POA and SOA challenging.

2.1.3 Aerosol Removal Mechanisms

Particles are ultimately removed from the atmosphere through either dry or wet deposition. Wet deposition is the process by which material in the air is scavenged by clouds, fog droplets, rain, or snow, and is consequently carried to a surface such as the ground, vegetation, or man-made structures. Dry deposition is the transport of gaseous or particulate species from the atmosphere onto surfaces in the absence of precipitation. The level of atmospheric turbulence, the chemical properties of the aerosol, and the nature of the surface the aerosol is deposited on are factors that influence the dry deposition of an aerosol. The relative importance of dry deposition versus wet deposition in a given system depends on the solubility of the species in water, the amount of precipitation in the area, terrain, and the type of surfaces available (Seinfeld and Pandis, 2006). Coarse mode particles are generally removed by dry deposition due to their large size creating a natural settling velocity and decreasing their water solubility.

2.1.4 Health Impacts of Fine Particulate Matter

The enormous burden of disease associated with exposure to $PM_{2.5}$ has been progressively recognized by governments and non-government organizations as a major public health concern. The most recent GBD study attributed approximately 4.1 million premature deaths to exposure to ambient $PM_{2.5}$ in 2016 (Gakidou et al., 2017). Various health impact assessments and epidemiological studies have identified a wide-range of health implications from ambient $PM_{2.5}$ exposure such as ischemic heart disease (e.g.

Ostro et al., 2010; WHO, 2006), low birth weight (e.g. Bell et al., 2010; Wilhelm et al., 2012), chronic obstructive pulmonary disease (e.g. Hogg et al., 2004; Silbajoris et al., 2011), type-2 diabetes (e.g. Chen et al., 2013), cancer (IARC, 2013), neurological disorders in adults (e.g. Ranft et al., 2009) and neurological development in children (e.g. Freire et al., 2010). Although emerging evidence on neurological effects are not conclusive, if further studies corroborate initial findings the global burden of disease associated with $PM_{2.5}$ could be significantly impacted. However, mortality and morbidity effects of $PM_{2.5}$ exposure are predominately in the respiratory and cardiovascular systems, with approximately two thirds accounted for by cardiovascular diseases alone (Brook et al., 2010).

When breathed in, $PM_{2.5}$ elicits adverse health effects by breaching the body's nature defences due to its small size and eventually moving deep into the respiratory system, and ultimately the circulatory system. Exposure to $PM_{2.5}$ has been shown to promote inflammatory modifications in the cardiovascular system, which may lead to atherosclerosis and infarction (Hoffmann et al., 2009; Schicker et al., 2009). Coagulation modifications caused by increased fibrinogen from $PM_{2.5}$ exposure eventually cause coronary artery disease (Brook et al., 2010). Respiratory system damage, causing COPD, asthma, and lung cancer, has been linked to inflammation and oxidative stress from activated of inflammatory cells (Chung and Adcock, 2008; Hogg et al., 2004; Silbajoris et al., 2011). The harmful effects of $PM_{2.5}$ have led to the development of annual mean and 24-hour air quality guidelines designed to limit population exposure.

Along with other criteria ground-level pollutants (O_3, NO_2, and SO_2) the World Health Organization (WHO) provides global Air Quality Guidelines (AQGs) for $PM_{2.5}$ to

limit the adverse health consequences of exposure. However, recent cohort studies show poor health associations at $PM_{2.5}$ exposure below the WHO guideline of 10 μg m^{-3} (Correia et al., 2013; Crouse et al., 2012; Pinault et al., 2016), thus no minimum $PM_{2.5}$ threshold has been identified below which adverse effects do not occur. The WHO AQG is provided in Table 2.1 along with interim targets. Interim targets are incremental steps provided for regions with high levels of $PM_{2.5}$ that, for each target achieved, is expected to offer significant acute and chronic health benefits (WHO, 2006). Despite these guidelines, it is estimated that over 85 % of the world's population live in regions that exceed the WHO guideline for annual average exposure of 10 μg m^{-3} (Brauer et al., 2016; van Donkelaar et al., 2016).

Table 2.1. WHO air quality guidelines and interim targets for annual mean $PM_{2.5}$ concentrations (WHO, 2006)

	$PM_{2.5}$ (μg m^{-3})	**Basis for selected level**
Air Quality Guideline (AQG)	10	Lowest level at which total, cardiopulmonary and lung cancer mortality have been shown to increase (> 95 % confidence) in response to long-term $PM_{2.5}$ exposure
Interim Target-3 (IT-3)	15	This level is shown to reduce mortality risk by 6 % [2-11 %] relative to IT-2. Other health benefits have been shown.
Interim Target-2 (IT-2)	25	This level is shown to reduce mortality risk by 6 % [2-11 %] relative to IT-1. Other health benefits have been shown.
Interim Target-1 (IT-1)	35	This level is associated with ~ 15 % higher long-term mortality risk relative to AQG level.

Few epidemiological and health impact studies have investigated the correlation between adverse health impacts and specific $PM_{2.5}$ chemical components. Elevated concentrations of elements found in $PM_{2.5}$ in trace amounts, such as Ni, V, Cu, Zn, K, Ti, As, and Cr have been implicated in increased cardiovascular mortality and morbidity (e.g. Chen and Lippmann, 2009; Ostro et al., 2007). Causal relationships between sulfate

and nitrate exposure and all-cause, cardiovascular, and respiratory mortality have been reported (WHO, 2013b; Atkinson et al., 2015), however controlled sulfate exposure experiments have only shown adverse health impacts at concentrations far exceeding ambient concentrations (Rohr and Wyzga, 2012). Work by Baumgartner et al., (2014) found that exposure to BC was more strongly associated with elevated systolic blood pressure, a marker for cardiovascular disease, than total PM mass. Janssen et al., (2011) suggests that adverse health effects associated with an increase in ambient BC concentrations would be greater than effects in increased $PM_{2.5}$ or PM_{10} concentration of the amount. Cheung et al., (2009) report correlations between oxidative potential and water-soluble and water-insoluble organic carbon (OC), and links between OA and mortality have also been described (Ostro et al., 2010). However, since OA is a dominant fraction of $PM_{2.5}$ mass, it is difficult to isolate the health outcomes from this component (Fuzzi et al., 2015). Although the role of chemical composition in the toxicity of ambient $PM_{2.5}$ is an active area of research, the current evidence is insufficient to determine the exposure-response curves for individual components needed for epidemiological studies. Thus, total $PM_{2.5}$ mass remains the most robust indicator of increased mortality and morbidity.

2.2 Ground-Based $PM_{2.5}$ Monitoring

Figure 2.1 shows the known locations of monitoring stations providing annual average $PM_{2.5}$ and PM_{10} measurements for the years 2008 – 2013 collected for the GBD from the WHO ambient air pollution in cities database, GBD collaborators, literature searches, and official monitoring networks (Brauer et al., 2016). Observations of PM_{10} are also included to provide increased spatial coverage in regions without direct $PM_{2.5}$

measurements and are scaled to represent $PM_{2.5}$ using available $PM_{2.5}/PM_{10}$ ratios (Brauer et al., 2016). Individual studies provide valuable $PM_{2.5}$ data, however are often short-term. Official monitoring networks are found in North America, Europe, Taiwan, and parts of Asia, with data intermittently available in other locations.

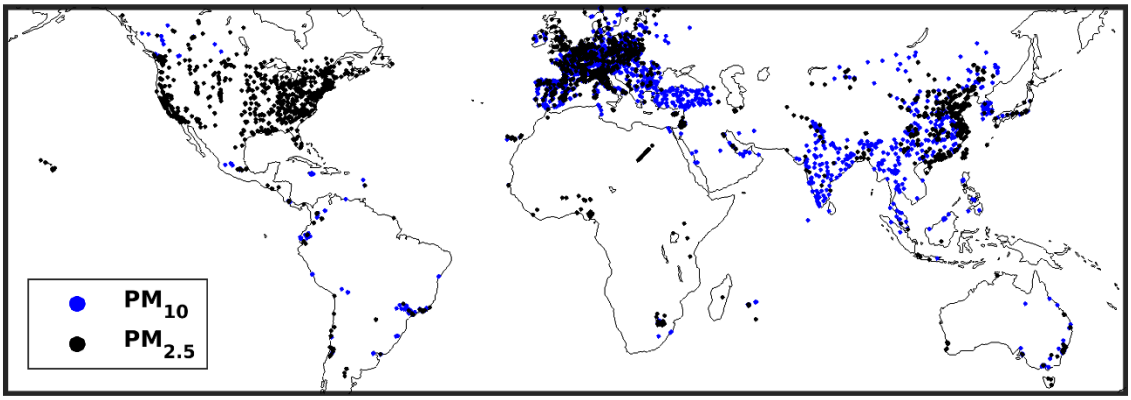

Figure 2.1. Known monitor locations with measured PM_{10} and $PM_{2.5}$, collected from 2008-2013 for the Global Burden of Disease.

In the United States, the Environmental Protection Agency as well as state and local agencies aggregate $PM_{2.5}$ data from close to 1000 monitoring sites and upload data into the Air Quality System (AQS) for easy access to users. Major networks that upload data into the AQS database include the Clean Air Status and Trends Network (CASTNET), the Speciation Trends Network (STN), and the Interagency Monitoring of Protected Visual Environments (IMPROVE). The two former networks monitor criteria pollutants for maintenance of public health and are often located in urban areas. On the other hand, IMPROVE was implemented as a long-term monitoring program to track changes in visibility and determine the causal mechanism for reduced visibility in national parks and wilderness areas. The National Air Pollution Surveillance Program (NAPS) is a Canadian network established in 1969 to monitor and assess the quality of

ambient air in the populated regions of Canada. There are currently 286 sites in 203 communities located in every province and territory. NAPS data are used to assess air quality trends and the impact on health and environment.

AirBase is the European air quality database that is maintained by the European Environment Agency (EEA). The database contains air quality monitoring data and information submitted by more than 30 participating countries throughout Europe. AirBase contains data from Euroairnet, the European air quality monitoring network that was developed in 1996 to support the EEA, as well as other country-based monitoring sites. The European Monitoring and Evaluation Program (EMEP) is another network that collects $PM_{2.5}$ data along with other criteria pollutants. EMEP is a scientifically based and policy-driven program under the Convention on Long-range Transboundary Air Pollution, signed in 1979, for international co-operation to solve transboundary air pollution.

Growing networks exist in parts of Asia, such as India and China, but data are often annually averaged, not archived, and measurement techniques and specific monitoring locations are often unknown. Data collected from the developing $PM_{2.5}$ monitoring network in China was not available at the time of this work. In addition, many locations provide PM_{10} measurements rather than $PM_{2.5}$, although useful for certain applications, does not provide accurate $PM_{2.5}$ information. Higher temporal resolution and direct measurements of $PM_{2.5}$ in these regions would provide much needed data for health-impact studies and evaluation of global CTMs and satellite-based $PM_{2.5}$ estimates.

2.3 Chemical Transport Models

Insight into the state of atmospheric constituents, such as aerosols and gases, can be accomplished in the absence of observations using modelling. Chemical transport models use emission inventories, meteorological data sets, and chemical and microphysical equations that represent aerosol and gaseous atmospheric processes to simulate the spatial and temporal evolution of aerosol and gaseous compounds. Atmospheric aerosol processes accounted for in CTMs include nucleation, wet and dry deposition, condensation, coagulation, atmospheric transport, and chemistry feedback mechanisms. The ability to successfully integrate these various processes into global and regional CTMs has only been possible as knowledge and understanding of aerosols has advanced over recent decades.

Chemical transport models have been used extensively to offer insight into the regional and global distribution of $PM_{2.5}$ mass and chemical constituents. Kim et al., (2015) used a CTM to integrate and interpret satellite, aircraft, and ground-based measurements in the Southeast US to understand sources and trends in aerosol concentrations. Source attribution of arctic BC concentrations by Xu et al., (2017) with a CTM found significant seasonally and altitude varying influence from Europe, Asia, and North America. Anenberg et al., (2010) used a global atmospheric model to estimate global population exposure to $PM_{2.5}$ and found estimated $PM_{2.5}$ mortality rates to be about 50 % higher than previous measurement-based estimates due to inclusion of rural and under-sampled regions. The power of CTMs has also been harnessed to investigate the effects of emission mitigation strategies. Lee et al., (2015) used an adjoint model to estimate the response of global $PM_{2.5}$-related mortality to changes in local precursor

emissions and reported significant regional variation. Reducing NH_3 emissions is Europe was shown to be the most important for reducing mortality associated with $PM_{2.5}$ exposure, whereas large global benefits are expected from reducing SO_2 emissions in South Asia rather than NH_3 (Lee et al., 2015). Megaritis et al., (2013) examined the response of European $PM_{2.5}$ concentrations for 50 % reductions in precursor gases and anthropogenic primary OA and found reducing NH_3 is expected to have the largest impact on reducing $PM_{2.5}$ in winter and summer. Overall, advancement of global and regional CTMs have led to increased understanding of the processes and sources affecting ground-level $PM_{2.5}$ concentrations.

2.4 Satellite Remote Sensing Estimates of $PM_{2.5}$

Satellites provide the spatiotemporal coverage needed to monitor atmospheric aerosol concentration at the global scale. Satellite remote sensing of aerosols measures solar backscatter and relies on aerosol-induced changes in reflectance. Retrieval algorithms use the measured backscatter to derive the aerosol optical depth (AOD), a dimensionless parameter that describes the columnar extinction (scattering + absorption) of solar radiation by aerosols. This technique has allowed for unprecedented global coverage for monitoring of atmospheric aerosols. Satellite retrievals have a data record extending more than a decade and provide one of the only long-term, observationally based data sources for determining ground-based aerosol concentrations in the extensive regions of world that lack monitoring.

Applications can benefit from design differences between satellite instruments and retrieval algorithms. For example, retrievals from the MODerate resolution Imaging

Spectroradiometer (MODIS) instrument (Levy et al., 2007) provide accurate AOD over dark surfaces with near-global daily coverage, but has experienced unknown changes to instrument sensitivity over time. The Multiangle Imaging SpectroRadiometer (MISR) instrument (Diner et al., 2005; Martonchik et al., 2009) has a narrower swath width compared to MODIS, taking about a week to complete global coverage, but has shown spectral stability throughout its lifetime (Zhang and Reid, 2010). The Sea-viewing Wide Field-of-view Sensor (SeaWiFS) (Hsu et al., 2013) is less accurate over land compared to MODIS and MISR , but provided instrument sensitivity over its entire mission from 1997 to 2010, making it relevant for trend studies.

The relationship between ground-level $PM_{2.5}$ concentrations and columnar AOD is influenced by the aerosol vertical profile, aerosol composition, and humidity, which depend on meteorology and emissions. Satellite-based estimates of $PM_{2.5}$ concentrations employ a CTM to simulate the ratio of ground-level $PM_{2.5}$ to columnar AOD. This technique was first demonstrated by Liu et al., (2004) using the GEOS (Goddard Earth Observing System)-Chem chemical transport model and AOD retrieved from the MISR instrument over the United States for 2001. This technique was further developed and extended globally to produce the first global, long-term mean, satellite-based estimates of ground-level $PM_{2.5}$ from 2001-2006 using data from the MISR and MODIS instruments (van Donkelaar et al., 2010). Boys et al., (2014) combined AOD from MISR and SeaWiFS instruments along with spatiotemporal variation of the $PM_{2.5}$ and AOD relationship from GEOS-Chem to create a time series of global $PM_{2.5}$ trends. Most recent global ground-based $PM_{2.5}$ estimates combine AOD from various satellite instruments

weighted inversely by error with respect to ground-based AOD measurements (van Donkelaar et al., 2016).

Despite the well-known adverse health effects of $PM_{2.5}$ exposure, ground-based measurement networks that monitor $PM_{2.5}$ are largely limited to North America and Europe, with emerging networks in Asia. Available measurements of PM_{10} outside of North America and Europe supplement the limited $PM_{2.5}$ measurements, but the extrapolation to $PM_{2.5}$ concentration is uncertain. Satellite remote sensing, coupled with a global chemical transport model, has become a powerful technique for estimating ground-level $PM_{2.5}$ concentrations where monitors do not exist. Satellite-based estimates of $PM_{2.5}$ show promising consistency with available *in situ* monitors, however uncertainty does exist. It is estimated that this uncertainty is driven by the modelled relationship between $PM_{2.5}$ and AOD that is used to infer $PM_{2.5}$ from total-column satellite AOD retrievals. SPARTAN was designed to evaluate and improve satellite-based estimates of $PM_{2.5}$ by collocating $PM_{2.5}$ measurements with AERONET sites that measure AOD. As shown in Figure 1.2, SPARTAN has significantly increased the number of sites with collocated measurements to provide empirical $PM_{2.5}$ to AOD relationships for evaluation of the modelled values, separating SPARTAN sampling sites from those of other networks and monitoring campaigns. In addition, SPARTAN has become the only global network that measures both $PM_{2.5}$ mass and chemical composition using consistent instrumentation and standardized protocols. SPARTAN offers a unique global dataset that contributes to the evaluation of global CTMs and ultimately the improvement of satellite-based estimates of $PM_{2.5}$.

Chapter 3 Global Variation in $PM_{2.5}$ Chemical Composition

This chapter draws on an article published in *Atmospheric Chemistry and Physics*, 16, 9629–9653, 2016, in which the author of this thesis is the co-lead author. Data obtained after publication has been included and all results updated. Additional information has also been included. All text and figures included are those of the author of this thesis, more details on author contributions are provided in Appendix A.

3.1 Introduction

Various adverse health impacts, such as cardiovascular disease and lung cancer, have been linked to ambient $PM_{2.5}$ exposure (WHO, 2006). The WHO annual average air quality guideline for $PM_{2.5}$ is set at 10 $\mu g\ m^{-3}$, however many regions far exceed this long-term recommendation (Brauer et al., 2016; van Donkelaar et al., 2015b). For example, it is estimated that 70 % of the population in East Asia in 2010 – 2012 were living above the WHO Interim Target-1 of 35 $\mu g\ m^{-3}$ annual average $PM_{2.5}$ exposure (van Donkelaar et al., 2015b). The influence of atmospheric aerosols on radiative forcing, the balance of incoming and outgoing energy in the atmosphere-Earth system, is the most uncertain agent contributing to climate change (IPCC, 2013). The absolute mass of aerosols, as well as their chemical composition, play a critical role in atmospheric visibility (Malm et al., 1994). Additional global $PM_{2.5}$ measurements are needed to increase the accuracy of global $PM_{2.5}$ concentration estimates, and to better understand $PM_{2.5}$ chemical components and the processes involved in its formation.

Measurements of $PM_{2.5}$ chemical composition provide information for understanding aerosol properties as well as the sources and processes contributing to $PM_{2.5}$ formation. Bell (2012) found that $PM_{2.5}$ mass and composition vary across US

counties and between seasons and are associated with variation in hospital admissions for cardiovascular and respiratory disease. Variation in hospitalizations were most closely associated with enhanced elemental carbon, Ni, and V in $PM_{2.5}$. Ostro et al. (2010) found that $PM_{2.5}$ components derived from fossil fuel combustion (SO_4^{2-} and OC) and from crustal origin (mineral and road dust) were associated with the greatest risks from cardiopulmonary disease and all-cause mortality. The health impacts of specific chemical components of $PM_{2.5}$ have been reviewed previously by Lippmann (2014) however, the long-term health impacts of specific chemical species remain not well understood. The lack of global monitoring of $PM_{2.5}$ chemical composition hinders health impact studies of various chemical mixtures (Bell et al., 2007). Sampling has been consistently conducted in North America (Hand et al., 2012b) and Europe (van Dingenen et al., 2004; Putaud et al., 2010) however, there remains a need for globally consistent measurements of PM mass and chemical composition.

Satellite remote sensing observations of columnar AOD provide information for estimating population exposure to $PM_{2.5}$ on a global scale, which is especially important for regions with little or no ground-based monitoring (Brauer et al., 2016; van Donkelaar et al., 2015b). Even regions with dense monitoring networks benefit from satellite observations to offer additional information on the temporal and spatial pattern of $PM_{2.5}$ (Kloog et al., 2011, 2013; Lee et al., 2012). Standardized measurements of $PM_{2.5}$, collocated with ground-based measurements of AOD, are needed to evaluate and improve satellite-based estimates of $PM_{2.5}$. To meet this need, the measurement network SPARTAN (Surface PARTiculate mAtter Network) is collocated with sites where ground-based AOD measurements are also made (Holben et al., 1998; Snider et al.,

2015). SPARTAN measurements include continuous sampling of $PM_{2.5}$ and PM_{coarse} ($PM_{10-2.5}$) mass and chemical composition over the period from June 2013 – July 2017 in densely-populated regions.

The ongoing effort to quantify global $PM_{2.5}$ chemical composition from SPARTAN measurements is discussed in this chapter. Section 3.2 describes the methods for inferring average $PM_{2.5}$ mass, chemical species, and definitions of aerosol categories (e.g. ammoniated sulfate, crustal material, sea salt) as a function of specific chemical species. Section 3.3 outlines the sources of uncertainty in reported measurements. Section 3.4 compares the relative chemical composition determined from SPARTAN to that from collocated previous studies, where available, and discusses the spatial and temporal variation in measured $PM_{2.5}$ chemical quantities. Conclusions are presented in section 3.5.

3.2 Inferring $PM_{2.5}$ Mass and Chemical Composition

SPARTAN collects $PM_{2.5}$ on 25 mm 2 μm pore-size PTFE filters (225-2726, SKC) with an Airphoton SS4i automated cascade filter sampler. Figure 3.1 shows a diagram of the filter assembly. Each filter sampler houses a removable plastic filter cartridge that protects seven sequentially sampled filter pairs as well as a field blank. Aerosols larger than a mean aerodynamic diameter above 10 μm are collected by a greased impactor plate. After passing the impactor plate, aerosols with a diameter between 2.5 μm and 10 μm (PM_{coarse}), are collected by a greased nuclepore filter membrane (custom grease-coated E8025-MB, SPI). $PM_{2.5}$ passes through the pores of the nuclepore filter to be collected on PTFE filters for analysis.

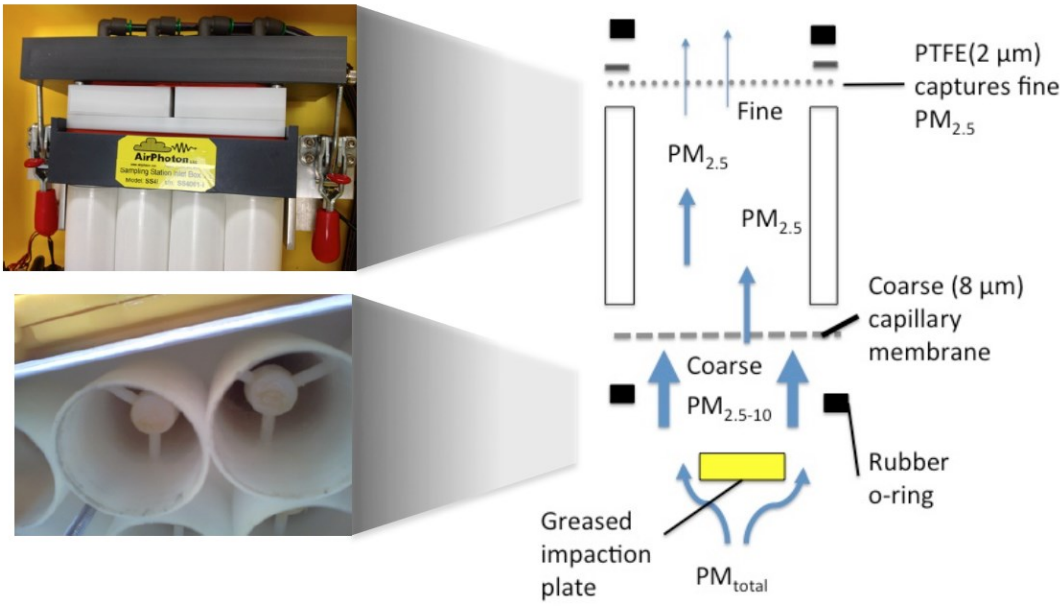

Figure 3.1. Diagram of AirPhoton filter assembly. Blue arrows represent the direction of air flow at 4 liters per minute. The air stream passes through a bug screen followed by a greased impaction plate to remove PM larger than 10 µm. The 8 µm capillary filter has 5 % porosity and removes PM_{coarse}. The 2 µm PTFE filter capture $PM_{2.5}$.

The SPARTAN sampling strategy is designed to be cost-effective and to minimize the loss of semi-volatile species, such as ammonium nitrate, by sampling a single diurnal cycle over a 9-day period. Sampling begins and ends at 09:00 local time when ambient temperatures are low and uses regular, staggered sampling periods as described in Appendix B8.4. When sampling is complete, filter cartridges are stored on site in sealed, air-tight containers at room temperature for a maximum of one week prior to shipment. The residence time of the filters in the sampling station (maximum 54 days), under ambient conditions removes the benefit of storing and shipping sampled filters under controlled temperatures. Discussion of possible sources of uncertainty from this protocol are found in section 3.3. Following the protocol used by The Interagency Monitoring of Protected Visual Environments (IMPROVE; Hand and Malm, 2006) in the

United States, filter cartridges are shipped from the sampling site to our handling facility at Dalhousie University at room temperature in sealed, air-tight containers.

Sampled filters are carefully removed from the protective cartridge to begin analysis (Appendix B2.0). When post-weighing (Appendix B1.0) and BC (Appendix B3.0) analysis of the sampled cartridge is complete, each filter is cut in half with a ceramic blade (Appendix B4.2) following the approaches of Zhang et al. (2013) and Gibson et al. (2009) to maximize the information extracted from the filters. One half of each filter is extracted for analysis through ion chromatography (IC) to determine water-soluble ion concentrations (Appendix B4.0, Thermo Dionex ICS-1000 and ICS-1100). The other filter half is analysed for trace element concentrations with inductively couple plasma – mass spectrometry (ICP-MS, Appendix B5.0, Thermo Scientific X-Series 2). All filter analysis is conducted at Dalhousie University following SPARTAN Standard Operating Procedures as described in detail in Appendix B1.0 – B5.0. The following sections describe the instruments and equations used to infer $PM_{2.5}$ chemical composition from the components measured through the SPARTAN filter analysis methods. Equations and methods developed here draw on existing knowledge in the literature and other monitoring networks to take advantage of all available information from each sampled filter.

3.2.1 Gravimetric Analysis

All filters (PTFE, nuclepore) are pre- and post-weighed using an Ultramicro Balance (100 ng precision) in a ISO level 4 (< 100 particle cm^{-3}) cleanroom environment between 30 – 40 % relative humidity (RH) and 20 – 23 °C. Filters are equilibrated in the

cleanroom for at least 24 hours and are passed under an electrostatic blower prior to weighing. Calibration masses (1 mg, 200 mg) and reference filters are weighed at the beginning of each weighing session. The mass (μg) accumulated on the filters is determined from the difference between the pre- and post-weights. Time-integrated flow rates at ambient pressure and temperature are used to define the air volume sampled to convert the mass to mass concentration reported in μg m^{-3}. When post-weighing is completed, the filters are subsequently analyzed to determine $PM_{2.5}$ chemical composition. Table 3.1 contains a summary of the equations and accompanying references used to infer $PM_{2.5}$ chemical composition.

Table 3.1. Summary of speciation definitions and associated references.

Species	Method	Species mass (μg)	Reference
SS	IC	$2.54[Na^+]_{SS}$, where $[Na^+]_{SS} = [Na^+]_{total} - 0.1[Al]$	Malm et al., 1994; Remoundaki et al., 2013
NH_4NO_3	IC	$1.29[NO_3^-]$	Malm et al., 1994
ASO_4	IC	$[SO_4^{2-}]_{non\text{-}SS} + [NH_4^+] - 0.29[NO_3^-]$, where $[SO_4^{2-}]_{non\text{-}SS} = [SO_4^{2-}]_{total} - 0.12[Na^+]$	Dabek-Zlotorzynska et al., 2011; Henning, 2003
Na_2SO_4	IC	$0.18[Na^+]_{SS}$	Dabek-Zlotorzynska et al., 2011; Henning, 2003
CM	ICP-MS	10 x ([Al] + [Mg] + [Fe])	Wang, 2015
EBC	SSR	$20.7 \times \ln(R/R_o)$	Taha et al., 2007
TEO	ICP-MS	1.47[V] + 1.27[Ni] + 1.25[Cu] + 1.24[Zn] + 1.32[As] + 1.2[Se] + 1.07[Ag] + 1.14[Cd] + 1.2[Sb] + 1.12[Ba] + 1.23[Ce] + 1.08[Pb]	Malm et al., 1994
$PBW_{inorganic}$	κ_m	$\sum_X [f_{m,X}(RH) - 1][X]$	Kreidenweis et al., 2008
PBW_{RM}	κ_m,	$RM(1 - 1/f_{m,RM})$	Jimenez et al., 2009
RM (35 % RH)	Mass balance	$[PM_{2.5}] - \{ [EBC] + [CM] + [TEO] + [NH_4NO_3] + [SS] + [ASO_4] + [NA_2SO_4] + [PBW_{inorganic}] \}$	This study
RM (0 % RH)	Mass balance, $\kappa_{m,OM} = 0.07$	$RM(35\ \%) - PBW_{RM}$	Jimenez et al., 2009; Sun et al., 2011

3.2.2 Equivalent Black Carbon

The term "equivalent black carbon" is used following Petzold et al. (2013) for black carbon concentrations derived from optical methods rather than thermal techniques.

The black carbon content of PTFE filters is derived from surface reflectance (R) measurements taken using a Smoke Stain Reflectometer (SSR, Diffusion Systems EEL 43M, London, UK) (Quincey et al., 2009). The relative change in surface reflectance (R/R_o), from accumulation of $PM_{2.5}$ on the PTFE filters, is logarithmically related to the black carbon concentration ($\mu g\ m^{-3}$) through equation (1),

$$[EBC] = \frac{-A}{qv} ln\left(\frac{R}{R_O}\right) \quad (1)$$

where A is the filter surface area (3.1 cm^2), v is the volume of air sampled (m^3) , R is the mean measured reflectance after sampling, R_o is the reflectance prior to sampling (100), and q is the product of the reflectivity path and the mass-specific absorption cross section (σ_{SSR}, $cm^2\ \mu g^{-1}$). The reflectivity path of the PTFE filters is taken to be 1.5 due to the thickness of the filters (Taha et al., 2007). The σ_{SSR} used here is 0.1 $cm^2\ \mu g^{-1}$ adjusted to the 620 nm detection peak of the SSR from 0.06 $cm^2\ \mu g^{-1}$ used in prior studies (e.g. Barnard et al., 2008; Bond and Bergstrom, 2006).

3.2.3 Crustal Material

Crustal material (CM) consists of resuspended road dust, desert dust, soil, and sand. Following the work of Wang (2015) that describes the elemental composition of natural desert dusts, it is generalized in this study that natural CM concentration is represented by 10*([Al] + [Fe] + [Mg]). CM is represented by elemental aluminum, iron, and magnesium due to their consistency in natural mineral dust samples and frequency above detection limits. Silicon and titanium are commonly included in equations inferring

crustal material, however silicon is not available in the ICP-MS analysis and titanium was found to contribute negligibly (< 1%) to CM mass.

3.2.4 Inorganic Species from Water-Soluble Ions

Concentrations of major water-soluble ions in $PM_{2.5}$, such as NO_3^-, SO_4^{2-}, NH_4^+, and Na^+, are determined from half of each filter. After the filter is cut in half it is spiked with 120 μL of HPLC-grade isopropyl alcohol (IPA) and immersed in 2.9 mL of 18 MΩ·cm deionized water. The filters are sonicated in the 4% IPA solution for 30 minutes prior to passing through a 0.45 μm membrane filter (Fisher Scientific) to remove solid matrix components. The filter extracts are then analyzed by ion chromatography with a Thermo Dionex ICS-1100 and a Thermo Dionex ICS-1000 (Mississauga, Ontario, Canada) that detects anions and cations, respectively. A 7-point (anions, 0.05 – 1.5 mg L^{-1}) and 6-point (cations, 0.1 – 2.0 mg L^{-1}) calibration curve is used with each IC run to convert conductivity measurements (μS*min) to amount (μg) of each ion. The limits of quantification of major water-soluble ions of interest are 0.02 μg mL^{-1} (NO_3^-), 0.03 μg mL^{-1} (SO_4^{2-}), 0.01 μg mL^{-1} (Na^+), 0.02 μg mL^{-1} (NH_4^+), 0.01 μg mL^{-1} (K^+), and 0.02 μg mL^{-1} (Mg^+). The determined amount of individual water-soluble ions is used to infer the concentrations of ammonium nitrate, sea salt, sodium sulfate, and ammoniated sulfate contained in the measured $PM_{2.5}$ mass.

To account for the sodium associated with crustal material, 10% of measured aluminum is taken to be associated with sodium and remove it from the total sodium concentration (Remoundaki et al., 2013). The IC system used for anion analysis does not accurately determine chloride concentrations, based on the 7-point standards used in each

run. Therefore, to account for the associated Cl sea salt concentration is represented as $2.54[Na^+]_{SS}$, based on the 1:1 molar ratio of Na^+:Cl^-. Following Henning (2003), sodium sulfate is calculated as a fraction of the measured sodium, $0.18[Na^+]_{SS}$. To account for sulfate in the form of sodium sulfate, 12% of the measured sulfate is removed from the total. Nonetheless, sodium sulfate is found to contribute negligibly to the total $PM_{2.5}$ mass (< 0.1%) at all sampling sites.

All measured nitrate is treated as neutralized by ammonium to form ammonium nitrate when in the aerosol form. The corresponding mass of ammonium nitrate is defined as $1.29[NO_3^-]$ based on the 1:1 molar ratio of NH_4^+:NO_3^-. Ammonium that is not in the form of ammonium nitrate, and sulfate that is not in the form of sodium sulfate, are assumed to be a mixture of ammonium bisulfate and ammonium sulfate. Thus, this mixture is referred to as ammoniated sulfate (ASO_4).

3.2.5 Particle-Bound Water Associated with Inorganic Species

The water uptake by individual inorganic components used here is described in detail by Snider et al. (2016), however it is summarized briefly below for completeness.

The single-parameter measure of aerosol hygroscopicity (κ), as developed by Kreidenweis et al. (2007,2008) is used to determine the mass of particle-bound water (PBW) from individual chemical species. The water uptake for the inorganic chemical components of ammonium nitrate, ammoniated sulfate, and sea salt are estimated. The mass of water associated with each component, *X*, is described by equation (2):

$$PBW_X = [X]\kappa_{m,X}\frac{RH}{100 - RH} \quad (2)$$

where κ_m is the κ-Kohler constant for mass of the component *X*. The κ parameter varies from 0 for insoluble compounds to over 1 for sea salt.

3.2.6 Trace Elemental Oxides

Trace elemental oxides (TEO) are the sum of the masses of trace elements measured by ICP-MS in their oxide form. The TEO fraction is less than 1 % of the total $PM_{2.5}$ mass and water uptake is treated as negligible.

3.2.7 Residual Matter

The analysis methods currently available do not allow for the direct measurement of organics in the collected $PM_{2.5}$ mass. Rather, the residual matter (RM) component, which is treated as mainly OA, is estimated through a mass balance approach. The total dry inorganic mass (IN_mass) from measured species and their associated water at 35% RH (PBW_{IN_mass}) is subtracted from the total $PM_{2.5}$ mass measured at 35 ± 5 % RH as shown in equation (3):

$$RM_{35\%} = PM_{2.5,35\%} - [IN\_mass] - \left[PBW_{IN\_mass}\right] \quad (3)$$

Negative RM values obtained from equation (2) are retained when they are less than 10% of the total $PM_{2.5}$ mass; values that exceed 10% of the total $PM_{2.5}$ mass are flagged and excluded from the mass average. It is found that negative RM values are obtained, on average, 2% of the time. RM at 0% RH is estimated by accounting for associated water using a hygroscopicity parameter $\kappa_{m,RM} = 0.1$, as described by Snider et al. (2016).

3.3 Sources of Uncertainty

The mass concentration of $PM_{2.5}$ can be separated into the measured PM mass collected on the filter (μg) and the volume sampled (m^{-3}). The uncertainty in the PM mass as determined through gravimetric analysis is estimated to be ± 4 μg, on average, from the 2σ standard deviation in the pre- and post-weighed triplicate filter mass measurements. The variance in the air volume sampled is estimated to be ± 10 % from flow measurements taken at the start and end of the sampling period.

The loss of semi-volatile species, such as ammonium nitrate, from filter samples is a concern for determination of $PM_{2.5}$ mass and chemical composition. As discussed in Section 3.2, the SPARTAN sampling protocol is designed to limit volatilization of semi-volatiles during sampling. To test for possible loss of semivolatile material when exposed to diurnal heating cycles, experiments were conducted using PTFE filters preloaded with known NH_4NO_3 mass. Results show that a moderate loss rate (~ 18 % of already collected material) can be expected while warm air (30 °C) is actively flows over the filters; however, loss rates (~ 2 %) are minimal when there is no active sampling. To test for mass loss while in the field, the trend in $PM_{2.5}$ and NH_4NO_3 mass across the seven sequentially sampled filters was examined. The first filter has a residence time of approximately 54 days and the last filter has a negligible residence time. Statistically insignificant trends where found from the first filter through to the last in each cartridge for both $PM_{2.5}$ (-0.09 ± 0.46 μg m^{-3} $position^{-1}$) and NH_4NO_3 (0.06 ± 0.15 μg m^{-3} $position^{-1}$). Filters are stored in closed petri-dishes after sampling, inhibiting the semi-volatile loss.

Uncertainty in the absolute EBC mass arises from the reflectivity path (± 30 %) and the absorption cross-section (± 30 %), which combine in quadrature for an uncertainty of ± 42 %. The percentage recovery of trace elements from Teflon filters was tested using a sequential extraction with 20 % nitric acid. In addition, each element was quantified using a 5-point (25 – 500 ppb) standard calibration curve and three internal calibration metals (Sn, In, Tb). Elemental composition of CM is found to vary by region (Wang, 2015b) contributing to the CM uncertainty of ± 30 %. Concentrations of water-soluble ions are quantified using standard curves with $r^2 > 98$ % and a mass uncertainty of < 10 % at environmentally relevant concentrations of sulfate, nitrate, ammonium, and sodium. Uncertainties in water-soluble ion yields are ± 5 %, except when close to the limit of detection (~ 0.1 μg m^{-3}). The extraction efficiency for water-soluble ions is > 95 %, based on filter spike tests. Evaluation of all SPARTAN analysis methods is an ongoing activity that will continue over time.

3.4 Chemical Composition Results

3.4.1 Overview

Within the period of June 2013 – July 2017 thirteen sampling sites collected $PM_{2.5}$ samples in diverse locations that include representation from arid regions (Ilorin, Nigeria; and Rehovot, Israel), coastal regions (Buenos Aires, Argentina; and Manila, Philippines) and developing megacities (e.g. Dhaka, Bangladesh; and Beijing, China). Gravimetrically weighed $PM_{2.5}$ concentrations span an order of magnitude from below 10 μg m^{-3} in Atlanta, USA to over 100 μg m^{-3} in Kanpur, India in the dry season. Figure 3.2 shows the location of SPARTAN sampling sites and a summary of the measured $PM_{2.5}$

mass and composition. Table 3.2 provides additional details of sampling sites, such as latitude, longitude, and elevation, as well as numerical concentrations. On average, across all sampling sites the relative composition of $PM_{2.5}$ is found to be 43 % RM, 19 % ASO_4, 12 % CM, 10 % EBC, 5.5 % NH_4NO_3, 2.6 % SS, and 1.0 % trace element oxides.

There is significant variation in the relative and absolute speciation in long-term averages of $PM_{2.5}$ chemical components. ASO_4 concentrations vary by an order of magnitude from 1 μg m^{-3} in summertime Buenos Aires to over 18 μg m^{-3} in Kanpur in the dry season.

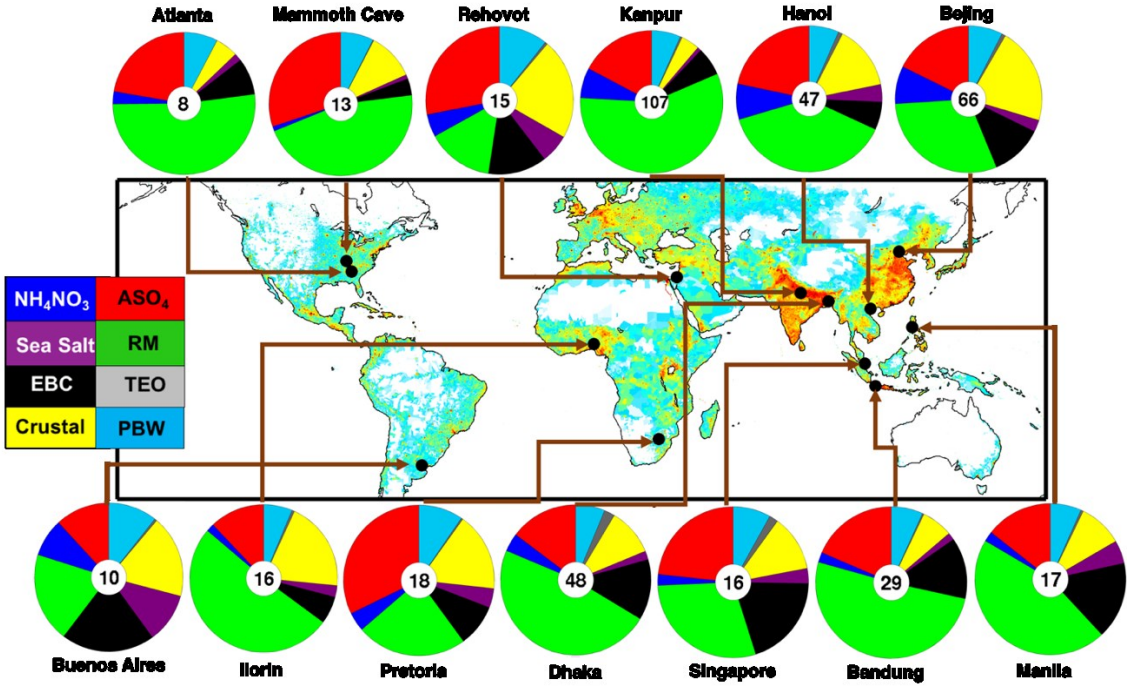

Figure 3.1. $PM_{2.5}$ mass concentration (inner white circle, μg m^{-3}) and composition mass fractions at 13 sampling sites. Sampling periods for each site are shown in Table 3.2.

However, the relative contribution of ASO_4 to total $PM_{2.5}$ mass has a weaker spatial variation of only 10-30% as increases in ASO_4 fraction coincide with increases in total $PM_{2.5}$. Absolute concentrations of NH_4NO_3 show larger spatial variation than ASO_4, varying by a factor of 74 from 0.1 $\mu g\ m^{-3}$ in Mammoth Cave, USA to 7.4 $\mu g\ m^{-3}$ in Kanpur. Relatively, NH_4NO_3 contributes 7 - 8 % to total $PM_{2.5}$ in Kanpur, Beijing, and Buenos Aires and less than 3 % in Bandung, Indonesia. The observed heterogeneity of NH_4NO_3 reflects both the spatial and temporal variation of NH_3 and NO_x ($NO + NO_2$) sources. Increases during the winter in Kanpur, Beijing, and Dhaka reflects more thermodynamic partitioning into the particle phase when temperatures are lower. In addition, it indicates significant background concentrations of precursor gases since emissions from agricultural activity are limited during winter months.

Table 3.2. $PM_{2.5}$ chemical composition and site information for each SPARTAN sampling site.

City, Country	Lat/Lon (°)	Elev.//Inst. Elev. (m)	Filters (*n*)	ASO_4	ANO_3	CM	SS	EBC	TEO	RM	PBW 35%RH	$PM_{2.5}$	K/Al	Zn/Al	Filter Sampling Period
Beijing, China	40.010/ 116.333	60// 7.5	146	11.7 (7.2)[a]	5.5 (5.9)	14.0 (7.0)	1.7 (2.3)	7.6 (3.0)	0.6 (0.4)	19.9 (15.6)	5.0 (2.8)	66.3 (27.0)	2.7	0.5	06/2013-01/2017
Bandung, Indonesia	-6.888/ 107.610	826// 20	121	5.7 (2.4)	0.7 (1.0)	2.0 (1.3)	0.5 (0.2)	4.0 (2.0)	0.1 (0.1)	15.6 (5.4)	2.1 (0.6)	28.6 (9.5)	6.8	0.5	01/2014-12/2016
Manila, Philippines	14.635/ 121.080	60// 10	63	2.6 (1.5)	0.4 (0.7)	1.7 (1.2)	0.9 (1.1)	3.0 (1.8)	0.1 (0.1)	8.2 (3.6)	1.2 (0.3)	17.5 (6.8)	6.5	1.1	02/2014-01/2016
Rehovot, Israel	31.907/ 34.810	20// 10	60	4.8 (2.0)	0.8 (0.5)	3.7 (5.5)	1.1 (0.8)	2.2 (1.6)	0.1 (0.1)	2.5 (2.5)	1.8 (0.7)	14.9 (4.4)	1.9	0.2	02/2015-12/2016
Dhaka, Bangladesh	23.728/ 90.398	20// 20	59	7.1 (4.7)	1.9 (2.1)	4.9 (3.7)	0.9 (0.6)	6.3 (3.9)	1.1 (1.3)	23.0 (14.8)	3.0 (1.5)	47.9 (22.6)	4.7	3.4	10/2013-11/2015
Buenos Aires, Argentina	-34.560/ 58.506	25// 7	54	1.2 (0.9)	0.9 (1.1)	1.9 (1.2)	1.1 (1.2)	2.1 (1.1)	0.1 (0.0)	2.1 (1.8)	1.1 (0.3)	10.2 (3.0)	2.9	0.3	10/2014-10/2016
Singapore, Singapore	1.298/ 103.780	10// 20	51	3.9 (2.3)	0.4 (0.5)	2.0 (0.5)	0.5 (0.3)	3.3 (1.5)	0.3 (0.2)	4.8 (4.9)	1.3 (0.4)	15.7 (4.4)	6.9	1.8	02/2016-07/2017
Ilorin, Nigeria	8.484/ 4.675	330// 10	40	1.9 (0.8)	0.3 (0.2)	3.1 (2.0)	0.4 (0.2)	1.0 (0.7)	0.1 (0.1)	8.1 (4.3)	1.0 (0.3)	15.7 (5.0)	2.9	0.5	03/2014-10/2015
Kanpur, India	26.519/ 80.233	130// 10	34	18.7 (14.4)	7.4 (6.7)	4.6 (2.8)	1.0 (0.5)	7.1 (6.3)	0.5 (0.4)	62.2 (51.3)	7.1 (5.0)	106.6 (76.9)	16.5	1.1	12/2013-11/2014
Atlanta, USA	33.688/ 84.290	250// 2	34	2.2 (0.9)	0.3 (0.1)	0.5 (0.5)	0.2 (0.1)	0.8 (0.7)	0.0 (0.0)	5.2 (1.7)	0.8 (0.2)	8.1 (4.6)	1.9	0.2	01/2013-05/2014
Mammoth Cave, USA	37.132/ -86.148	235// 7	20	3.9 (2.5)	0.1 (0.1)	1.4 (1.5)	0.1 (0.1)	0.5 (0.3)	0.0 (0.0)	6.0 (4.3)	1.0 (0.6)	13.1 (7.9)	0.9	0.1	06/2014-08/2014
Hanoi, Vietnam	21.048/ 105.800	10// 20	18	9.9 (5.9)	3.6 (2.8)	6.5 (7.0)	1.8 (2.5)	2.8 (1.5)	0.4 (0.7)	17.7 (9.7)	3.0 (0.7)	47.1 (19.1)	6.3	3.7	05/2015-03/2016
Pretoria, South Africa	-25.756/ 28.280	1310// 10	7	5.7 (1.1)	0.7 (0.3)	3.0 (1.3)	0.7 (0.4)	1.6 (0.8)	0.1 (0.0)	4.2 (2.9)	1.7 (0.3)	17.8 (2.4)	2.8	0.2	04/2016-06/2016
SPARTAN mean (% mass)	**All sites**		707	18.7 (11)%	5.5 (5.3)%	11.5 (9.5)%	2.6 (2.5)%	10.1 (6.0)%	1.0 (0.8)%	42.6 (34)%	7.2 (3.4)%	34.2 (2.9)	4.6	0.73	06/2013-07/2017

[a]Values in parentheses are 1σ standard deviations. RH = Relative Humidity, ANO_3 = ammonium nitrate, ASO_4 = ammoniated sulfate, CM = crustal material, SS = sea salt, EBC = equivalent black carbon, TEO = trace element oxides, RM = residual matter, PBW = particle-bound water. Mean Na_2SO_4 was not significant (< 0.1 μg m^{-3}) at any SPARTAN site.

Similar to secondary inorganics, CM concentrations span a factor of 28 across 13 sampling sites, from 0.5 μg m^{-3} in Atlanta to 14 μg m^{-3} in Beijing. Apart from dust storms, there is no clear regional or temporal pattern in CM concentrations, however there is a factor of 5 variation in the relative contribution to total $PM_{2.5}$. Huang et al. (2015) found minimal seasonal variation in global anthropogenic dust using Cloud-Aerosol Lidar with Orthogonal Polarization (CALIOP) measurements. However, larger anthropogenic dust burdens were found in eastern China, India, and North Africa, due to higher population densities, heavy urban traffic (Huang et al., 2015), and year-round agricultural biomass burning (Justice et al., 1996). The relative importance of anthropogenic dust from local traffic can be assessed using Zn:Al ratios; zinc has been shown to come predominantly from tire wear (Begum et al., 2010; Councell et al., 2004) whereas Al is mostly natural in origin (Zhang et al., 2006). Elevated Zn:Al ratios (> 3) are observed in large developing cities (e.g. Dhaka, Bangladesh and Hanoi, Vietnam), but ratios below 0.3 are found in Rehovot, Mammoth Cave, and Atlanta.

Black carbon concentrations vary by a factor of 8 across sampling sites, from 0.5 μg m^{-3} in Mammoth Cave to over 6 μg m^{-3} in Beijing, Kanpur, and Dhaka. Sea salt has a minimal influence on total $PM_{2.5,}$ except in Buenos Aires and Rehovot where coastal winds transport oceanic sea salt inland. The TEO component contributes negligibly to total $PM_{2.5}$ mass (~1 %), but is mainly composed of Zn, Pb, Ni, Cu, and Ba, indicating mainly anthropogenic sources. The average PBW contribution to total $PM_{2.5}$ mass is approximately 7 %, close to the contribution from EBC of 10 %.

The inferred RM fraction of measured $PM_{2.5}$ mass is implicitly treated as predominantly OA. Following the approach of Munchak et al. (2011), the ratio of water-

soluble K to Al is used as a marker for wood smoke: a known source of organic aerosol. Average site-specific K:Al ratios range from less than 1 (e.g. Mammoth Cave) to 16 in Kanpur, where combustion activity is apparent. An average K:Al ratio (13) was also observed in Singapore during the period of August – November 2015, a period of significant biomass burning in Indonesia (Koplitz et al., 2016). Significant correlation (r^2 = 0.73) is found between K:Al and RM, supporting the attribution that RM is mostly composed of organics.

3.4.2 Literature Comparison Overview

Major chemical components measured by SPARTAN are compared to available literature studies in the same region within the last 10 years. The comparison is focused on relative $PM_{2.5}$ chemical composition due to the temporal misalignment with previous studies. Particle-bound water is omitted since it is not measured in available literature studies. Trace element oxides are also omitted from the comparison due to their negligible contribution to total mass. If no dust or crustal material concentration is reported, CM is calculated as defined in Section 3.2.3 from reported trace element concentrations. Reported OC concentrations do not include any heteroatoms associated with the carbon atoms. Therefore, organic mass (OM) is calculated from OC concentrations using OM:OC ratios from Philip et al., (2014) with updates from Canagaratna et al. (2015).

Figure 3.3 provides a summary of the relative contribution of dry (0% RH) major chemical components to total dry $PM_{2.5}$ mass from SPARTAN measurements and collocated literature studies; only measurements in Mammoth Cave are temporally coincident. SPARTAN and comparison studies find that 10 – 30 % of measured $PM_{2.5}$ is

ASO_4 and 5 – 20% is CM. The relative contribution of EBC from SPARTAN measurements agree within 5% of previous studies, except in Bandung and Kanpur. SPARTAN measurements and prior studies find that NH_4NO_3 contributes to a small fraction (< 5 %) of total $PM_{2.5}$, except in Beijing and Kanpur, suggesting significant influence from industrial and agricultural activity. All studies find that sea salt has minimal influence on total $PM_{2.5}$ mass concentration (< 3 %). The RM component derived from SPARTAN measurements is consistent with the combined organic and unknown masses from prior studies, offering further evidence that the SPARTAN RM component is predominantly organic.

3.4.3 Individual Site Characteristics

The characteristics of the individual sampling sites are discussed here in more detail. Measured chemical components are examined and related local and regional anthropogenic activity. References to land type are derived from Latham et al., (2014) unless stated otherwise.

3.4.3.1 Beijing, China

The SPARTAN sampling site is located at Tsinghua University, 15 km northwest of the downtown core and is the longest-running SPARTAN site, with over 3 years of near-continuous sampling. This large urban centre has agricultural areas to the west and the Gobi Desert to the north. Beijing has the third-highest $PM_{2.5}$ concentration (69 $\mu g\ m^{-3}$), the third-highest ASO_4 (12 $\mu g\ m^{-3}$), and the highest CM fraction (16 $\mu g\ m^{-3}$) of all SPARTAN sites. Significant urban NO_x emissions near agricultural sources of NH_3 combine to influence the pronounced NH_4NO_3 concentrations; these concentrations are

$PM_{2.5}$ mass = μg m^{-3} (1σ/√n), components = % (1σ)		
This study	**Prior Study 1**	**Prior Study 2**
Beijing $PM_{2.5}$: 66 (2), *n* = 146  9.0 (10)% ANO_3, 19 (12)% ASO_4, 2.9 (3.8)% SS, 22 (13)% CM, 13 (5.0)% EBC, 33 (27)% RM	(Yang et al., 2011a) 2005-2006, OM/OC = 1.7, $PM_{2.5}$: 119(40)  11 (7)% ANO_3, 17 (10)% ASO_4, 1.3 (0.6)% SS, 19 (3)% CM, 7 (5)% EC, 33 (16)% OM, 10 (10)% Unk	(Oanh et al., 2006) 2001-2004, OM/OC = 1.7 $PM_{2.5}$: 136 (45)  12 (1.5)% ANO_3, 20 (1.8)% ASO_4, 1.2 (1.2)% SS, 5 (3)% CM, 9 (7)% EBC, 29 (22)% OM, 24 (24)% Unk
Bandung $PM_{2.5}$: 29 (1), *n* = 121  2.3 (3.6)% ANO_3, 20 (8)% ASO_4, 1.8 (1.0)% SS, 6.8 (5.2)% CM, 14 (7.2)% EBC, 55 (19)% RM	(Oanh et al., 2006) 2001-2004. OM/OC = 2.2, $PM_{2.5}$: 45.5(10.6),  13(4)% ANO_3, 21(3)% ASO_4, 1.6(0.2)% SS, 6.6(0.5)% CM, 19 (4)% EBC, 36(11)% RM	(Lestari and Mauliadi, 2009a) 2001- 2007, OM/OC = 2.2 $PM_{2.5}$: 43.5(10.5)  4(6)% ANO_3, 4(4)% ASO_4, 3(2)% SS, 23(21)% CM, 24(14)% EBC, 42(35)% RM
Manila $PM_{2.5}$: 18 (1), *n* = 63  2.4 (4)% ANO_3, 16 (9)% ASO_4, 5.4 (6.7)% SS, 11 (7)% CM, 18 (11)% EBC, 48 (22)% RM	(Cohen et al., 2009) 2001-2007, OM/OC = 2.1, $PM_{2.5}$: 46 (19), 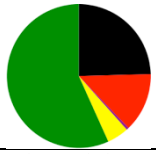 ANO_3 N/A 14 (9)% ASO_4, 0.6 (1.5)% SS, 5 (1.7)% CM, 25 (11)% EBC, 57(22)% OM,	
Kanpur $PM_{2.5}$: 107 (13), *n* = 34  7.4 (6.7)% ANO_3, 19 (14)% ASO_4, 1.0 (0.5)% SS, 4.3 (3.0)% CM, 7.0 (6.3)% EBC, 61 (49)% RM	(Behera and Sharma, 2010b) Oct. 2007 – Jan 2008, OM/OC = 2.2, $PM_{2.5}$: 172 (73), 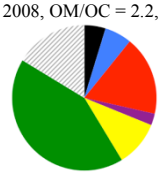 6.1 (1.3)% ANO_3, 18 (4)% ASO_4, 2.6 (0.6)% SS, 10 (3)% CM, 4.8 (1.1)% EC, 42 (9)% OM, 16 (10)% Unk	(Ram et al., 2012) Dec 2008 – Feb 2009, OM/OC = 2.2 $PM_{2.5}$: 158 (47)  6.6(4)% ANO_3, 13 (5)% ASO_4, 1.5 (0.9)% SS, 12 (6)% CM* 3 (1.1)% EC, 57 (23)% OM, 6 (24)% Unk *Assuming CM = [Ca]/0.034 (Wang, 2015a)
Mammoth Cave NP $PM_{2.5}$: 13.1 (2), *n* = 20  1.2 (1.0)% ANO_3, 33 (21)% ASO_4, 1.1 (1.1)% SS, 12 (12)% CM, 4.1 (2.7)% EBC, 49 (36)% RM	(IMPROVE, 2015) June-Aug. 2014, OM/OC = 2.0, $PM_{2.5}$: 10.0 (5.8),  2.4 (2.5)% ANO_3, 36 (17)% ASO_4, 0.3 (1.6)% SS, 7 (8)% CM, 3 (3)% EC, 34 (30)% OM, 17% Unk+H_2O	
Atlanta $PM_{2.5}$: 8.1 (1), *n* = 34  3.1 (1.5)% ANO_3, 24 (9)% ASO_4, 1.8 (1.0)% SS, 13 (6)% CM, 9.1 (8.1)% EBC, 48 (23)% RM	(Butler et al., 2003) Mar. 1999 –2000 Feb, OM/OC = 2.0, $PM_{2.5}$: 24.2  4 (0.2)% ANO_3, 28 (1.0)% ASO_4, 10 (0.8)% CM, 3 (0.2)% EC, 55 (5)% OM,	EPA Jan-May (USEPA, 2015), OM/OC = 2.0 $PM_{2.5}$: 8.5  12 (5)% ANO_3, 23 (15)% ASO_4, 1.4 (0.6)% SS 12 (5)% CM, 9.3 (5)% EC, 43 (36)% OM,
Hanoi $PM_{2.5}$: 47 (5), *n* = 18  9.3 (7.2)% ANO_3, 26 (15)% ASO_4, 4.6 (6.4)% SS, 13 (16)% CM, 7.3 (3.9)% EBC, 41 (24)% RM	(Cohen et al., 2010a). 2001 –2008 OM/OC = 2.1, $PM_{2.5}$: 54 (33)  ANO_3 N/A 29 (20)% ASO_4, 0.6 (1.4)%SS 13 (7)% CM, 8 (3)% EBC, 40 (19)% OM, 2 (2)% Unk + ANO_3	

Figure 3.2. Comparison of SPARTAN dry (0% RH) chemical composition with 11 available collocated previous studies. The numbers in parentheses show the 1σ standard deviation of average masses. The numbers of filters sampled is indicated by *n*. Dark green fractions from previous studies show organic mass, light green indicates RM, black indicates black carbon, red indicates ammoniated sulfate, blue indicates ammonium nitrate, purple indicates sea salt, yellow indicates crustal material, and grey stripes indicate unknown. OM/OC ratios are from Philip et al., (2014b) with updates from Canagaratna et al., (2015). SPARTAN mass fractions are normalized to 100 % after omission of species not found in previous studies.

elevated in winter months, reflecting thermodynamic partitioning into the particle phase. There is an observed high CM component is the spring, showing regional, natural influence from the north. The average Zn:Al ratio (0.51) is low compared to other large cities also indicative of a natural dust component. The lowest coarse-mode Zn:Al ratio is measured in April 2014 (0.07) and April 2015 (0.06) during the annual dust storm season. These low Zn:Al ratios are balanced out by urban dust sources throughout the year. Lin et al., (2015) found evidence of high CM concentrations in industrial areas of Beijing.

Relative masses from SPARTAN measurements show consistency compared to previous studies. The SPARTAN ASO_4 fraction (19 %) is similar to both Yang et al., (2011a) (17 %) and Oanh et al., (2006) (20 %), and the RM fraction (37 %) is close to the combined OM (33 %, 29 %) and unknown fractions (10 %, 24 %) from previous studies. The NH_4NO_3 contribution to $PM_{2.5}$ (8.5 %) in Beijing is higher than almost all other SPARTAN sites, however lower than in previous studies (11 – 12 %), possibly due to different sampling years. Differences in the definition of CM between SPARTAN and other studies are implicated in the significant difference between SPARTAN (25 %) and Oanh et al., (2006) (5 %) and slightly higher than Yang et al., (2011b) (19 %).

3.4.3.2 Bandung, Indonesia

The Institute of Technology Bandung is the host institution for the SPARTAN site in Bandung, located about 5 km from the downtown and surrounded by mountains and agriculture. The average $PM_{2.5}$ concentration of 31 μg m^{-3} is dominated by RM, making up 55 % of the total mass. The elevated RM fraction, compared to other SPARTAN sites, suggests high influence from open fires associated with cropland clearly and agricultural waste burning. Organic mass fractions have been shown to rise above 70 % during burning episodes (Fujii et al., 2014). Significant sources of SO_2, such as volcanic activity in addition to industrial emissions, can explain the relatively high ASO_4 fraction compared to the NH_4NO_3 and CM fractions and ASO_4 at other sites (e.g. Dhaka and Manila). Measured coarse-mode Zn:Al ratios drop from the annual mean of 0.21 to 0.09 during an influx of volcanic ash from the Sinabang volcano during August to September 2014, providing evidence of volcanic influence on the region.

Two previous studies were found for comparison to SPARTAN measurements in Bandung, Oanh et al., (2006) and Lestari and Mauliadi, (2009) that measured from 2001 – 2004 and 2001-2007, respectively. The SPARAN ASO_4 fraction of 21 % is identical to that reported by Oanh et al., (2006) but considerably higher than that reported by Lestari and Mauliadi, (2009) (4 %). Due to volcanic activity in this region, ASO_4 concentrations are expected to vary significantly between years due to the significant, short-term impact of volcanic sources. The BC mass fraction reported in both previous studies (19 % and 25 %) is higher than the 13 % contribution determined from SPARTAN measurements. A more recent study of BC in Indonesian cities (2011) also found a higher BC contribution to $PM_{2.5}$ mass (18 %) than measured by SPARTAN (Santoso et al., 2013). The RM

fraction determined from SPARTAN measurements show a 54 % contribution to $PM_{2.5}$, however previous studies found smaller fractions of 36 % and 42 %. Ammonium nitrate is found to have a minimal contribution to SPARTAN $PM_{2.5}$ mass (2 %), which is lower than that reported by Oanh et al., (2006) (13 %) but close to that from Lestari and Mauliadi, (2009) (4 %).

3.4.3.3 Manila, Philippines

The SPARTAN sampling site in Manila, Philippines is located at the Manila Observatory, just outside the central business district at an altitude 40 meters higher in elevation. Thus, it is expected that the $PM_{2.5}$ mass measured is lower than the downtown core. Nonetheless, the measured $PM_{2.5}$ concentration of 18 $\mu g\ m^{-3}$ is influenced by vehicular and industrial emissions, as described by Cohen et al., (2009) The relative contribution of EBC to total $PM_{2.5}$ (25 %) is the highest of all sites. The high EBC fraction is consistent with previous studies and is attributable to high use of diesel engines (Cohen et al., 2009). In addition to EBC agreement, the ASO_4 mass fraction (16 %) measured by SPARTAN is similar to Cohen et al., (2009). However, the RM fraction is lower than the OM reported by Cohen et al., (2009) (43 % vs. 57 %) whereas the CM fraction is higher. It is possible that the higher CM reflects SPARTAN measurement error and leads to an underestimate of RM. These differences could also reflect the temporal mismatch between the two studies as emissions may change over the 10-year gap between campaigns.

3.4.3.4 Dhaka, Bangladesh

Dhaka is a very densely populated city (17 000 people km^{-2}) in a country where more than half the land is used for agriculture (Ahmed, 2014). The SPARTAN site is in the middle of the city centre, on the roof of a University of Dhaka building, and is influenced by air masses transported from the Indogangetic Plain (Begum et al., 2012). Measured $PM_{2.5}$ concentrations are 52 μg m^{-3}, the fourth-highest of all SPARTAN sites. Local sources include coal combustion, biomass burning, heavy road traffic, and dust (Begum et al., 2010, 2012). The EBC concentration in Dhaka, 8.4 μg m^{-3}, is the second-highest of all locations and can be explained by the abundant diesel engines in the city (Begum et al., 2012). Begum et al., (2012) found that crop and bush burning on the local and regional scales contribute significantly to OM; the RM fraction estimated by SPARTAN is 41 %. The Zn:Al ratio of 3.4 is among the highest at SPARTAN sites, suggesting a large contribution of urban sources to measured dust concentrations (5.9 μg m^{-3}).

3.4.3.5 Ilorin, Nigeria

Ilorin is a city of approximately 500,000 people and is surrounded by short shrub vegetation and agricultural growth. The sampler is located on a rooftop on the University of Ilorin campus, 15 km east of the city centre. The RM fraction in Ilorin is among the highest of SPARTAN sites, accounting for two-thirds of the total $PM_{2.5}$ mass, and is influenced by seasonal biomass burning events. The ASO_4 fraction (12 %) is lower than most SPARTAN sites due to sparse industrial activity. The CM fraction is comparable to other sites, except during dust storms. During a reported dust storm, between 14 April to 2 May 2015, the measured CM component accounted for nearly two-thirds of the total $PM_{2.5}$. During the dust storm the PM_{coarse} Zn:Al ratio decreased to 0.01 from the 0.25

average on non-storm samples, demonstrating the utility of Zn:Al ratios for identifying the relative contribution of natural and anthropogenic dust sources.

3.4.3.6 Kanpur, India

The SPARTAN sampler is located at the Institute of Technology Kanpur campus, 10 km northwest of the city centre. The city of Kanpur is located in the Indogangetic Plain where there is extensive agricultural and industrial activity (Ram et al., 2012). Sampling took place during the periods of December 2013 – May 2014 and September – November 2014, capturing one dry season. The average $PM_{2.5}$ concentration was 99 μg m^{-3}, the highest of all SPARTAN sites. Measured ASO_4 (17.6 μg m^{-3}, 19 %), NH_4NO_3 (6.8 μg m^{-3}, 7.4 %), and RM (54.6 μg m^{-3}, 59 %) are also the highest of all sites. The molar ratio of $[NH_4^+]$:$[SO_4^{2-}]$ is also higher than at other sites, suggesting excess ammonia in the region. Elevated background ammonia has been observed by satellite (Clarisse et al., 2009) that could explain the significant NH_4NO_3 contribution to $PM_{2.5}$ at this site. Elevated K:Al ratios provide evidence of burning activity in the winter months, leading to the RM contribution found during the sampling period. Prominent Zn concentrations were measured in Kanpur, in agreement with those reported by Misra et al., (2014) indicating an anthropogenic dust source.

The relative contribution of major species CM, ASO_4, NH_4NO_3, and sea salt are consistent with previous studies (Behera and Sharma, 2010a; Chakraborty et al., 2015; Ram et al., 2012) that sampled during months consistent with those sampled by SPARTAN. SPARTAN ASO_4 and NH_4NO_3 mass fractions (19 %, 7.4 %) compare well with those reported by Ram et al., (2012) (13 %, 6.1 %) and Behera and Sharma, (2010) (18 %, 6.6 %). The combined mass of SPARTAN NH_4NO_3 and ASO_4 (26 %) compares

well with that measured by Chakraborty et al., (2015) (28 %), however the measured organic mass fraction from Chakraborty et al., (2015) is 70%, higher than the SPARTAN RM fraction of 59 %. The combined organic and unknown mass fractions from Ram et al., (2012) and Behera and Sharma (2010) account for 63 % and 58 % of the $PM_{2.5}$ mass, similar to the SPARTAN RM fraction. The highest measured SPARTAN $PM_{2.5}$ and RM concentrations occur in December, consistent with recent work by Villalobos et al., (2015), who attribute this maximum to increased agricultural burning coupled with stagnant air.

3.4.3.7 Buenos Aires, Argentina

The city of Buenos Aires has a population of approximately 12 million and is surrounded by grassland and agricultural activity to the west and the Atlantic Ocean on the East. The SPARTAN site is located on the CITEDEF campus, 20 km west of the city centre. Total $PM_{2.5}$ (10 $\mu g\ m^{-3}$) and the RM mass fraction (31 %) are lower than other sampling sites, likely influenced by clean maritime air. Proximity to the ocean explains the relatively high contribution of sea salt to $PM_{2.5}$ (6 %) compared to other sampling sites. In contrast, the EBC contribution is 17%, higher than at most sites, reflecting significant local diesel combustion (Jasan et al., 2009).

3.4.3.8 Rehovot, Israel

The sampling site is located on a rooftop at the Weizmann Institute, 20 km south of Tel Aviv and 11 km from the Mediterranean Sea. The region surrounding the city of Rehovot consists of semi-arid cropland and experiences occasional dust storms. The average $PM_{2.5}$ concentration is 16 $\mu g\ m^{-3}$ consisting primarily of ASO_4 (29 %), CM (20

%), and RM (16 %), although the RM fraction is among the lowest of all sampling sites. The sea salt contribution is 4 % of total mass, reflecting the influence from the Mediterranean or a dust contribution to sodium concentrations. Daily sampling was initiated during the Lag Ba'Omer festival (May 7 – 18, 2015) when many bonfires are lit throughout the city. During this time, the combined contribution to total $PM_{2.5}$ from ASO_4 and NH_4NO_3 exceeded 75 %. The observed K:Al ratio during the festival exceeded 30, reflecting the significant burning activity.

Filter sampling during the period of February 4 – 13, 2015 provided the opportunity to measure a severe dust storm. The Zn:Al ratio of the measured PM_{coarse} was 0.02, significantly lower than the average of 0.3. The absolute mass collected on the PM_{coarse} filter was 950 μg, 50 % of which was CM. The remaining 50 % of the PM_{coarse} was measured to be 13 % from the combined sea salt, ASO_4, and NH_4NO_3, and 35 % from RM. The RM fraction may reflect an incomplete extraction of trace elements used in the CM equation, or it is possible that the desert dust carries absorbed organic material (Falkovich et al., 2004).

3.4.3.9 Mammoth Cave National Park, USA

This temporary SPARTAN site was deployed for comparison with measurements made by the IMPROVE network (Solomon et al., 2014). For this purpose, the sampling procedure was altered to be temporally consistent with the 1-in-3 day, 24 hour samples collected by IMPROVE. Filter samples were obtained from June to August 2014. The sampling site is in Mammoth Cave National Park in Kentucky, approximately 35 km from the small town of Bowling Green and surrounded by mountainous terrain and

grassland. Therefore, it is expected that $PM_{2.5}$ sources are largely non-local and is considered a background site.

Comparison of daily values show that SPARTAN measurements are consistent for $PM_{2.5}$ mass ($r^2 = 0.76$, slope = 1.12) and sulfate ($r^2 = 0.86$, slope = 1.03). In addition, the relative contribution of major chemical components from IMPROVE vs. SPARTAN show consistency: ASO_4 (36 % vs. 33 %), NH_4NO_3 (2.4 % vs. 1.2 %), CM (7% vs. 11 %), and EBC (3.0 % vs. 5.6 %). The combined OM, unknown, and water fraction from IMPROVE is 51 %, similar to the SPARTAN RM mass fraction of 49 %.

3.4.3.10 Atlanta, USA

The temporary sampling site in South Dekalb, 15 km east of downtown Atlanta, is used for comparison of SPARTAN values taken temporally consistent with those from the USEPA Chemical Speciation Network sampler (Solomon et al., 2014). The collocation spanned a 4-month period from winter to spring 2014. The mass fractions from SPARTAN and the EPA for CM, sea salt, EBC, and ASO_4 agree to within 2 %. The EPA OM fraction (43 %) is consistent with the RM fraction from SPARTAN (48 %), providing evidence that the RM fraction is primarily organic in nature. In addition to comparison with measurements from the EPA, the relative contribution of major chemical components to total $PM_{2.5}$ from SPARTAN are consistent with those from Butler et al., (2003): CM(12 % vs. 10 %), ASO_4 (23 % vs. 28 %), NH_4NO_3 (3.5 % vs. 4 %), and RM vs. OM (48 % vs. 55 %). However, the EBC contribution to SPARTAN $PM_{2.5}$ (11 %) is over 3-fold higher than Butler et al., (2003) (3 %), reflecting the heterogeneity of BC sources and the 14-year gap between measurements. The difference in the ASO_4 fraction could indicate a decrease in SO_2 emissions, over the past 10 years

significant decreases in $PM_{2.5}$ have been observed near this site and across the eastern US.

3.4.3.11 Singapore, Singapore

Singapore is a densely-populated city-state of nearly 8000 people km^{-2}. The sampling site is located near the center of the city, on a rooftop of the National University of Singapore. Singapore experiences low EBC and CM concentrations, both accounting for 3 % of the total measured $PM_{2.5}$ mass, likely due to the mixed transportation system that includes taxis, rail, and bicycles. A elevated Zn:Al ratio of 1.5 implies that the CM measured is anthropogenic in origin. SPARTAN measurements from late summer/autumn 2015 who significant influence from biomass burning events in Indonesia. $PM_{2.5}$ concentrations increased steadily from 32 $\mu g\ m^{-3}$ in August to 120 $g\ m^{-3}$ in September. Over the same period, the RM mass fraction increased from 44 % to 62 % and the K:Al ratio climbed from 7.2 to between 17 and 24, signifying significant wood smoke influence.

3.4.3.12 Hanoi, Vietnam

Hanoi is an inland megacity surrounded by grassland and agriculture. The sampling site is located on the rooftop of the Institute of Geophysics at the Vietnam Academy of Science and Technology, approximately 5 km northwest of the downtown core. The Zn:Al ratio of 3.7 is the highest of any SPARTAN site and indicates significant traffic and tire wear, specifically influencing the measured CM mass fraction of 14 %. Motorbikes are the primary form of transportation in Hanoi and the dominate source of transportation-based $PM_{2.5}$. (Hieu et al., 2013) .

One study was found that reports $PM_{2.5}$ composition measured in Hanoi and is used to compare with SPARTAN measurements. SPARTAN $PM_{2.5}$ composition is generally consistent with that reported by Cohen et al., (2010), however slight differences are likely due to differences in sampling location and season. The ammoniated sulfate fraction measured by SPARTAN is 26 % versus the 29 % reported by Cohen et al., (2010). Sulfate concentrations tend to be lower in the spring/summer seasons when SPARTAN measurements were taken, which may explain the discrepancy. The SPARTAN EBC mass fraction is 10 %, close to the value reported by Cohen et al., (2010) of 8 %, whereas the SPARTAN RM (51 %) and CM (16 %) fractions are slightly higher, as shown in Figure 3.3.

3.4.3.13 Pretoria, South Africa

The SPARTAN sampling station is located 12 km east of the downtown core of Pretoria, a high-altitude (1300 m) industrial city surrounded by grasslands and agriculture. Measurements at this site span a period of 2 months. Preliminary measurements show a low average $PM_{2.5}$ concentration of 6.4 $\mu g\ m^{-3}$ with the most significant contribution from CM and EBC (22 %), and one of the lowest contributions from RM (14 %). The Zn:Al ratio of 0.69 indicates an anthropogenic source.

3.5 Conclusions

A global network that uses consistent instrumentation in densely-populated cities to measure $PM_{2.5}$ mass and chemical composition has been established. Standardized protocols and equations have been developed to infer $PM_{2.5}$ chemical composition based on gravimetric weighing, reflectance measurements, and measured concentrations of

water-soluble ions and trace elements. Long-term average concentrations of ammoniated sulfate, ammonium nitrate, equivalent black carbon, sea salt, crustal material, and residual mass, that is assumed to be primarily organic, have been determined at 13 sites in 11 countries between 2013 - 2017. The all-site average concentration is 20 ± 11 % ammoniated sulfate, 13.4 ± 9.9 % crustal material, 11.9 ± 8.4 % equivalent black carbon, 4.7 ± 3.0 % ammonium nitrate, 2.3 ± 1.6 % sea salt, 1.0 ± 1.1 % trace element oxides, 7.2 ± 3.3 % particle-bound water at 35 % RH, and 40 ± 24 % residual matter.

Several $PM_{2.5}$ components vary by an order of magnitude across sampling sites. Ammoniated sulfate ranges from 1 $\mu g\ m^{-3}$ in Buenos Aires to 17 $\mu g\ m^{-3}$ in Kanpur during the dry season. Ammonium nitrate concentrations vary from 0.2 $\mu g\ m^{-3}$ in Mammoth cave to 6.8 $\mu g\ m^{-3}$ in Kanpur during the dry season. Equivalent BC ranged from 0.7 $\mu g\ m^{-3}$ in Mammoth Cave to over 8 $\mu g\ m^{-3}$ in Kanpur and Dhaka. Elevated ammoniated sulfate concentrations are found to be coincident with enhancements in other $PM_{2.5}$ components. For example, there is a high degree of correlation ($r^2 = 0.92$) between ammoniated sulfate and residual matter across SPARTAN sites.

The Zn:Al ratio is shown to be effective for understanding sources of crustal material in $PM_{2.5}$ and PM_{coarse} filter samples. Crustal material span the same range as ammoniated sulfate, reaching as low at 1 $\mu g\ m^{-3}$ in Buenos Aires and as high as 16 $\mu g\ m^{-3}$ in Beijing. The Zn:Al ratios measured at sampling sites provide an indication of the relative influence of natural and anthropogenic dust; ratios higher than 0.5 identified sites significantly influenced by road dust (e.g. Hanoi, Kanpur, Manila, Dhaka). Low Zn:Al ratios were apparent during natural dust storms (e.g. Rehovot). Other sites, such as

Beijing and Buenos Aires, show evidence of significant influence from both natural and anthropogenic dust sources. Anthropogenic dust sources have generally been neglected in global models but this work shows that understanding these sources warrants further attention.

The K:Al ratio is used as a marker for wood smoke. Enhanced K:Al ratios were observed in Singapore during a period of intense biomass burning events in Indonesia where plumes influenced this sampling site from July – November 2015. Agricultural burning in Kanpur during the dry season and bonfires in Rehovot during the Lag Ba'Omer festival also lead to elevated K:Al ratios. There is significant correlation between K:Al ratios and RM concentrations ($r^2 = 0.73$), supporting the attribution that the RM fraction is predominately organic since biomass burning has been shown to significantly influence organic mass.

SPARTAN measurements show general consistency with available studies at SPARTAN sampling locations. Although the previous studies and SPARTAN sulfate fractions are within 4% of fractions measured at 8 of the 10 collocated, though temporally non-coincident, studies. Dedicated temporally consistent collocation with IMPROVE in Mammoth Cave yielded a high degree of consistency with daily sulfate (r^2 =0.86, slope=1.03), daily $PM_{2.5}$ (r^2 =0.76, slope=1.12), and mean fractions for all major $PM_{2.5}$ components within 2 %. Crustal material is typically consistent with the previous measurements, at 5–15% composition. SPARTAN equivalent black carbon ranged broadly, from 3% (Singapore) to 25% (Manila), and matched within a few percent of most previous works. Ammonium nitrate (4%) generally matched other sites, though it was sometimes lower, as in Beijing and Atlanta. Sea salt was consistently low, as found

in previous measurements. Sea salt fractions were highest in Buenos Aires and Rehovot (6 %), reflecting natural coastal aerosols. SPARTAN residual matter is consistent with the combined organic and unknown masses. Comparing with collocated measurements supports the expectation that most of the RM is partially organic. Residual matter could also include unaccounted-for particle-bound water, measurement error, and possibly unmeasured inorganic materials.

These measurements provide chemical and physical data for future research to help understand the temporal and spatial variation of global $PM_{2.5}$ concentrations. Collocation with sun photometer measurements of AOD connects satellite observations to ground-based measurements and provides information needed to evaluate chemical transport model simulations of $PM_{2.5}$ mass, composition, and the $PM_{2.5}$ to AOD ratio. As sampling expands, SPARTAN will provide long-term data on fine aerosol variability from around the world.

Chapter 4 Global Sources of Fine Particulate Matter: Interpretation of $PM_{2.5}$ Chemical Composition Observed by the Surface Particulate Matter Network using a Global Chemical Transport Model

4.1 Introduction

Exposure to ambient $PM_{2.5}$ is a leading risk factor for increased mortality and morbidity (Dockery et al., 1993; Pope et al., 2009) .The Global Burden of Disease study attributed 4.1 million premature deaths to $PM_{2.5}$ exposure in 2016 (Gakidou et al., 2017). A strong need exists to understand the sources contributing to this $PM_{2.5}$ burden to inform mitigation efforts (West et al., 2016). $PM_{2.5}$ formation is influenced by a range of emission sources, atmospheric transport, and atmospheric chemistry (Fuzzi et al., 2015). A chemical transport model constrained by observations offers a powerful tool to understand these sources. Until recently, measurements of $PM_{2.5}$ mass and chemical composition were largely limited to North America and Europe, with different networks using a variety of sampling techniques and standards to determine chemical composition. A global dataset of ground-based measurements of $PM_{2.5}$ composition could offer valuable information to understand the sources and processes that control the spatial diversity of $PM_{2.5}$ mass and chemical composition.

The relationship between emissions and $PM_{2.5}$ is complex. $PM_{2.5}$ can be emitted directly as particles from combustion or mechanical processes. $PM_{2.5}$ can also form and grow in the atmosphere through the condensation of low volatility products of atmospheric chemical reactions or inorganic and organic precursors (Fuzzi et al., 2015; Pandis et al., 1995). Chemical transport models have been applied to represent this

complexity through source apportionment studies aimed at characterizing the global sources contributing to $PM_{2.5}$ mass and composition. These applications include the direct use of global chemical transport models (Lelieveld et al., 2015), with increasingly fine resolution (Punger and West, 2013). Although insightful, simulations could benefit from stronger observational constraints to evaluate and improve accuracy and spatial representativeness.

Two observational datasets have emerged recently with information about the global distribution of $PM_{2.5}$ mass and composition, a dedicated ground-based network of $PM_{2.5}$ composition, and increasingly accurate satellite-based estimates of $PM_{2.5}$ mass. SPARTAN measures ground-based $PM_{2.5}$ mass and chemical composition using consistent instrumentation and standardized chemical analysis techniques in diverse global locations with high population densities relevant for health. Measurements from SPARTAN include $PM_{2.5}$ samples collected on Teflon filters that are analyzed for mass and chemical composition of $PM_{2.5}$ including sulfate, nitrate, ammonium, black carbon, mineral dust, and sea salt (Snider et al., 2015, 2016). Satellite-based estimates of $PM_{2.5}$ mass complement the ground-based measurement network by offering additional global constraints on $PM_{2.5}$ mass at resolution finer than global simulations. Case studies investigating the effects of model resolution on calculated $PM_{2.5}$ mortality rates find that those calculated from coarse (2° x 2.5°) resolution are systematically lower than those calculated using finer (e.g. 0.5° x 0.66°) resolution (Kodros et al., 2016; Li et al., 2016b; Punger and West, 2013). The latest global satellite-based $PM_{2.5}$ estimates combine observations from multiple retrieval algorithms (Hsu et al., 2006, 2013, Levy et al., 2007, 2013, Lyapustin et al., 2011a, 2011b; Martonchik et al., 2009) and instruments (MODIS,

MISR, SeaWiFs) weighted inversely by error with respect to ground-based AOD measurements from AERONET (Holben et al., 1998) with additional statistical constraints from ground-based $PM_{2.5}$ measurements (Shaddick et al., 2017; van Donkelaar et al., 2016).

Ground-based measurements of $PM_{2.5}$ mass and composition from SPARTAN are interpreted with the global chemical transport model, GEOS-Chem, constrained by satellite-derived $PM_{2.5}$ to gain insight into the main sources determining the spatial distribution of $PM_{2.5}$ mass and composition. The annual average influence of seven emission source categories on global population-weighted $PM_{2.5}$ are explored.

4.2 Methods

4.2.1 SPARTAN Filter Measurements and Analysis

SPARTAN is an ongoing, long-term project that measures aerosol mass, water-soluble ions, trace elements, and aerosol optical properties at globally-dispersed, densely-populated areas of relevance to human health. Chapter 3 provides an overview of SPARTAN, including the post-sampling analysis methods. More details on post-sampling analytical procedures and SPARTAN site selection and maintenance criteria are found in Appendix B. Instrumentation includes an Airphoton 3-wavelength integrating nephelometer and an Airphoton SS4i automated filter sampler. The focus is on the latter here. Each sampler houses a protective, removable cartridge that contains 7 sequentially active filter pairs, plus a field blank. Filter samples have been collected at 11 regionally representative sites from 2 months to over 3 years. The AirPhoton SS4i sampler uses a greased impaction plate to remove PM larger than 10 μm in diameter and a pre-weighed

Nuclepore filter membrane (8 μm pore size, greased, SPI) to remove PM with diameter from 10 to 2.5 μm. The $PM_{2.5}$ is then collected on a pre-weighed PTFE filter (2 μm pore size, SKC).

An extensive overview of the SPARTAN $PM_{2.5}$ sampling methodology, filter analysis protocols, equations used to reconstruct $PM_{2.5}$ mass from chemical composition, and the filter-based hygroscopicity parameter, κ, are provided in Chapter 3 and Appendix B. Briefly, filters are pre- and post-weighed in triplicate using a Sartorius Ultramicro balance with 0.1 μg precision that undergoes daily calibrations. The overall combined uncertainty (± 2σ) is ± 4 μg. All gravimetric analysis is performed in a cleanroom facility with controlled temperature at 20 to 23 °C and relative humidity at 35 ± 5 % following USEPA protocols. Recorded flow rates at ambient pressure and temperature at site locations are used to determine the sampled air volume to provide $PM_{2.5}$ mass concentrations in μg m^{-3}. The black carbon content of $PM_{2.5}$ on PTFE filters is derived from triplicate measurements of surface reflectance using the Diffusion Systems EEL 43M smoke stain reflectometer (Quincey et al., 2009). After reflectance measurements are taken each filter is divided in half using a ceramic blade, similar to the approaches of Zhang et al., (2013) and Gibson et al., (2009). One filter half is extracted for analysis for water-soluble ions SO_4^{2-}, NO_3^-, NH_4^+, K^+, and Na^+ through ion chromatography using a Thermo Dionex ICS-1100 for anions and a Thermo Dionex ICS-1000 for cations (Gibson et al., 2013a, 2013b). The other filter half is extracted for analysis for trace elements, including the crustal components Al, Mg, and Fe, via inductively coupled plasma – mass spectrometry (Thermo Scientific X-series 2). The residual matter component, estimated

by subtracting the dry inorganic mass and particle-bound water from total $PM_{2.5}$ mass, is expected to be predominately organic (Snider et al., 2016).

4.2.1.1 Uncertainty from Collocated Measurements

Whole-system uncertainty in total $PM_{2.5}$ mass and chemical component concentrations are estimated using collocated filter sampling stations at three sampling sites in characteristically low (Halifax, Canada), moderate (Toronto, Canada) and high (Beijing, China) $PM_{2.5}$ locations. Collocated sampling is a comprehensive means of estimating measurement uncertainty since the entire measurement process is duplicated for each collocated data pair from sample collection through laboratory analysis (Hyslop and White, 2008; Solomon et al., 2014). During the collocation period of three weeks, each sampler collected 18, 24-hour samples (48-hour samples in Halifax) on PTFE filters beginning at 09:00 local time. Uncertainty is calculated as described in the US Code of Federal Regulations, Part 58 (Ambient Air Quality Surveillance), Appendix A, Section 4.2. For each collocated data pair, the relative percent difference, d_i, is calculated using equation 4:

$$d_i = \frac{X_i - Y_i}{(X_i + Y_i)/2} * 100 \quad (4)$$

where X_i and Y_i are the species concentrations from the two sampling stations. The coefficient of variation upper bound is then calculated using equation 5:

$$CV(upper\ bound) = \sqrt{\frac{n * \sum_{i=1}^{n} d_i^2 - (\sum_{i=1}^{n} d_i)^2}{2n(n-1)}} * \sqrt{\frac{n-1}{\chi^2_{0.1,n-1}}} \quad (5)$$

where n is the number of data pairs, and $\chi^2_{0.1,n-1}$ is the upper 10th percentile of a chi-squared distribution with $n - 1$ degrees of freedom. The factor of 2 in the denominator adjusts for the error in d_i from two measurements.

Table 4.1 provides a summary of uncertainty estimates for each of the collocated sampling sites, as well as the network average. Network-average seasonal uncertainties are lowest for $PM_{2.5}$ (4.6 %) and sulfate (4.0 %), and largest for nitrate (9.2 %) and BC (9.0 %). Table 4.1 shows that for $PM_{2.5}$ mass, SO_4^{2-}, and NH_4^+ the estimated uncertainty increases with increased ambient $PM_{2.5}$ concentration, whereas the opposite trend is found for NO_3^- and dust, suggesting that higher concentrations of trace elements used to estimate dust concentrations are quantified.

Table 4.1. Summary of uncertainty (%) for $PM_{2.5}$ and major chemical components.

		$PM_{2.5}$		SO_4^{2-}		NH_4^+		NO_3^-		BC		SS		Dust		RM	
Location	n	F	S	F	S	F	S	F	S	F	S	F	S	F	S	F	S
Halifax	18	10	3	4	1	6	2	30	10	20	7	17	5	20	6	16	5
Toronto	18	15	5	13	4	13	4	28	9	32	10	27	9	16	5	19	6
Beijing	14	17	5	16	5	22	7	21	7	25	8	11	4	15	5	38	12
Network	50	15	5	13	4	17	5	29	9	29	9	23	7	19	6	27	9

Uncertainty (%) is calculated using equation 5. 'F' indicates uncertainty calculated for individual filters. 'S' indicates estimated seasonal uncertainty determined from the average number of filters collected in a 90-day period. 'n' shows the number of filters sampled. SS = sea salt.

Figure 4.1 shows comparisons of daily mean concentrations on individual filters from three sampling sites for $PM_{2.5}$ mass, major water-soluble ions, dust, residual matter, and BC. The r^2 is 0.95 or better for $PM_{2.5}$, SO_4^{2-}, NO_3^-, NH_4^+, and sea salt (SS).

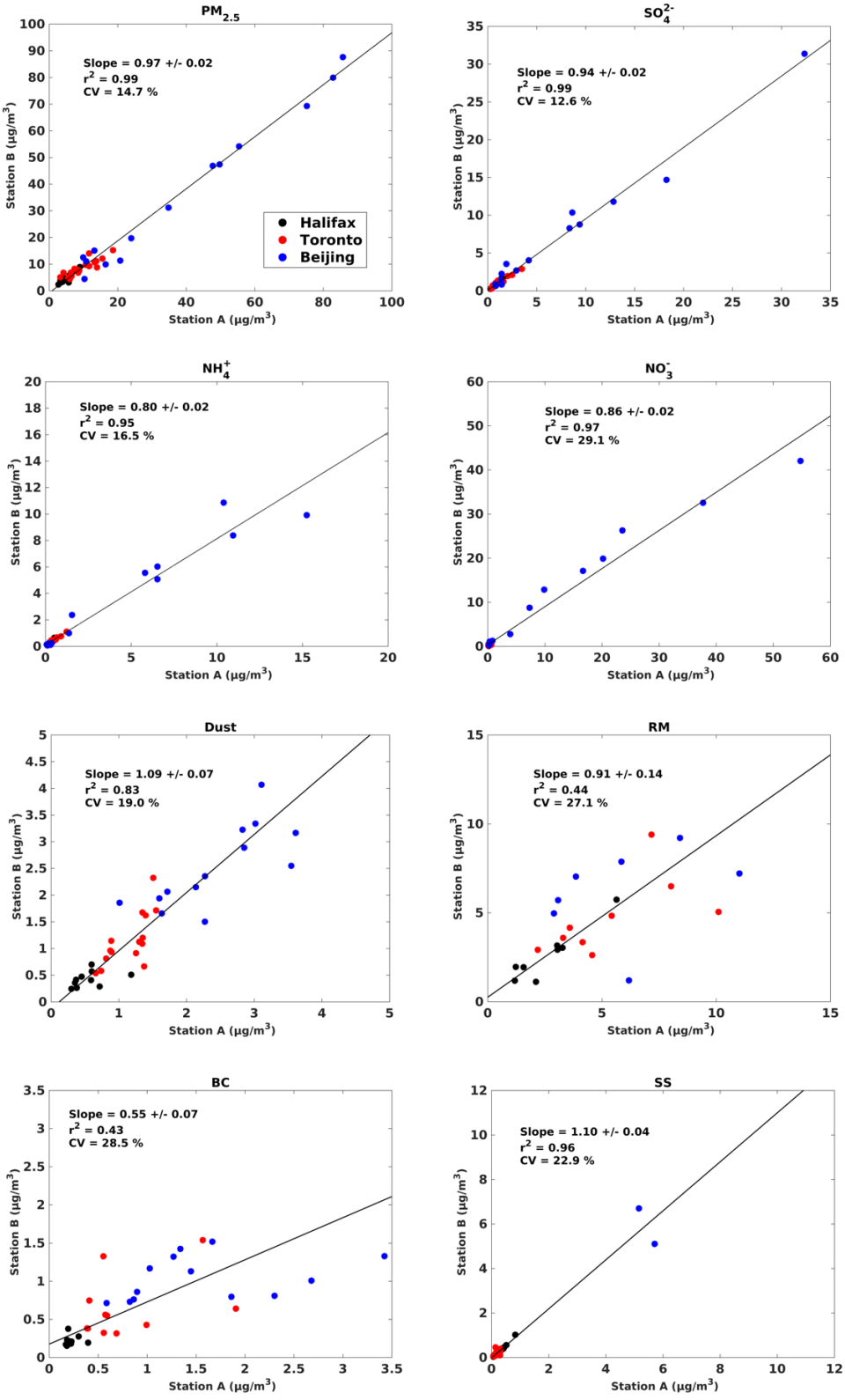
PM2.5
Slope = 0.97 +/- 0.02
r2 = 0.99
CV = 14.7 %
Halifax
Toronto
Beijing
SO4 2-
Slope = 0.94 +/- 0.02
r2 = 0.99
CV = 12.6 %
NH4 +
Slope = 0.80 +/- 0.02
r2 = 0.95
CV = 16.5 %
NO3 -
Slope = 0.86 +/- 0.02
r2 = 0.97
CV = 29.1 %
Dust
Slope = 1.09 +/- 0.07
r2 = 0.83
CV = 19.0 %
RM
Slope = 0.91 +/- 0.14
r2 = 0.44
CV = 27.1 %
BC
Slope = 0.55 +/- 0.07
r2 = 0.43
CV = 28.5 %
SS
Slope = 1.10 +/- 0.04
r2 = 0.96
CV = 22.9 %
Station A (µg/m3)
Station B (µg/m3)

Figure 4.1. Summary of daily comparisons between two collocated sampling stations located in Halifax, Toronto, and Beijing. CV indicates the coefficient of variation upper bound as calculated by equation 5.

4.2.2 GEOS-Chem Simulation

The GEOS-Chem 3-dimensional chemical transport model (v11.01, http://geos-chem.org) is used to determine the daily distribution of the mass concentrations of the major chemical components of $PM_{2.5}$. GEOS-Chem solves for the evolution of atmospheric aerosols and gases using assimilated meteorology from the NASA Goddard Earth Observing System (GEOS), global and regional emission inventories, and algorithms that represent the physics and chemistry of atmospheric processes. The simulation uses assimilated meteorological observations (GEOS MERRA-2) for the year 2014 at 2° x 2.5° horizontal resolution with 47 vertical levels from the surface to approximately 80 km altitude.

SPARTAN measurements are used to inform developments to the simulation. We include the anthropogenic fugitive, combustion, and industrial dust (AFCID) emission inventory, which Philip et al., (2017) found to increase correlation with SPARTAN fine dust measurements from 0.06 to 0.66. Simulated total $PM_{2.5}$ mass concentration is calculated at 35 % RH using the kappa hygroscopicity formulation (Petters and Kreidenweis, 2007) used by SPARTAN, as described by Snider et al., (2016) for increased consistency compared to the Atmospheric Inorganic Model (AIM) (Wexler and Clegg, 2002) and laboratory measurements. Also included is an aqueous-phase mechanism for secondary organic aerosol (SOA) formation from isoprene from Marais et

al., (2016) that increases simulated OM and reduces bias versus SPARTAN measurements.

GEOS-Chem simulates coupled atmospheric oxidant-aerosol chemistry (Bey et al., 2001; Park et al., 2004) including the sulfate-nitrate-ammonium system (Park et al., 2004), mineral dust (Fairlie et al., 2007; Zhang et al., 2013a), sea salt (Jaeglé et al., 2011), primary (Park et al., 2003; Wang et al., 2011) and secondary (Marais et al., 2016; Pye et al., 2010) carbonaceous aerosols. Gas-aerosol partitioning is calculated using the ISOROPIA II thermodynamic equilibrium model (Fountoukis and Nenes, 2007) as implemented by Pye et al., (2009). Aerosols affect photolysis frequencies using RH-dependent and composition dependent aerosol optical properties following Martin et al., (2003) with updated dust optics by Ridley et al., (2012) and brown carbon by Hammer et al., (2016). Organic mass (OM) from primary organic carbon is calculated using spatially and seasonally varying values following Philip et al., (2014b) with updates from Canagaratna et al., (2015). Total $PM_{2.5}$ mass concentration is calculated at 35 % RH using a kappa hygroscopicity formulation (Petters and Kreidenweis, 2007) for consistency with SPARTAN measurement protocols, the AIM model, and laboratory measurements, as described by Snider et al., (2016).

The simulation uses the Emissions Database for Global Atmospheric Research (EDGAR) version 4.3 inventory (Crippa et al., 2016) and the MIX regional anthropogenic emission inventory for 29 Asian regions and countries (Li et al., 2017b). Other emissions include open fire emissions (GFED4) (Giglio et al., 2013), biogenic emissions (Guenther et al., 2006), soil NO_x (Hudman et al., 2012), lightning NO_x

(Murray et al., 2012), aircraft emissions (Stettler et al., 2011; Wang et al., 1998), and volcanic SO_2 emissions (Fisher et al., 2011).

The HEMCO module (Keller et al., 2014) is used to facilitate sensitivity simulations that separate emissions into source categories. Sensitivity simulations for the year 2014 are performed for which emissions from individual source categories were removed to calculate the contribution of sources to $PM_{2.5}$ mass and composition. Source categories selected for investigation follow those of Lelieveld et al., (2015) and are described in Table 4.2. The anthropogenic fugitive, combustion, and industrial dust is distributed equally across the industry, power generation, and transport sectors. Gridded population estimates from the Socioeconomic Data and Applications Center (SEDAC) for 2015 are employed to calculate population-weighted mean $PM_{2.5}$ mass for each source category and $PM_{2.5}$ chemical component.

Table 4.2. List and description of sensitivity simulation used to investigate source categories contributing to $PM_{2.5}$ mass and composition.

Source Category	Description of Contributing Emissions
Residential Energy Use	household energy use for cooking and heating, including biofuel use, generators, and small combustion sources
Industry	emissions from manufacturing, transformation, chemical, pulp and paper industry, oil refineries, and fuel/oil production
Power Generation	emissions from burning of fossil fuels for public power consumption
Agriculture	predominately gaseous ammonia emissions associated with fertilizer use and domesticated animals
Transport	emissions from road and non-road transport including air and ship traffic
Open Fires	boreal and temperate forest fires, peatland, savanna, grassland, and shrubland fires, agricultural waste burning, and deforestation and degradation
Other Sources	mineral dust from arid and semi-arid regions, also including organics from biogenic sources, lightning NO_x, volcanic sulfur emissions, and oceanic sea salt and dimethyl sulfide (DMS)

4.2.3 Constraining the Simulation with Satellite-Based $PM_{2.5}$

Satellite observations of AOD offer an additional constraint on the global $PM_{2.5}$ distribution at spatial scale commensurate with population density distributions (van Donkelaar et al., 2010). To reduce uncertainties in $PM_{2.5}$ exposure estimates owing to model resolution (e.g. Li et al., 2016a; Punger and West, 2013), satellite-derived $PM_{2.5}$ concentrations (van Donkelaar et al., 2016) for the year 2014 are used to redistribute GEOS-Chem $PM_{2.5}$ mass and composition from 2° x 2.5° to the 0.1° x 0.1° resolution following Lee et al., (2015). This approach is evaluated below.

Table 4.3 shows the Pearson's correlation coefficient between SPARTAN measurements and $PM_{2.5}$ components from the model (r) and simulated values scaled by local satellite-derived $PM_{2.5}$ (r_{sat}). For most $PM_{2.5}$ components, downscaling to satellite-derived $PM_{2.5}$ increases the correlation in capturing the spatial diversity of $PM_{2.5}$. Correlations tend to increase, most notably for OM (r_{sat} = 0.92 vs. r = 0.64) as well as total $PM_{2.5}$ mass (r_{sat} = 0.93 vs. r = 0.88), ammonium (r_{sat} = 0.86 vs. r = 0.81), and black carbon (r_{sat} = 0.67 vs. r = 0.61). The root-mean-square-error of simulated total $PM_{2.5}$ decreased from 13.3 $\mu g\ m^{-3}$ to 12.8 $\mu g\ m^{-3}$. Therefore, all values of total $PM_{2.5}$ mass and chemical composition reported herein are from the downscaled simulation (scaled by the local annual ratio of $PM_{2.5,sat}$ to $PM_{2.5,model}$) at 0.1° x 0.1° resolution.

Table 4.3. Correlation coefficient from comparison between SPARTAN measurements and simulation-only (r) and simulation-satellite (r_{sat}) ground-level $PM_{2.5}$ concentrations

Component	r	r_{sat}
Total $PM_{2.5}$ mass	0.88	0.93
Organic Mass	0.64	0.92
Secondary Inorganic Aerosols	0.89	0.87
Ammonium	0.81	0.86
Sulfate	0.95	0.78
Nitrate	0.82	0.85
Black Carbon	0.61	0.67
Dust	0.67	0.57
Sea Salt	-0.25	0.06

4.3 Sources Affecting $PM_{2.5}$ Mass and Composition

4.3.1 Global Distribution of $PM_{2.5}$ Chemical Composition

Figure 4.2 shows the annual mean simulated $PM_{2.5}$ chemical composition with overlaid concentric circles depicting concentrations at SPARTAN sites. The center of each concentric circle indicates the measured value, and corresponding downscaled simulated concentration indicated by the outer ring. Differences between the outer ring and background map represent the effects of sampling the simulation for the same months as the measurements versus complete annual sampling. These seasonal sampling effects are generally much smaller than the global spatial variation, providing evidence of temporal representativeness. Inset values represent the global population-weighted mean concentration inferred from the downscaled simulation. Table 4.4 contains numerical values of measured and simulated concentrations for the specified sampling periods of SPARTAN sampling sites. The spatial variation of SPARTAN site-mean concentrations

exceeds a factor of five (e.g. Kanpur vs. Buenos Aires) for most $PM_{2.5}$ major chemical components, as described in more detail in the following sections.

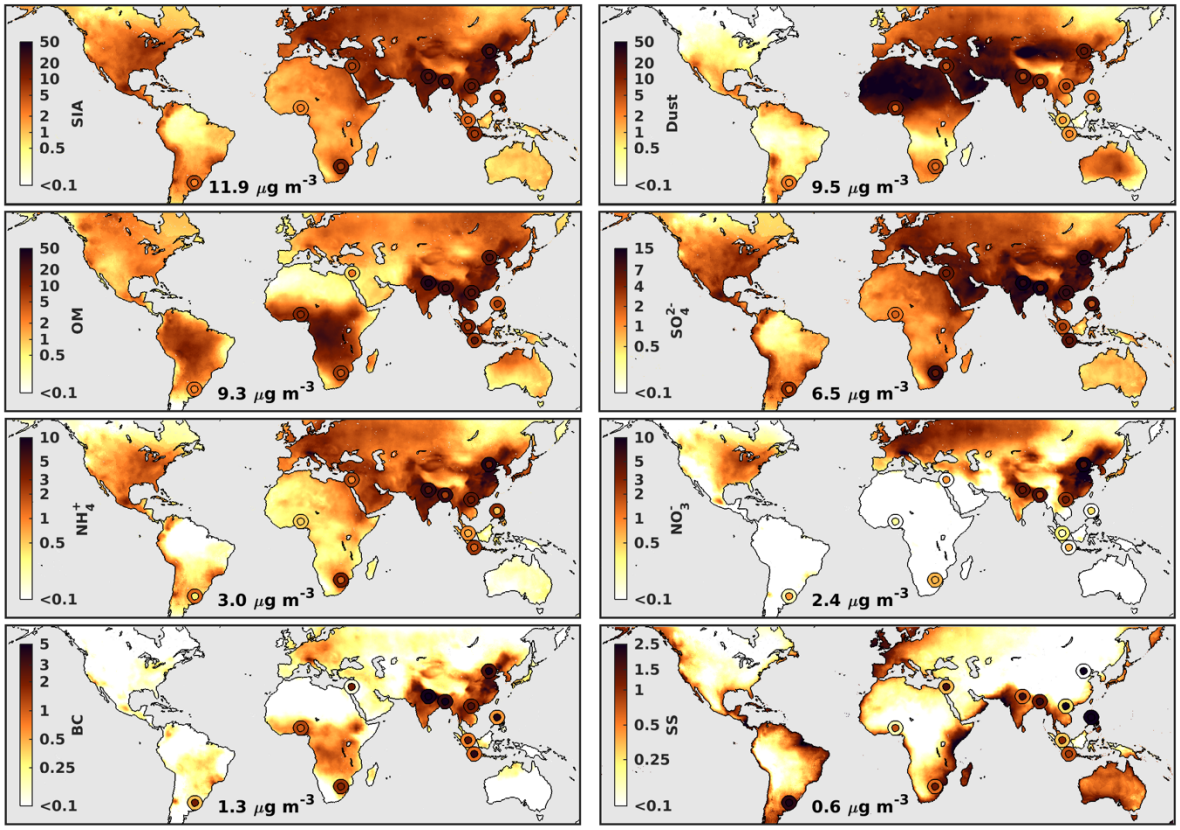

Figure 4.2. Global simulated annual mean $PM_{2.5}$ composition. Values from SPARTAN observations are overlaid as colored circles surrounded by concentric circles showing simulated values sampled coincident months. Concentrations are shown at 35% relative humidity. Abbreviations are secondary inorganic aerosol (SIA), organic mass (OM; residual mass from SPARTAN), black carbon (BC), and sea salt (SS). Inset values indicate reduced major axis regression statistics for the measured and simulated values for each chemical component, and global population-weighted average $PM_{2.5}$ concentration resulting from each chemical component. Unit for color bars is μg m^{-3}. Grey denotes water.

SPARTAN measurements of secondary inorganic aerosol (SIA) vary by a factor of 8 across sampling sites and account for over 20% of total $PM_{2.5}$ mass at sampling sites, except Manila, Philippines (16%) and Ilorin (15%). The downscaled simulation captures the spatial heterogeneity of SIA concentrations (r = 0.87). SIA tends to be overestimated at SPARTAN sites, including an overestimate of nitrate concentrations in Beijing. SIA dominates population-weighted $PM_{2.5}$, accounting for 37 % globally.

Table 4.4. $PM_{2.5}$ mass and composition at SPARTAN sites from measurements (Obs.) and GEOS-Chem simulation (GC).

Site	Lat, Lon (°)	Date Range	$PM_{2.5}$		SIA		SO_4^{2-}		NH_4^+		NO_3^-		RM/OM		Dust		BC		Sea Salt	
			Obs.	GC	Obs.	GC	Obs.	GC	Obs.	GC	Obs.	GC	Obs.	GC	Obs.	GC	Obs.	GC	Obs.	GC
Beijing, China	40.01, 116.33	06/2013-01/2017	67.1 ± 9.9[a]	75.0	19.7 ± 2.1	36.3	11.2 ± 1.4	13.3	3.6 ± 0.6	9.0	4.9 ± 1.4	14	21.9 ± 5.9	17.7	14.7 ± 2.4	17.9	7.3 ± 2.1	3.0	3.6 ± 0.8	0.1
Bandung, Indonesia	-6.888, 107.61	01/2014-12/2016	30.8 ± 4.5	20.0	7.6 ± 0.8	9.9	5.6 ± 0.7	7.2	1.4 ± 0.2	2.6	0.6 ± 0.2	0.1	16.2 ± 4.4	6.8	2.2 ± 0.4	1.6	3.9 ± 1.1	0.9	0.9 ± 0.2	0.8
Manila, Philippines	14.64, 121.08	02/2014-01/2016	19.2 ± 2.8	24.0	3.0 ± 0.3	12.0	2.1 ± 0.3	9.1	0.5 ± 0.1	2.9	0.4 ± 0.1	0.0	7.5 ± 2.0	3.7	1.9 ± 0.4	3.9	4.3 ± 1.2	0.6	2.5 ± 0.6	3.8
Rehovot, Israel	31.91, 34.81	02/2015-12/2016	17.5 ± 2.6	23.0	6.4 ± 0.7	7.7	4.7 ± 0.6	5.6	0.9 ± 0.1	2.0	0.8 ± 0.2	0.1	2.7 ± 0.7	0.7	4.6 ± 0.9	14.1	2.1 ± 0.6	0.1	1.7 ± 0.4	0.4
Dhaka, Bangladesh	23.73, 90.398	10/2013-11/2015	49.9 ± 7.3	79.0	11.3 ± 1.1	28.0	7.1 ± 0.9	15.1	2.2 ± 0.4	7.2	2.0 ± 0.6	5.7	25.2 ± 6.8	30.2	5.5 ± 1.0	15.7	5.8 ± 1.7	3.7	2.0 ± 0.5	1.3
Buenos Aires, Argentina	34.56, -58.51	10/2014-10/2016	10.7 ± 1.6	15.0	2.5 ± 0.3	6.2	1.3 ± 0.2	4.4	0.4 ± 0.1	1.5	0.8 ± 0.2	0.3	2.1 ± 0.6	3.2	1.7 ± 0.3	2.8	2.2 ± 0.6	0.5	2.3 ± 0.5	2.2
Ilorin, Nigeria	8.481, 4.526	03/2014-10/2015	15.8 ± 2.3	17.5	2.4 ± 0.2	1.9	1.7 ± 0.2	1.3	0.5 ±0.1	0.5	0.2 ± 0.1	0.1	8.4 ± 2.3	7.8	3.1 ± 0.6	6.4	1.0 ± 0.3	1.2	0.7 ± 0.2	0.2
Singapore, Singapore	1.298, 103.78	02/2016-02/2017	15.8 ± 2.3	15.6	4.0 ± 0.4	3.5	3.2 ± 0.4	2.2	0.6 ± 0.1	0.9	0.2 ± 0.1	0.4	5.2 ± 1.4	10.3	1.9 ± 0.4	0.9	3.8 ± 1.1	0.6	1.0 ± 0.2	0.4
Kanpur, India	26.52, 80.232	12/2013-11/2014	71.9 ± 10.6	94.0	18.6 ± 1.9	29.2	10.2 ± 1.3	16.6	4.6 ± 0.8	7.6	3.8 ± 1.1	5.0	40.2 ± 10.9	35.5	5.6 ± 1.1	23.7	5.6 ± 1.6	5.0	1.8 ± 0.4	0.6
Hanoi, Vietnam	21.05, 105.8	05/2015-03/2016	50.9 ± 7.5	45.0	17.2 ± 1.8	17.1	10.1 ± 1.3	10.0	3.4 ± 0.6	4.5	3.7 ± 1.1	2.6	17.9 ± 4.9	21.7	8.4 ± 1.6	3.7	2.9 ± 0.9	2.1	4.5 ± 1.0	0.3
Pretoria, South Africa	-25.76, 28.279	04/2016-06/2016	17.5 ± 2.6	30.6	7.3 ± 0.7	15.7	5.3 ±0.7	11.3	1.4 ± 0.2	3.7	0.6 ± 0.2	0.7	4.3 ± 1.2	7.5	2.8 ± 0.5	5.1	1.8 ± 0.5	1.7	1.3 ± 0.3	0.7

[a]Values displayed after the ± in the obs. column represent the estimated measurement uncertainty as described in section 4.3.1.1. Values reported in μg m^{-3} under ambient conditions and for a measured RH of 30-40%, and simulated RH of 35%.

Measured concentrations of crustal material (dust) vary by an order of magnitude from < 2 μg m^{-3} (e.g. Buenos Aires) to 3 – 5 μg m^{-3} in many cities (e.g. Ilorin and Rehovot, Israel), to over 5 μg m^{-3} (Dhaka, Bangladesh; Hanoi, Vietnam; and Kanpur), and exceed 14 μg m^{-3} in Beijing. Enhanced dust mass in Rehovot and Ilorin is expected to be predominately mineral dust, due to arid influence. However, pronounced dust in urban cities throughout South and Southeast Asia cannot be fully explained by mineral dust sources; elevated measured Zn:Al ratios at these sites suggest an urban component. The remaining positive bias in simulated values is driven by an overestimate in the simulated mineral dust source. Simulated dust concentrations are primarily mineral over the arid and semi-arid regions of North Africa, the Middle East, and Central Asia, primarily AFCID in urban areas of Southeast Asia, and a combination of the two in Beijing. Dust contributes 29 % to global population-weighted mean $PM_{2.5}$ concentrations, making it the second largest global $PM_{2.5}$ contributor.

As discussed in section 4.3, SPARTAN does not yet directly measure organic aerosol content; rather the inferred residual matter is expected to be mainly organic, based on comparison with independent organic measurements (Snider et al., 2016). SPARTAN residual concentrations are highest throughout Asia where values exceeding 10 μg m^{-3} are observed at all SPARTAN sites except Manila and Singapore. The lowest RM concentrations are found in Buenos Aires (2.1 μg m^{-3}) and Rehovot (2.7 μg m^{-3}). The broad consistency in spatial variation of SPARTAN RM and simulated OM (r = 0.92) provides supporting evidence that SPARTAN RM is dominated by organics. Simulated OM is enhanced over broad regions of South Asia, East Asia, and tropical Africa. Prior work has found that organic mass is a leading global $PM_{2.5}$ chemical component for mean

concentrations (Philip et al., 2014a) and trends (Li et al., 2017a). Organic mass is found to continue to play a major role in population-weighted $PM_{2.5}$ over 2013-2015, following SIA and dust to contribute 28 %.

Sulfate accounts for over 50% of SIA at all sampling sites, except Buenos Aires (46%), and accounts for approximately 6.5 μg m^{-3} of population-weighted $PM_{2.5}$ concentrations. SPARTAN measurements of sulfate concentrations exceed 5 μg m^{-3} at most sites in South and East Asia, in contrast with concentrations less than 2 μg m^{-3} in Buenos Aires and Ilorin. The simulation generally captures the spatial distribution of measured sulfate concentrations (r = 0.78). Observations from the OMI satellite instrument have drawn attention to the pronounced SO_2 concentrations from coal combustion in East and South Asia (Krotkov et al., 2016), and sensitivity simulations have shown the influence of coal burning to the large $PM_{2.5}$ burden over China (Ma et al., 2017). The simulation reveals the spatial scale of the sulfate enhancement associated with these SO_2 sources. Modest measured enhancements are found in Rehovot, with associated regional scale enhancements across the Middle East. McLinden et al., (2016) found evidence of missing SO_2 sources in the Middle East that could contribute to the regional sulfate burden. Low simulated concentrations across North America and Europe reflect the success of SO_2 emission controls over recent decades (Greenstone, 2001; Hand et al., 2012a; Li et al., 2016a; Stjern et al., 2011).

The spatial pattern of measured ammonium concentrations largely follows that of measured sulfate (r = 0.96) associated with the formation of ammonium sulfate and ammonium bisulfate. Measured ammonium is also associated with measured nitrate (r = 0.93) as discussed further below. Ammonium contributes less than 10% to measured

$PM_{2.5}$ concentrations with a population-weighted mean concentration of 3.0 μg m^{-3}. IASI satellite observations have revealed pronounced NH_3 enhancements across East and South Asia (Clarisse et al., 2009; Kharol et al., 2013), where enhanced ammonium concentrations are apparent. Simulated ammonium concentrations are significantly correlated with measurements (r = 0.86), although overestimated. A possible explanation of this overestimation is incomplete aerosol neutralization by organic inhibition of ammonia uptake not represented in the simulation (Kim et al., 2015; Silvern et al., 2017).

Figure 4.3 shows the extent of neutralization of aerosol in the observations and the simulation. The simulated aerosol is fully neutralized (f = 0.95 mol mol^{-1}) whereas the measured aerosol has a median extent of neutralization of 0.64 mol mol^{-1}. Recent studies (e.g. Kim et al., 2015; Pye et al., 2018; Silvern et al., 2017) report deviation from complete aerosol neutralization in the Southeast United States during summer when organic aerosol is in excess of sulfate (Kim et al., 2015; Marais et al., 2016). Laboratory experiments conducted by Liggio et al., (2011) proposed that uptake of ammonia by sulfuric acid aerosol is hindered by competition from organic gases, significantly reducing the rate of aerosol neutralization. Other laboratory studies have suggested that phase separation occurs with mixing of organic and sulfate aerosols, allowing the organics to coat the sulfate minimizing exposure to ambient gases and subsequent neutralization (Bertram et al., 2011; You and Bertram, 2013). Incomplete neutralization in observed $PM_{2.5}$ at SPARTAN sites (f < 1) provides supporting evidence of competition between organics and ammonia, inhibiting ammonium sulfate formation.

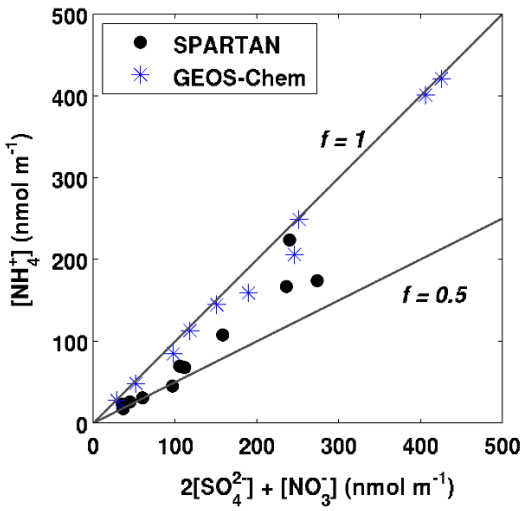

Figure 4.3. Extent of neutralization at SPARTAN sites from measurements and the GEOS-Chem simulation. Extent of neutralization is given by $f = [NH_4^+]/(2[SO_4^{2-}] + [NO_3^-])$ for an externally-mixed sulfate-nitrate-ammonium (SNA) aerosol. Solid lines correspond to different extents of neutralization; $f = 1$ is a fully neutralized aerosol such as ammonium sulfate and $f = 0.5$ for ammonium bisulfate.

The degree of spatial variation in measured nitrate reflects the availability of nitric acid and excess ammonia to form ammonium nitrate. The highest measured concentrations are observed in Beijing (4.9 μg m^{-3}), Kanpur (3.8 μg m^{-3}), and Hanoi (3.7 μg m^{-3}), whereas the lowest are in Ilorin and Singapore (0.2 μg m^{-3}). The simulation generally reproduces the low measured concentrations at most sites (r = 0.85); however, simulated concentrations are biased low at most sites while biased high at northern sites (Beijing, Kanpur, and Dhaka). These discrepancies may reflect processes related to thermodynamic equilibrium between the gas and particle phase, aerosol neutralization as discussed above, and uncertainty in NH_3 emissions (Paulot et al., 2014). It is possible that semi-volatile ammonium nitrate is lost from the filters, however the SPARTAN sampling procedure is designed to limit loss of semi-volatile species, such as ammonium nitrate (Snider et al., 2015). In addition, Chapter 3 reports statistically insignificant trends in $PM_{2.5}$ and ammonium nitrate mass when comparing the mass collected on the first sampled filter (54-day residence time in instrument) and the last filter sampled (negligible

residence time). The simulated population-weighted mean nitrate concentration is 2.4 μg m^{-3}, driven by elevated concentrations in East Asia, South Asia and Europe.

BC concentrations vary by a factor of 7 across SPARTAN sites, with concentrations exceeding 5 μg m^{-3} in Beijing (7.3 μg m^{-3}), Dhaka (5.8 μg m^{-3}) and Kanpur (5.6 μg m^{-3}) and as low as 1.0 μg m^{-3} in Ilorin. The GEOS-Chem simulation reveals the regional nature of the BC enhancements from a variety of combustion sources in East China and the Indo-Gangetic Plain. The downscaled simulation generally captures the BC concentrations at most SPARTAN sites (r = 0.67), suggesting skill in capturing the heterogeneous sources of this primary $PM_{2.5}$ component at the global scale. Population-weighted mean BC concentration is an order of magnitude lower than SIA at 4 %.

Sea salt concentrations are low in both the measurements and simulation, yielding a negligible population-weighted concentration of 0.5 μg m^{-3}.

4.3.2 SPARTAN Site Characteristics

SPARTAN composition measurements support the site-specific source attribution from sensitivity simulations. Below, SPARTAN measurements of $PM_{2.5}$ mass and chemical composition are further interpreted to understand sources. Source categories selected for investigation follow those of (Lelieveld et al., 2015) and are described in Table 4.2. The presentation is grouped by region, the left column of all figures (4.4 – 4.9) shows measured $PM_{2.5}$ composition at the indicated SPARTAN site. The remaining bars in each figure show the contribution of seven source categories to simulated concentrations of each major $PM_{2.5}$ chemical component. Measurement uncertainty (CV)

for each chemical component is calculated as described in section 4.3. SPARTAN measurement error bars shown in Figure 4.4 – 4.9 are calculated as:

$$error = \frac{CV}{\sqrt{n}} \quad (6)$$

where *n* is the number of measurements. Sampling periods are found in Table 4.4.

4.3.2.1 East Asia

Figure 4.4 shows the measured $PM_{2.5}$ composition and source attribution at two SPARTAN sites located in East Asia: Beijing, China and Hanoi, Vietnam. Measured $PM_{2.5}$ composition is dominated by residual matter (likely organics), followed by dust and sulfate at each site. All seven source categories have a meaningful contribution to major chemical components except sea salt; accounting for the measured annual mean $PM_{2.5}$ concentration of 67 μg m^{-3} in Beijing and 51 μg m^{-3} in Hanoi. Residential energy use and industry dominate the OM component of $PM_{2.5}$ through burning of solid fuels for domestic cooking, space heating, and industrial purposes (Lu et al., 2011). Bonjour et al., (2013) estimate approximately 50% of the 2010 population in China and Vietnam burned solid fuels for domestic use. Open fires and natural sources also contribute to OM in Hanoi due to transport of seasonal biomass burning plumes from Southeast Asia and the oxidation of biogenic volatile organic compounds (VOCs). SPARTAN measurements indicate that dust accounts for 22% of $PM_{2.5}$ in Beijing and 17% in Hanoi. In Beijing, contributions from both natural mineral dust and anthropogenic activity are observed, consistent with prior work (Philip et al., 2017; Snider et al., 2016; Zhang et al., 2015). Simulated dust concentrations in Hanoi are driven by anthropogenic activity and underestimate the observations. Sulfate concentrations are influenced primarily by

emissions from industry and power generation. Numerous studies have reported that decreasing SO_2 emissions from power generation in East Asia are being partially offset by rising SO_2 emissions from industrial activity (Klimont et al., 2013; Lu et al., 2011; Xu, 2011). Ma et al., (2017) estimate that coal combustion contributes to 40% of the total $PM_{2.5}$ in Chinese cities. Ammonium concentrations are mostly agricultural NH_3 and affected by formation with sulfate and nitrate. Agricultural activity has the largest impact on nitrate concentrations due to the limiting role that ammonia can play in ammonium nitrate formation (Pandis et al., 1995; Pinder and Adams, 2007; Wang et al., 2013). Industrial sources of NO_x also contribute to nitrate formation in East Asia (Kharol et al., 2013; Wang et al., 2013). The positive bias in simulated nitrate in Beijing could reflect missing processes (Heald et al., 2012; Silvern et al., 2017) or loss of semi-volatile species from the measurements. BC has two primary source categories: residential energy and industrial activity. Overall, each of the investigated source categories are active in East Asia and contribute to the complex $PM_{2.5}$ mixture measured by SPARTAN.

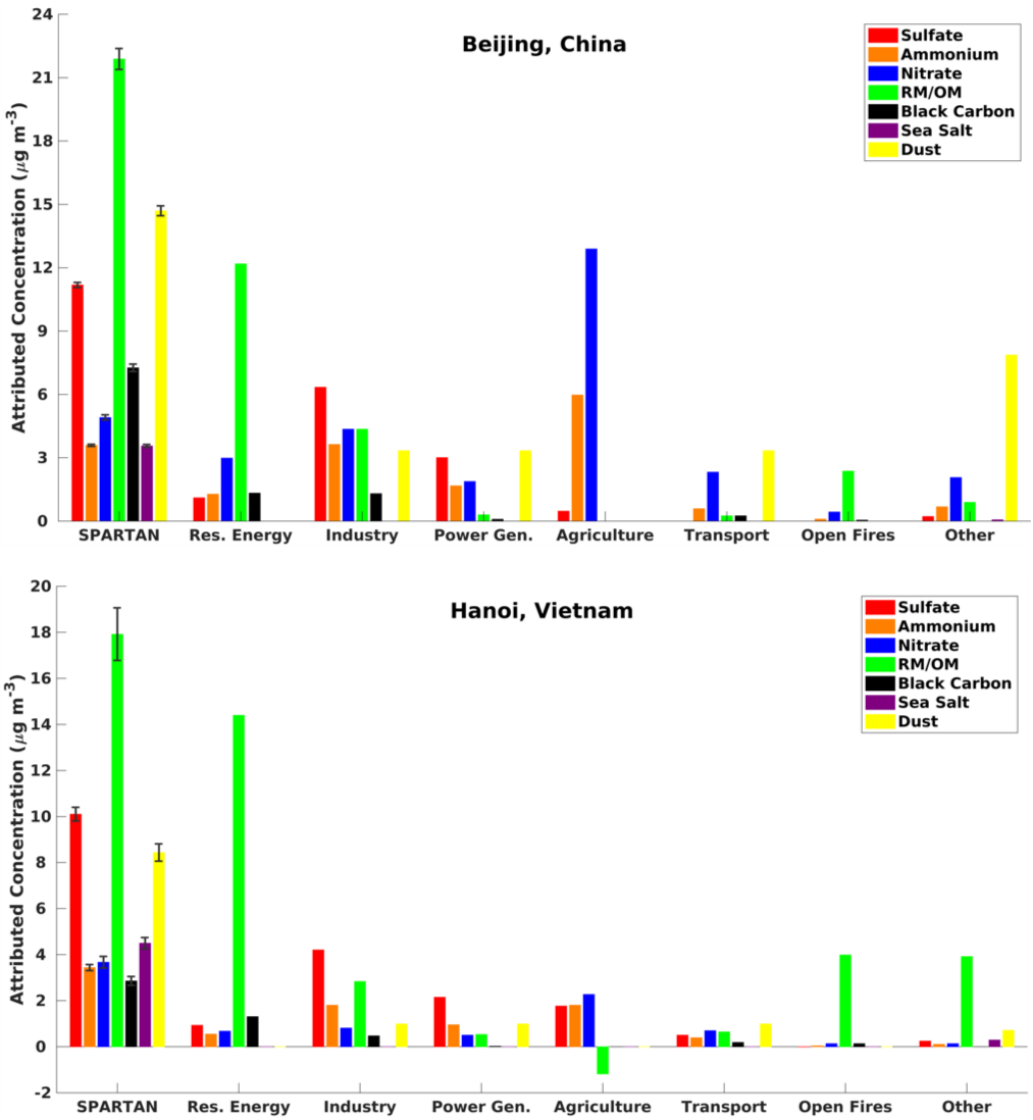

Figure 4.4. Measured $PM_{2.5}$ chemical composition (left column) and the contribution of seven source categories to simulated concentrations of each major chemical component (right columns) for two sites in East Asia: Beijing, China; and Hanoi, Vietnam.

4.3.2.2 Southeast Asia

Figure 4.5 shows the measured $PM_{2.5}$ composition and source attribution at three SPARTAN sites in Southeast Asia: Bandung, Indonesia; Manila, Philippines; and Singapore. The residential energy use source category has the largest impact on OM concentrations in Bandung and Manila through burning of solid fuels in domestic

cooking and heating, sources that are underestimated in the simulation. Bonjour et al., (2013) estimated that in 2010, at least 50% of the population in Indonesia and the Philippines burn solid fuels for domestic cooking. Open fires dominate OM concentrations in Singapore where seasonal biomass burning events throughout Southeast Asia significantly impact ground-level air quality (Chang et al., 2015; Koplitz et al., 2016). The bias in the simulation could reflect errors in representing long range transport. Singapore exhibits a minor increase in OM when emissions from agriculture are removed due to increased aerosol acidity as this ammonia source neutralizes acidic components. Significant contribution to sulfate concentrations arise from the industry and power generation source categories from SO_2 emissions from burning of high-sulfur containing fossil fuels in boilers, limestone kilns, furnaces, and power plants. A minor source of sulfate is the natural source category as atmospheric oxidation of oceanic DMS (Boucher et al., 2002), and in Bandung, nearby volcanos (Lestari and Mauliadi, 2009b). The low measured and simulated nitrate concentration at all three sites reflect ambient temperatures that thermodynamically limit NH_4NO_3 formation. The dust component of $PM_{2.5}$ in Southeast Asia is dominated by anthropogenic dust from industry, power generation, and transport in this region.

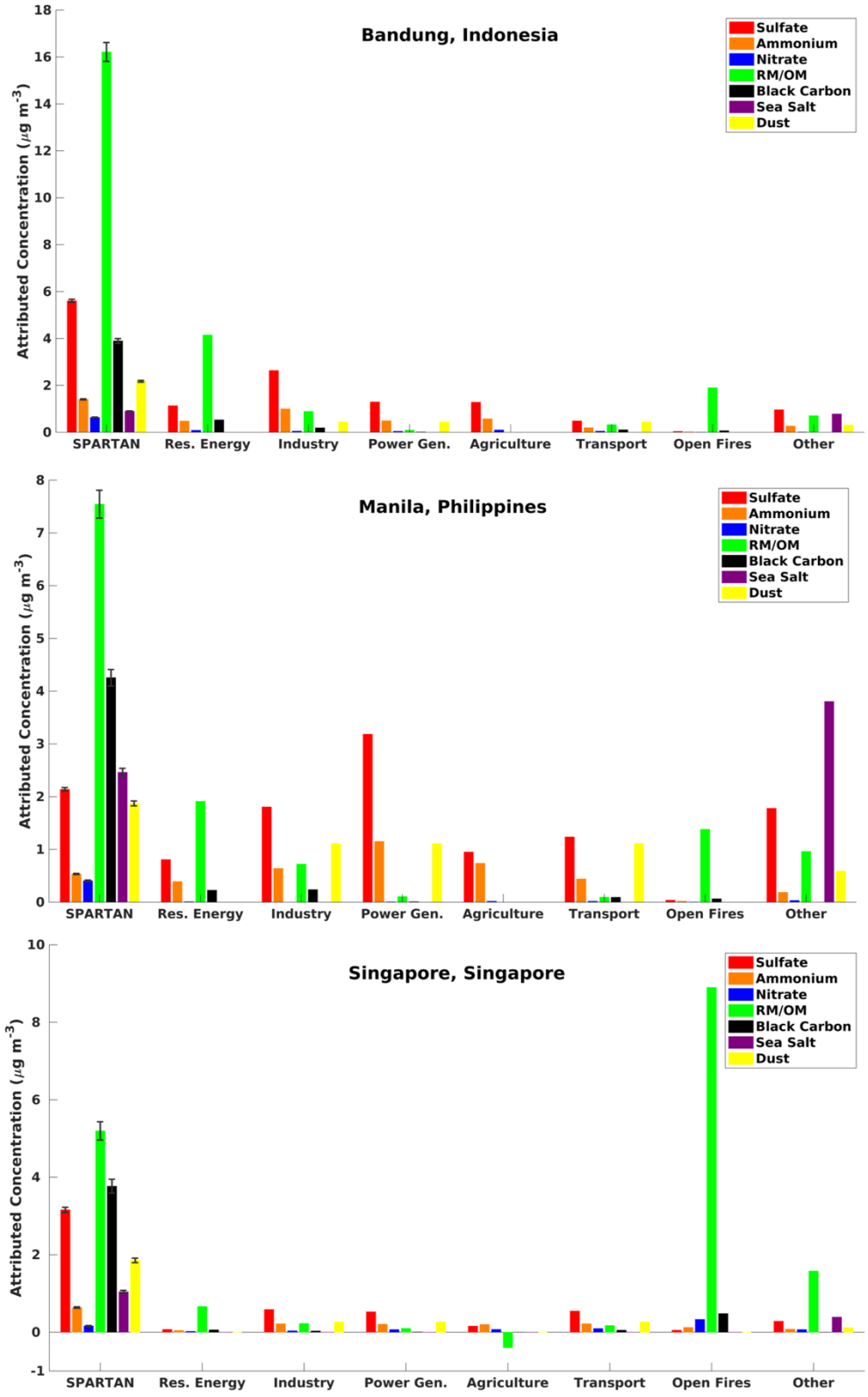

Figure 4.5. Measured $PM_{2.5}$ chemical composition (left column) and the contribution of seven source categories to simulated concentrations of each major chemical component (right columns)

for three sites in Southeast Asia: Bandung, Indonesia; Manila, Philippines; and Singapore, Singapore

4.3.2.3 South Asia

Figure 4.6 shows the measured $PM_{2.5}$ composition and source attribution at two SPARTAN sites located in South Asia: Kanpur, India and Dhaka, Bangladesh. Overall consistency is found across the two simulated source attribution plots. Kanpur is situated in the Indo-Gangetic plain where significant agricultural and industrial activity occur (Ram et al., 2012) and persistent stagnant air in winter enhances particulate matter concentrations (Kumar et al., 2017). Dhaka is subjected to air masses transported from the Indo-Gangetic plain (Begum et al., 2012) as well as strong local emission sources. The residential energy use source category is the largest simulated contributor to $PM_{2.5}$ in Kanpur and Dhaka by substantially influencing OM as well as BC. Bonjour et al., (2013) estimate that 58% of the population in India and 91% of the population in Bangladesh in 2010 burn solid fuels for domestic heating and cooking. Sulfate concentrations are most heavily influenced by the power generation and industry source categories. Generally there has been an increase in SO_2 emissions from India, driven by rapid economic development (Lu et al., 2011, 2013). Fioletov et al., (2016) found that coal-fired power plants account for nearly all major SO_2 emission sources seen by OMI in India, with growth of a factor of two over 2005-2014, and a factor of three in the Chhattisgarh and Odisha regions, located south of the SPARTAN site in Kanpur and west of the site in Dhaka. The main fuel for the iron and steel industry is coal, resulting in SO_2 emissions from this sector as well (Klimont et al., 2013; Lu et al., 2011). Current legislation does not require the installation of flue gas desulfurization in either the industrial or power generation sectors (Klimont et al., 2013; Krotkov et al., 2016). Elevated observed

ammonia concentrations (Clarisse et al., 2009) suggest excess ammonia to readily form ammonium sulfate, explaining the changes in ammonium when emissions from industry and power generation are altered. Dust is a notable contributor to $PM_{2.5}$ in South Asia, accounting for 11% of total $PM_{2.5}$ in Dhaka and 8% in Kanpur. Anthropogenic dust accounts for the majority of dust in South Asia, however natural sources also play a role. Previous studies (e.g. Begum et al., 2004; Chinnam et al., 2006; Dey et al., 2004; Gautam et al., 2009; Ram et al., 2012; Zheng et al., 2016) have found evidence of transport of desert dust from the western Thar Desert, Northeast Africa, and the Gulf region.

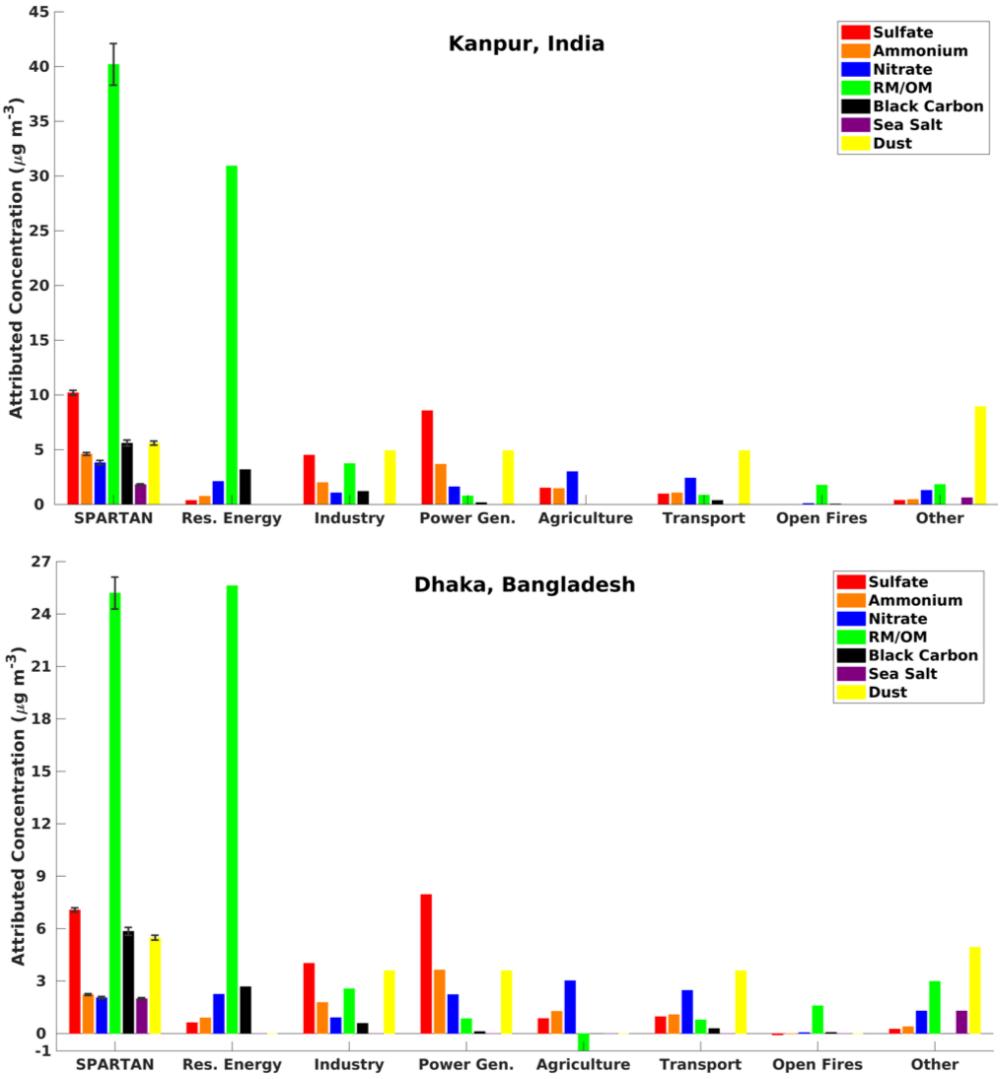

Figure 4.6. Measured $PM_{2.5}$ chemical composition (left column) and the contribution of seven source categories to simulated concentrations of each major chemical component (right columns) for two sites in South Asia: Kanpur, India; and Dhaka, Bangladesh.

4.3.2.4 South America

Figure 4.7 shows the measured $PM_{2.5}$ composition and source attribution in Buenos Aires, Argentina. Distinct from other SPARTAN sites, sensitivity simulations suggest most $PM_{2.5}$ arises from natural sources. SPARTAN measurements corroborate this conclusion with 21% of $PM_{2.5}$ from sea salt, 20% from organics, and 16% from mineral dust. Mineral dust from the arid desert region to the northwest of the city

influences the dust content of $PM_{2.5}$ at this site (Zheng et al., 2016). Substantial cropland to the west and tree covered areas to the north (Latham et al., 2014) indicate a source secondary organic aerosol from oxidation of biogenic emissions of VOCs such as isoprene and other monoterpenes. The flux of oceanic DMS influences sulfate concentrations (Boucher et al., 2002). Industry and power generation are also notable sources of sulfate in Buenos Aires. Open fires from deforestation activity in the Amazon produce plumes that affect air quality in Argentina (Freitas et al., 2005; Reddington et al., 2015). Organic content increases when ammonia emissions from agriculture are removed due to increased aerosol acidity.

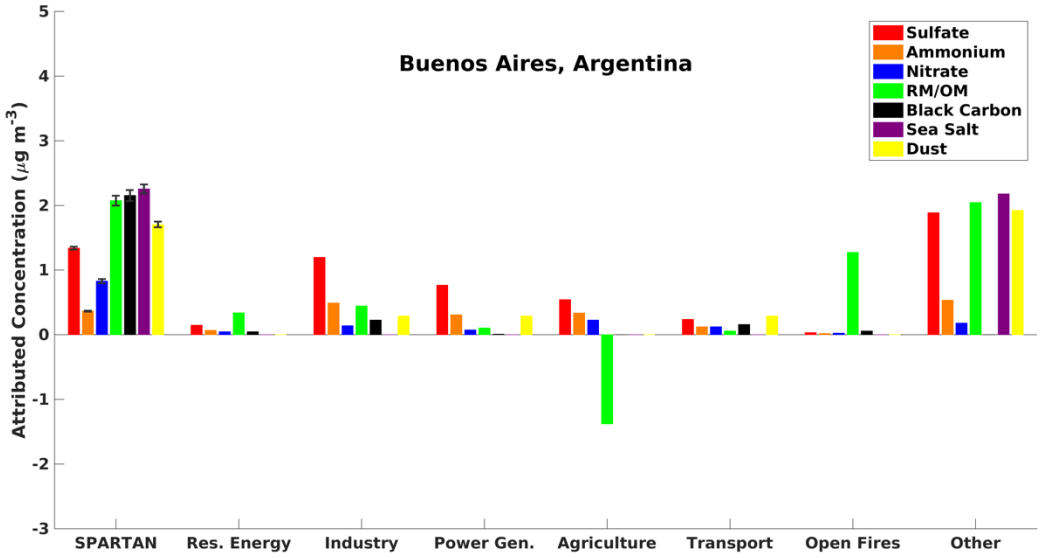

Figure 4.7. Measured $PM_{2.5}$ chemical composition (left column) and the contribution of seven source categories to simulated concentrations of each major chemical component (right columns) for the site in South America: Buenos Aires, Argentina.

4.3.2.5 Middle-East

Figure 4.8 shows the measured $PM_{2.5}$ composition and source attribution at the Middle East site in Rehovot, Israel. Natural sources are the leading source category in this region, dominated by desert dust; SPARTAN measurements indicate that 26% of

$PM_{2.5}$ is dust but also suggest that the GEOS-Chem simulation is overestimating this source. Power generation has the largest anthropogenic impact on $PM_{2.5}$ concentrations and is the leading source of sulfate at this site from oxidation of emitted SO_2. The Middle East is among the largest SO_2 emitting regions in the world from oil fields and refineries (Fioletov et al., 2016; Krotkov et al., 2016; McLinden et al., 2016). Transport of air masses from other Middle Eastern countries and Europe have been shown to influence ground-level concentrations (e.g.Formenti et al., 2001; Graham et al., 2004) Notable changes in ammonium are found when sources of sulfate are removed, suggesting elevated background NH_3. Clarisse et al., (2009) reported NH_3 columns well above background level in the Nile River Delta, southwest of the sampling site. Elevated temperatures thermodynamically inhibit formation of particulate nitrate.

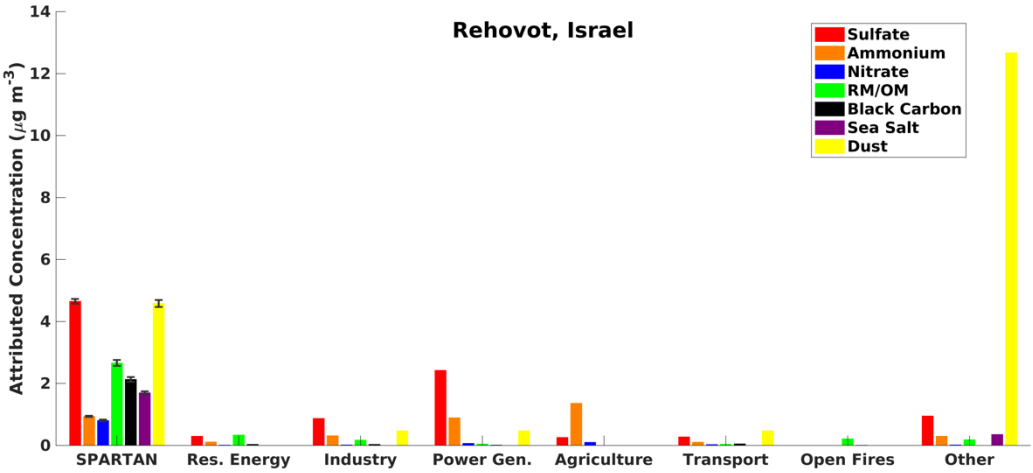

Figure 4.8. Measured $PM_{2.5}$ chemical composition (left column) and the contribution of seven source categories to simulated concentrations of each major chemical component (right columns) for the site in Middle East: Rehovot, Israel.

4.3.2.6 Sub-Saharan Africa

Figure 4.9 shows the measured $PM_{2.5}$ composition and source attribution in Ilorin, Nigeria and Pretoria, South Africa. Both sites have measured $PM_{2.5}$ concentration below

20 μg m^{-3} that is mostly composed of residual (organic) matter, dust, and sulfate. Pronounced natural dust concentrations in Ilorin arise from the Sahara Desert where seasonal Harmattan trade winds advect fine dust to West Africa (Ridley et al., 2012). Both sites experience a large influence from the open fires and residential energy use source categories. Ilorin is downwind of seasonal biomass burning events in West Africa (Generoso et al., 2003), whereas open fires in central Africa affect South Africa (Generoso et al., 2003). Burning of solid fuels (e.g. biofuel and coal) for domestic stoves, cookers, and heaters accounts for the influence of residential energy category on organic, sulfate, and black carbon concentrations. Bonjour et al., (2013) estimate that in 2010 approximately 74% of households used solid fuels for domestic cooking in Nigeria. Natural sources of OM in $PM_{2.5}$ are biogenic VOCs from surrounding vegetation and grasslands. Unlike many other SPARTAN sites, the industry and power generation source categories have minimal influence on $PM_{2.5}$ concentrations in Ilorin. However, power generation and industry are leading contributing source categories to sulfate in the industrialized city of Pretoria.

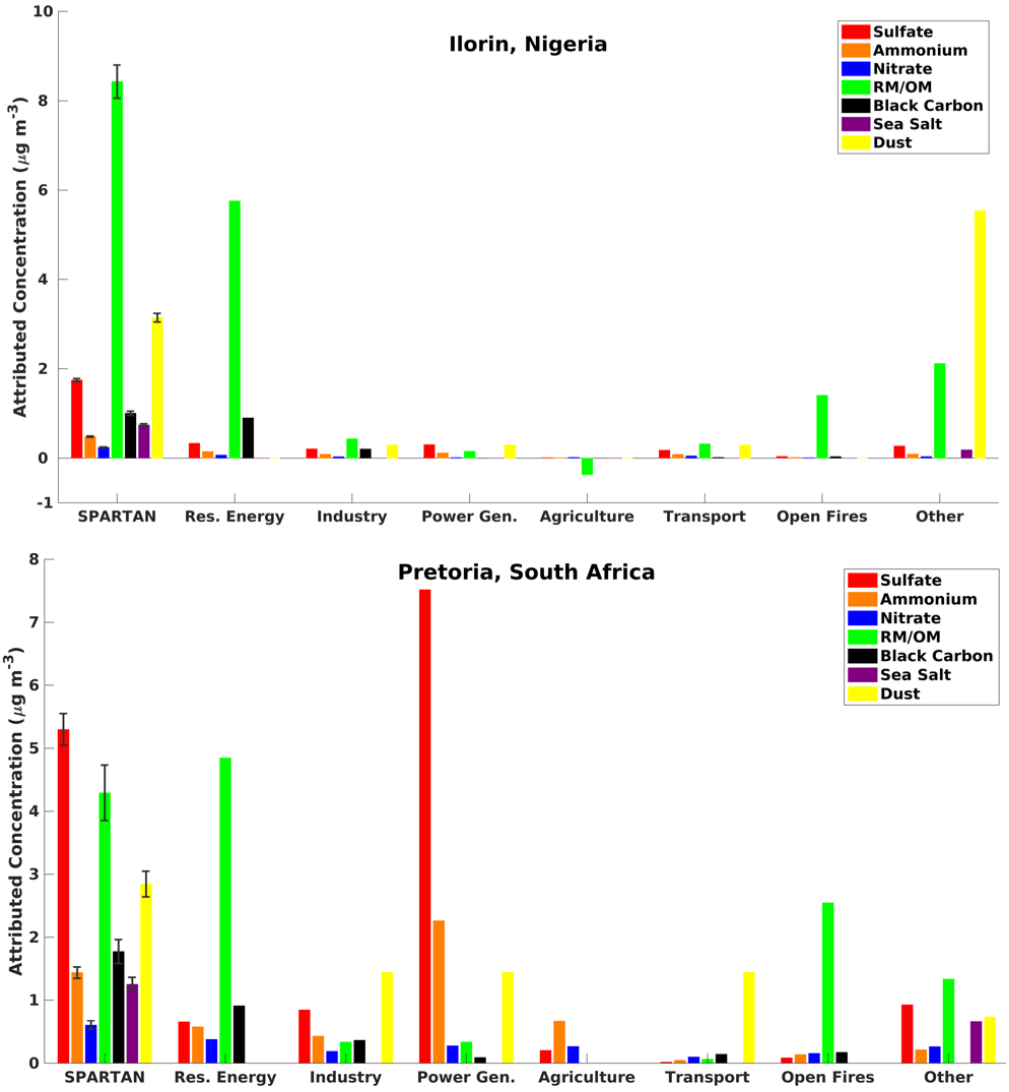

Figure 4.9. Measured $PM_{2.5}$ chemical composition (left column) and the contribution of seven source categories to simulated concentrations of each major chemical component (right columns) for two sites in Sub-Saharan Africa: Ilorin, Nigeria; and Pretoria, South Africa.

4.3.3 Global $PM_{2.5}$ Source Categories

Broad consistency between measured and simulated $PM_{2.5}$ composition provide validity for utilizing sensitivity simulations to explore the influence of source categories to global population-weighted $PM_{2.5}$. Figure 4.10 shows the impact of seven source categories to $PM_{2.5}$ as determined from sensitivity simulations that separately exclude each source. Values inset show the global population-weighted mean $PM_{2.5}$

concentrations from each source. Note that the sum of $PM_{2.5}$ concentrations from the seven source sectors exceeds the global mean $PM_{2.5}$ concentration due to non-linearity in modeled aerosol processes, primarily affecting nitrate, ammonium, and SOA.

Six primarily anthropogenic categories contribute 76% of global $PM_{2.5}$ exposure. The residential energy use sector has the largest anthropogenic contribution, responsible for 21 % (7.9 $\mu g\ m^{-3}$) of population-weighted $PM_{2.5}$. This residential category primarily includes small combustion sources for domestic heating, cooking, and waste disposal. These biofuel sources, diesel generators and burning of household waste, produce a large amount of indoor and outdoor carbonaceous $PM_{2.5}$ with implications for human health (Anenberg et al., 2010; Balakrishnan et al., 2013; Lelieveld et al., 2015; Philip et al., 2014a). The contribution of this source category to outdoor $PM_{2.5}$ is most pronounced in the populous areas of South Asia, East Asia, and Africa. Lacey et al., (2016) found that the elimination of solid fuel cookstoves over a 20-year period could avoid 22.5 million premature deaths associated with outdoor $PM_{2.5}$.

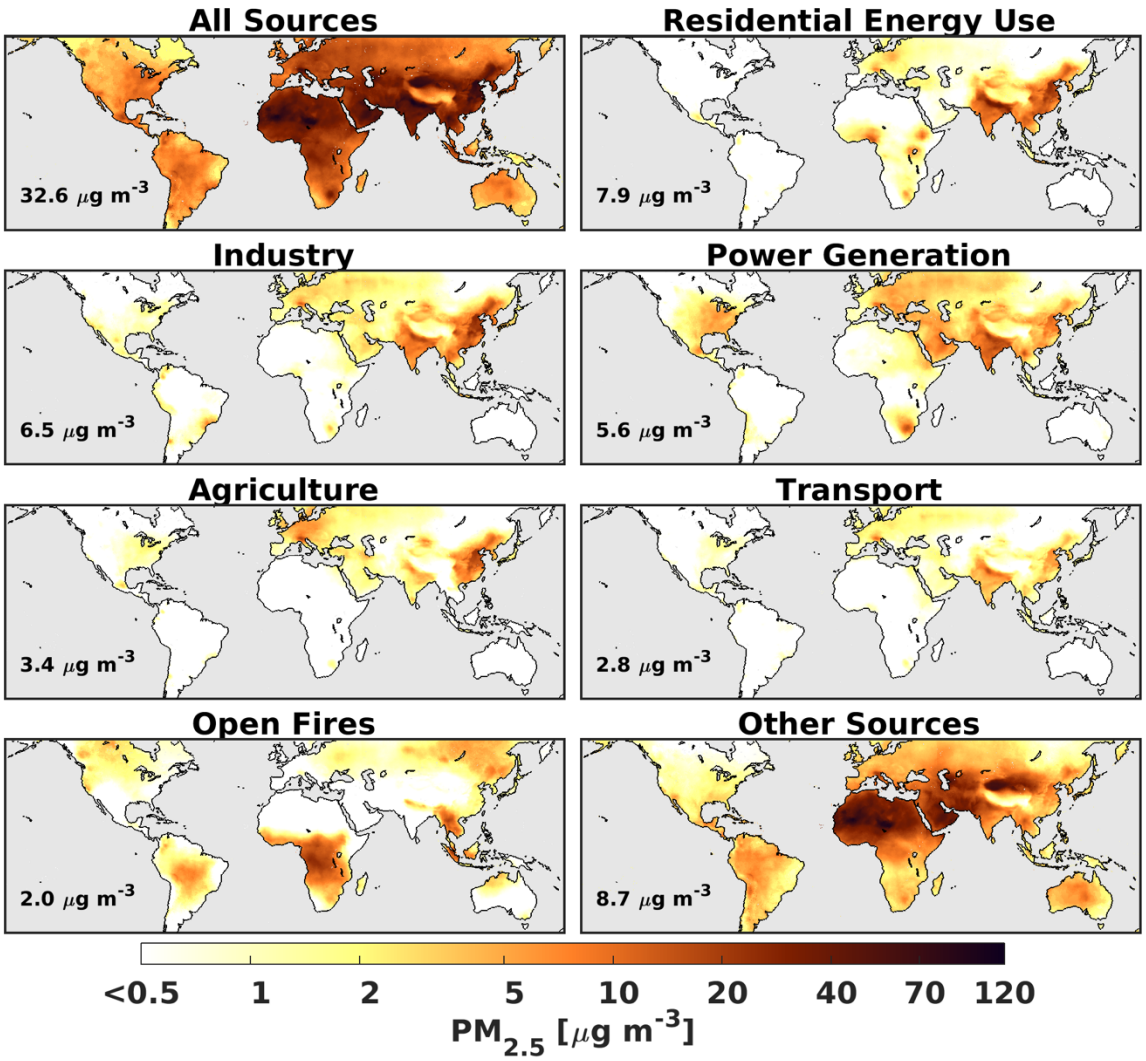

Figure 4.10. Global simulated annual mean total $PM_{2.5}$ mass (top left) and contribution from seven source categories at 35% RH following measurement protocols. Inset values display the global population-weighted average $PM_{2.5}$ concentration from each source category. Grey denotes water.

Industry is the second largest anthropogenic source category contributing to 18% (6.5 μg m^{-3}) of population-weighted $PM_{2.5}$. Emissions from the industry source category include manufacturing of iron, steel, pulp, and paper, as well as oil refineries and fuel production. Industry contributes significantly to $PM_{2.5}$ in China and India, and has a notable impact near major urban areas in the Americas, Europe, and Southeast Asia. The

impact is highest in emerging economies and industrialized countries, in part due to international trade (Lin et al., 2014; Zhang et al., 2017).

The four remaining anthropogenic categories are responsible for 37 % of population-weighted $PM_{2.5}$. Power generation, although not the leading source in any one region, makes a prominent contribution of 15 % to global population-weighted $PM_{2.5}$. Emissions of SO_2 and NO_x from fossil fuel fired power plants are readily oxidized in the atmosphere to sulfate and nitrate, leading to enhanced $PM_{2.5}$ concentrations, especially in South Asia, East Asia, and North America. Agriculture, primarily NH_3 and NO_x from fertilizer and domesticated animals, contributes 9 % to global-population weighted $PM_{2.5}$. Agriculture is the leading source category in most of Europe and one of the leading sources over much of China and parts of India, similar to the findings of Lelieveld et al., (2015). The $PM_{2.5}$ contribution from agricultural activity is largest where both a large nitric acid burden exists from NO_x emissions and where excess ammonia is available. Transportation emissions contribute 8 % of global population-weighted $PM_{2.5}$ through emissions of NO_x ($NO + NO_2$), organics, BC, and SO_2; the most heavily influenced regions are East Asia, Southeast Asia, and the Indo-Gangetic plain. Emissions of carbonaceous aerosol and gaseous organic compounds from open fires comprise only 5% of population-weighted mean $PM_{2.5}$ concentrations. However, open fires can dominate $PM_{2.5}$ mass in large parts of the tropical and boreal forests.

All sources not clearly controlled by mitigation strategies, primarily natural in origin, are lumped into a single “other sources” category described in Table 4.2. This combined Other category contributes 24 % of population-weighted $PM_{2.5}$. Sources include mineral dust that dominates $PM_{2.5}$ in arid and semi-arid regions of North Africa,

the Middle East, Central Asia, and Australia. The size distribution of lofted dust aerosols extends from the coarse mode into the fine mode of $PM_{2.5}$ that can remain suspended and undergo long range transport (Ginoux et al., 2001; Prospero et al., 2002). Natural sources of biogenic organic compounds, NO_x from soil, and microbial activity of oceanic dimethyl sulfide contribute to a diffuse $PM_{2.5}$ background.

4.4 Conclusion

This initial interpretation of globally dispersed ambient $PM_{2.5}$ mass and composition measurements from SPARTAN with the GEOS-Chem model, with development motivated by SPARTAN measurements and constrained by satellite-based estimates of $PM_{2.5}$, identified a promising level of consistency along with areas for further model development. The consistency between simulated and SPARTAN-measured components provide confidence in utilizing the sensitivity simulations to identify the ambient $PM_{2.5}$ sources with prominent influence on population-weighted $PM_{2.5}$. The pronounced global contributions from residential energy use (21 %), industry (18 %), and power generation (15 %) warrant further attention. Consistency between SPARTAN $PM_{2.5}$ composition and the attributed contribution from seven source categories suggests validity of source attribution from sensitivity simulations and provides additional insight into regional biases in simulated $PM_{2.5}$ composition. OA remains underestimated at most SPARTAN sites, reiterating that development is needed to aerosol processes (e.g. SOA formation) and emission inventories that control this primary component (e.g. residential energy use and open fires). Although improvements to the dust simulation and emissions have been implemented in recent model versions

(e.g. Philip et al., 2017; Zhang et al., 2013a), further attention is needed to mineral and AFCID emission inventories to address regional differences (Ridley et al., 2016). Evidence of incomplete sulfate neutralization at SPARTAN sites, which is not captured in the simulation, warrants additional investigation as this may partially explain the overestimate of simulated ammonium and nitrate concentrations. Additional ground-based, global measurements of $PM_{2.5}$ mass and composition will also be important to evaluate and improve these source attribution estimates.

Chapter 5 Interpretation of the Relationship Between Ground Level Fine Particulate Matter and Columnar Aerosol Optical Depth using Measurements from SPARTAN

5.1 Introduction

Ambient $PM_{2.5}$ is increasingly recognized as the leading environmental risk factor for global burden of disease (Gakidou et al., 2017). Nonetheless, ground-based observations of $PM_{2.5}$ have insufficient global coverage to provide long-term global estimates of $PM_{2.5}$ that can be used to estimate population exposure. Satellite remote sensing of AOD, when combined with constraints from CTMs, offers a promising method of estimating population exposure to $PM_{2.5}$ on a global scale (van Donkelaar et al., 2015; van Donkelaar et al., 2010). Global satellite-derived $PM_{2.5}$ estimates have been used extensively to estimate population exposure to $PM_{2.5}$ and assess the health impacts of long-term exposure (Anderson et al., 2012; Brauer et al., 2016; Chen et al., 2017; Cohen et al., 2017; Gakidou et al., 2017; Pinault et al., 2016). However, the relationship between AOD and $PM_{2.5}$ is complex. AOD is a measure of the columnar aerosol extinction at ambient relative humidity at the time of observation, which is usually daytime, while $PM_{2.5}$ is a measure of the 24-hour ground-level mass from particles with aerodynamic diameter of 2.5 μm or smaller, at controlled relative humidity (usually 30 – 50%, depending on the measurement network). Few collocated ground-based measurements of AOD and $PM_{2.5}$ exist until recently, and $PM_{2.5}$ measurement standards (e.g. relative humidity) can vary across networks. Satellite retrievals of AOD complicate the interpretation of $PM_{2.5}$ to AOD relationships due to errors in retrieved AOD. Collocated ground-based measurements of the $PM_{2.5}$ to AOD relationship are needed to

evaluate modeled values of this relationship and to assess the factors that contribute to its global variation.

SPARTAN is designed to evaluate and enhance satellite-based estimates of $PM_{2.5}$ by measuring $PM_{2.5}$ concentrations, composition, and scatter continuously at sites that also measure AOD (Snider et al., 2015). SPARTAN includes sampling on air filters and with a nephelometer to provide long-term, daily, and hourly $PM_{2.5}$ information in populated regions. Results have so far been collected at 15 sites spread over 4 continents. Collocating $PM_{2.5}$ and ground-based AOD measurements provides the unique ability to measure the relationship between $PM_{2.5}$ and AOD. SPARTAN measurements of ground scatter also provide the ability to interpret the factors that influence $PM_{2.5}$ to AOD relation, such as the aerosol vertical profile. A chemical transport model (GEOS-Chem) is used to simulate the $PM_{2.5}$ to AOD ratio to interpret the measurements from SPARTAN and other sites where collocated $PM_{2.5}$ and AOD measurements are available.

In Section 5.2 the data, including $PM_{2.5}$ measurement methods, ground-based AOD measurements, and the global chemical transport model used in this study is briefly described. In Section 5.3 empirical measurements of the $PM_{2.5}$ to AOD ratio are interpreted using modeled values to understand the global variation of this ratio. This analysis offers insight into the factors influencing the spatial variation in the relationship between $PM_{2.5}$ and AOD as well as sources of potential biases in the modeled relationship.

5.2 Materials and Methods

5.2.1 SPARTAN Measurements

SPARTAN is a network of ground-based instruments that measure particulate matter mass concentrations and composition through filter impaction and incorporates continuous monitoring through nephelometry (Snider et al., 2015). All SPARTAN sites are collocated with AERONET sunphotometers (Holben et al., 1998) to obtain ground-based measurements of the relationship between ground level daily mean $PM_{2.5}$ and total-column AOD measurements during daytime satellite overpass times. Details on site selection criteria and set-up are provided in Appendix B8.0. To date, all SPARTAN instruments are designed and manufactured by AirPhoton LLC (www.airphoton.com). The attributes of these instruments include low maintenance, portability, field readiness, and highly autonomous operation. The collocated $PM_{2.5}$ mass, scatter, and AOD measurements yield the daily $PM_{2.5}$/AOD ratio (η; $\mu g\ m^{-3}$).

5.2.1.1 Filter Measurements

SPARTAN $PM_{2.5}$ measurements are made by collecting $PM_{2.5}$ on PTFE filters that are housed in a protective, removable plastic cartridge that contains 8 filter pairs, and are sampled sequentially over a period of 9-days each using an AirPhoton SSi automated sampler. Each 8-slot filter cartridge protects the filters during transport. $PM_{2.5}$ is collected on a pre-weighted PTFE filter (2 μm pore size, SKC) that samples one diurnal cycle over a period of 9 days.

After air sampling is complete the sampled cartridges are shipped to the central SPARTAN laboratory at Dalhousie University for analysis. Post-sampling analysis

begins with gravimetric filter weighing. Capillary membrane and PTFE filters are equilibrated for 24 hours before weighing on a Sartorius Ultramicro Balance (with a 0.1 μg detection limit) in a clean room with controlled temperature (21±1.5 ˚C) and humidity (35±5% RH), following EPA protocols (USEPA, 1998). Potential static build-up is eliminated using an electrostatic blower. Absolute mass values are converted to mass concentration of $PM_{2.5}$, PM_{10}, and $PM_{10-2.5}$ by dividing accumulated filter mass by total air flow (with units of μg m^{-3}). More detail on the SPARTAN weighing procedure are provided in Appendix B1.0.

5.2.1.2 Nephelometry

The AirPhoton 3-wavelength integrating nephelometer is a continuous sampling, optically based device measuring total particulate scatter (b_{sp}) at red (632 nm), green (532 nm), and blue (450 nm) wavelengths over the angular range 7˚ to 170˚. The AirPhoton nephelometer records backscatter (b_{bks}) information between 92˚ and 170˚. The inlet is a 10 cm length of copper 1/4 inch tubing ending with a plastic inlet designed to prevent insects and large particles from entering the nephelometer chamber. Inlet wall losses for particles below 2.5 μm are expected to be less than 2% (Liu et al. 2011). Detail on maintaining nephelometers is provided in Appendix B6.0. The nephelometer airflow is not dried so that the ambient nature of measured aerosol scatter is consistent with aerosol scatter observed by satellite and to reduce concerns about evaporation of semi-volatile components. The nephelometer light scattering by aerosols, b_{sp}, is recorded at 15-second intervals that are averaged to 1 hour, $b_{sp,1h}$. All nephelometer scatter measurements are interpolated to 550 nm via the Ångström exponent to match those typically reported for satellite AOD. Hourly scatter values for which RH > 80% or $b_{sp,532}$ > 2500 Mm^{-1}

(nonlinear regime, Snider et al. 2016) are omitted. Relative fluctuations in dry aerosol scatter are anchored to an absolute filter mass to infer daily average $PM_{2.5}$ concentrations as described by Snider et al., (2016).

5.2.2 Ground-Based Measurements of Aerosol Optical Depth

AOD_{sat} is defined as the ground-based measurement of AOD reported by AERONET (Holben et al., 1998) averaged from 10:00 to 12:00 and 13:00 to 15:00 local time to include a range of satellite overpass times. AERONET provides multi-wavelength AOD measurements with a low uncertainty of < 0.02 (Holben et al., 2001). All-points level 2.0 or 1.5 cloud screened data (Appendix B7.0, Smirnov et al., 2000) are used at all sampling sites. The AOD is interpolated to 550 nm via the Ångström exponent.

5.2.3 Global Chemical Transport Model

The GEOS-Chem 3-D global chemical transport model (v11.01; geos-chem.org) is used to calculate the daily global distribution of $PM_{2.5}$ and AOD. The model is driven by assimilated meteorology from the Goddard Earth Observing System (GEOS) at the NASA Global Modeling Assimilation Office (GMAO). Our global simulation is at 2° x 2.5° horizontal resolution. The simulation uses assimilated meteorological observations (GEOS MERRA-2) for the year 2014 at 2° x 2.5° horizontal resolution. The simulation has 47 vertical levels from ground level up to approximately 80 km. The surface layer is approximately 100 meters in height. The model calculates the 3-D distribution of particulate matter and AOD with time steps of 10 minutes for transport and 20 minutes for chemistry.

The GEOS-Chem aerosol simulation includes oxidant-aerosol chemistry (Bey et al., 2001; Park et al., 2004) including the sulfate-nitrate-ammonium system (Park et al., 2004), mineral dust (Fairlie et al., 2007; Zhang et al., 2013a), sea salt (Jaeglé et al., 2011), and primary (Park et al., 2003; Wang et al., 2011) and secondary (Marais et al., 2016; Pye et al., 2010) carbonaceous aerosols. Gas-aerosol partitioning are computed using the ISOROPIA II thermodynamic module (Fountoukis and Nenes, 2007). The OM is estimated from primary OC using the spatially and seasonally varying values from OMI (Ozone Monitoring Instrument) NO_2 and AMS (Aerosol Mass Spectrometer) measurements following Philip et al. (2014), with updates from Canagaratna et al. (2015). Aerosol optical depth is calculated using the RH-dependent aerosol optical properties from Martin et al. (2003) with updates from Drury et al. (2008) and Ridley et al. (2012) and brown carbon by Hammer et al., (2016). The simulation uses the Emissions Database for Global Atmospheric Research (EDGAR) version 4.3 inventory (Crippa et al., 2016) and the MIX regional anthropogenic emission inventory for 29 Asian regions and countries (Li et al., 2017b). The anthropogenic fugitive, combustion, and industrial dust (AFCID) emission inventory of Philip et al., (2017) is included. Other emissions included are open fires from the Global Fire Emissions Database (GFED4) (Giglio et al., 2013) biogenic emissions (Guenther et al., 2006), soil NO_x (Hudman et al., 2012), lightning NO_x (Murray et al., 2012), aircraft emissions (Stettler et al., 2011; Wang et al., 1998), and volcanic SO_2 emissions (Fisher et al., 2011).

The modeled relationship between aerosol mass and relative humidity is applied for each aerosol type to calculate $PM_{2.5}$ for relative humidity values that correspond to U.S. Environmental Protection Agency standards (35% relative humidity) that are used

by SPARTAN. Daily values of the $PM_{2.5}$ to AOD relationship (η; μg m^{-3}) is calculated as the ratio of ground level $PM_{2.5}$ (μg m^{-3}) at 35% relative humidity to the total-column AOD at ambient relative humidity. AOD is averaged from 10:00 to 12:00 hours and from 13:00 to 15:00 hours local time to correspond to a range of satellite overpass times. Simulated values are sampled for the same months as the observations, weighted by the number of daily observations obtained in each month.

5.2.4 Statistical Terms Used

To estimate the bias in simulated variables, mean fractional bias (MFB) is used and is defined as:

$$\text{MFB} = \frac{1}{n}\left(\frac{\sum_{i=1}^{n}(M_i - O_i)}{\sum_{i=1}^{n}\frac{(M_i + O_i)}{2}}\right) \quad (7)$$

where M_i is the modeled value of the parameter in question, O_i is the corresponding observed value, and n is the number of observations.

5.3 Results

5.3.1 Global variation of $PM_{2.5}$ to AOD relationship

Table 5.1 contains empirical and simulated values of η ($PM_{2.5}/AOD_{sat}$) and related variables. Mean $PM_{2.5}$ concentrations varied by an order of magnitude across sampling sites from 6.4 μg m^{-3} in Fort McMurray, Canada to 66.0 μg m^{-3} in Beijing, China. Mean AOD varied by a factor of 16, ranging from 0.05 in Lethbridge, Canada to 0.83 in Kanpur, India. Mean simulated $PM_{2.5}$ at measurement sites varied by a factor of 17 with

the highest concentration also found in Beijing (60.1 μg m^{-3}) and lowest concentration in Buenos Aires, Argentina (3.5 μg m^{-3}). The simulated AOD varies by a factor of 17 across sites with the highest AOD in Dhaka, Bangladesh (0.61) and the lowest in Lethbridge (0.04). The MFB of simulated versus measured $PM_{2.5}$ concentrations is -18.1 %. The MFB between empirical and simulated AOD is -15.8%. The simulation moderately underestimates values of $PM_{2.5}$ and AOD across sampling sites, which motivates the use of satellite AOD and additional constraints from ground-based monitors to improve $PM_{2.5}$ estimates as developed by van Donkelaar et al., (2016).

Figure 5.1 shows the annual mean distribution of daily η values from GEOS-Chem with overlaid circles depicting measured and coincident modeled η values. The highest measured η values are found in Buenos Aires, Argentina (135 μg m^{-3}); Lethbridge, Canada (135 μg m^{-3}); and Pretoria, South Africa (127 μg m^{-3}). Measured η values also exceed 100 μg m^{-3} in Beijing, China; Kanpur, India; Bandung, Indonesia; Fresno, USA; and Rehovot, Israel. With the exception of Lethbridge and Buenos Aires, the simulation similarly shows elevated η values at these cities where strong $PM_{2.5}$ sources contribute to enhancements in ground-based aerosol with respect to the column. In addition, regions with strong influence from non-hygroscopic aerosols show enhanced η values, as their dry (35% RH) volume is similar to that under ambient conditions. The lowest measured η values are found in Downsview, Canada (27 μg m^{-3}); Dhaka, Bangladesh (40 μg m^{-3}); and Singapore (40 μg m^{-3}). The simulation similarly shows lower η values at locations with elevated AOD with respect to ground-based aerosol concentrations.

Table 5.1. Global coincident values of measured and simulated $PM_{2.5}$, AOD, and related variables.

Host City, Country	Time Period (mm/yyyy)	Site Coordinates		$PM_{2.5}$ (μg m^{-3})		$AOD_{10\text{-}14h}$		$\overline{\eta} = \frac{\overline{PM_{2.5,24h}}}{\overline{AOD_{sat}}}$ (μg m^{-3})		$\frac{\overline{AOD_{sat}}}{\overline{b_{sp,sat}}}$ (T_1^{-1}, km)		$\frac{\overline{b_{sp,24h}}}{\overline{PM_{2.5,24h}}}$ (T_3^{-1}, m^2 g^{-1})		$\frac{\overline{b_{sp,10-14h}}}{\overline{b_{sp,24h}}}$ (T_2^{-1})	
		Lat	Lon	Obs.	GC	Obs.	GC	Obs.	GC	Obs.	GC	Obs.	GC	Obs.	GC
Beijing, China	12/2013 - 01/2017	40.01	116.333	66.0 ± 1.8[a]	48.7 ± 2.5	0.63 ± 0.03	0.25 ± 0.02	105.1 ± 0.2	192.7 ± 9.9	1.01 ± 0.01	2.03 ± 0.01	3.89 ± 0.03	4.2 ± 0.8	2.03 ± 0.02	0.62 ± 0.00
Bandung, Indonesia	05/2014 - 09/2016	-6.888	107.61	34.9 ±1.2	6.6 ± 0.5	0.33 ± 0.02	0.05 ± 0.01	104.8 ± 0.8	141.3 ± 11.6	2.37 ± 0.21	2.66 ± 0.01	3.82 ± 0.01	7.2 ± 10.5	0.90 ± 0.01	0.42 ± 0.00
Singapore, Singapore	02/2016 – 02/2017	1.298	103.78	15.7 ± 0.4	7.6 ±0.7	0.41 ± 0.05	0.12 ± 0.01	39.7 ± 0.2	64.1 ± 5.5	7.35 ± 0.06	1.94 ± 0.01	4.06 ± 0.04	11.5 ± 8.2	0.81 ± 0.02	0.72 ± 0.00
Rehovot, Israel	09/2015 – 12/2016	31.907	34.81	17.3 ± 0.9	22.7 ± 1.9	0.19 ± 0.01	0.20 ± 0.02	101.8 ± 0.8	104.8 ± 10.2	3.08 ± 0.02	2.59 ± 0.01	3.02 ± 0.02	3.8 ± 1.1	1.20 ± 0.01	0.96 ± 0.00
Ilorin, Nigeria[b]	03/2014 - 10/2015	8.481	4.526	18.2 ± 1.0	13.5 ± 9.5	0.32 ± 0.02	0.87 ± 0.03	54.6 ± 1.0	20.5 ± 10.9	n/a	n/a	n/a	n/a	n/a	n/a
Dhaka, Bangladesh	03/2014 - 07/2015	23.728	90.398	40.4 ± 2.4	28.6 ± 7.6	0.80 ± 0.07	0.31 ± 0.02	40.3 ± 2.0	104.9 ± 30.5	0.95 ± 0.05	2.05 ± 0.00	10.42 ± 0.01	10.9 ± 43.8	1.43 ± 0.02	0.76 ± 0.00
Kanpur, India[b]	12/2013- 11/2014	26.519	80.232	59.9 ± 6.0	37.7± 5.6	0.83 ± 0.07	0.27 ± 0.01	113.0 ± 3.5	181.3 ± 22.1	n/a	n/a	n/a	n/a	n/a	n/a
Downsview, Canada	07/2017 – 11/2017	43.78	-79.47	8.3 ± 0.5	9.7 ± 0.9	0.27 ± 0.05	0.11 ± 0.01	27.2 ± 0.3	86.6 ± 8.0	12.66 ± 0.28	2.53 ± 0.01	4.32 ± 0.01	5.2 ± 1.9	0.77 ± 0.11	0.87 ± 0.00
Buenos Aires, Argentina	10/2014 – 01/2016	-34.556	-58.506	10.8 ± 0.7	8.3 ± 0.6	0.08 ± 0.01	0.12 ± 0.01	134.9 ± 2.2	69.6 ± 5.4	0.60 ± 0.01	3.38 ± 0.01	5.73 ± 0.02	5.7 ± 2.3	1.96 ± 0.03	0.76 ± 0.00
Sherbrooke, Canada	06/2017 – 08/2017	45.379	-71.931	7.1 ± 0.4	7.4 ± 0.5	0.15 ± 0.02	0.09 ± 0.01	47.5 ± 1.2	85.0 ± 4.6	8.26 ± 0.29	3.03 ± 0.00	3.81 ± 0.01	4.9 ± 1.9	0.71 ± 0.06	0.86 ± 0.00
Hanoi, Vietnam	05/2015 – 08/2015	21.048	105.801	41.4 ± 3.5	18.0 ± 10.2	0.55 ± 0.07	0.52 ± 0.04	64.5 ± 3.6	32.9 ± 7.8	3.23 ± 0.16	2.44 ± 0.00	2.06 ± 0.01	16.2 ± 60.7	1.75 ± 0.07	0.84 ± 0.00
Manila, Philippines[b]	02/2014 - 05/2014	14.635	121.077	17.2 ± 0.9	6.4 ± 0.2	0.21 ± 0.03	0.15 ± 0.02	72.7 ± 1.3	44.2 ± 1.4	n/a	n/a	n/a	n/a	n/a	n/a
Lethbridge, Canada	09/2017 – 11/2017	49.682	-112.869	17.3 ± 3.7	3.2 ± 0.4	0.05 ± 0.01	0.05 ± 0.01	134.6 ± 26.2	63.0 ± 1.6	3.65 ± 0.47	4.28 ± 0.00	3.71 ± 0.05	3.8 ± 1.4	0.85 ± 0.16	0.96 ± 0.00
Halifax, Canada[b]	06/2017 – 10/2017	44.638	-63.594	16.4 ± 8.0	5.3 ± 0.8	0.21 ± 0.09	0.08 ± 0.02	83.3 ± 16.9	65.3 ± 9.8	n/a	n/a	n/a	n/a	n/a	n/a
Pretoria, South Africa	04/2016 – 06/2016	-25.757	28.279	17.9 ± 1.4	9.7 ± 0.1	0.14 ± 0.01	0.08 ± 0.01	127.3 ± 5.0	122.2 ± 0.2	1.59 ± 0.05	3.37 ± 0.00	3.35 ± 0.04	4.0 ± 0.2	1.45 ± 0.09	0.61 ± 0.00
Fresno, USA*	01/2013 – 12/2016	36.785	-119.774	14.7 ± 0.4	6.4 ± 0.3	0.12 ± 0.01	0.06 ± 0.01	121.6 ± 0.2	109.0 ± 5.7	n/a	n/a	n/a	n/a	n/a	n/a
Mammoth Cave, USA*	06/2013 – 12/2016	37.132	-86.143	6.9 ± 0.2	11.4 ± 0.3	0.13 ± 0.01	0.10 ± 0.01	53.2 ± 0.3	109.1 ± 2.5	n/a	n/a	n/a	n/a	n/a	n/a
Bondville, USA*	01/2013 – 12/2016	40.05	-88.373	7.4 ± 0.2	11.1 ± 0.4	0.13 ± 0.01	0.10 ± 0.01	57.2 ± 0.3	110.1 ± 3.5	n/a	n/a	n/a	n/a	n/a	n/a
Fort McMurray, Canada*	01/2013 – 11/2016	56.752	-111.47	6.5 ± 0.6	5.7 ± 1.1	0.13 ± 0.02	0.06 ± 0.01	72.7 ± 4.9	135.6 ± 30.9	n/a	n/a	n/a	n/a	n/a	n/a

[a] Values following ± indicate standard error, [b]SPARTAN sites without optical-quality nephelometer measurements coincident with filter-based measurements. *Non-SPARTAN sampling sites.

Moderate to high simulated η values are also observed in locations with enhanced ground-level aerosol from anthropogenic activity, such as over the Eastern United States as well as East and South Asia. Elevated η values are also found over mountainous regions as the atmospheric column is reduced by elevation. The outer circle in Figure 5.1 depicting the modeled η coincident with measurements is generally comparable to the annual mean implying that modeled η from the time periods shown in Table 5.1 are representative of the annual mean. Simulated η values at sampling sites generally fall within a factor of two of the empirical value. The MFB between empirical and modeled η is 1.6 %, significantly lower than that for $PM_{2.5}$ and AOD, indicating that application of η leads to lower bias in satellite-derived $PM_{2.5}$ than pure simulated $PM_{2.5}$. This cancellation of bias in AOD and $PM_{2.5}$ implies common factors such as emissions affect bias in their simulation. The simulation of η is further examined to develop its application for satellite-derived $PM_{2.5}$.

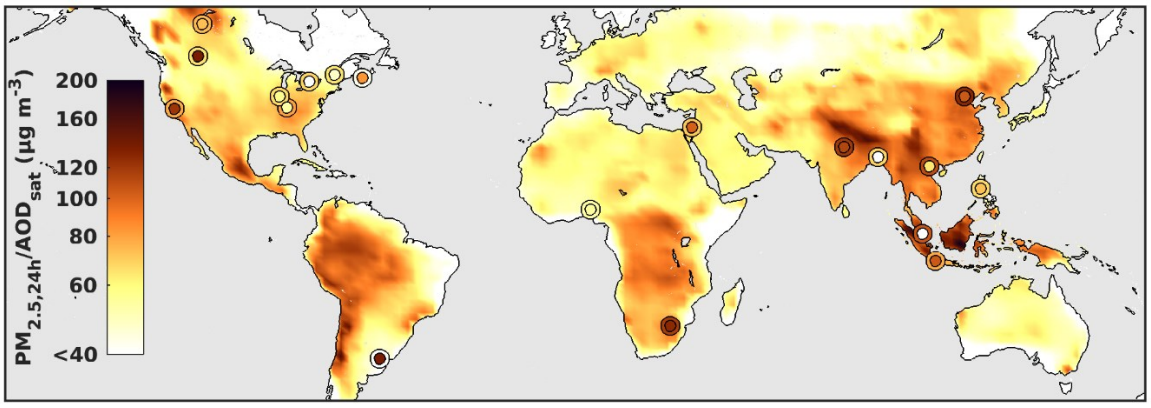

Figure 5.1. Annual mean simulated η (ratio of ground-level $PM_{2.5,24h}$ at 35% relative humidity to total-column, AOD_{sat}). Values from in situ observations are overlaid as colored circles inside larger circles showing modeled values sampled for the same months. Grey denotes water.

5.3.2 η decomposition

To offer further insight into the spatial variation in η, this ratio is decomposed into three contributing factors:

$$\eta = \underbrace{\left(\frac{b_{sp,10-14h}}{AOD_{10-14h}}\right)}_{T1}\underbrace{\left(\frac{b_{sp,24h}}{b_{sp,10-14h}}\right)}_{T2}\underbrace{\left(\frac{PM_{2.5,24h}}{b_{sp,24h}}\right)}_{T3} \quad (8)$$

The first term (T1) is the ratio of ground scatter to AOD at satellite overpass times. T1 can be thought of as an effective inverse scale height as it is related to be the height, *H*, for which aerosol scatter would be constant above ground level to obtain the measured AOD if it were distributed vertically according to $b_{sp}(z) \sim e^{-z/H}$. The second term (T2) is the ratio of 24 hour near-ground scatter ($b_{sp,24h}$) to that at satellite overpass times ($b_{sp,10\text{-}14h}$) and accounts for diurnal variation. The third term is the ratio of 24-hour $PM_{2.5}$ concentration ($PM_{2.5,24h}$) to 24-hour scatter ($b_{sp,24h}$) and is the inverse mass scattering efficiency.

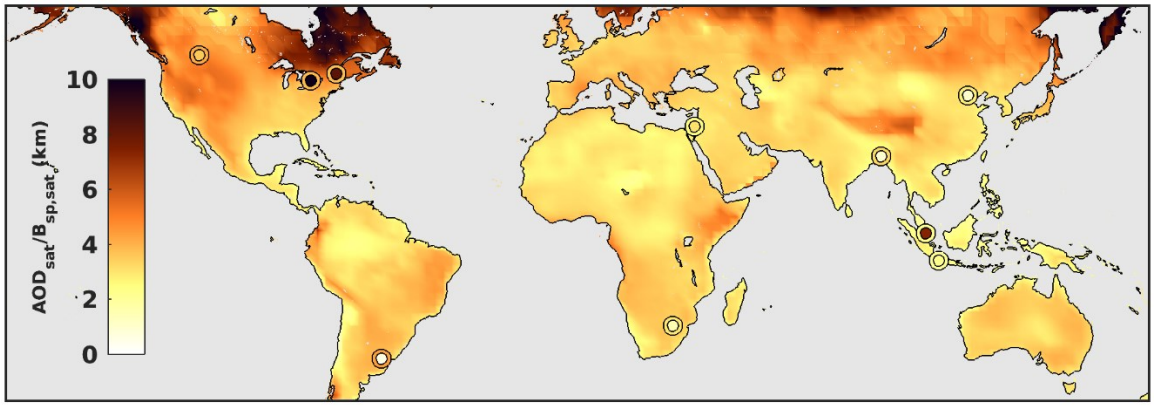

Figure 5.2. Annual mean modeled effective scale height (ratio of total-column $AOD_{10\text{-}14h}$ to ground scatter) at satellite overpass times (1000 to 1200 and 1300 to 1500 hours local time). Values from in situ observations are overlaid as colored circles on larger circles showing modeled values sampled for the same months. Grey indicates water or regions where RH exceeds 80 % at satellite overpass time.

Figure 5.2 shows the annual mean distribution of modeled effective scale height (T_1^{-1}) with overlaid circles depicting the measured values along with modeled values coincidently sampled with measurements. The highest measured scale heights are found in Downsview, Canada (12.4 km); Sherbrooke, Canada (8.3 km); and Singapore (7.4 km) while the lowest are measured in Buenos Aires, Argentina (0.6 km); Dhaka, Bangladesh (1.0 km); and Beijing, China (1.0 km). Elevated effective scale heights (> 5 km) are observed at sites where ground level $PM_{2.5}$ is low and aerosol transported in the atmospheric column over the site leads to an increased effective scale height. Sites with high effective scale heights are also those with low to moderate η demonstrating the inverse relationship between η and effective scale height. Low effective scale heights (< 2 km) are observed at sites where aerosol sources tend to be local and anthropogenic. The MFB between simulated and measured effective scale height is 11.7 %, indicating a slight overestimate in modeled values across 11 sampling sites.

Figure 5.3 shows the extinction vertical profiles as simulated by GEOS-Chem. Regions with pronounced ground-level aerosol sources have lower effective scale heights with extinction profiles that peak in the mixed layer. At sites where measured effective scale height is underestimated by the simulation (e.g. Downsview, Sherbrooke, and Singapore), it is expected that magnitude of the simulated aerosol vertical profile is underestimated. Nonetheless, the simulated aerosol vertical profiles provide insight into the sources influencing the measured effective scale heights. The majority of sites are most heavily influenced by sulfate and organic mass at the surface due to local, anthropogenic sources. This contribution extends throughout the mixed layer and decreases with elevation. In Rehovot and Beijing, mineral dust contributes to the aerosol

profile at the surface and throughout the atmospheric column suggesting a local source as well as an impact from dust transport above the site. Simulated aerosol vertical profiles also provide insight into potential biases affecting discrepancies between measured and simulated effective scale height. For example, the sites located in Singapore and Bandung, Indonesia show significant influence from sea salt at the surface that does not correspond to ground-based filter measurements. Rather, the model grid box that contains these sites also contains ocean that is expected to lead to this bias. Underestimated effective scale heights suggest local aerosol sources may not be well represented.

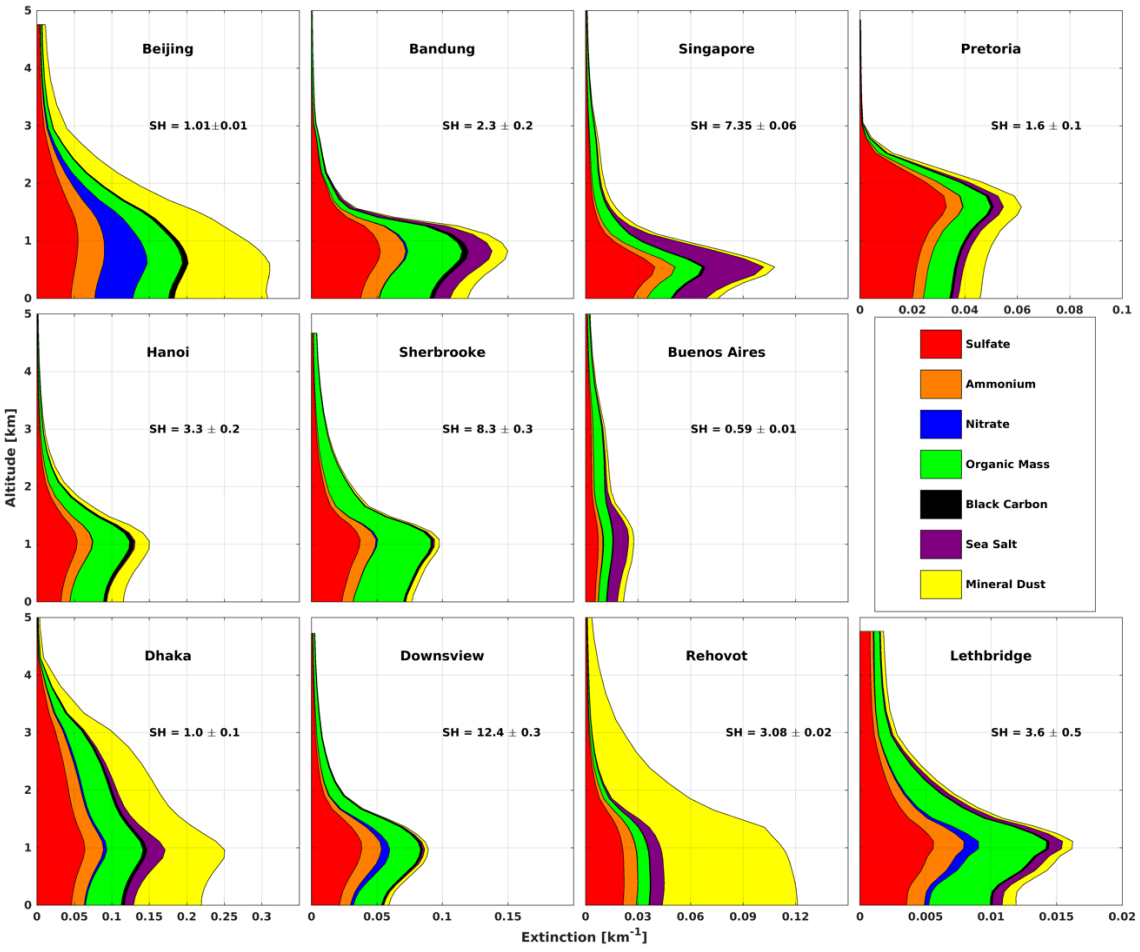

Figure 5.3. Extinction vertical profiles at sampling sites showing the contribution of individual chemical components to total extinction. The model is sampled during the same months as measurements. The measured effective scale heights (SH) with standard error are included for each site.

Figure 5.4 shows the annual mean distribution of mass scattering efficiency (T_3^{-1}, σ_{sp}) with overlaid circles depicting measured values along with modeled values coincidently sampled with measurements. The highest measured σ_{sp} is found in Dhaka, Bangladesh (10.4 m^2 g^{-1}) and the lowest is found in Hanoi, Vietnam (2.1 m^2 g^{-1}). The σ_{sp} as defined here (ratio of scatter at ambient RH to $PM_{2.5}$ at 35 % RH) is driven by hygroscopicity, which is a function of chemical composition and aerosol size distribution; aerosol density may also play a role. Calculating σ_{sp} using this method allows for representation of the average condition of the aerosol, and relates to AOD that is retrieved at ambient RH. Therefore, the high σ_{sp} observed in Dhaka can be related to elevated ambient RH during the sampling period coupled with aerosol composition dominated by hygroscopic species. The simulation predicts higher σ_{sp} along the coast and in regions with elevated ambient RH and contribution from inorganic, hygroscopic aerosol species. The MFB between measured and simulated σ_{sp} is 30.9 %, indicating significant overestimation at sampling sites.

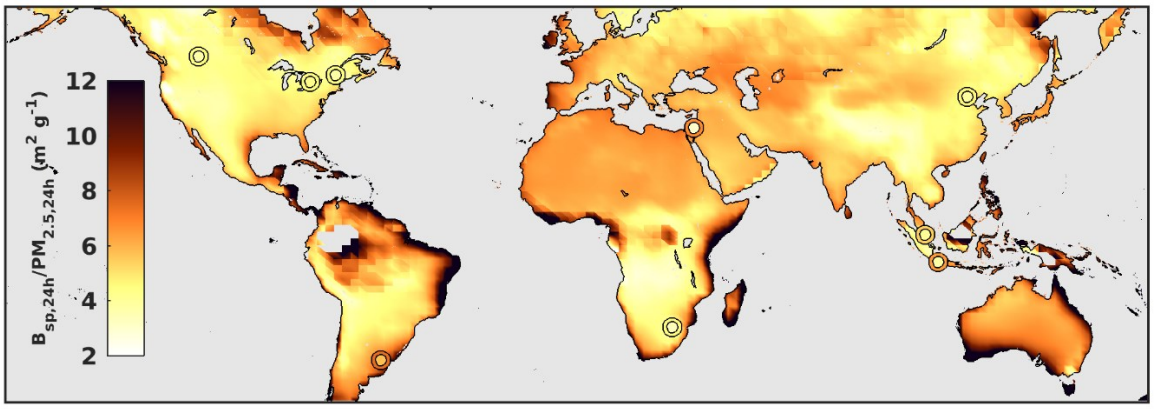

Figure 5.4. Annual mean mass scattering efficiency (ratio of daily ground-level scatter to $PM_{2.5}$ mass concentration). Values from in situ observations are overlaid as colored circles on larger circles showing modeled values sampled coincidently. Grey indicates water or regions where daily average RH exceeds 80 %.

Figure 5.5 shows the annual mean distribution of diurnal variation (T_2^{-1}) with overlaid circles depicting measured values along with modeled values coincidently sampled with measurements. The diurnal variation ranges from 0.7 in Sherbrooke, Canada to 2.0 in Beijing, China and Buenos Aires, Argentina. Low diurnal variation (< 0.8) indicates the daily average aerosol concentration is higher than at satellite overpass times and is experienced at sites where aerosol concentrations are local and influenced by transport. High diurnal variation (> 1.2) is observed at sites where aerosol concentrations are dominated by local sources. The MFB between measured and simulated diurnal variation is -27.0 %, showing that the simulation underestimates the diurnal variation at sampling sites.

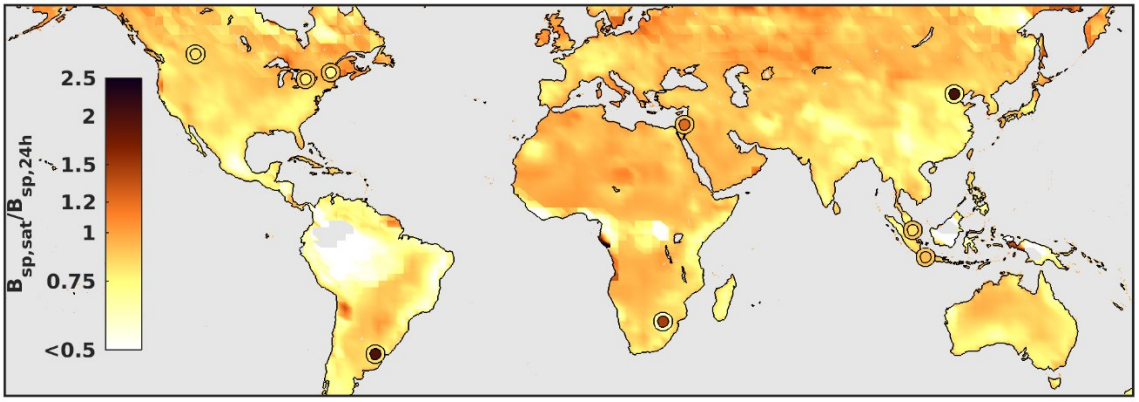

Figure 5.5. Annual mean diurnal variation (ratio of ground scatter at satellite overpass time versus 24-hour average). Values from in situ observations are overlaid as colored circles on larger circles showing modeled values sampled coincidently. Grey indicates water or regions where daily average RH and/or at satellite overpass time exceeds 80 %.

5.4 Conclusions

An initial analysis of the global relationship between ground level $PM_{2.5}$ and columnar AOD is completed. Measurements from the SPARTAN network as well as sites with collocated $PM_{2.5}$ and AOD within 1 km, are interpreted with the GEOS-Chem

chemical transport model. Empirical η values are found to vary spatially by a factor of 5. Although the simulated $PM_{2.5}$ and AOD values are biased low compared to measurements, modeled η shows consistency with measured values (MFB = 1.6 %) at sampling sites. Increased number of sampling sites will allow for further investigation into the factors influencing the spatial variation of η. The suite of instruments at SPARTAN sampling sites provides the ability to analyze η variability by decomposing the relationship into three dependent terms: the ratio of ground level scatter to total-column AOD (effective scale height), mass scattering efficiency, and diurnal variation in ground level scatter. The MFB between measured and simulated effective scale height (11.7 %) highlights the model skill in representing the spatial distribution of this variable. Simulated aerosol vertical profiles provide an additional means of interpreting empirical effective scale heights and understanding sources contributing to their variation. The MFB between simulated and measured mass scattering efficiency (30.9 %) and diurnal variation (-27.0 %) shows significant discrepancy at SPARTAN sampling sites. Further evaluation is needed to understand the factors that lead to this bias. Overall, this comparison demonstrates the importance and utility of the $PM_{2.5}$ to AOD relationship as well as the necessity to measure and evaluate the factors that affect the relationship.

Chapter 6 Conclusion

6.1 Summary

A federated network of ground-based monitoring through multi-day filter-based sampling of $PM_{2.5}$ and continuous sampling through nephelometry has been developed. The Surface PARTiculate mAtter Network (SPARTAN) is a grass-roots network designed to evaluate and improve satellite-based estimates of fine particulate matter ($PM_{2.5}$) for health effects research. Sampling site locations are chosen in densely-populated urban areas in regions with limited long-term, publically available ground-based measurements. This thesis presents work from three projects that use $PM_{2.5}$ measurements from SPARTAN to understand the global variation of $PM_{2.5}$, chemical composition, the sources contributing to global $PM_{2.5}$, and the relationship between $PM_{2.5}$ and columnar AOD.

In Chapter 3 long-term average $PM_{2.5}$ composition is inferred from filter-based measurements using standardized protocols based on gravimetric weighing, reflectance measurements, ion chromatography, and inductively coupled plasma-mass spectrometry. Long-term average concentrations of ammoniated sulfate, ammonium nitrate, equivalent black carbon, sea salt, crustal material, and residual mass that is treated as primarily organic mass, have been determined at 13 sites in 11 countries between 2013 - 2017. Significant spatial variation in absolute concentrations of major chemical components was found between SPARTAN sites, however the relative contribution shows lower variability. The average relative contribution ($\pm$ 1 σ SD) from all sites is 20 $\pm$ 11 % ammoniated sulfate, 13.4 $\pm$ 9.9 % crustal material, 11.9 $\pm$ 8.4 % equivalent black carbon,

4.7 ± 3.0 % ammonium nitrate, 2.3 ± 1.6 % sea salt, 1.0 ± 1.1 % trace element oxides, 7.2 ± 3.3 % particle-bound water at 35 % RH, and 40 ± 24 % residual mass. Temporally-consistent measurements between SPARTAN and IMPROVE in Mammoth Cave, USA show a high degree of consistency for $PM_{2.5}$ mass ($r^2 = 0.76$, slope = 1.12), sulfate ($r^2 = 0.86$, slope = 1.03), and agreement to within 2 % for mean fractions of all major components. Application of Zn:Al ratios for understanding the relative influence of natural and anthropogenic dust in particulate matter samples was demonstrated and highlighted significant anthropogenic dust influence in urban locations.

In Chapter 4, SPARTAN $PM_{2.5}$ mass and chemical composition measurements are interpreted using a global chemical transport model constrained by local satellite-derived $PM_{2.5}$ estimates. Measured secondary inorganic aerosol (SIA) concentrations vary across sites by a factor of 8 from 2.4 μg m^{-3} in Ilorin, Nigeria to 19.7 μg m^{-3} in Beijing, China. The spatial variation in measured SIA is well captured by the constrained simulation (r = 0.87) and accounts for the majority of global population-weighted ambient $PM_{2.5}$ (37 %, 11.9 μg m^{-3}). The measured variation in residual/organic mass (r = 0.92) and dust (r = 0.57) are also reasonably well represented by the constrained simulation, and contribute significantly to global population-weighted $PM_{2.5}$ concentrations of 9.3 μg m^{-3} for organics and of 9.5 μg m^{-3} for dust. Sensitivity simulations are used to investigate the contribution of seven source categories to ambient $PM_{2.5}$. Leading anthropogenic source categories contributing to global population-weighted $PM_{2.5}$ are residential energy use (20 %), industry (19 %), and power generation (17 %).

Sensitivity simulations are used to provide source attribution estimates for SPARTAN chemical composition measurements in regions represented by SPARTAN sites. Sites located in East Asia and South Asia have significant influence from all major chemical components, but are dominated by organics, dust, and sulfate. Residential energy use dominates organic mass concentrations, while industry and power generation both play a role in influencing sulfate concentrations. The relative contribution of natural and anthropogenic dust sources is found to be site-specific due to proximity of sampling locations to arid and semi-arid natural source regions. Measurements at sites in Southeast Asia show RM/OM, black carbon, and sulfate to be primary contributors to $PM_{2.5}$ mass, however chemical component concentrations are generally underestimated by the simulation. Unlike other sampling sites, $PM_{2.5}$ mass at the South American site in Buenos Aires is not dominated by any one component and concentrations are driven by natural sources with notable impact from open fires and industry. The measured $PM_{2.5}$ in Rehovot, Israel is primarily influenced by dust and sulfate, arising from natural desert dust sources and power generation. Measured $PM_{2.5}$ at sites in Sub-Saharan Africa are dominated by RM/OM, dust, and sulfate. The RM/OM concentrations at both sites experience significant influence from residential energy use and open fires, however sulfate sources are found to be site-specific.

Chapter 5 presents an initial comparison of empirical and simulated relationships of ground-based $PM_{2.5}$ and columnar AOD (η) is presented. Measured values of η are shown to vary by a factor of 5 across sampling sites and simulated global η vary by almost an order of magnitude, highlighting the degree of spatial heterogeneity of this relationship. Although the simulation is found to underestimate $PM_{2.5}$ (MFB = -18.1 %)

and AOD (MFB = -15.8), the MFB in simulated η values at sampling sites is found to be 1.6 %, indicating that application of η leads to lower bias in satellite-derived $PM_{2.5}$ than pure simulated $PM_{2.5}$.

6.2 Future Work

The main goal of this thesis was to develop the Surface Particulate Matter Network through testing of $PM_{2.5}$ sampling instruments, deployment at sampling sites, and the standardization of gravimetric analysis and chemical analysis techniques such as ion chromatography, inductively-coupled plasma – mass spectrometry, and filter reflectance. There results of these careful measurements were used to define aerosol composition (e.g. ammoniated sulfate, dust, sea salt) for presentation consistent with established measurement networks in North America. Measurements are then used to offer insight into the global variation of ambient $PM_{2.5}$.

The measurement techniques used in this grass-roots network are continuously evaluated to provide the most reliable data possible. Refinement and continued understanding of uncertainty associated with measured $PM_{2.5}$ mass and inferred chemical composition is ongoing work. Collocated precision estimates presented in Chapter 4 provide a "top-down" estimate of measurement uncertainty and have identified areas of the chemical analysis for continued investigation. Upcoming experiments will seek to provide additional detail on the sources of estimated uncertainty and may identify procedural changes to reduce uncertainty and systematic error.

Recent collaborations provide potential for direct measurement of organics and to better understand the SPARTAN residual mass component. Fourier Transform – Infrared

Spectroscopy of PTFE filters is a non-destructive technique that is being developed to determine organic carbon, organic mass, and elemental carbon concentrations (Weakley et al., 2016). Recent technique development for nebulizing filter extracts for analysis with an Aerosol Mass Specrotrometer (AMS) can also provide information on organic mass. Although in the early stages, application of both techniques to SPARTAN filters and filter extracts will require limited procedural changes and provide a wealth of information for understanding the organic fraction of global $PM_{2.5}$.

The current deployment at SPARTAN sites of upgraded nephelometers with improved accuracy will provide more sampling sites with sufficient optical quality to examine the decomposition of the $PM_{2.5}$ to AOD relationship. In addition, including lidar observations could provide a direct way of evaluating the simulated aerosol vertical profiles to investigate potential sources of bias. Deployment of additional sampling sites in the diverse regions that still lack ground-based monitoring, such as Sub-Saharan Africa, South America, and the Middle-East will provide additional insight the global variation of the $PM_{2.5}$ mass. Opportunities to expand instrumentation at some SPARTAN locations, such as inclusion of a lidar for direct measurement of the aerosol vertical profile above sampling sites, would be valuable.

The work presented here provides a foundation for the future growth of SPARTAN and gives insight into the opportunities the SPARTAN dataset offers for advancing research into the health impacts of $PM_{2.5}$. The extensive global coverage offered by satellite remote sensing and chemical transport models is needed to better understand the connection between $PM_{2.5}$ composition and adverse health effects. Measurements from SPARTAN, especially when additional information and sites are

acquired as described above, are uniquely positioned to evaluate and improve global chemical transport models and ground-based concentrations inferred from satellite remote sensing.

As done in Chapter 4, SPARTAN measurements can be used to inform model developments to increase the accuracy of simulated $PM_{2.5}$ mass and chemical composition. Measurements of the organic aerosol component in SPARTAN filter samples will allow for further insight into the factors leading to the underestimation of organic mass in the GEOS-Chem simulation. Further development of the mineral and anthropogenic dust simulations, as well as the hygroscopic mass growth of $PM_{2.5}$ components, is also needed to capture the observed spatial variation. Constraining simulations with measurements will lead to enhanced understanding of aerosol processes and emission sources in various regions. In addition, an expansion of the work presented in Chapter 5 will provide the necessary assessment of the simulated $PM_{2.5}$ to AOD relationship using empirical measurements. This includes determination of the factors driving the spatial variation in the $PM_{2.5}$ to AOD relationship, understanding possible regional biases, and ultimately leading to model developments that reduce uncertainty in the simulated values.

The Multi-Angle Imager for Aerosols (MAIA) being developed by NASA's Jet Propulsion Laboratory uses a multi-angle polarimeter with broad spectral range to comprehensively measure aerosol properties from space. Global measurements of $PM_{2.5}$ composition, as provided by SPARTAN, are needed as part of this mission to derive $PM_{2.5}$ composition from MAIA data.

Improved estimates $PM_{2.5}$ chemical composition with global coverage will enable epidemiological and health impact studies to better assess the relationship between individual components and health outcomes. Establishing an understanding of the differential toxicity of $PM_{2.5}$ components have the potential to significantly impact the development of ambient air quality standards and targeted control strategies, leading to a profound benefit on global public health. The growth and improvement of SPARTAN measurements provides the much-needed data to advance research using the integrated approach of coupling measurements with models and information from satellite remote sensing.

References

Ahmed, S.: Food and Agriculture in Bangladesh, Encycl. Food Agric. Ethics, 785–791, doi:10.1007/978-94-007-6167-4, 2014.

Anderson, R. H., Butland, B. K., van Donkelaar, A., Brauer, M., Strachan, D. P. and Clayton, T.: Satellite-based Estimates of Ambient Air Pollution and Global Variations in Childhood Asthma Prevalence, Environ. Health Perspect., 120(9), 1333–1340, doi:doi:10.1289/ ehp.1104724, 2012.

Anenberg, S. C., Horowitz, L. W., Tong, D. Q. and West, J. J.: An estimate of the global burden of anthropogenic ozone and fine particulate matter on premature human mortality using atmospheric modeling, Environ. Health Perspect., 118(9), 1189–1195, doi:doi:10.1289/ehp.0901220, 2010.

Atkinson, R. W., Mills, I. C., Walton, H. A. and Anderson, H. R.: Fine particle components and health—a systematic review and meta-analysis of epidemiological time series studies of daily mortality and hospital admissions, J. Expo. Sci. Environ. Epidemiol., 25(2), 208–214, doi:10.1038/jes.2014.63, 2015.

Balakrishnan, K., Ghosh, S., Ganguli, B., Sambandam, S., Bruce, N., Barnes, D. F. and Smith, K. R.: State and national household concentrations of PM2.5 from solid cookfuel use: results from measurements and modeling in India for estimation of the global burden of disease., Environ. Heal., 12, 77, doi:10.1186/1476-069X-12-77, 2013.

Barnard, J. C., Volkamer, R. and Kassianov, E. I.: Estimation of the mass absorption cross section of the organic carbon component of aerosols in the Mexico City Metropolitan Area (MCMA), Atmos. Chem. Phys., 8, 6665–6679, doi:10.5194/acpd-8-10189-2008, 2008.

Baumgartner, J., Zhang, Y., Schauer, J. J., Huang, W., Wang, Y. and Ezzati, M.: Highway proximity and black carbon from cookstoves as a risk factor for higher blood pressure in rural China, Proc. Natl. Acad. Sci., 111(36), 13229–13234, doi:10.1073/pnas.1317176111, 2014.

Begum, B. A., Kim, E., Biswas, S. K. and Hopke, P. K.: Investigation of sources of atmospheric aerosol at urban and semi-urban areas in Bangladesh, Atmos. Environ., 38(19), 3025–3038, doi:10.1016/j.atmosenv.2004.02.042, 2004.

Begum, B. A., Biswas, S. K., Markwitz, A. and Hopke, P. K.: Identification of sources of fine and coarse particulate matter in Dhaka, Bangladesh, Aerosol Air Qual. Res., 10(4), 345–353, doi:10.4209/aaqr.2009.12.0082, 2010.

Begum, B. A., Hossain, A., Nahar, N., Markwitz, A. and Hopke, P. K.: Organic and Black Carbon in PM2.5 at an Urban Site at Dhaka, Bangladesh, Aerosol Air Qual. Res., 12(6), 1062–1072, doi:10.4209/aaqr.2012.05.0138, 2012.

Behera, S. N. and Sharma, M.: Composition for an Urban Atmosphere, Aerosol Sci. Technol., 44 (January 2015), 983–992, doi:10.1080/02786826.2010.504245, 2010a.

Behera, S. N. and Sharma, M.: Reconstructing primary and secondary components of PM2.5 composition for an urban atmosphere, Aerosol Sci. Technol., 44(11), 983–992, doi:10.1080/02786826.2010.504245, 2010b.

Bell, M.L., HEI Health Review Committee. Assessment of the health impacts of particulate matter characteristics. *Res. Rep.* - Health Eff. Inst.,161, 2012.

Bell, M. L., Dominici, F., Ebisu, K., Zeger, S. L. and Samet, J. M.: Spatial and temporal variation in PM2.5 chemical composition in the United States for health effects studies, Environ. Health Perspect., 115(7), 989–995, doi:10.1289/ehp.9621, 2007.

Bell, M. L., Belanger, K., Ebisu, K., Gent, J. F., Lee, H. J., Koutrakis, P. and Leaderer, B. P.: Parental Exposure to Fine Particulate Matter and Birth Weight, Epidemiology, 21(6), 884–891, doi:10.1097/EDE.0b013e3181f2f405, 2010.

Bellouin, N., Boucher, O., Haywood, J. and Reddy, M. S.: Global estimate of aerosol direct radiative forcing from satellite measurements, Nature, 438(7071), 1138–1141, doi:10.1038/nature04348, 2005.

Bertram, A. K., Martin, S. T., Hanna, S. J., Smith, M. L., Bodsworth, A., Chen, Q., Kuwata, M., Liu, A., You, Y. and Zorn, S. R.: Predicting the relative humidities of liquid-liquid phase separation , efflorescence , and deliquescence of mixed particles of ammonium sulfate , organic material , and water using the organic-to-sulfate mass ratio of the particle and the oxygen-to-carbon, Atmos. Chem. Phys., 11, 10995–11006, doi:10.5194/acp-11-10995-2011, 2011.

Bey, I., Jacob, D. J., Yantosca, R. M., Logan, J. A., Field, B. D., Fiore, A. M., Li, Q., Liu, H. Y., Mickley, L. J. and Schultz, M. G.: Global modeling of tropospheric chemistry with assimilated meteorology : Model description and evaluation, J. Geophys. Res., 106, 73–95, doi:10.1029/2001JD000807, 2001.

Bond, T. C. and Bergstrom, R. W.: Light Absorption by Carbonaceous Particles: An Investigative Review, Aerosol Sci. Technol., 40(1), 27–67, doi:10.1080/02786820500421521, 2006.

Bonjour, S., Adair-rohani, H., Wolf, J., Bruce, N. G., Mehta, S., Prüss-ustün, A., Lahiff, M., Rehfuess, E. A., Mishra, V. and Smith, K. R.: Solid Fuel Use for Household Cooking : Country and Regional Estimates for 1980 – 2010, Environ. Health Perspect., 121(7), 784–791, 2013.

Boucher, O., Moulin, C., Belviso, S., Aumont, O., Bopp, L., Cosme, E., von Kuhlmann, R., Lawrence, M. G., Pham, M., Reddy, M. S., Sciare, J. and Venkataraman, C.: Sensitivity study of dimethylsulphide (DMS) atmospheric concentrations and sulphate aerosol indirect radiative forcing to the DMS source representation and oxidation, Atmos. Chem. Phys. Discuss., 2(4), 1181–1216, doi:10.5194/acpd-2-1181-2002, 2002.

Boys, B. L., Martin, R. V, van Donkelaar, A., Macdonell, R. J., Hsu, N. C., Cooper, M. J., Yantosca, R. M., Lu, Z., Streets, D. G., Zhang, Q. and Wang, S. W.: Fifteen-Year Global Time Series of Satellite-Derived Fine Particulate Matter, Environ. Sci. Technol., 48, 11109–11118, doi:10.1021/es502113p, 2014.

Brauer, M., Amann, M., Burnett, R. T., Cohen, A., Dentener, F., Ezzati, M., Henderson, S. B., Krzyzanowski, M., Martin, R. V, Van Dingenen, R., van Donkelaar, A. and Thurston, G. D.: Exposure assessment for estimation of the global burden of disease attributable to outdoor air pollution., Environ. Sci. Technol., 46(2), 652–60, doi:10.1021/es2025752, 2012.

Brauer, M., Freedman, G., Frostad, J., van Donkelaar, A., Martin, R. V., Dentener, F., Dingenen, R. van, Estep, K., Amini, H., Apte, J. S., Balakrishnan, K., Barregard, L., Broday, D., Feigin, V., Ghosh, S., Hopke, P. K., Knibbs, L. D., Kokubo, Y., Liu, Y., Ma, S., Morawska, L., Sangrador, J. L. T., Shaddick, G., Anderson, H. R., Vos, T., Forouzanfar, M. H., Burnett, R. T. and Cohen, A.: Ambient Air Pollution Exposure Estimation for the Global Burden of Disease 2013, Environ. Sci. Technol., 50(1), 79–88, doi:10.1021/acs.est.5b03709, 2016.

Brook, R. D., Rajagopalan, S., Pope, C. A., Brook, J. R., Bhatnagar, A., Diez-Roux, A. V., Holguin, F., Hong, Y., Luepker, R. V., Mittleman, M. A., Peters, A., Siscovick, D., Smith, S. C., Whitsel, L. and Kaufman, J. D.: Particulate matter air pollution and cardiovascular disease: An update to the scientific statement from the american heart association, Circulation, 121(21), 2331–2378, doi:10.1161/CIR.0b013e3181dbece1, 2010.

Butler, A. J., Andrew, M. S. and Russell, A. G.: Daily sampling of PM2.5 in Atlanta: Results of the first year of the Assessment of Spatial Aerosol Composition in Atlanta study, J. Geophys. Res. Atmos., 108(D7), 8415, doi:10.1029/2002JD002234, 2003.

Canagaratna, M. R., Jimenez, J. L., Kroll, J. H., Chen, Q., Kessler, S. H., Massoli, P., Ruiz, L. H., Fortner, E., Williams, L. R., Wilson, K. R., Surratt, J. D., Donahue, N. M., Jayne, J. T. and Worsnop, D. R.: Elemental ratio measurements of organic compounds using aerosol mass spectrometry : characterization , improved calibration , and implications, Atmos. Chem. Phys., 15, 253–272, doi:10.5194/acp-15-253-2015, 2015.

Chakraborty, A., Bhattu, D., Gupta, T., Tripathi, S. N. and Canagaratna, M. R.: Real-time measurements of ambient aerosols in a polluted Indian city: Sources, characteristics, and processing of organic aerosols during foggy and nonfoggy periods, J. Geophys. Res. Atmos., 120, 9006–9019, doi:10.1002/2015JD023419.Received, 2015.

Chang, C.-H., Hsiao, Y.-L. and Hwang, C.: Evaluating Spatial and Temporal Variations of Aerosol Optical Depth and Biomass Burning over Southeast Asia Based on Satellite Data Products, Aerosol Air Qual. Res., 15(7), 2625–2640, doi:10.4209/aaqr.2015.10.0589, 2015.

Chen, H., Burnett, R. T., Kwong, J. C., Villeneuve, P. J., Goldberg, M. S. and Brook, R. D.: Risk of Incident Diabetes in Relation to Long-term Exposure to Fine Particulate Matter in Ontario, Canada, Environ. Health Perspect., 804(2), 804–811, doi:10.1289/ehp.1205958, 2013.

Chen, H., Kwong, J. C., Copes, R., Hystad, P., van Donkelaar, A., Tu, K., Brook, J. R., Goldberg, M. S., Martin, R. V., Murray, B. J., Wilton, A. S., Kopp, A. and Burnett, R. T.: Exposure to ambient air pollution and the incidence of dementia: A population-based cohort study, Environ. Int., 108(May), 271–277, doi:10.1016/j.envint.2017.08.020, 2017.

Chen, L. C. and Lippmann, M.: Effects of metals within ambient air particulate matter (PM) on human health., Inhal. Toxicol., 21(1), 1–31, doi:10.1080/08958370802105405, 2009.

Cheung, K. L., Polidori, A., Ntziachristos, L., Tzamkiozis, T., Samaras, Z., Cassee, F. R., Gerlofs, M. and Sioutas, C.: Chemical characteristics and oxidative potential of particulate matter emissions from gasoline, diesel, and biodiesel cars, Environ. Sci. Technol., 43(16), 6334–6340, doi:10.1021/es900819t, 2009.

Chinnam, N., Dey, S., Tripathi, S. N. and Sharma, M.: Dust events in Kanpur, northern India: Chemical evidence for source and implications to radiative forcing, Geophys. Res. Lett., 33(8), 1–4, doi:10.1029/2005GL025278, 2006.

Chung, K. F. and Adcock, I. M.: Multifaceted mechanisms in COPD: Inflammation, immunity, and tissue repair and destruction, Eur. Respir. J., 31(6), 1334–1356, doi:10.1183/09031936.00018908, 2008.

Clarisse, L., Clerbaux, C., Dentener, F., Hurtmans, D. and Coheur, P.-F.: Global ammonia distribution derived from infrared satellite observations, Nat. Geosci., 2(7), 479–483, doi:10.1038/ngeo551, 2009.

Cohen, A. J., Brauer, M., Burnett, R., Anderson, H. R., Frostad, J., Estep, K., Balakrishnan, K., Brunekreef, B., Dandona, L., Dandona, R., Feigin, V., Freedman, G., Hubbell, B., Jobling, A., Kan, H., Knibbs, L., Liu, Y., Martin, R., Morawska, L., Pope, C. A., Shin, H., Straif, K., Shaddick, G., Thomas, M., van Dingenen, R., van Donkelaar, A., Vos, T., Murray, C. J. L. and Forouzanfar, M. H.: Estimates and 25-year trends of the global burden of disease attributable to ambient air pollution: an analysis of data from the Global Burden of Diseases Study 2015, Lancet, 389(10082), 1907–1918, doi:10.1016/S0140-6736(17)30505-6, 2017.

Cohen, D. D., Stelcer, E., Santos, F. L., Prior, M., Thompson, C. and Pabroa, P. C. B.: Fingerprinting and source apportionment of fine particle pollution in Manila by IBA and PMF techniques: A 7-year study, X-Ray Spectrom., 38(November 2008), 18–25, doi:10.1002/xrs.1112, 2009.

Cohen, D. D., Crawford, J., Stelcer, E. and Bac, V. T.: Characterisation and source apportionment of fine particulate sources at Hanoi from 2001 to 2008, Atmos. Environ., 44(3), 320–328, doi:10.1016/j.atmosenv.2009.10.037, 2010a.

Cohen, D. D., Crawford, J., Stelcer, E. and Bac, V. T.: Characterisation and source apportionment of fine particulate sources at Hanoi from 2001 to 2008, Atmos. Environ., 44(3), 320–328, doi:10.1016/j.atmosenv.2009.10.037, 2010b.

Correia, A. w., Arden Pope III, C., Dockery, D. W., Wang, Y., Ezzati, M. and Dominici, F.: The effect of air pollution control on life expectancy in the United States: an analysis of 545 US counties for the period 2000 to 2007, Epidemiology, 24(1), 23–31, doi:10.1097/EDE.0b013e3182770237.The, 2013.

Councell, T. B., Duckenfield, K. U., Landa, E. R. and Callender, E.: Tire-wear particles as a source of zinc to the environment, Environ. Sci. Technol., 38(15), 4206–4214, doi:10.1021/es034631f, 2004.

Crippa, M., Janssens-Maenhout, G., Dentener, F., Guizzardi, D., Sindelarova, K., Muntean, M., Van Dingenen, R. and Granier, C.: Forty years of improvements in European air quality: Regional policy-industry interactions with global impacts, Atmos. Chem. Phys., 16(6), 3825–3841, doi:10.5194/acp-16-3825-2016, 2016.

Crouse, D. L., Peters, P. A., van Donkelaar, A., Goldberg, M. S., Villeneuve, P. J., Brion, O., Khan, S., Atari, D. O., Jerrett, M., Pope, C. A., Brauer, M., Brook, J. R., Martin, R. V., Stieb, D. and Burnett, R. T.: Risk of nonaccidental and cardiovascular mortality in relation to long-term exposure to low concentrations of fine particulate matter: A canadian national-level cohort study, Environ. Health Perspect., 120(5), 708–714, doi:10.1289/ehp.1104049, 2012.

Dabek-Zlotorzynska, E., Dann, T. F., Kalyani Martinelango, P., Celo, V., Brook, J. R., Mathieu, D., Ding, L. and Austin, C. C.: Canadian National Air Pollution Surveillance (NAPS) PM2.5 speciation program: Methodology and PM2.5 chemical composition for the years 2003-2008, Atmos. Environ., 45(3), 673–686, doi:10.1016/j.atmosenv.2010.10.024, 2011.

Dey, S., Tripathi, S. N., Singh, R. P. and Holben, B. N.: Influence of dust storms on the aerosol optical properties over the Indo-Gangetic basin, J. Geophys. Res. D Atmos., 109(20), 1–13, doi:10.1029/2004JD004924, 2004.

Diner, D. J., Braswell, B. H., Davies, R., Gobron, N., Hu, J., Jin, Y., Kahn, R. A., Knyazikhin, Y., Loeb, N., Muller, J. P., Nolin, A. W., Pinty, B., Schaaf, C. B., Seiz, G. and Stroeve, J.: The value of multiangle measurements for retrieving structurally and radiatively consistent properties of clouds, aerosols, and surfaces, Remote Sens. Environ., 97(4), 495–518, doi:10.1016/j.rse.2005.06.006, 2005.

Dockery, D. W., Pope, C. A., Xiping, X., Spengler, J. D., Ware, J. H., Fay, M. E., Ferris, B. G. and Speizer, F. E.: An Association Between Air Pollution and Mortality in Six U.S. Cities, N. Engl. J. Med., 329(24), 1753–1759, doi:10.1056/NEJM199312093292401, 1993.

Driscoll, C., Lawrence, G. and Bulger, A.: Acidic Deposition in the Northeastern United States- Sources and Inputs, Ecosystem Effects, and Management Strategies, Bioscience, 51(3), 180–198, doi:10.1641/0006-3568, 2001.

Driscoll, C. T., Driscoll, K. M., Mitchell, M. J. and Raynal, D. J.: Effects of acidic deposition on forest and aquatic ecosystems in New York State, Environ. Pollut., 123(3), 327–336, doi:10.1016/S0269-7491(03)00019-8, 2003.

Drury, E., Jacob, D. J., Wang, J., Spurr, R. J. D. and Chance, K.: Improved algorithm for MODIS satellite retrievals of aerosol optical depths over western North America, J. Geophys. Res. Atmos., 113(16), doi:10.1029/2007JD009573, 2008.

Fairlie, D. T., Jacob, D. J. and Park, R. J.: The impact of transpacific transport of mineral dust in the United States, Atmos. Environ., 41(6), 1251–1266, doi:10.1016/j.atmosenv.2006.09.048, 2007.

Falkovich, A. H., Schkolnik, G., Ganor, E. and Rudich, Y.: Adsorption of organic compounds pertinent to urban environments onto mineral dust particles, J. Geophys. Res., 109(D2), doi:10.1029/2003JD003919, 2004.

Fioletov, V. E., Mclinden, C. A., Krotkov, N., Li, C., Joiner, J., Theys, N., Carn, S. and Moran, M. D.: A global catalogue of large SO 2 sources and emissions derived from the Ozone Monitoring Instrument, Atmos. Chem. Phys. Discuss., (May), 1–45, doi:10.5194/acp-2016-417, 2016.

Fisher, J. A., Jacob, D. J., Wang, Q., Bahreini, R., Carouge, C. C., Cubison, M. J., Dibb, J. E., Diehl, T., Jimenez, J. L., Leibensperger, E. M., Lu, Z., Meinders, M. B. J., Pye, H. O. T., Quinn, P. K., Sharma, S., Streets, D. G., van Donkelaar, A. and Yantosca, R. M.: Sources, distribution, and acidity of sulfate-ammonium aerosol in the Arctic in winter-spring, Atmos. Environ., 45(39), 7301–7318, doi:10.1016/j.atmosenv.2011.08.030, 2011.

Formenti, P., Andreae, M. O., Andreae, T. W., Galani, E., Vasaras, A., Zerefos, C., Amiridis, V., Orlovsky, L., Karnieli, A., Wendisch, M., Wex, H., Holben, B. N., Maenhaut, W. and Lelieveld, J.: Aerosol optical properties and large-scale transport of air masses : Mediterranean during summer 1998, J. Geophys. Res., 106, 9807–9826, doi:10.1029/2000JD900609, 2001.

Forouzanfar, M. H. and Collaborators: Global , regional , and national comparative risk assessment of 79 behavioural , environmental and occupational , and metabolic risks or clusters of risks , 1990 – 2015 : a systematic analysis for the Global Burden of Disease Study 2015, Lancet, 388, 1990–2015, doi:10.1016/S0140-6736(16)31679-8, 2016.

Fountoukis, C. and Nenes, a: ISORROPIA II: a computationally efficient thermodynamic equilibrium model for K+–Ca2+–Mg2+–NH4+–Na+–SO42−–NO3−–Cl−–H2O aerosols, Atmos. Chem. Phys., 7(17), 4639–4659, doi:10.5194/acp-7-4639-2007, 2007.

Freire, C., Ramos, R., Puertas, R., Lopez-Espinosa, M.-J., Julvez, J., Aguilera, I., Cruz, F., Fernandez, M.-F., Sunyer, J. and Olea, N.: Association of traffic-related air pollution with cognitive development in children, J. Epidemiol. Community Heal., 64(3), 223–228, doi:10.1136/jech.2008.084574, 2010.

Freitas, S. R., Longo, K. M., Silva Dias, M. A. F., Silva Dias, P. L., Chatfield, R., Prins, E., Artaxo, P., Grell, G. A. and Recuero, F. S.: Monitoring the transport of biomass burning emissions in South America, Environ. Fluid Mech., 5(1–2), 135–167, doi:10.1007/s10652-005-0243-7, 2005.

Fujii, Y., Iriana, W., Oda, M., Puriwigati, A., Tohno, S., Lestari, P., Mizohata, A. and Setiyo, H.: Characteristics of carbonaceous aerosols emitted from peatland fi re in Riau , Sumatra , Indonesia, Atmos. Environ., 87, 164–169, doi:10.1016/j.atmosenv.2014.01.037, 2014.

Fuzzi, S., Baltensperger, U., Carslaw, K., Decesari, S., Denier Van Der Gon, H., Facchini, M. C., Fowler, D., Koren, I., Langford, B., Lohmann, U., Nemitz, E., Pandis, S., Riipinen, I., Rudich, Y., Schaap, M., Slowik, J. G., Spracklen, D. V., Vignati, E., Wild, M., Williams, M. and Gilardoni, S.: Particulate matter, air quality and climate: Lessons learned and future needs, Atmos. Chem. Phys., 15(14), 8217–8299, doi:10.5194/acp-15-8217-2015, 2015.

Gakidou, E., Afshin, A., Abajobir, A. A., Abate, K. H., Abbafati, C., Abbas, K. M., Abd-Allah, F., Abdulle, A. M., Abera, S. F., Aboyans, V., Abu-Raddad, L. J., Abu-Rmeileh, N. M. E., Abyu, G. Y., Adedeji, I. A., Adetokunboh, O., Afarideh, M., Agrawal, A., Agrawal, S., Ahmad Kiadaliri, A., Ahmadieh, H., Ahmed, M. B., Aichour, A. N., Aichour, I., Aichour, M. T. E., Akinyemi, R. O., Akseer, N., Alahdab, F., Al-Aly, Z., Alam, K., Alam, N., Alam, T., Alasfoor, D., Alene, K. A., Ali, K., Alizadeh-Navaei, R., Alkerwi, A., Alla, F., Allebeck, P., Al-Raddadi, R., Alsharif, U., Altirkawi, K. A., Alvis-Guzman, N., Amare, A. T., Amini, E., Ammar, W., Amoako, Y. A., Ansari, H., Antó, J. M., Antonio, C. A. T., Anwari, P., Arian, N., Ärnlöv, J., Artaman, A., Aryal, K. K., Asayesh, H., Asgedom, S. W., Atey, T. M., Avila-Burgos, L., Avokpaho, E. F. G. A., Awasthi, A., Azzopardi, P., Bacha, U., Badawi, A., Balakrishnan, K., Ballew, S. H., Barac, A., Barber, R. M., Barker-Collo, S. L., Bärnighausen, T., Barquera, S., Barregard, L., Barrero, L. H., Batis, C., Battle, K. E., Baune, B. T., Beardsley, J., Bedi, N., Beghi, E., Bell, M. L., Bennett, D. A., Bennett, J. R., Bensenor, I. M., Berhane, A., Berhe, D. F., Bernabé, E., Betsu, B. D., Beuran, M., Beyene, A. S., Bhansali, A., Bhutta, Z. A., Bikbov, B., Birungi, C., Biryukov, S., Blosser, C. D., Boneya, D. J., Bou-Orm, I. R., Brauer, M., Breitborde, N. J. K., Brenner, H., et al.: Global, regional, and national comparative risk assessment of 84 behavioural, environmental and occupational, and metabolic risks or clusters of risks, 1990-2016: A systematic analysis for the Global Burden of Disease Study 2016, Lancet, 390(10100), 1345–1422, doi:10.1016/S0140-6736(17)32366-8, 2017.

Gautam, R., Liu, Z., Singh, R. P. and Hsu, N. C.: Two contrasting dust-dominant periods over India observed from MODIS and CALIPSO data, Geophys. Res. Lett., 36(6), 1–5, doi:10.1029/2008GL036967, 2009.

Gaydos, T. M. and Stanier, C. O.: Modeling of in situ ultrafine atmospheric particle formation in the eastern United States, J. Geophys. Res., 110(D7), D07S12, doi:10.1029/2004JD004683, 2005.

Generoso, S., Bréon, F.-M., Balkanski, Y., Boucher, O. and Schulz, M.: Improving the seasonal cycle and interannual variations of biomass burning aerosol sources, Atmos. Chem. Phys., 3(4), 1211–1222, doi:10.5194/acp-3-1211-2003, 2003.

Gibson, M. D., Heal, M. R., Bache, D. H., Hursthouse, A. S., Beverland, I. J., Craig, S. E., Clark, C. F., Jackson, M. H., Guernsey, J. R. and Jones, C.: Using Mass Reconstruction along a Four-Site Transect as a Method to Interpret PM 10 in West-Central Scotland , United Kingdom Using Mass Reconstruction along a Four-Site Transect as a Method to Interpret PM 10 in West-Central Scotland , United Kingdom, J. Air Waste Manag. Assoc., 59, 1429–1436, doi:10.3155/1047-3289.59.12.1429, 2009.

Gibson, M. D., Pierce, J. R., Waugh, D., Kuchta, J., Chisholm, L., Duck, T. J., Hopper, J. T., Beauchamp, S., King, G. H., Franklin, J. E., Leaitch, W. R., Wheeler, A. J., Li, Z., Gagnon, G. A. and Palmer, P. I.: Identifying the sources driving observed PM2.5 temporal variability over Halifax, Nova Scotia, during BORTAS-B, Atmos. Chem. Phys., 13(1), 1–13, doi:10.5194/acp-13-1-2013, 2013a.

Gibson, M. D., Heal, M. R., Li, Z., Kuchta, J., King, G. H., Hayes, A. and Lambert, S.: The spatial and seasonal variation of nitrogen dioxide and sulfur dioxide in Cape Breton Highlands National Park, Canada, and the association with lichen abundance, Atmos. Environ., 64, 303–311, doi:10.1016/j.atmosenv.2012.09.068, 2013b.

Giglio, L., Randerson, J. T. and Werf, G. R. Van Der: Analysis of daily , monthly , and annual burned area using the fourth-generation global fire emissions database (GFED4), J. Geophys. Res. Biogeosciences, 118, 317–328, doi:10.1002/jgrg.20042, 2013.

Ginoux, P., Chin, M., Tegen, I., Goddard, T. and In-, G.: Sources and distributions of dust aerosols simulated with the GOCART model, J. Geophys. Res., 106, 20255–20273, doi:10.1029/2000JD000053, 2001.

Graham, B., Falkovich, A. H., Rudich, Y., Maenhaut, W., Guyon, P. and Andreae, M. O.: Local and regional contributions to the atmospheric aerosol over Tel Aviv , Israel : a case study using elemental , ionic and organic tracers, Atmos. Environ., 38, 1593–1604, doi:10.1016/j.atmosenv.2003.12.015, 2004.

Greenstone, M.: The Impacts of Environmental Regulations on Industrial Activity : Evidence from the 1970 and 1977 Clean Air Act Amendments and the Census of Manufactures, J. Polit. Econ., 110(6), 1175–1219, doi:10.1086/342808, 2001.

Griffin, R. J., Cocker, D. R. I., Flagan, R. C. and Seinfeld, J. H.: Organic aerosol formation from the oxidation of biogenic hydrocardons, , 104(1998), 3555–3567, doi:10.1029/1998JD100049, 1999.

Guenther, A., Karl, T., Harley, P., Wiedinmyer, C., Palmer, P. I. and Geron, C.: Estimates of global terrestrial isoprene emissions using MEGAN (Model of Emissions of Gases and Aerosols from Nature), Atmos. Chem. Phys. Discuss., 6(1), 107–173, doi:10.5194/acpd-6-107-2006, 2006.

Hammer, M. S., Martin, R. V., van Donkelaar, A., Buchard, V., Torres, O., Ridley, D. A. and Spurr, R. J. D.: Interpreting the ultraviolet aerosol index observed with the OMI satellite instrument to understand absorption by organic aerosols: Implications for atmospheric oxidation and direct radiative effects, Atmos. Chem. Phys., 16(4), 2507–2523, doi:10.5194/acp-16-2507-2016, 2016.

Hand, J. L. and Malm, W. C.: Review of the IMPROVE Equation for Estimating Ambient Light Extinction Coefficients, Colorado State University, Fort Collins., 2006.

Hand, J. L., Schichtel, B. A., Malm, W. C. and Pitchford, M. L.: Particulate sulfate ion concentration and SO 2 emission trends in the United States from the early 1990s through 2010, Atmos. Chem. Phys., 12, 10353–10365, doi:10.5194/acp-12-10353-2012, 2012a.

Hand, J. L., Schichtel, B. a, Pitchford, M., Malm, W. C. and Frank, N. H.: Seasonal composition of remote and urban fine particulate matter in the United States, J. Geophys. Res., 117(D5), D05209, doi:10.1029/2011JD017122, 2012b.

Heald, C. L., Collett, J. ., Lee, T., Benedict, K. B., Schwandner, F. M., Li, Y., Clarisse, L., Hurtmans, D. R., Van Damme, M., Clerbaux, C., Coheur, P. F., Philip, S., Martin, R. . and Pye, H.: Atmospheric ammonia and particulate inorganic nitrogen over the United States, Atmos. Chem. Phys., 12(21), 10295–10312, doi:10.5194/acp-12-10295-2012, 2012.

Henning, S.: Seasonal variation of water-soluble ions of the aerosol at the high-alpine site Jungfraujoch (3580 m asl), J. Geophys. Res., 108(D1), 1–10, doi:10.1029/2002JD002439, 2003.

Hieu, V. Van, Quynh, L. X., Ho, P. N. and Hens, L.: Health Risk Assessment of Mobility-Related Air Pollution in Ha Noi, Vietnam, J. Environ. Prot. (Irvine,. Calif)., 4(10), 1165–1172, doi:10.4236/jep.2013.410133, 2013.

Hoek, G., Krishnan, R. M., Beelen, R., Peters, A., Ostro, B., Brunekreef, B. and Kaufman, J. D.: Long-term air pollution exposure and cardio- respiratory mortality: a review, Environ. Heal., 12(1), 43, doi:10.1186/1476-069X-12-43, 2013.

Hoffmann, B., Moebus, S., Dragano, N., Stang, A., Möhlenkamp, S., Schmermund, A., Memmesheimer, M., Bröcker-Preuss, M., Mann, K., Erbel, R. and Jöckel, K. H.: Chronic residential exposure to particulate matter air pollution and systemic inflammatory markers, Environ. Health Perspect., 117(8), 1302–1308, doi:10.1289/ehp.0800362, 2009.

Hogg, J. C., Chu, F., Utokaparch, S., Woods, R., Elliott, W. M., Buzatu, L., Cherniack, R. M., Rogers, R. M., Sciurba, F. C., Coxson, H. O. and Paré, P. D.: The Nature of Small-Airway Obstruction in Chronic Obstructive Pulmonary Disease, N. Engl. J. Med., 350(26), 2645–2653, doi:10.1056/NEJMoa032158, 2004.

Holben, B. N., Eck, T. F., Slutsker, I., Tanre, D., Buis, J. ., Setzer, A., Vermote, E., Reagan, J. A., Kaufman, Y. J., Nakajima, T., Lavenu, F., Jankowiak, I. and Smirnov, A.: AERONET - A Federated Instrument Network and Data Archive for Aerosol Characterization, Remote Sens. Environ., 4257(66), 1–16, doi:10.1016/S0034-4257(98)00031-5, 1998.

Holben, B. N., Tanré, D., Smirnov, a., Eck, T. F., Slutsker, I., Abuhassan, N., Newcomb, W. W., Schafer, J. S., Chatenet, B., Lavenu, F., Kaufman, Y. J., Castle, J. Vande, Setzer, a., Markham, B., Clark, D., Frouin, R., Halthore, R., Karneli, a., O'Neill, N. T., Pietras, C., Pinker, R. T., Voss, K. and Zibordi, G.: An emerging ground-based aerosol climatology: Aerosol optical depth from AERONET, J. Geophys. Res., 106(D11), 12067, doi:10.1029/2001JD900014, 2001.

Hsu, N. C., Tsay, S. C., King, M. D. and Herman, J. R.: Deep Blue retrievals of Asian aerosol properties during ACE-Asia, IEEE Trans. Geosci. Remote Sens., 44(11), 3180–3195, doi:10.1109/TGRS.2006.879540, 2006.

Hsu, N. C., Jeong, M. J., Bettenhausen, C., Sayer, A. M., Hansell, R., Seftor, C. S., Huang, J. and Tsay, S. C.: Enhanced Deep Blue aerosol retrieval algorithm: The second generation, J. Geophys. Res. Atmos., 118(16), 9296–9315, doi:10.1002/jgrd.50712, 2013.

Huang, J. P., Liu, J. J., Chen, B. and Nasiri, S. L.: Detection of anthropogenic dust using CALIPSO lidar measurements, Atmos. Chem. Phys., 15(20), 11653–11665, doi:10.5194/acp-15-11653-2015, 2015.

Hudman, R. C., Moore, N. E., Mebust, A. K., Martin, R. V., Russell, A. R., Valin, L. C. and Cohen, R. C.: Steps towards a mechanistic model of global soil nitric oxide emissions: Implementation and space based-constraints, Atmos. Chem. Phys., 12(16), 7779–7795, doi:10.5194/acp-12-7779-2012, 2012.

Husar, R. B., Husar, J. D. and Martin, L.: Distribution of continental surface aerosol extinction based on visual range data, Atmos. Environ., 34(29–30), 5067–5078, doi:10.1016/S1352-2310(00)00324-1, 2000.

Hyslop, N. P. and White, W. H.: An evaluation of interagency monitoring of protected visual environments (IMPROVE) collocated precision and uncertainty estimates, Atmos. Environ., 42(11), 2691–2705, doi:10.1016/j.atmosenv.2007.06.053, 2008.

IMPROVE: Reconstructing Light Extinction from Aerosol Measurements., 2015.

IPCC: Climate Change 2013: The Physical Science Basis. Contribution of Working Group I to the Fifth Assessment Report of the Intergovernmental Panel on Climate Change, 5th ed., edited by T. F. Stocker, D. Qin, G.-K. Plattner, M. M. B. Tignor, S. K. Allen, J. Boschung, A. Nauels, Y. Xia, V. Bex, and P. M. Midgeley, Cambrige University Press, Cambridge, United Kingdom and New York, NY, USA., 2013.

Jacob, D. J.: Heterogeneous chemistry and tropospheric ozone, Atmos. Environ., 34, 2131–2159, doi:10.1016/S1352-2310(99)00462-8, 2000.

Jaeglé, L., Quinn, P. K., Bates, T. S., Alexander, B. and Lin, J. T.: Global distribution of sea salt aerosols: New constraints from in situ and remote sensing observations, Atmos. Chem. Phys., 11(7), 3137–3157, doi:10.5194/acp-11-3137-2011, 2011.

Janssen, N. A. H., Hoek, G., Simic-Lawson, M., Fischer, P., van Bree, L., ten Brink, H., Keuken, M., Atkinson, R. W., Anderson, H. R., Brunekreef, B. and Cassee, F. R.: Black Carbon as an Additional Indicator of the Adverse Health Effects of Airborne Particles Compared with PM10 and PM2.5, Environ. Health Perspect., 119(12), 1691–1699, doi:10.1289/ehp.1003369, 2011.

Jasan, R. C., Pla, R. R., Invernizzi, R. and Santos, M. Dos: Characterization of atmospheric aerosol in Buenos Aires , Argentina, J. Radioanal. Nucl. Chem., 281, 101–105, doi:10.1007/s10967-009-0071-1, 2009.

Jimenez, J. L., Canagaratna, M. R., Donahue, N. M., Prevot, a. S. H., Zhang, Q., Kroll, J. H., DeCarlo, P. F., Allan, J. D., Coe, H., Ng, N. L., Aiken, a. C., Docherty, K. S., Ulbrich, I. M., Grieshop, A. P., Robinson, a. L., Duplissy, J., Smith, J. D., Wilson, K. R., Lanz, V. a., Hueglin, C., Sun, Y. L., Tian, J., Laaksonen, A., Raatikainen, T., Rautiainen, J., Vaattovaara, P., Ehn, M., Kulmala, M., Tomlinson, J. M., Collins, D. R., Cubison, M. J., Dunlea, J., Huffman, J. A., Onasch, T. B., Alfarra, M. R., Williams, P. I., Bower, K., Kondo, Y., Schneider, J., Drewnick, F., Borrmann, S., Weimer, S., Demerjian, K., Salcedo, D., Cottrell, L., Griffin, R., Takami, A., Miyoshi, T., Hatakeyama, S., Shimono, A., Sun, J. Y., Zhang, Y. M., Dzepina, K., Kimmel, J. R., Sueper, D., Jayne, J. T., Herndon, S. C., Trimborn, a. M., Williams, L. R., Wood, E. C., Middlebrook, A. M., Kolb, C. E., Baltensperger, U., Worsnop, D. R., Dunlea, E. J., Huffman, J. A., Onasch, T. B., Alfarra, M. R., Williams, P. I., Bower, K., Kondo, Y., Schneider, J., Drewnick, F., Borrmann, S., Weimer, S., Demerjian, K., Salcedo, D., Cottrell, L., Griffin, R., Takami, A., Miyoshi, T., Hatakeyama, S., Shimono, A., Sun, J. Y., Zhang, Y. M., Dzepina, K., Kimmel, J. R., Sueper, D., Jayne, J. T., Herndon, S. C., Trimborn, a. M., Williams, L. R., Wood, E. C., Middlebrook, A. M., Kolb, C. E., Baltensperger, U., Worsnop, D. R., Dunlea, J., Huffman, J. A., et al.: Evolution of Organic Aerosols in the Atmosphere, Science (80-.)., 326(5959), 1525–1529, doi:10.1126/science.1180353, 2009.

Jones, A., Roberts, D. . and Slingo, A.: A climate model study of indirect radiative forcing by anthropogenic sulphte aerosols, Nature, 370, 450–453, doi:10.1038/370450a0, 1994.

Jung, J., Adams, P. J. and Pandis, S. N.: Simulating the size distribution and chemical composition of ultrafine particles during nucleation events, Atmos. Environ., 40(13), 2248–2259, doi:10.1016/j.atmosenv.2005.09.082, 2006.

Justice, C. O., Kendall, J. D., Dowty, P. R. and Scholes, R. J.: Satellite remote sensing of fires during the SAFARI campaign using NOAA advanced very hugh resolution radiometer data, J. Geophys. Res., 101(D19), 23851–23863, doi:10.1029/95JD00623, 1996.

Keller, C. A., Long, M. S., Yantosca, R. M., Silva, A. M. Da, Pawson, S. and Jacob, D. J.: HEMCO v1.0 : a versatile , ESMF-compliant component for calculating emissions in atmospheric models, Geosci. Model Dev., 7, 1409–1417, doi:10.5194/gmd-7-1409-2014, 2014.

Kerminen, V.-M. and Wexler, A. S.: Growth laws for atmospheric aerosol particles: An examination of the bimodality of the accumulation mode, Atmos. Environ., 29(22), 3263–3275, doi:10.1016/1352-2310(95)00249-X, 1995.

Kerminen, V.-M., Virkkula, A., Hillamo, R., Wexler, A. S. and Kulmala, M.: Secondary organics and cloud condensation nuclei production, J. Geophys. Res., 105, 9255–9264, doi:10.1029/1999JD901203, 2000.

Kharol, S. K., Martin, R. V, Philip, S., Vogel, S., Henze, D. K., Chen, D., Wang, Y., Zhang, Q. and Heald, C. L.: Persistent sensitivity of Asian aerosol to emissions of nitrogen oxides, Geophys. Res. Lett., 40, 1021–1026, doi:10.1002/grl.50234, 2013.

Kim, P. S., Jacob, D. J., Fisher, J. A., Travis, K., Yu, K., Zhu, L., Yantosca, R. M. and Sulprizio, M. P.: Sources , seasonality , and trends of southeast US aerosol : an integrated analysis of surface , aircraft , and satellite observations with the GEOS-Chem chemical transport model, Atmos. Chem. Phys., 15, 10411–10433, doi:10.5194/acp-15-10411-2015, 2015.

Klimont, Z., Smith, S. J. and Cofala, J.: The last decade of global anthropogenic sulfur dioxide: 2000–2011 emissions, Environ. Res. Lett., 8(1), 14003, doi:10.1088/1748-9326/8/1/014003, 2013.

Kloog, I., Koutrakis, P., Coull, B. A., Lee, H. J. and Schwartz, J.: Assessing temporally and spatially resolved PM2.5 exposures for epidemiological studies using satellite aerosol optical depth measurements, Atmos. Environ., 45(35), 6267–6275, doi:10.1016/j.atmosenv.2011.08.066, 2011.

Kloog, I., Ridgway, B., Koutrakis, P., Coull, B. A. and Schwartz, J. D.: Long- and short-term exposure to PM2.5 and mortality: using novel exposure models., Epidemiology, 24(4), 555–61, doi:10.1097/EDE.0b013e318294beaa, 2013.

Kodros, J. K., Wiedinmyer, C., Ford, B., Cucinotta, R., Gan, R., Magzamen, S. and Pierce, J. R.: Global burden of mortalities due to chronic exposure to ambient PM 2.5 from open combustion of domestic waste, Environ. Res. Lett., 11(October), 124022, doi:10.1088/1748-9326/11/12/124022, 2016.

Kong, S., Han, B., Bai, Z., Chen, L., Shi, J. and Xu, Z.: Receptor modeling of PM2.5, PM10 and TSP in different seasons and long-range transport analysis at a coastal site of Tianjin, China., Sci. Total Environ., 408(20), 4681–94, doi:10.1016/j.scitotenv.2010.06.005, 2010.

Koplitz, S. N., Mickley, L. J., Marlier, M. E., Buonocore, J. J., Kim, P. S., Liu, T., Sulprizio, M. P., DeFries, R. S., Jacob, D. J., Schwartz, J., Pongsiri, M. and Myers, S. S.: Public health impacts of the severe haze in Equatorial Asia in September–October 2015: demonstration of a new framework for informing fire management strategies to reduce downwind smoke exposure, Environ. Res. Lett., 11(9), 94023, doi:10.1088/1748-9326/11/9/094023, 2016.

Kreidenweis, S. M., Petters, M. D. and DeMott, P. J.: Single-parameter estimates of aerosol water content, Environ. Res. Lett., 3(3), 35002, doi:10.1088/1748-9326/3/3/035002, 2008.

Krotkov, N. A., Mclinden, C. A., Li, C., Lamsal, L. N., Celarier, E. A., Marchenko, S. V, Swartz, W. H., Bucsela, E. J., Joiner, J., Duncan, B. N., Boersma, K. F., Veefkind, J. P., Levelt, P. F., Fioletov, V. E., Dickerson, R. R., Hao, H., Lu, Z. and Streets, D. G.: Aura OMI observations of regional SO 2 and NO 2 pollution changes from 2005 to 2015, Atmos. Chem. Phys., 16(7), 4605–4629, doi:10.5194/acp-16-4605-2016, 2016.

Kumar, M., Raju, M. P., Singh, R. K., Singh, A. K., Singh, R. S. and Banerjee, T.: Wintertime characteristics of aerosols over middle Indo-Gangetic Plain: Vertical profile, transport and radiative forcing, Atmos. Res., 183, 268–282, doi:10.1016/j.atmosres.2016.09.012, 2017.

Lacey, F. G., Henze, D. K., Lee, C. J., van Donkelaar, A., and Martin, R. V: Transient climate and ambient health impacts due to national solid fuel cookstove emissions, Proc. Natl. Acad. Sci. U. S. A., 114(6), 1269–1274, doi:10.1073/pnas.1612430114, 2017.

Laden, F., Schwartz, J., Speizer, F. E. and Dockery, D. W.: Reduction in fine particulate air pollution and mortality: Extended follow-up of the Harvard Six Cities study., Am. J. Respir. Crit. Care Med., 173(6), 667–72, doi:10.1164/rccm.200503-443OC, 2006.

Latham, J., Cumani, R., Rosati, I. and Bloise, M., 2014. Global land cover share (GLC-SHARE) database beta-release version 1.0-2014. *FAO: Rome, Italy*.

Lee, C. J., Martin, R. V., Henze, D. K., Brauer, M., Cohen, A. and van Donkelaar, A.: Response of global particulate-matter-related mortality to changes in local precursor emissions, Environ. Sci. Technol., 49(7), 4335–4344, doi:10.1021/acs.est.5b00873, 2015.

Lee, H. J., Coull, B. A., Bell, M. L. and Koutrakis, P.: Use of satellite-based aerosol optical depth and spatial clustering to predict ambient PM2.5 concentrations, Environ. Res., 118, 8–15, doi:10.1016/j.envres.2012.06.011, 2012.

Lelieveld, J., Evans, J. S., Fnais, M., Giannadaki, D. and Pozzer, A.: The contribution of outdoor air pollution sources to premature mortality on a global scale., Nature, 525(7569), 367–71, doi:10.1038/nature15371, 2015.

Lestari, P. and Mauliadi, Y. D.: Source apportionment of particulate matter at urban mixed site in Indonesia using PMF, Atmos. Environ., 43(10), 1760–1770, doi:http://dx.doi.org/10.1016/j.atmosenv.2008.12.044, 2009a.

Lestari, P. and Mauliadi, Y. D.: Source apportionment of particulate matter at urban mixed site in Indonesia using PMF, Atmos. Environ., 43(10), 1760–1770, doi:10.1016/j.atmosenv.2008.12.044, 2009b.

Levy, R. C., Remer, L. A., Mattoo, S., Vermote, E. F. and Kaufman, Y. J.: Second-generation operational algorithm: Retrieval of aerosol properties over land from inversion of Moderate Resolution Imaging Spectroradiometer spectral reflectance, J. Geophys. Res. Atmos., 112(13), 1–21, doi:10.1029/2006JD007811, 2007.

Levy, R. C., Mattoo, S., Munchak, L. A., Remer, L. A., Sayer, A. M., Patadia, F. and Hsu, N. C.: The Collection 6 MODIS aerosol products over land and ocean, Atmos. Meas. Tech., 6(11), 2989–3034, doi:10.5194/amt-6-2989-2013, 2013.

Li, C., Martin, R. V, Boys, B. L., van Donkelaar, A., and Ruzzante, S.: Evaluation and application of multi-decadal visibility data for trend analysis of atmospheric haze, Atmos. Chem. Phys., 16, 2435–2457, doi:10.5194/acp-16-2435-2016, 2016a.

Li, C., Martin, R. V., van Donkelaar, A., Boys, B. L., Hammer, M. S., Xu, J. W., Marais, E. A., Reff, A., Strum, M., Ridley, D. A., Crippa, M., Brauer, M. and Zhang, Q.: Trends in Chemical Composition of Global and Regional Population-Weighted Fine Particulate Matter Estimated for 25 Years, Environ. Sci. Technol., 51(19), 11185–11195, doi:10.1021/acs.est.7b02530, 2017a.

Li, M., Zhang, Q., Kurokawa, J., Woo, J., He, K., Lu, Z., Ohara, T., Song, Y., Streets, D. G., Carmichael, G. R., Cheng, Y., Hong, C., Huo, H., Jiang, X., Kang, S., Liu, F., Su, H. and Zheng, B.: MIX : a mosaic Asian anthropogenic emission inventory under the international collaboration framework of the MICS-Asia and HTAP, Atmos. Chem. Phys., 17, 935–963, doi:10.5194/acp-17-935-2017, 2017b.

Li, Y., Henze, D. K., Jack, D. and Kinney, P. L.: The influence of air quality model resolution on health impact assessment for fine particulate matter and its components, Air Qual. Atmos. Heal., 9(1), 51–68, doi:10.1007/s11869-015-0321-z, 2016b.

Liggio, J., Li, S., Vlasenko, A., Stroud, C. and Makar, P.: Depression of Ammonia Uptake to Sulfuric Acid Aerosols by Competing Uptake of Ambient Organic Gases, Environ. Sci. Technol., 45(7), 2790–2796, doi:10.1021/es103801g |, 2011.

Lin, C., Li, Y., Yuan, Z., Lau, A. K. H., Li, C. and Fung, J. C. H.: Using satellite remote sensing data to estimate the high-resolution distribution of ground-level PM2.5, Remote Sens. Environ., 156, 117–128, doi:10.1016/j.rse.2014.09.015, 2015.

Lin, J., Pan, D., Davis, S. J., Zhang, Q., He, K., Wang, C., Streets, D. G., Wuebbles, D. J. and Guan, D.: China's international trade and air pollution in the United States., Proc. Natl. Acad. Sci. U. S. A., 111, 1736–41, doi:10.1073/pnas.1312860111, 2014.

Lippmann, M.: Toxicological and epidemiological studies of cardiovascular effects of ambient air fine particulate matter (PM2.5) and its chemical components: Coherence and public health implications., Crit. Rev. Toxicol., 44(4), 299–347, doi:10.3109/10408444.2013.861796, 2014.

Liu, C.-N., Chen, S.-C. and Tsai, C.-J.: A Novel Multifilter PM10 - PM2.5 Sampler (MFPPS), Aerosol Sci. Technol., 45(12), 1480–1487, doi:10.1080/02786826.2011.602135, 2011.

Liu, Y., Park, R. J., Jacob, D. J., Li, Q., Kilaru, V. and Sarnat, J. A.: Mapping annual mean ground-level PM 2.5 concentrations using Multiangle Imaging Spectroradiometer aerosol optical thickness over the contiguous United States, J. Geophys. Res., 109(D22), D22206, doi:10.1029/2004JD005025, 2004.

Lu, Z., Zhang, Q. and Streets, D. G.: Sulfur dioxide and primary carbonaceous aerosol emissions in China and India , 1996 – 2010, Atmos. Chem. Phys., 11, 9839–9864, doi:10.5194/acp-11-9839-2011, 2011.

Lu, Z., Streets, D. G., Foy, B. De and Krotkov, N. A.: Ozone Monitoring Instrument Observations of Interannual Increases in SO2 Emissions from Indian Coal-Fired Power Plants during 2005 − 2012, , 47, 13993–14000, doi:10.1021/es4039648, 2013.

Lyapustin, A., Martonchik, J., Wang, Y., Laszlo, I. and Korkin, S.: Multiangle implementation of atmospheric correction (MAIAC): 1. Radiative transfer basis and look-up tables, J. Geophys. Res. Atmos., 116(3), doi:10.1029/2010JD014985, 2011a.

Lyapustin, A., Wang, Y., Laszlo, I., Kahn, R., Korkin, S., Remer, L., Levy, R. and Reid, J. S.: Multiangle implementation of atmospheric correction (MAIAC): 2. Aerosol algorithm, J. Geophys. Res. Atmos., 116(3), doi:10.1029/2010JD014986, 2011b.

Ma, Q., Cai, S., Wang, S., Zhao, B., Martin, R. V., Brauer, M., Cohen, A., Jiang, J., Zhou, W., Hao, J., Frostad, J., Forouzanfar, M. H. and Burnett, R. T.: Impacts of coal burning on ambient PM2.5 pollution in China, Atmos. Chem. Phys. Discuss., (17), 4477–4491, doi:10.5194/acp-2016-601, 2017.

Malm, W. C., Sisler, J. F., Huffman, D., Eldred, R. A. and Cahill, T. A.: Spatial and seasonal trends in particle concentration and optical extinction in the United States, J. Geophys. Res., 99, 1347–1370, doi:10.1029/93JD02916, 1994.

Marais, E. A., Jacob, D. J., Jimenez, J. L., Campuzano-Jost, P., Day, D. A., Hu, W., Krechmer, J., Zhu, L., Kim, P. S., Miller, C. C., Fisher, J. A., Travis, K., Yu, K., Hanisco, T. F., Wolfe, G. M., Arkinson, H. L., Pye, H. O. T., Froyd, K. D., Liao, J. and McNeill, V. F.: Aqueous-phase mechanism for secondary organic aerosol formation from isoprene: Application to the southeast United States and co-benefit of SO2 emission controls, Atmos. Chem. Phys., 16(3), 1603–1618, doi:10.5194/acp-16-1603-2016, 2016.

Martin, R. V: Global and regional decreases in tropospheric oxidants from photochemical effects of aerosols, J. Geophys. Res., 108(D3), 4097, doi:10.1029/2002JD002622, 2003.

Martonchik, J. V, Kahn, R. a and Diner, D. J.: Retrieval of aerosol properties over land using MISR observations, in Satellite Aerosol Remote Sensing over Land, pp. 267–293., 2009.

McInniss, L., Bergin, M. and Ogren, J.: Apportionment of light scattering and hygroscopic growth to aerosol composition, Geophys. Res. Lett., 25(4), 513–516, doi:10.1029/98GL00127, 1998.

McLinden, C. A., Fioletov, V., Shephard, M. W., Krotkov, N., Li, C., Martin, R. V., Moran, M. D. and Joiner, J.: Space-based detection of missing sulfur dioxide sources of global air pollution, Nat. Geosci., 9(May), 1–7, doi:10.1038/ngeo2724, 2016.

Megaritis, A. G., Fountoukis, C., Charalampidis, P. E., Pilinis, C. and Pandis, S. N.: Response of fine particulate matter concentrations to changes of emissions and temperature in Europe, Atmos. Chem. Phys., 13(6), 3423–3443, doi:10.5194/acp-13-3423-2013, 2013.

Miller, F. J., Gardner, D. E., Graham, J. A., Lee, R. E., Wilson, W. E. and Bachmann, J. D.: Size Considerations for Establishing a Standard for Inhalable Particles, J. Air Pollut. Control Assoc., 29(6), 610–615, doi:10.1080/00022470.1979.10470831, 1979.

Mishra, S. K. and Tripathi, S. N.: Modeling optical properties of mineral dust over the Indian Desert, J. Geophys. Res. Atmos., 113(23), 1–19, doi:10.1029/2008JD010048, 2008.

Misra, A., Gaur, A., Bhattu, D., Ghosh, S., Dwivedi, A. K., Dalai, R., Paul, D., Gupta, T., Tare, V., Mishra, S. K., Singh, S. and Tripathi, S. N.: An overview of the physico-chemical characteristics of dust at Kanpur in the central Indo-Gangetic basin, Atmos. Environ., 97, 386–396, doi:10.1016/j.atmosenv.2014.08.043, 2014.

Munchak, L. A., Schichtel, B. A., Sullivan, A. P., Holden, A. S., Kreidenweis, S. M., Malm, W. C. and Collett, J. L.: Development of wildland fire particulate smoke marker to organic carbon emission ratios for the conterminous United States, Atmos. Environ., 45(2), 395–403, doi:10.1016/j.atmosenv.2010.10.006, 2011.

Murray, L. T., Jacob, D. J., Logan, J. A., Hudman, R. C. and Koshak, W. J.: Optimized regional and interannual variability of lightning in a global chemical transport model constrained by LIS/OTD satellite data, J. Geophys. Res. Atmos., 117(20), 1–14, doi:10.1029/2012JD017934, 2012.

Oanh, K., Upadhyay, N., Zhuang, Y., Hao, Z.-P., Murthy, D. V. S., Lestari, P., Villarin, J. T., Chengchua, K., Co, H. X. and Dung, N. T.: Particulate air pollution in six Asian cities: Spatial and temporal distributions, and associated sources, Atmos. Environ., 40(18), 3367–3380, doi:10.1016/j.atmosenv.2006.01.050, 2006.

OECD: The Economic Consequences of Outdoor Air Pollution, Paris., 2016.

Ostro, B., Feng, W. Y., Broadwin, R., Green, S. and Lipsett, M.: The effects of components of fine particulate air pollution on mortality in California: Results from CALFINE, Environ. Health Perspect., 115(1), 13–19, doi:10.1289/ehp.9281, 2007.

Ostro, B., Lipsett, M., Reynolds, P., Goldberg, D., Hertz, A., Garcia, C., Henderson, K. D. and Bernstein, L.: Long-term exposure to constituents of fine particulate air pollution and mortality: Results from the California Teachers Study, Environ. Health Perspect., 118(3), 363–369, doi:10.1289/ehp.0901181, 2010.

Pandis, S. N. and Cruz, C. N.: The effect of organic coatings on the cloud condensation nuclei activation of inorganic atmospheric aerosol, J. Geophys. Res., 103(98), doi:10.1029/98JD00979, 1998.

Pandis, S. N., Wexler, A. S. and Seinfeld, J. H.: Dynamics of Tropospheric Aerosols, J. Phys. Chem., 99(24), 9646–9659, doi:10.1021/j100024a003, 1995.

Park, R., Jacob, D., Kumar, N. and Yantosca, R.: Regional visibility statistics in the United States: Natural and transboundary pollution influences, and implications for the Regional Haze Rule, Atmos. Environ., 40(28), 5405–5423, doi:10.1016/j.atmosenv.2006.04.059, 2006.

Park, R. J., Jacob, D. J., Chin, M. and Martin, R. .: Sources of carbonaceous aerosols over the United States and implications for natural visibility, J. Geophys. Res., 108(D12), doi:10.1029/2002JD003190, 2003.

Park, R. J., Jacob, D. J., Field, B. D., Yantosca, R. M. and Chin, M.: Natural and transboundary pollution influences on sulfate-nitrate-ammonium aerosols in the United States: Implications for policy, J. Geophys. Res. D Atmos., 109(15), doi:10.1029/2003JD00473, 2004.

Paulot, F., Jacob, D. J., Pinder, R. W., Bash, J. O., Travis, K. and Henze, D. K.: Ammonia emissions in the United States , European Union , and China derived by high-resolution inversion of ammonium wet deposition data : Interpretation with a new agricultural emissions inventory (MASAGE _ NH3), J. Geophys. Res. Atmos., 119, 4343–4364, doi:10.1002/2013JD021130.Received, 2014.

Petters, M. D. and Kreidenweis, S. M.: A single parameter representation of hygroscopic growth and cloud condensation nucleus activity, Atmos. Chem. Phys., 7(2), 1081–1091, doi:10.5194/acp-13-1081-2013, 2007.

Petzold, A., Ogren, J. A., Fiebig, M., Laj, P., Li, S.-M., Baltensperger, U., Holzer-Popp, T., Kinne, S., Pappalardo, G., Sugimoto, N., Wehrli, C., Wiedensohler, A. and Zhang, X.-Y.: Recommendations for reporting "black carbon" measurements, Atmos. Chem. Phys., 13(16), 8365–8379, doi:10.5194/acp-13-8365-2013, 2013a.

Petzold, a., Ogren, J. a., Fiebig, M., Laj, P., Li, S. M., Baltensperger, U., Holzer-Popp, T., Kinne, S., Pappalardo, G., Sugimoto, N., Wehrli, C., Wiedensohler, a. and Zhang, X. Y.: Recommendations for reporting black carbon measurements, Atmos. Chem. Phys., 13, 8365–8379, doi:10.5194/acp-13-8365-2013, 2013b.

Philip, S., Martin, R. V, van Donkelaar, A., Lo, J. W., Wang, Y., Chen, D., Zhang, L., Kasibhatla, P. S., Wang, S., Zhang, Q., Lu, Z., Streets, D. G., Bittman, S. and Macdonald, D. J.: Global Chemical Composition of Ambient Fine Particulate Matter for Exposure Assessment, Environ. Sci. Technol., 48, 13060–13068, doi:10.1021/es502965b, 2014a.

Philip, S., Martin, R. V., Pierce, J. R., Jimenez, J. L., Zhang, Q., Canagaratna, M. R., Spracklen, D. V., Nowlan, C. R., Lamsal, L. N., Cooper, M. J. and Krotkov, N. a.: Spatially and seasonally resolved estimate of the ratio of organic mass to organic carbon, Atmos. Environ., 87, 34–40, doi:10.1016/j.atmosenv.2013.11.065, 2014b.

Philip, S., Martin, R. V., Snider, G., Weagle, C. L., van Donkelaar, A., Brauer, M., Henze, D. K., Klimont, Z., Venkataraman, C., Guttikunda, S. K. and Zhang, Q.: Anthropogenic fugitive, combustion, and industrial dust is significant, underrepresented fine particulate matter source in global atmospheric models, Environ. Res. Lett., 12(44018), doi:10.1088/1748-9326/aa65a4, 2017.

Pinault, L., Tjepkema, M., Crouse, D. L., Weichenthal, S., van Donkelaar, A., Martin, R. V., Brauer, M., Chen, H. and Burnett, R. T.: Risk estimates of mortality attributed to low concentrations of ambient fine particulate matter in the Canadian community health survey cohort, Environ. Heal., 15(1), 18, doi:10.1186/s12940-016-0111-6, 2016.

Pinder, R. W. and Adams, P. J.: Ammonia Emission Controls as a Cost-Effective Strategy for Reducing Atmospheric Particulate Matter in the Eastern United States, Environ. Sci. Technol., 41(2), 380–386, doi:10.1021/es060379a CCC:, 2007.

Pope, C. A., Ezzati, M. and Dockery, D. W.: Fine-particulate air pollution and life expectancy in the United States., N. Engl. J. Med., 360(4), 376–86, doi:10.1056/NEJMsa0805646, 2009.

Prospero, J. M., Ginoux, P., Torres, O., Nicholson, S. E. and Gill, T. E.: Environmental characterization of global sources of atmospheric soil dust identified with the NIMBUS 7 Total Ozone Mapping Spectrometer (TOMS) absorbing aerosol product, Rev. Geophys., 40, 1002, doi:10.1029/2000RG000095, 2002.

Punger, E. M. and West, J. J.: The effect of grid resolution on estimates of the burden of ozone and fine particulate matter on premature mortality in the USA, Air Qual. Atmos. Heal., 6, 563–573, doi:10.1007/s11869-013-0197-8, 2013.

Putaud, J. P., Van Dingenen, R., Alastuey, A., Bauer, H., Birmili, W., Cyrys, J., Flentje, H., Fuzzi, S., Gehrig, R., Hansson, H. C., Harrison, R. M., Herrmann, H., Hitzenberger, R., Hüglin, C., Jones, A. M., Kasper-Giebl, A., Kiss, G., Kousa, A., Kuhlbusch, T. A. J., Löschau, G., Maenhaut, W., Molnar, A., Moreno, T., Pekkanen, J., Perrino, C., Pitz, M., Puxbaum, H., Querol, X., Rodriguez, S., Salma, I., Schwarz, J., Smolik, J., Schneider, J., Spindler, G., ten Brink, H., Tursic, J., Viana, M., Wiedensohler, A. and Raes, F.: A European aerosol phenomenology - 3: Physical and chemical characteristics of particulate matter from 60 rural, urban, and kerbside sites across Europe, Atmos. Environ., 44(10), 1308–1320, doi:10.1016/j.atmosenv.2009.12.011, 2010.

Pye, H., Liao, H., Wu, S., Mickley, L. J., Jacob, D. J., Henze, D. J. and Seinfeld, J. H.: Effect of changes in climate and emissions on future sulfate-nitrate-ammonium aerosol levels in the United States, J. Geophys. Res. Atmos., 114(1), 1–18, doi:10.1029/2008JD010701, 2009.

Pye, H. O. T., Chan, A. W. H., Barkley, M. P. and Seinfeld, J. H.: Global modeling of organic aerosol: The importance of reactive nitrogen (NOx and NO3), Atmos. Chem. Phys., 10(22), 11261–11276, doi:10.5194/acp-10-11261-2010, 2010.

Pye, H. O. T., Zuend, A., Fry, J. L., Isaacman-VanWertz, G., Capps, S. L., Appel, K. W., Foroutan, H., Xu, L., Ng, N. L. and Goldstein, A. H.: Coupling of organic and inorganic aerosol systems and the effect on gas-particle partitioning in the southeastern United States, Atmos. Chem. Phys. Discuss., (July), 1–25, doi:10.5194/acp-2017-623, 2018.

Quincey, P., Butterfield, D., Green, D., Coyle, M. and Cape, N. J.: An evaluation of measurement methods for organic, elemental and black carbon in ambient air monitoring sites, Atmos. Environ., 43(32), 5085–5091, doi:10.1016/j.atmosenv.2009.06.041, 2009.

Ram, K., Sarin, M. M. and Tripathi, S. N.: Temporal trends in atmospheric $PM_{2.5}$, PM_{10}, elemental carbon, organic carbon, water-soluble organic carbon, and optical properties: impact of biomass burning emissions in the Indo-Gangetic Plain., Environ. Sci. Technol., 46(2), 686–95, doi:10.1021/es202857w, 2012.

Ranft, U., Schikowski, T., Sugiri, D., Krutmann, J. and Krämer, U.: Long-term exposure to traffic-related particulate matter impairs cognitive function in the elderly, Environ. Res., 109(8), 1004–1011, doi:10.1016/j.envres.2009.08.003, 2009.

Reddington, C. L., Butt, E. W., Ridley, D. A., Artaxo, P., Morgan, W. T., Coe, H. and Spracklen, D. V: Air quality and human health improvements from reductions in deforestation-related fire in Brazil, Nat. Geosci., 8(October), doi:10.1038/NGEO2535, 2015.

Remoundaki, E., Kassomenos, P., Mantas, E., Mihalopoulos, N. and Tsezos, M.: Composition and mass closure of PM2.5 in urban environment (Athens, Greece), Aerosol Air Qual. Res., 13(1), 72–82, doi:10.4209/aaqr.2012.03.0054, 2013.

Ridley, D. A., Heald, C. L. and Ford, B.: North African dust export and deposition: A satellite and model perspective, J. Geophys. Res. Atmos., 117(2), 1–21, doi:10.1029/2011JD016794, 2012.

Ridley, D. A., Heald, C. L., Kok, J. F. and Zhao, C.: An observationally-constrained estimate of global dust aerosol optical depth, Atmos. Chem. Phys. Discuss., (May), 1–31, doi:10.5194/acp-2016-385, 2016.

Robinson, A. L., Donahue, N. M., Shrivastava, M. K., Weitkamp, E. A., Sage, A. M., Grieshop, A. P., Lane, T. E., Pierce, J. R. and Pandis, S. N.: Rethinking Organic Aerosols: Semivolatile Emissions and Photochemical Aging, Science (80-.)., 315(March), 1259–1262, doi:10.1126/science.1133061, 2007.

Rohr, A. C. and Wyzga, R. E.: Attributing health effects to individual particulate matter constituents, Atmos. Environ., 62, 130–152, doi:10.1016/j.atmosenv.2012.07.036, 2012.

Santoso, M., Lestiani, D. D. and Hopke, P. K.: Atmospheric black carbon in PM 2 . 5 in Indonesian cities, J. Air Waste Manag. Assoc., 63(9), 1022–1025, doi:10.1080/10962247.2013.804465, 2013.

Schicker, B., Kuhn, M., Fehr, R., Asmis, L. M., Karagiannidis, C. and Reinhart, W. H.: Particulate matter inhalation during hay storing activity induces systemic inflammation and platelet aggregation, Eur. J. Appl. Physiol., 105(5), 771–778, doi:10.1007/s00421-008-0962-9, 2009.

Seinfeld, J. H. and Pandis, S. N.: Atmospheric Chemistry and Physics: From Pollution to Climate Change, Second., John Wiley & Sons, Inc., Hoboken, New Jersey, 2006.

Seinfeld, J. H. and Pandis, S. N.: Atmopsheric Chemistry and Physics: From Air Pollution to Climate Change, Third., John Wiley & Sons, Inc., Hoboken, New Jersey., 2016.

Shaddick, G., Thomas, M. L., Green, A., Brauer, M., van Donkelaar, A., Burnett, R., Chang, H. H., Cohen, A., Dingenen, R. Van, Dora, C., Gumy, S., Liu, Y., Martin, R., Waller, L. A., West, J., Zidek, J. V. and Prüss-Ustün, A.: Data integration model for air quality: A hierarchical approach to the global estimation of exposures to ambient air pollution, J. R. Stat. Soc. Ser. C Appl. Stat., 231–253, doi:10.1111/rssc.12227, 2017.

Silbajoris, R., Osornio-Vargas, A. R., Simmons, S. O., Reed, W., Bromberg, P. A., Dailey, L. A. and Samet, J. M.: Ambient particulate matter induces interleukin-8 expression through an alternative NF-??B (nuclear factor-kappa B) mechanism in human airway epithelial cells, Environ. Health Perspect., 119(10), 1379–1383, doi:10.1289/ehp.1103594, 2011.

Silvern, R. F., Jacob, D. J., Kim, P. S., Marais, E. A., Turner, J. R., Campuzano-Jost, P. and Jimenez, J. L.: Inconsistency of ammonium–sulfate aerosol ratios with thermodynamic models in the eastern US: a possible role of organic aerosol, Atmos. Chem. Phys., 17(8), 5107–5118, doi:10.5194/acp-17-5107-2017, 2017.

Smirnov, A., Holben, B. N., Eck, T. F., Dubovik, O. and Slutsker, I.: Cloud-screening and quality control algorithms for the AERONET database, Remote Sens. Environ., 73(3), 337–349, doi:10.1016/S0034-4257(00)00109-7, 2000.

Snider, G., Weagle, C. L., Martin, R. V., van Donkelaar, A., Conrad, K., Cunningham, D., Gordon, C., Zwicker, M., Akoshile, C., Artaxo, P., Anh, N. X., Brook, J., Dong, J., Garland, R. M., Greenwald, R., Griffith, D., He, K., Holben, B. N., Kahn, R., Koren, I., Lagrosas, N., Lestari, P., Ma, Z., Vanderlei Martins, J., Quel, E. J., Rudich, Y., Salam, A., Tripathi, S. N., Yu, C., Zhang, Q., Zhang, Y., Brauer, M., Cohen, A., Gibson, M. D. and Liu, Y.: SPARTAN: a global network to evaluate and enhance satellite-based estimates of ground-level particulate matter for global health applications, Atmos. Meas. Tech., 8, 505–521, doi:10.5194/amt-8-505-2015, 2015.

Snider, G., Weagle, C. L., Murdymootoo, K. K., Ring, A., Ritchie, Y., Stone, E., Walsh, A., Akoshile, C., Anh, N. X., Balasubramanian, R., Brook, J., Qonitan, F. D., Dong, J., Griffith, D., He, K., Holben, B. N., Kahn, R., Lagrosas, N., Lestari, P., Ma, Z., Misra, A., Norford, L. K., Quel, E. J., Salam, A., Schichtel, B., Segev, L., Tripathi, S., Wang, C., Yu, C., Zhang, Q., Zhang, Y., Brauer, M., Cohen, A., Gibson, M. D., Liu, Y., Martins, J. V., Rudich, Y. and Martin, R. V.: Variation in global chemical composition of PM2.5: emerging results from SPARTAN, Atmos. Chem. Phys., 16(15), 9629–9653, doi:10.5194/acp-16-9629-2016, 2016.

Solomon, P. A., Crumpler, D., Flanagan, J. B., Jayanty, R. K. M., Rickman, E. E. and McDade, C. E.: U.S. National PM $_{2.5}$ Chemical Speciation Monitoring Networks—CSN and IMPROVE: Description of networks, J. Air Waste Manage. Assoc., 64(12), 1410–1438, doi:10.1080/10962247.2014.956904, 2014.

Stettler, M. E. J., Eastham, S. and Barrett, S. R. H.: Air quality and public health impacts of UK airports. Part I: Emissions, Atmos. Environ., 45(31), 5415–5424, doi:10.1016/j.atmosenv.2011.07.012, 2011.

Stjern, C. W., Stohl, A. and Kristjánsson, J. E.: Have aerosols affected trends in visibility and precipitation in Europe ?, J. Geophys. Res., 116, doi:10.1029/2010JD014603, 2011.

Sun, Y. L., Zhang, Q., Schwab, J. J., Demerjian, K. L., Chen, W. N., Bae, M. S., Hung, H. M., Hogrefe, O., Frank, B., Rattigan, O. V. and Lin, Y. C.: Characterization of the sources and processes of organic and inorganic aerosols in New York city with a high-resolution time-of-flight aerosol mass apectrometer, Atmos. Chem. Phys., 11(4), 1581–1602, doi:10.5194/acp-11-1581-2011, 2011.

Taha, G., Box, G. P., Cohen, D. D. and Stelcer, E.: Black Carbon Measurement using Laser Integrating Plate Method, Aerosol Sci. Technol., 41(3), 266–276, doi:10.1080/02786820601156224, 2007.

USEPA: Chemical Speciation Network Database, 2015.

van Dingenen, R., Raes, F., Putaud, J. P., Baltensperger, U., Charron, A., Facchini, M. C., Decesari, S., Fuzzi, S., Gehrig, R., Hansson, H. C., Harrison, R. M., Hüglin, C., Jones, A. M., Laj, P., Lorbeer, G., Maenhaut, W., Palmgren, F., Querol, X., Rodriguez, S., Schneider, J., Ten Brink, H., Tunved, P., Tørseth, K., Wehner, B., Weingartner, E., Wiedensohler, A. and Wåhlin, P.: A European aerosol phenomenology - 1: Physical characteristics of particulate matter at kerbside, urban, rural and background sites in Europe, *Atmos. Environ.*, 38(16), 2561–2577, doi:10.1016/j.atmosenv.2004.01.040, 2004.

van Donkelaar, A., Martin, R. V., Spurr, R. J. D. and Burnett, R. T.: High-Resolution Satellite-Derived PM $_{2.5}$ from Optimal Estimation and Geographically Weighted Regression over North America, *Environ. Sci. Technol.*, 49(17), 10482–10491, doi:10.1021/acs.est.5b02076, 2015a.

van Donkelaar, A., Martin, R. V., Brauer, M. and Boys, B. L.: Use of satellite observations for long-term exposure assessment of global concentrations of fine particulate matter, *Environ. Health Perspect.*, 123, 135–143, doi:10.1289/ehp.1408646, 2015b.

van Donkelaar, A., Martin, R. V, Brauer, M., Hsu, N. C., Kahn, R. A., Levy, R. C., Lyapustin, A., Sayer, A. M. and Winker, D. M.: Global Estimates of Fine Particulate Matter using a Combined Geophysical-Statistical Method with Information from Satellites , Models , and Monitors, *Environ. Sci. Technol.*, 50, 3762–3772, doi:10.1021/acs.est.5b05833, 2016.

van Donkelaar, A., Martin, R. V, Brauer, M., Kahn, R., Levy, R., Verduzco, C. and Villeneuve, P. J.: Global estimates of ambient fine particulate matter concentrations from satellite-based aerosol optical depth: development and application., *Environ. Health Perspect.*, 118(6), 847–855, 2010.

Villalobos, A. M., Amonov, M. O., Shafer, M. M., Devi, J. J., Gupta, T., Tripathi, S. N., Rana, K. S., Mckenzie, M., Bergin, M. H. and Schauer, J. J.: Source apportionment of carbonaceous fine particulate matter (PM2.5) in two contrasting cities across the Indo-Gangetic Plain, Atmos. Pollut. Res., 6(3), 398–405, doi:10.5094/APR.2015.044, 2015.

Wang, J. L.: Mapping the global dust storm records: Review of dust data sources in supporting modeling/climate study, Curr. Pollut. Reports, 1(2), 82–94, doi:10.1007/s40726-015-0008-y, 2015a.

Wang, J. X. L.: Mapping the Global Dust Storm Records: Review of Dust Data Sources in Supporting Modeling/Climate Study, Curr. Pollut. Reports, 1(2), 82–94, doi:10.1007/s40726-015-0008-y, 2015b.

Wang, Q., Jacob, D. J., Fisher, J. A., Mao, J., Leibensperger, E. M., Carouge, C. C., Sager, P. Le, Kondo, Y., Jimenez, J. L., Cubison, M. J. and Doherty, S. J.: Sources of carbonaceous aerosols and deposited black carbon in the Arctic in winter-spring : implications for radiative forcing, Atmos. Chem. Phys., 11, 12453–12473, doi:10.5194/acp-11-12453-2011, 2011.

Wang, Y., Logan, J. a. and Jacob, D. J.: Global Simulation of tropospheric O3-NOx-hydrocarbon chemistry: 2. Model evaluation and global ozone budget, J. Geophys. Res., 103(D9), 10727–10755, doi:10.1029/98JD00157, 1998.

Wang, Y., Zhang, Q. Q., He, K., Zhang, Q. and Chai, L.: Sulfate-nitrate-ammonium aerosols over China : response to 2000 – 2015 emission changes of sulfur dioxide , nitrogen oxides , and ammonia, Atmos. Chem. Phys., 13, 2635–2652, doi:10.5194/acp-13-2635-2013, 2013.

Weakley, A. T., Takahama, S. and Dillner, A. M.: Ambient aerosol composition by infrared spectroscopy and partial least-squares in the chemical speciation network: Organic carbon with functional group identification, Aerosol Sci. Technol., 50(10), 1096–1114, doi:10.1080/02786826.2016.1217389, 2016.

West, J. J., Cohen, A., Dentener, F., Brunekreef, B., Zhu, T., Armstrong, B., Bell, M. L., Brauer, M., Carmichael, G., Costa, D. L., Dockery, D. W., Kleeman, M., Krzyzanowski, M., Künzli, N., Liousse, C., Lung, S. C. C., Martin, R. V., Pöschl, U., Pope, C. A., Roberts, J. M., Russell, A. G. and Wiedinmyer, C.: "What We Breathe Impacts Our Health: Improving Understanding of the Link between Air Pollution and Health," Environ. Sci. Technol., 50(10), 4895–4904, doi:10.1021/acs.est.5b03827, 2016.

Wexler, A. S. and Clegg, S. L.: Atmospheric aerosol models for systems including the ions H^+, NH_4^+, Na^+, SO_4^{2-}, NO_3^-, Cl^-, Br^-, and H_2O, J. Geophys. Res., 107(D14), 4207, doi:10.1029/2001JD000451, 2002.

WHO: International Agency for Research on Cancer: Outdoor air pollution a leading environmental cause of cancer deaths, Geneva, Switzerland., 2013.

WHO: Review of Evidence on Health Aspects of Air Pollution – REVIHAAP, Technical report, The WHO European Centre for Environment and Health, WHO Regional Office for Europe, Bonn, 2013.

WHO: WHO Air quality guidelines for particulate matter, ozone, nitrogen dioxide and sulfur dioxide – global update 2005, World Health Organization, Geneva, Switzerland, 2006.

Wild, M.: Global dimming and brightening, J. Geophys. Res., 114(D10), doi:10.1029/2008JD011470, 2009.

Wilhelm, M., Ghosh, J. K., Su, J., Cockburn, M., Jerrett, M. and Ritz, B.: Traffic-Related Air Toxics and Term Low Birth Weight in Los Angeles County, Environ. Health Perspect., 120(1), 132–138, doi:10.1289/ehp.1103408, 2012.

Xu, J. W., Martin, R. V., Morrow, A., Sharma, S., Huang, L., Richard Leaitch, W., Burkart, J., Schulz, H., Zanatta, M., Willis, M. D., Henze, D. K., Lee, C. J., Herber, A. B. and Abbatt, J. P. D.: Source attribution of Arctic black carbon constrained by aircraft and surface measurements, Atmos. Chem. Phys., 17(19), 11971–11989, doi:10.5194/acp-17-11971-2017, 2017.

Xu, Y.: Improvements in the operation of SO2 scrubbers in Chinas coal power plants, Environ. Sci. Technol., 45(2), 380–385, doi:10.1021/es1025678, 2011.

Yang, F., Tan, J., Zhao, Q., Du, Z., He, K., Ma, Y., Duan, F. and Chen, G.: Characteristics of $PM_{2.5}$ speciation in representative megacities and across China, Atmos. Chem. Phys., 11(11), 5207–5219, doi:10.5194/acp-11-5207-2011, 2011a.

Yang, F., Tan, J., Zhao, Q., Du, Z., He, K., Ma, Y., Duan, F., Chen, G. and Zhao, Q.: Characteristics of PM2.5 speciation in representative megacities and across China, Atmos. Chem. Phys., 11, 5207–5219, doi:10.5194/acp-11-5207-2011, 2011b.

Yang, F., Tan, J., Zhao, Q., Du, Z., He, K., Ma, Y., Duan, F., Chen, G. and Zhao, Q.: Characteristics of PM2.5 speciation in representative megacities and across China, Atmos. Chem. Phys., 11(11), 5207–5219, doi:10.5194/acp-11-5207-2011, 2011c.

You, Y. and Bertram, A. K.: Liquid – liquid phase separation in particles containing organics mixed with ammonium sulfate , ammonium bisulfate , ammonium nitrate or sodium chloride, Atmos. Chem. Phys., 13, 11723–11734, doi:10.5194/acp-13-11723-2013, 2013.

Zanobetti, A. and Schwartz, J.: A Novel Approach to Estimate Distributed Lag Model Between Hospital Admissions and Ozone: A Multi-City Time Series Analysis, Epidemiology, 20(6) [online] Available from: http://journals.lww.com/epidem/Fulltext/2009/11001/A_Novel_Approach_to_Estimate_Distributed_Lag_Model.153.aspx, 2009.

Zhang, J. and Reid, J. S.: A decadal regional and global trend analysis of the aerosol optical depth using a data-assimilation grade over-water MODIS and Level 2 MISR aerosol products, Atmos. Chem. Phys., 10(22), 10949–10963, doi:10.5194/acp-10-10949-2010, 2010.

Zhang, K. M. and Wexler, A. S.: A hypothesis for growth of fresh atmospheric nuclei, J. Geophys. Res., 107(D21), 4577, doi:10.1029/2002JD002180, 2002.

Zhang, L., Kok, J. F., Henze, D. K., Li, Q. and Zhao, C.: Improving simulations of fine dust surface concentrations over the western United States by optimizing the particle size distribution, Geophys. Res. Lett., 40(12), 3270–3275, doi:10.1002/grl.50591, 2013a.

Zhang, L., Liu, L., Zhao, Y., Gong, S., Zhang, X., Henze, D. K., Capps, S. L., Fu, T.-M., Zhang, Q. and Wang, Y.: Source attribution of particulate matter pollution over North China with the adjoint method, Environ. Res. Lett., 10, 84011, doi:10.1088/1748-9326/10/8/084011, 2015.

Zhang, Q., Jiang, X., Tong, D., Davis, S. J., Zhao, H. and Geng, G.: Transboundary health impacts of transported global air pollution and international trade, Nature, 543(7647), 705–709, doi:10.1038/nature21712, 2017.

Zhang, R., Suh, I., Zhao, J., Zhang, D., Fortner, E. C., Tie, X., Molina, L. T. and Molina, M. J.: Atmospheric new particle formation enhanced by organic acids., Science, 304(5676), 1487–90, doi:10.1126/science.1095139, 2004.

Zhang, R., Jing, J., Tao, J., Hsu, S. C., Wang, G., Cao, J., Lee, C. S. L., Zhu, L., Chen, Z., Zhao, Y. and Shen, Z.: Chemical characterization and source apportionment of PM2.5 in Beijing: Seasonal perspective, Atmos. Chem. Phys., 13, 7053–7074, doi:10.5194/acp-13-7053-2013, 2013b.

Zhang, W.-J., Sun, Y.-L., Zhuang, G.-S. and Xu, D.-Q.: Characteristics and seasonal variations of PM2.5, PM10, and TSP aerosol in Beijing., Biomed. Environ. Sci., 19(6), 461–8, 2006.

Zheng, Y., Zhao, T., Che, H., Liu, Y., Han, Y., Liu, C., Xiong, J., Liu, J. and Zhou, Y.: A 20-year simulated climatology of global dust aerosol deposition, Sci. Total Environ., 557–558, 861–868, doi:10.1016/j.scitotenv.2016.03.086, 2016.

Appendix A Author Contributions

Chapter 3 contains results published in *Atmospheric Chemistry and Physics* with the following reference:

Snider, G., **Weagle, C. L.**, Murdymootoo, K. K., Ring, A., Ritchie, Y., Stone, E., Walsh, A., Akoshile, C., Anh, N. X., Balasubramanian, R., Brook, J., Qonitan, F. D., Dong, J., Griffith, D., He, K., Holben, B. N., Kahn, R., Lagrosas, N., Lestari, P., Ma, Z., Misra, A., Norford, L. K., Quel, E. J., Salam, A., Schichtel, B., Segev, L., Tripathi, S., Wang, C., Yu, C., Zhang, Q., Zhang, Y., Brauer, M., Cohen, A., Gibson, M. D., Liu, Y., Martins, J. V., Rudich, Y., and Martin, R. V.: Variation in global chemical composition of PM2.5: emerging results from SPARTAN, Atmos. Chem. Phys., 16, 9629-9653, **2016**.

All text included in this thesis is rephrased from the published manuscript to include only sections where the author of this thesis made substantial contribution. This includes the collection and quality assurance of all data, development of aerosol categories, and interpretation of collected data at all SPARTAN sites.

Randall Martin provided guidance and supervision throughout the project. Co-authors include the SPARTAN advisory committee who offer advice for the advancement of SPARTAN, coop students who assisted in completing filter weighing and lab analysis, and site operators at institutions that host SPARTAN sampling sites that are responsible for operating and maintaining instrumentation.

Appendix B SPARTAN Standard Operating Procedures

The SPARTAN Standard Operating Procedures have been written and developed by the author of this thesis. Network procedures are continuously evaluated for quality control and quality assurance of all SPARTAN data.

B1.0 Filter Weighing Procedure

B1.1 General Information

The first step in the SPARTAN filter sampling process is pre-weighing the filters to obtain their masses prior to sampling. These pre-sampling masses are compared to the post-sampling masses to infer the mass of $PM_{2.5}$ or PM_{coarse} collected on the filters during sampling. All filter weighing is conducted in a temperature and relative humidity controlled clean room in the Health and Environment Research Centre (HERC) in the Life Sciences Research Institute at Dalhousie University. This section describes the procedure for pre-weighing and post-weighing Teflon and Nuclepore filters.

Prior to pre-weighing each filter must be placed into a clean petri dish and given a label that is used to identify each individual filter until the filter is ultimately destroyed through the filter extraction procedures (section B4.0 and B5.0). All filters are required to equilibrate in the cleanroom environment for at least 24 hours prior to weighing. Following US EPA procedures, the cleanroom must have a relative humidity between 30-40 % and a temperature between 20-25 °C.

B1.2 Maintaining the Cleanroom

Filter weighing is at the center of SPARTAN data analysis, quality control during the weighing process is the first step to producing reliable data. The following instructions are followed to ensure that the cleanroom remains as clean as possible and that any accumulated dust is removed prior to the weighing session.

1. Remove shoes prior to entering the cleanroom, and put on a clean pair of socks. Use a lint brush to pull any lint off shirt, sweater and any other articles of clothing that will be reaching over workspace. Put on a pair of provided nitrile gloves.
2. Replace petri dish lids of filters that were previously left out to equilibrate. Stack in a safe and convenient location.
3. Spray methanol onto a lint-free tissue wipe and wipe down tables, scale, laptop and any other workspace or instrument you will be using. Next, spray anti-static solution onto a lint-free tissue and wipe down these same areas. Note:
    - Do not spray solution directly onto any of the instruments, and
    - Be sure to wipe down areas which are closer to workspace before areas that are less likely to encounter the filters.
4. Ensure balance is level using the indicator bubble on the top of the balance, as shown in Figure B.1. If the bubble is not in the indicator circle, use the leveling wheels at the base of the instrument to level it.

5. Thoroughly wipe the precision forceps with methanol using a small lint-free tissue, being careful not to get any residue stuck on the tip of the forceps

Figure B.1. Indicator bubble on the top of the microbalance. Ensure that the bubble is inside the solid black lines as shown.

B1.3 Microbalance Calibration

Proper functioning of the microbalance is essential for a successful weighing session. Therefore, at the beginning of every weighing session the microbalance is calibrated to ensure its accuracy. It is important to be sure there is nothing on the scale and that the table is not bumped during calibration. Do not rest hands on the table or move things around on the table while calibrating. The following steps are followed to calibrate the microbalance:

1. On the balance (Sartorius microbalance model SE2-F), enter '202122'. This code indicates the beginning of the calibration procedure for the range of weights the balance will encounter. Then, select 'S CAL' to begin the calibration.
2. Continue to press 'select' until 'set preload' appears at bottom left of the display and then press 'start'. There will be a 'C' that appears in center of display; wait until this goes away and a weight comes onto screen (i.e. 0.0000 mg) before moving to the next step.

3. Press ‘select’ until ‘SCAL: Internal adjustment’ appears, and press ‘start’. Wait until this procedure is finished and a weight comes up on the display.
4. Press ‘select’ until ‘SCAL: internal linearization’ appears, and press ‘start’. Wait until this procedure is finished and again a weight comes up on the display.
5. Press the CF button, and wait until a weight comes up on screen.
6. At this point, the weight displayed should be 0.0000 mg. If not, tare the balance.

B1.4 Calibration Weights and Lab Blanks

Standard metal weights and lab blanks (blank filters that remain in the clean room) are weighed at the beginning of each weighing session to ensure the balance is working correctly. These data are saved over the long-term to track the clean room conditions.

1. Open filter blanks and calibration Excel spreadsheet and record the date, temperature, relative humidity, and the name of the person conducting the weighing. The masses of the calibration weights and lab blank standards are recorded in this spreadsheet.
2. Ensure all surfaces and forceps have air-dried from the anti-static cleaning procedure.
3. Remove 200 mg weight, 1 mg weight and plastic forceps from the calibration kit. Begin by weighing the 200 mg calibration weight:
    - Pick up the metal weight with the plastic forceps.
    - Hold the weight approximately 15 cm below the de-ionizing blower for approximately 3 seconds.

- Open scale lid and place the weight in the center of pedestal and close lid.
- Allow weight measurement on display to remain constant for 20 seconds, before recording the final weight
- Repeat the steps above for the 1 mg calibration weight.

4. To guarantee the weight found is reliable, repeat the measurement two more times for each calibration weight.
    - The average of the three measurements for each calibration should be within ±0.0030 mg of the expected value with a standard deviation being less than 0.0020 mg.
    - If not within these guidelines, try recalibrating the scale and repeat measurements.
    - If still not within these guidelines, there may be a problem with the microbalance; consult instruction manual or see lab tech.
5. After returning the metal weights to the calibration kit, weigh the lab blanks as follows:
    - Use the precision forceps to pick up the first lab blank from the petri dish, being sure to only touch the edge of the filter with the tips of the forceps.
    - Hold filter approximately 15 cm below the ionizing blower for approximately 3 seconds.
    - Open scale, place in center of pedestal and close lid.
    - Allow weight measurement on display to remain constant for 20 seconds, before recording that final weight on computer spreadsheet.

6. Remove filter from pedestal, again by grabbing the edge of the filter with the precision forceps, and replace in petri dish, being careful not to accidentally grab the pedestal.
    - Wait until the display has remained at a constant measurement for at least 20 seconds.
    - If that constant measurement is 0.0000 mg, proceed to next step.
    - If that constant measurement is not 0.0000 mg, press the 'tare' button and wait until the display button reads 0.0000 mg before moving to the next step.
7. Repeat steps 8 and 9 for all available lab blank standards. To reduce the possibility of error, complete the triplicate measurements in a random order.
8. Confirm that the lab blank weights are reliable using the following information:
    - Compare the average of the measurements for each filter to previous measurements.
    - The average for each filter is within ±0.0010 mg of the previously found average and more importantly that the standard deviations are no larger than 0.0010 mg (ideally below 0.0005 mg.)
    - If these requirements are not met, ensure the microbalance is calibrated correctly.

NOTE: Please see lab technician if measurements are not stabilizing, if they are repeatedly inconsistent or if any other issues arise.

B1.5 Weighing Sampled Filters

1. Make sure the filters to be weighed have been equilibrated in the cleanroom environment for at least 24 hours.
2. Following the calibration procedure, make sure that the relative humidity in the clean room is between 30-40%, and the temperature between 20 - 25 °C. There is a humidifier and two dehumidifiers in the clean room, as well as one dehumidifier located just outside the clean room. These can be used to manipulate the humidity in the clean room if it is not within the 30-40% range. DO NOT weigh the filters if the temperature and humidity are not within the ranges mentioned above, as this will affect the quality of SPARTAN data.
3. Open the Excel spreadsheet for the SPARTAN site corresponding to the filter labels and record your name, the date, temperature, and relative humidity. Create a copy of the spreadsheet to ensure that no mass data are accidentally lost during the weighing session.
4. Use the precision forceps to pick up the filters from the petri dish. As with the lab blanks, pick up the filters by grabbing the edge of the filter with the tips of the forceps.
5. Place filter approximately 15 cm below the de-ionizing blower for approximately 3 seconds.
6. Open the scale lid and gently place the filter in the center of pedestal and close the lid as shown in Figure B.2.

Figure B.2. Example of filter positioned in the center of the balance pedestal

7. Allow weight measurement on display to remain constant for 20 seconds before recording that final weight in the Excel spreadsheet.
8. Remove filter from pedestal, again by grabbing the edge of the filter with the precision forceps, and place in petri dish, being careful not to grab the pedestal with the forceps.
    - Wait until the display has remained at a constant measurement for at least 20 seconds.
    - If that constant measurement is 0.0000 mg, proceed to next step.
    - If that constant measurement is not 0.0000 mg, press the ‘tare’ button and wait until the display button reads 0.0000 mg before moving to the next step.
9. Repeat steps 2-6 for all filters to be weighed.
10. Confirm the weights found for these filters are reliable by repeating measurements in a random order for a total of three measurements for each filter.

- **For filters**: The measurements are acceptable if the standard deviations are no larger than 0.0100 mg and ideally below 0.0050 mg. If these requirements are not met, ensure the microbalance is calibrated correctly and working properly before repeating steps 2-9.
- **For field blanks**: The measurements are acceptable if the standard deviations are no larger than 0.0150 mg. The field blanks should not increase or decrease more than 0.0300 mg from the pre-sampled weights. If these requirements are not met, ensure the microbalance is calibrated correctly and working properly before repeating steps 2-9.

11. After all weighing is complete, place the precision forceps back in the holder. Cover and place the weighed filters back in the appropriate tray.

B2.0 Filter Cartridge Shipping, Receiving, and Processing

Various precautions are taken throughout cartridge assembly, shipment, and disassembly to protect the filters from contamination. This section describes shipping procedures, proper handling of sampled cartridges once received at Dalhousie, and determination of air volume sampled.

B2.1 Cartridge Assembly

Each cartridge is assembled within 2 weeks of when it is required by the site operator. This provides enough time to allow for shipment time to any site, even if unexpected delays arise. The tools needed for the cartridge assembly process are:

- Hex key (opening cartridge)
- Two pairs of clean tweezers
- Custom-made plug remover (see Figure 3.1)
- Methanol (for wiping tweezers, cleaning parts)
- Milli-Q water (for cleaning parts)

Figure B.3 describes the order of operations for assembly of a cartridge. For example, for the thick half of the cartridge that is split into 2 2x2 blocks as shown in Figure B.5, a metal grid is inserted into the cartridge, followed by the filter, plastic washer, and o-rings. It is important to place the filters in the proper slot according to the filter label. For example, a filter labelled with a “1T”, must go in the number one slot on the PTFE side of the cartridge.

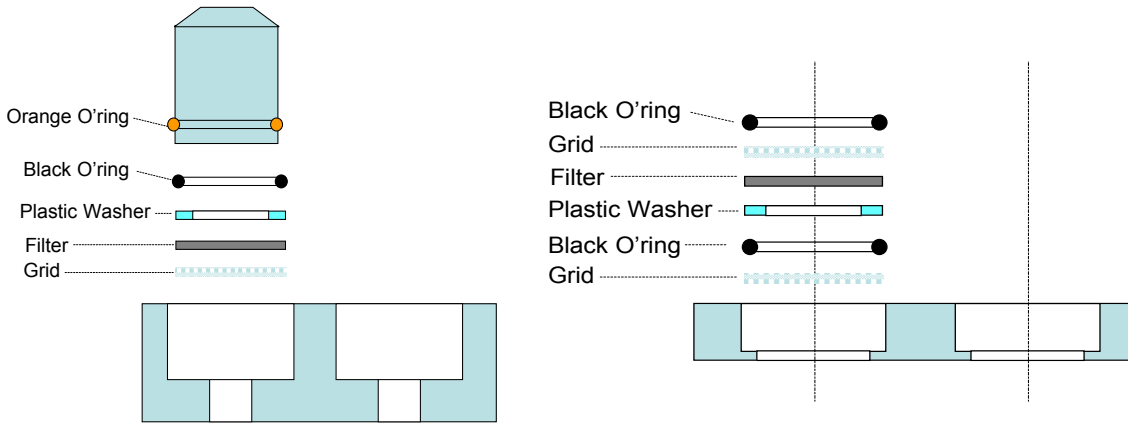

Figure B.3. Cartridge assembly scheme. Left is TOP half (teflon), right is BOTTOM half (nuclepore).

Once the cartridge is assembled, a log sheet for the cartridge must be prepared. The log sheet with the cartridge number (e.g. CHTS-024) is recorded on the log sheet. One of the two small labels on each of the filter petri-dishes must be transferred to the appropriate column and row on the log sheet.

B2.2 Cartridge Shipping

After a cartridge is successfully assembled and the log sheet prepared, the cartridge is placed inside three sealable plastic bags. The log sheet is placed inside the outermost bag to ensure it remains with the cartridge. Next, the cartridge is placed inside a box and transport to the Dunn building to be shipped to the sampling site. The box containing the cartridge is then wrapped in bubble-wrap and then placed inside a bubble-wrap envelope. Finally, the cartridge is shipped to the sampling site by way of a courier (e.g. UPS or FedEx).

Once the tracking information is obtained it is forwarded on to the site operator so they know to expect the cartridge. After a cartridge finishes sampling, it is returned to Dalhousie in the same manner it was shipped out: triple-bagged, inside a box, bubble-wrapped, and including a copy of the log sheet.

B2.3 Cartridge Receiving

Upon receiving a sampled cartridge from a site operator, ensure that a copy of the sampling log sheet (e.g. Figure B.4) is included. If no log sheet is included, contact the site operator to provide a scanned copy of the log sheet. Original log sheets are not necessary but a copy must be obtained for data processing and SPARTAN records.

Note that the log sheet shown in Figure B.4 has all the necessary information provided, however for some sampled cartridges this will not be the case. It is imperative to request more detailed information from site operators if data are missing. If flow measurements are missing and the site operator is unable to provide written record of measured flow rates, the sample volume cannot be accurately calculated and the conversion from mass to concentration is not possible. Therefore, it is important to stress the need to record flow rates to site operators.

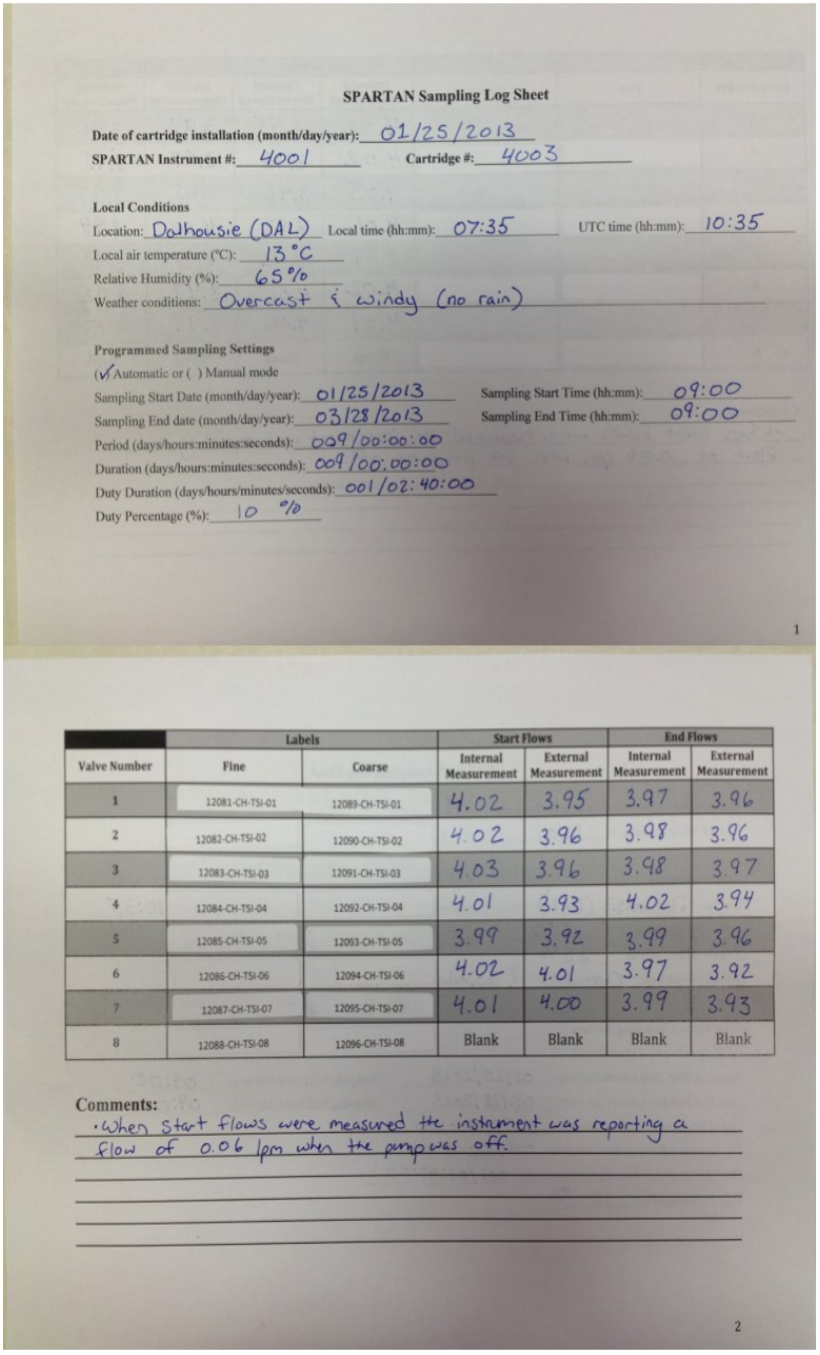

SPARTAN Sampling Log Sheet

Date of cartridge installation (month/day/year): 01/25/2013

SPARTAN Instrument #: 4001 Cartridge #: 4003

Local Conditions

Location: Dalhousie (DAL) Local time (hh:mm): 07:35 UTC time (hh:mm): 10:35

Local air temperature (°C): 13°C

Relative Humidity (%): 65%

Weather conditions: Overcast & windy (no rain)

Programmed Sampling Settings

(✓) Automatic or ( ) Manual mode

Sampling Start Date (month/day/year): 01/25/2013 Sampling Start Time (hh:mm): 09:00

Sampling End date (month/day/year): 03/28/2013 Sampling End Time (hh:mm): 09:00

Period (days/hours:minutes:seconds): 009/00:00:00

Duration (days/hours:minutes:seconds): 009/00:00:00

Duty Duration (days/hours/minutes/seconds): 001/02:40:00

Duty Percentage (%): 10 %

1

	Labels		Start Flows		End Flows	
Valve Number	Fine	Coarse	Internal Measurement	External Measurement	Internal Measurement	External Measurement
1	12081-CH-TSI-01	12089-CH-TSI-01	4.02	3.95	3.97	3.96
2	12082-CH-TSI-02	12090-CH-TSI-02	4.02	3.96	3.98	3.96
3	12083-CH-TSI-03	12091-CH-TSI-03	4.03	3.96	3.98	3.97
4	12084-CH-TSI-04	12092-CH-TSI-04	4.01	3.93	4.02	3.94
5	12085-CH-TSI-05	12093-CH-TSI-05	3.99	3.92	3.99	3.96
6	12086-CH-TSI-06	12094-CH-TSI-06	4.02	4.01	3.97	3.92
7	12087-CH-TSI-07	12095-CH-TSI-07	4.01	4.00	3.99	3.93
8	12088-CH-TSI-08	12096-CH-TSI-08	Blank	Blank	Blank	Blank

Comments:

- When start flows were measured the instrument was reporting a flow of 0.06 lpm when the pump was off.

2

Figure B.4. Properly completed SPARTAN sampling log sheet.

After the date of receiving the cartridge is recorded in the SPARTAN shipping and receiving log, the cartridge is transported to the chemical analysis lab on Dalhousie's Sexton campus to be disassembled.

Figure B.5. Foreground: a disassembled SPARTAN cartridge showing the two top 2x2 blocks as well as the bottom 2x8 block.

Once received, the cartridge is taken to Sexton campus to room N310, where all chemical analysis is completed. There you will find a drawer labeled “IN FIELD”, which contains filter petri dishes labeled [Site Code]-[Cartridge #] (e.g. INKA-004). Individual filters are then labeled, e.g. 13161-INKA-1T. All filters from a given cartridge are grouped and transported together.

Disassemble and unload the cartridge in the HEPA-filtered hood, being sure to turn off the blower. Leaving the blower on often results in filters blowing out of the clean environment onto an unclean surface where contamination renders them unusable for chemical analysis. First place a fresh large Kim-wipe in the HEPA hood before disassembling to provide a guaranteed clean working area. The tools needed for cartridge disassembly are the same as those for cartridge assembly, described in section B2.1. Remove all 8 screws with hex key. Separate cartridge halves by flipping over the two 2x2 top halves containing the PTFE filters. Wipe tweezers with methanol and proceed to place filters in the appropriately labeled petri-dishes being sure to only grab the edge of

the filters. Teflon filters (opaque white) go in dishes labeled 1T, 2T,…, 8T, corresponding to the slots they were placed in the cartridge. Nuclepore filters (translucent, very delicate) go in dishes labeled 1N, 2N,…, 8N. NB: If any anomalies are observed, a photo of the filter in the petri-dish (so that the filter label is apparent) should be taken and sent to a SPARTAN site manager.

When cartridge disassembly is complete, the filters are transported (inside three sealed plastic bags) to the HERC clean room facility where post-weighing and black carbon analysis are completed. Refer to section B1.0 for the filter weighing procedure and section B3.0 for the BC analysis procedure.

B2.4 Converting Mass Measurements to Mass Concentrations

Each cartridge has its own digital "Cartridge Analysis" Excel spreadsheet like that shown below in Figure B.6. The average $PM_{2.5}$ mass concentrations for each sampling site are reported in Tables 3.2 and 4.4.

CHTS-018 Analysis

Duty Minutes 24

PM2.5 Sampling Date Range	Filter ID	PM mass (ug)	PM Error	Average Flow (lpm)	Volume (m3)	PM2.5 (ug/m3)	Error
03/01/2016 - 03/10/2016	13273-CHTS-1T	69.97	2.14	3.95	0.853	**82.01**	8.57
03/10/2016 - 03/19/2016	13274-CHTS-2T	76.93	0.44	3.59	0.776	**99.09**	9.93
03/19/2016 - 03/28/2016	13275-CHTS-3T	37.70	1.08	3.50	0.756	**49.89**	5.19
03/28/2016 - 04/06/2016	13276-CHTS-4T	45.97	1.99	3.65	0.788	**58.31**	6.35
04/06/2016 - 04/15/2016	13277-CHTS-5T	64.83	1.34	4.00	0.864	**75.04**	7.66
04/15/2016 - 04/24/2016	13278-CHTS-6T	36.53	1.37	4.00	0.864	**42.28**	4.52
04/24/2016 - 05/03/2016	13279-CHTS-7T	63.20	0.24	3.85	0.831	**76.06**	7.61
BLANK	13280-CHTS-8T	4.07	0.93	0.00	0.000		
					Average:	**68.95**	7.12

PMcoarse Sampling Date Range	Filter ID	PM mass (ug)	PM Error	Average Flow (lpm)	Volume (m3)	PMcoarse (ug/m3)	Error
03/01/2016 - 03/10/2016	13281-CHTS-1N	110.23	1.80	3.95	0.853	**129.21**	8.31
03/10/2016 - 03/19/2016	13282-CHTS-2N	88.20	1.95	3.59	0.776	**113.60**	10.15
03/19/2016 - 03/28/2016	13283-CHTS-3N	78.67	1.84	3.50	0.756	**104.10**	5.12
03/28/2016 - 04/06/2016	13284-CHTS-4N	74.13	3.09	3.65	0.788	**94.04**	6.32
04/06/2016 - 04/15/2016	13285-CHTS-5N	81.53	1.80	4.00	0.864	**94.37**	7.68
04/15/2016 - 04/24/2016	13286-CHTS-6N	60.97	1.76	4.00	0.864	**70.56**	4.40
04/24/2016 - 05/03/2016	13287-CHTS-7N	69.67	1.63	3.85	0.831	**83.84**	7.81
BLANK	13288-CHTS-8N	29.53	0.44	0.00	0.000		
					Average:	**100.98**	7.11

Figure B.6. Raw mass of collected PM (micrograms) combined with flow rates (lpm = liters per minute) and sampling time determine the mass concentration during each sampling period. Total volume sampled is provided in cubic meters (m^3).

Digital log sheets should follow the above template for standardization where:

- PM mass (μg) is the raw post-weighed mass from gravimetric analysis
- PM error is 1 standard deviation from the triplicate pre- and post-weighing:

$$\Delta PM_{tot} = \sqrt{(\Delta PM_{pre})^2 + (\Delta PM_{post})^2}$$

- Average flow is the mean of the pre- and post-measured external flow, and the error is estimated 10 % of the average measured flow rate
- Volume sampled is calculated as: (flow rate x time sampled) / 1000
- PM mass concentration is PM mass divided by the sampled volume; error is calculated as (PM = PM mass; v = volume):

$$\delta PM\ conc. = \sqrt{\left(\frac{\delta PM}{PM}\right)^2 + \left(\frac{\delta v}{v}\right)^2}$$

B3.0 Determining Equivalent Black Carbon

B3.1 General Information

After filter post-weighing is complete, equivalent black carbon (EBC), a surrogate of elemental carbon, is measured by incandescent light surface reflectance. All EBC analysis is completed in the HERC cleanroom facility using the Smoke Stain Reflectometer shown in Figure B7. Surface reflectance estimates actual BC content, which approximates elemental carbon concentrations (Petzold et al., 2013a). The average EBC concentrations for each sampling site are reported in Tables 3.2 and 4.4.

B3.2 Smoke Stain Reflectometer Measurement Procedure

1. Turn on the SSR

The power switch is located on the rear panel of the device. Upon turning the SSR on, the display will read "100" with no decimal place. The device is ready to use once the display begins showing numbers with a single decimal place as shown in Figure B.7.

Figure B.7. Smoke Stain Reflectometer, including display, cylindrical optical unit, circular mask, and calibration plate

2. Calibration of reflectometer optical unit

The SSR is required to be calibrated prior to every measurement session. The reflectometer optical unit is the large cylindrical device shown in Figure B.7. When the device is powered the light inside the reflectometer optical unit should be on. The circular mask is the flat circular portion shown in Figure B.7 between the optical unit can calibration plate, which fits around the bottom end of the reflectometer optical unit. Place the optical unit on top of the white portion of the calibration standard. The readout should be close to 100.0. Try to keep the small hole of the circular mask as centered and still as possible.

Leave the SSR on and centered over the white disk for 15 minutes to allow it to stabilize prior to calibration. After pushing the "CAL" button, the system displays 100.0. If after pressing "CAL" button the readout does not stabilize at 100, press "CAL" again. After the SSR stabilizes at 100 on the white portion of the calibration disk, move the optical unit over to the grey panel of the calibration unit. Once on the grey calibration panel, the SSR readout is required to be 36 ± 1.5. If the SSR does not give the required readout, repeat the calibration procedure on the white calibration panel. If after three attempts to calibrate the SSR the required readouts are not obtained, report the issue to a SPARTAN manager as it is likely the bulb in the optical unit needs to be replaced.

3. Sampled Teflon and Nuclepore filters

After the SSR has been calibrated, place a sampled Teflon filter at the center of the circular mask. If the filters are not centered the SSR will not display a consistent reading. All readings from sampled filters must be taken over the white calibration disk.

Finally, measure the reflectance R of each filter three times (non-consecutively) with the lights in the clean room turned off.

B4.0 Filter Analysis for Water-Soluble Ions

B4.1 General Information

Before completing the water-soluble ion filter extraction procedure, ensure that all filters are post-weighted and SSR analysis is completed since filter extraction is a destructive technique. Filters are cut in half with a ceramic blade prior to extraction; half of each filter is extracted for water-soluble ion analysis. The steps necessary to obtain anion and cation data by ion chromatography from sampled filters are outlined below. The average mass concentrations for major water-soluble ions from each sampling site are reported in Tables 3.2 and 4.4.

B4.2 Filter Extraction Procedure and Analysis for Water-Soluble Ions

B4.2.1 Cutting 25 mm Filters in Half

- There is a custom plastic filter holder that allows for an accurate 50-50 split of the filters.
- To use, place the filter in the center of the cutting board and place cover (with narrow slit) on top. Use the ceramic knife to cut the filter in half. The alignment of all parts of the filter holder is shown in Figure B.8.
- Carefully clean the knife and the surfaces touching the filter between each filter with methanol and Kim-wipe.

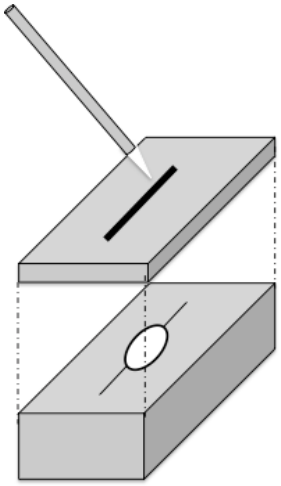

Figure B.8. Plastic filer holder alignment. Slit on the top half of the holder allows for cutting of the filter with a ceramic blade.

B4.2.2 Water-Soluble Ion Extraction Procedure

- Place one half of each filter in an appropriately labeled, clean and dry 20 mL vial. The 20 mL and 8 mL must be completely dried (air-dried, covered with a lint-free tissue wipe, such as a KimWipe, to prevent dust accumulation) before beginning this step.
- Ensure that the side of the filter that has collected sample is facing up.
- Add 120 μL of HPLC-grade isopropyl alcohol (IPA) directly on the filter.
- Add 2.9 mL of 18 MΩ·cm deionized water to the vial containing the filter and the added IPA
- Sonicate filter and 4% IPA solution for 30 minutes
- Use a clean 6 mL syringe to transfer the filter extract (~3 mL) from the 20 mL to an appropriately labelled 8 mL amber vial as shown by Figure B.9. A PTFE membrane filter head with pore size of 0.45-micron must be used on the syringe to complete the transfer to the amber vial to remove any particulates in solution.

- Filter extracts are stored in the lab fridge for IC analysis

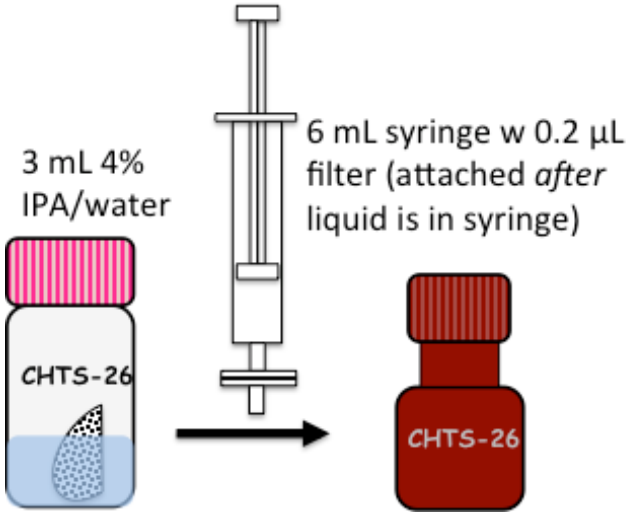

Figure B.9. Transfer of liquid extract from 20 mL pink vials to 8 mL amber vials. Amber vials are washed once with methanol, 3 times with water, and allowed to completely air-dry before use.

B4.2.3 Preparing Standard Ion Solutions and Eluent for Ion Chromatography

New standard ion solutions are prepared at the beginning of every week to use with each IC run completed within 7 days. Anion standards are made using Dionex Seven Anion Standard Solution (50 mL, Product # 056933). Cation standards are made using Dionex Six Cation-II Standard (50 mL, Product # 046070). The concentrations of the ions present in each standard solution are found in Table B.1.

Table B.1. Ions and corresponding concentrations (Conc.) in Dionex Standard Solutions. Reference ions used for standard labels are bolded.

Anion	Conc. (mg L^{-1})	Cation	Conc. (mg L^{-1})
F^-	20	Li^+	50
Cl^-	30	Na^+	200
NO_2^-	**100**	**NH_4^+**	**250**
Br^-	100	K^+	500
NO_3^-	100	Mg^{2+}	250
PO_4^-	150	Ca^{2+}	500
SO_4^{2-}	150	-	-

Most of the standards are prepared using a two-step dilution. For this, the volume indicated in Table B.2 and Table B.3 is transferred to a volumetric flask using a

micropipette and then diluted to the mark with 18 MΩ·cm deionized water. Next, the solution is transferred to a clean and dry 50 mL vial for storage throughout the week. The lowest concentration standards in Table B.2 and Table B.3 (STD 0.1 and lower) are prepared by serial dilution from STD 0.5. The standard stock solutions are stored in a drawer at room temperature, away from direct sources of light. The standard solutions are only to be used up to the expiry date indicated on the bottle, provided by the manufacturer.

Table B.2. Method of preparation summary for anion standard solutions.

Standard Label	Reference ion Concentration	Method of preparation
STD 1.5	1.5 mg L^{-1}	375 µL anion sol^n in 25 mL flask
STD 1.0	1.0 mg L^{-1}	250 µL anion sol^n in 25 mL flask
STD 0.75	0.75 mg L^{-1}	188 µL anion sol^n in 25 mL flask
STD 0.5	0.5 mg L^{-1}	125 µL anion sol^n in 25 mL flask
STD 0.25	0.25 mg L^{-1}	63 µL anion sol^n in 25 mL flask
STD 0.1	0.1 mg L^{-1}	2.00 mL of STD 0.5 in **10 mL** flask
STD 0.05	0.05 mg L^{-1}	1.00 mL of STD 0.5 in **10 mL** flask

Table B.3. Method of preparation summary for cation standard solutions.

Standard Label	Reference ion Concentration	Method of preparation
STD 2.0	2.0 mg L^{-1}	200 µL cation sol^n in 25 mL flask
STD 1.5	1.5 mg L^{-1}	150 µL cation sol^n in 25 mL flask
STD 1.0	1.0 mg L^{-1}	100 µL cation sol^n in 25 mL flask
STD 0.75	0.75 mg L^{-1}	75 µL cation sol^n in 25 mL flask
STD 0.5	0.5 mg L^{-1}	50 µL cation sol^n in 25 mL flask
STD 0.25	0.25 mg L^{-1}	25 µL cation sol^n in 25 mL flask
STD 0.1	0.1 mg L^{-1}	2.00 mL of STD 0.5 in **10 mL** flask

New anion and cation eluents are made for each individual run using 18 MΩ·cm deionized water obtained on the same day.

The anion eluent is 4.5 mM sodium carbonate and 0.8 mM sodium bicarbonate. Use the 25 mM sodium carbonate (26.50 g Na_2CO_3 powder in 1L 18 MΩ·cm deionized water) and 25 mM sodium bicarbonate stock solution (21.00 g $NaHCO_3$ powder in 1L 18

MΩ·cm deionized water) to make 2 L of anion eluent for each run. To make anion eluent solution:

1. Add 36 mL of 0.25 mM sodium carbonate solution in 2 L volumetric flask
2. Add 6.4 mL of 0.25 mM sodium bicarbonate solution to the *same* 2 L volumetric flask as the sodium carbonate.
3. Fill to 2 L mark with 18 MΩ·cm deionized water.

The cation eluent is 20 mM methane sulfonic acid (MSA, >99% pure). To make cation eluent solution:

1. Add 1.31 mL of MSA to a 1 L volumetric flask using a micropipette
2. Fill to 1 L mark with 18 MΩ·cm deionized water.

B4.2.4 Preparing Filter Extracts for Anion and Cation Analysis

Following the multiple stages of processing these samples and careful preparation of standards and eluent, it is important to follow the steps below to prevent contamination and/or mixing up samples when transferring from 8 mL amber vials to the PolyVials (Thermo Scientific #079797) used in the IC auto samplers.

1. Label PolyVials with the same labels as those on the 8 mL amber vials to prevent confusion. It is best to line up samples in numerical order.
2. Use a pipette set at 500 μL and disposable 100 – 1000 μL pipette tips for transferring the samples to the PolyVials.

3. Transfer 500 μL, one sample at a time, from the 8 mL amber vials to the PolyVials using a new pipette tip for each sample. Be sure to dispose of the pipette tip immediately after pipetting the sample to avoid cross-contamination.
4. After pipetting the sample, place the cap on the PolyVial to avoid putting two samples in one PolyVial.
5. Repeat steps 1 – 4 for the standard solutions.

Along with the samples, each sequence contains a full set of standards (7 points for anions, 6 points for cations) for obtaining a calibration curve to relate the reported conductivity to ion concentration. Deionized water blanks are also included throughout each sequence. For anions, waters are included between every 4 vials that contain ions (standard or sample), however for cations a water is placed between every vial to prevent carryover.

Once all samples are prepared, the sample sequence is set up on the respective IC system, and the baseline from running eluent through the IC system is stable, the sequence can be started. A full anion and cation sequence each take approximately 21 hours to finish.

B4.2.5 Calculating Ion Masses for Ion Chromatography Results

Results from the IC systems are reported as the peak area (μS*min). The Chromeleon software installed on the IC systems use the peak areas and known ion concentrations from the standard solutions to create a calibration plot that is used to convert peak area to mass (μg) for all samples. The correlation coefficient for each ion must be > 0.95 for the calibration curve to be considered valid. For various reasons, the Chromeleon software that automatically selects peaks does not always select an

appropriate baseline for every sample and standard. To ensure the most accurate masses possible, all ion peaks are inspected by hand and modified before obtaining the output from IC. The extraction volume is combined with the calculated masses and the air volume sampled for the given filter, to provide mass concentrations in $\mu g\ m^{-3}$.

B5.0 ICP-MS Filter Extraction & Analysis

B5.1 General Information

As described in section B4.2.1, all filters are cut in half with a ceramic blade and one half is extracted for water-soluble ions while the other is extracted for trace element analysis. Here the steps necessary to extract filters for trace element analysis via inductive couple plasma – mass spectrometry (ICP-MS) by the Clean Water Lab on Dalhousie University's Sexton Campus are outlined.

B5.2 Filter Extraction Procedure for Trace Element Analysis

B5.2.1 Trace Element Extraction Procedure

1. The day before a planned extraction, obtain ICP-MS vials and caps from the Clean Water Lab. Cap the vials and rinse twice with approximately 5mL of 18 MΩ·cm deionized water.
2. Soak all vials overnight with 10% trace metal grade nitric acid (10 mL 18 MΩ·cm deionized water with 1 mL acid) at room temperature.
3. The next day properly dispose of acidified water and label vials.

4. Place a filter half directly into pre-washed 10 mL sample vial using methanol-wiped tweezers. For Teflon filters only, add 30 μL of IPA directly onto filter surface and allow ~ 10 seconds for IPA to absorb into filter.
5. Add 2.80 mL of 18 MΩ·cm deionized water followed by 250 μL of concentrated trace metal grade nitric acid to the vials. Note: Teflon filters tend to float above the liquid. Use the provided black, acid resistance plastic tweezers to push Teflon filters down against vial walls until fully submerged.
6. Place 50 mL plastic containers in heating block and add 30 mL of distilled water to each heating container.
7. Carefully place each vial in a plastic container with the blue cap loosely sitting on the vial to allow vapor to escape.
8. Place plastic reflux lids over each container. Distilled water will bathe the samples within the vials.
9. Turn on the heating block and set to heat at 97 °C for 2 hours. Total heating time in fume hood will take 2 hours and 20 minutes, allowing for approximately ~20 minutes for the heating black to warm-up.
10. After the heating time has elapsed, remove the extracts from the heating block and allow to cool to room temperature.
11. Once extracts are cooled, total volume will be below 3 mL mark. To ensure known volume is submitted for analysis, fill the sample vial to the 3 mL reference line.
12. Once all vials are filled to 3 mL mark, remove filters using acid-resistant black tweezers and submit for ICP-MS analysis in the Clean Water Lab.

Figure B.10 provides a summary and visual representation of the extraction procedure for trace elements.

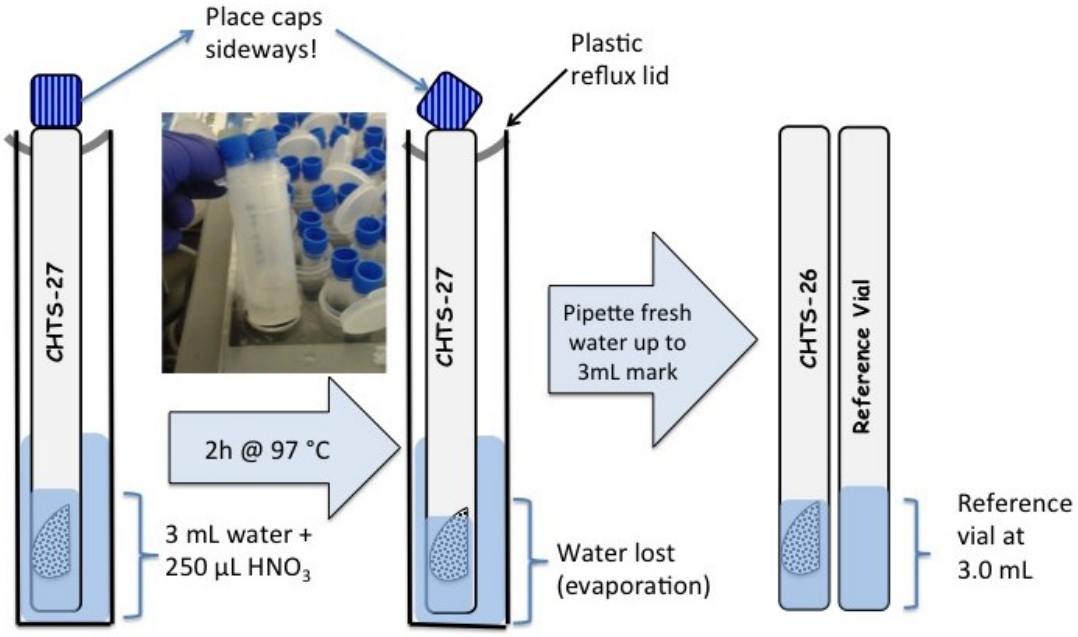

Figure B.10. Summary of trace metal extraction procedure and illustration of vial arrangement in the heating block.

B6.0 Nephelometer Data Quality Assurance and Quality Control

B6.1 Purpose and Applicability

This quality assurance/control procedure describes the practices for conducting nephelometer performance checks and calibrations. A set of performance checks are performed to check the state of the nephelometer under normal operating conditions, without special preparation or adjustment. These permit the Site Manger to determine if maintenance and/or repairs are necessary, if recalibration is warranted, or if adjustment to operation should be made. On-site calibrations are performed when nephelometers are

operating as expected, but to correct excess baseline drift in scattering measurements and to prolong the normal, on-site operation of the nephelometer. As material is accumulated on the walls of the nephelometer tube, cleaning of the nephelometer tube becomes necessary. When this point is reached, the nephelometer is sent to the SPARTAN Central Lab at Dalhousie University for maintenance, cleaning, and recalibration before being returned to the site. The ultimate aim of this protocol is to ensure the integrity of the SPARTAN scattering data and assess the data for accuracy.

B6.2 Nephelometer Performance Checks

B6.2.1 Responsibilities

Frequency: Every 2 months coinciding with on-site cartridge change and/or reported issue or event by Site Operator

Responsibility of: SPARTAN Site Manager

Responsibilities include:

- Coordinate with site operator to receive nephelometer data on a regular basis (at least monthly).
- Process raw nephelometer data to look at markers for performance checks (see Section B6.2.2 Parameters for Performance Checks)
- Direct appropriate corrective action if indicated by performance checks.
- Review and identify flagging of data due to failed performance check.
- Document performance check result in the site-specific log
- Assess timeline for on-site calibration and central lab calibration/cleaning

B6.2.2 Parameters for Performance Checks

There are a number of variables that are recorded by the nephelometer that are used in calculating scatter. Therefore, it is necessary to assess the stability of the sensors used to measure these variables. This is done by creating times series plots of all relevant variables and checking data as outlined below.

- The variance in reference sensor signals should not be more than 10%.
- Dark PMT values should be significantly lower than PMT measurements at all three wavelengths for both forward and backward. The value and magnitude of the PMT signal is specific for each nephelometer, however and example is shown below in Figure B.11.

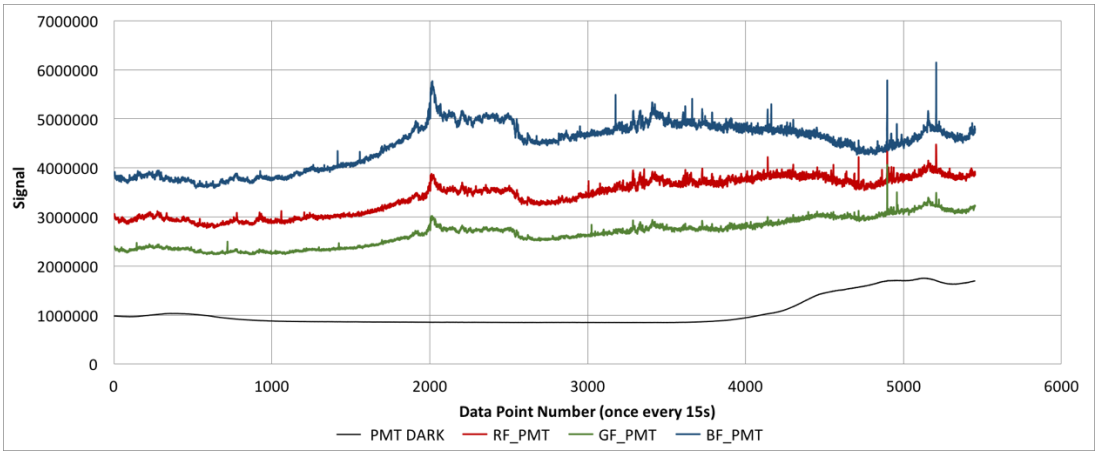

Figure B.11: Dark PMT signal (PMT DARK) compared to the forward PMT signal at each wavelength

- Check that the following is true in scatter measurements: red > green > blue
- Dark reference sensor values are significantly lower than reference measurements at all wavelengths. Similar to PMT signals, reference

sensor signals vary between nephelometers. An example is shown below in Figure B.12.

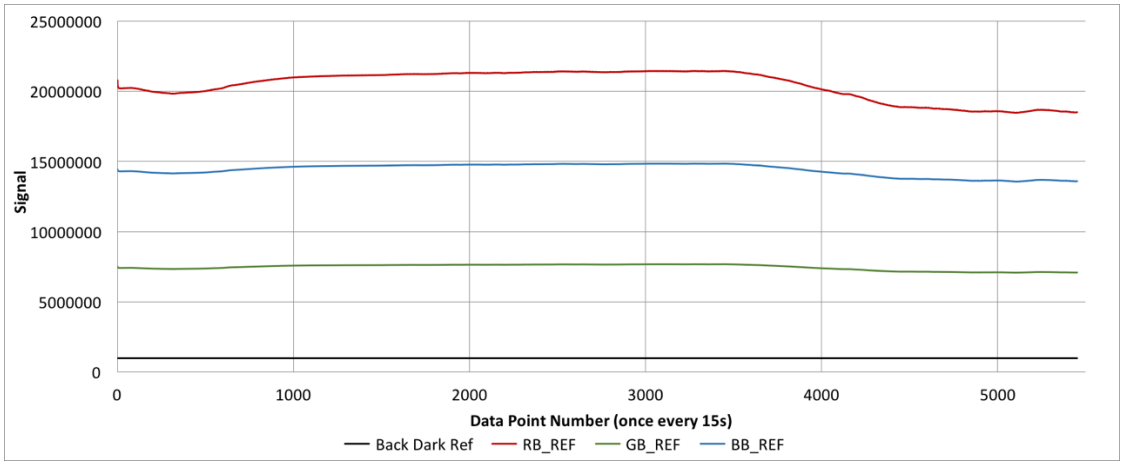

Figure B.12: Back scatter dark reference signal compared to back scatter reference signal at each wavelength

- Time series plots of temperature, RH, and pressure should be compared to that of the dark reference sensor measurements. Ambient conditions should not show a similar signal/pattern to the dark reference measurement.

B6.3 Nephelometer Calibration

Nephelometer calibration is fundamental to obtaining accurate scatter data. Whenever a calibration is performed, it is compared to the previous calibration conducted at Dalhousie University to evaluate the validity of the performed calibration. The step-by-step instructions for calibrating the nephelometer are found below in section B6.3.3.

B6.3.1 Determining Calibration Frequency

Nephelometers sample continuously at a flow rate of approximately 3.4 lpm and as a result are prone to accumulation of dirt inside the nephelometer tube where scatter measurements are made. When possible on-site calibrations are performed to maintain

and assess the condition of the nephelometer and correct for accumulation of dirt inside the nephelometer, even when a clean air reference system (CR) is installed at the site. However, over time the amassing of dirt inside the nephelometer will be too much for on-site calibrations and the nephelometer will require detailed maintenance, cleaning, and calibration at the SPARTAN Central Lab at Dalhousie University.

Determining the frequency of on-site and central lab calibrations is an ongoing process. It is the responsibility of the Site Manager to continually assess the need for calibration during performance checks. There are various metrics that are used to determine the frequency of nephelometer recalibration but generally,

- **On-site calibrations** are recommended when the baseline drift reaches 15 % of the average total green scatter ($< B_{sp,532} >$) at the site.
- **When on-site calibrations are not possible, detailed cleaning and calibration** are required when the baseline drift reaches 30 % of $< B_{sp,532} >$ at the site.
    - **If on-site calibrations are possible**, detailed cleaning and recalibration will be conducted after 2 on-site calibrations have been performed. Therefore, three consecutive on-site recalibrations should not be performed, rather when the third is due the nephelometer will be returned to the SPARTAN Central Lab.

Every SPARTAN site operates with a clean air reference system that is programmed to perform a clean air reference (for baseline drift correction) once every 24 hours. Therefore, the correction values calculated from clean air reference periods are used to determine the magnitude of baseline drift. For sites where the clean air reference is not

automatically applied to the scatter measurements the baseline drift can also be determined by inspection of the baseline in the $B_{sp,532}$ time series.

B6.3.2 Required Equipment

There is a minimal amount of equipment required for the calibration of a nephelometer, whether on-site or at the central SPARTAN Lab at Dalhousie University. The following two gases (> 99% purity) are required for every nephelometer calibration:

- N_2 or clean air (Clean Air Reference system can be used as clean air source) cylinder.
- CO_2 cylinder

Additional equipment required:

- Regulator for gas cylinders
- Clean plastic tubing
- Inlet for gases to run into nephelometer
- AirPhoton program for determining calibration configuration variables (NephCal1.1.htm)

B6.3.3 Calibration Procedure

Whether a calibration is conducted on-site or at the central SPARTAN lab at Dalhousie University, the procedure is the same with the exception of sections ***in bold italic font*** as a few extra steps are required for on-site calibrations. The steps to be taken are as follows:

1. Transfer any data on the nephelometer memory card to a computer ***for transfer to the Site Manager***.

2. Disconnect fan from Clean Air Reference (CR) system
3. Turn CR system ON in MANUAL mode and let run for 10 minutes
4. Turn off CR system, but leave the nephelometer ON
    - The scatter from the clean air and CO_2 need to be in the same file for processing.
5. Connect CO_2 to nephelometer and let run for 10 minutes
6. Turn OFF nephelometer
7. Remove nephelometer memory card and transfer file with CR and CO_2 to computer.
    - Scatter from N_2, or clean air, and CO_2 are compared to the scatter values from the previous calibration to guarantee consistency. ***On-site exception: the site operator will send the data file to the site manager to assessment.***
8. Open NephCal1.1.htm and load in data file
9. Get configuration numbers from NephCal program and transfer to config.txt file. ***On-site exception: site manager will send the new config.txt file to the site operator via email.***
    - Set CR values to zero in the config.txt file.
10. Insert the memory card back into the nephelometer.
11. Turn the nephelometer ON and wait 10 seconds for the nephelometer to set the new calibration values
12. Turn the nephelometer OFF and remove the memory card to confirm that the config.txt file is no longer on the card.

13. Create a new config.txt file to dump the configuration information on the nephelometer
    - In a blank config.txt file use the following command: DUMP=1. ***On-site exception: site manager will send this config.txt file to the site operator.***
    - Save the new config.txt file to the memory card and reinsert in the nephelometer.
    - Turn the nephelometer ON and wait 10 seconds for the nephelometer to take the new config.txt file
    - Turn the nephelometer OFF and remove the memory card
    - Copy the resulting DUMP.txt file on the memory card to your local device for saving in the SPARTAN nephelometer database
14. Return the nephelometer to normal operation

B6.3.4 On-site Calibration

The ability to conduct on-site calibrations are an ideality, many SPARTAN sites do not have easy access to the gases required for calibration of the nephelometer. In the case that a site does have a clean air reference system and easy access to CO_2 (and N_2 if no clean air reference system), then on-site calibrations will be conducted. The frequency of on-site calibrations are site-specific and are scheduled as determined by the protocol described in section B6.3.1 Determining Calibration Frequency.

B6.3.5 Cleaning and Calibration at SPARTAN Central Lab at Dalhousie University

Upon receiving the nephelometer from the site, a physical condition check of the outer nephelometer body needs to be conducted and all information recorded in a SPARTAN Service Report (see B6.4 SPARTAN Service Report). After external physical

check is complete the cleaning of the nephelometer tube is to be completed. This requires removing the nephelometer tube from the body. Supplies required for removing the tube from the body and cleaning the nephelometer tube are:

1. Clean cloth
2. Lint-free tissues (e.g. Kim-wipes)
3. Methanol
4. Water
5. Hex-keys
6. Screwdriver
7. Wrench

After cleaning of the nephelometer tube is complete, any remaining dust or lint needs to be blown away using compressed air. Once this is completed the nephelometer is reassembled and the calibration is completed following the steps outlined in section B6.3.3 Calibration Procedure

B6.4 SPARTAN Service Report

Figure B.13 shows the blank SPARTAN Service Report. The SPARTAN Service Report is an easy way for team members to record the condition of a nephelometer upon arrival and if necessary, steps taken to return the nephelometer to normal operation before return to the site. When the nephelometer tube is removed from the body of the instrument for cleaning and/or inspection, it is required that photos be taken and the condition be recorded in the service report. If the actions required to return the nephelometer to normal operation cannot be completed at Dalhousie University, the nephelometer is shipped to the manufacturer, AirPhoton LLC, where an initial

description of the state of the nephelometer is appreciated and allows for faster repair. It is important to keep accurate records of the history of every nephelometer, therefore it is necessary to fill out a SPARTAN Service Report for every nephelometer that enters the lab even if minimal work is performed.

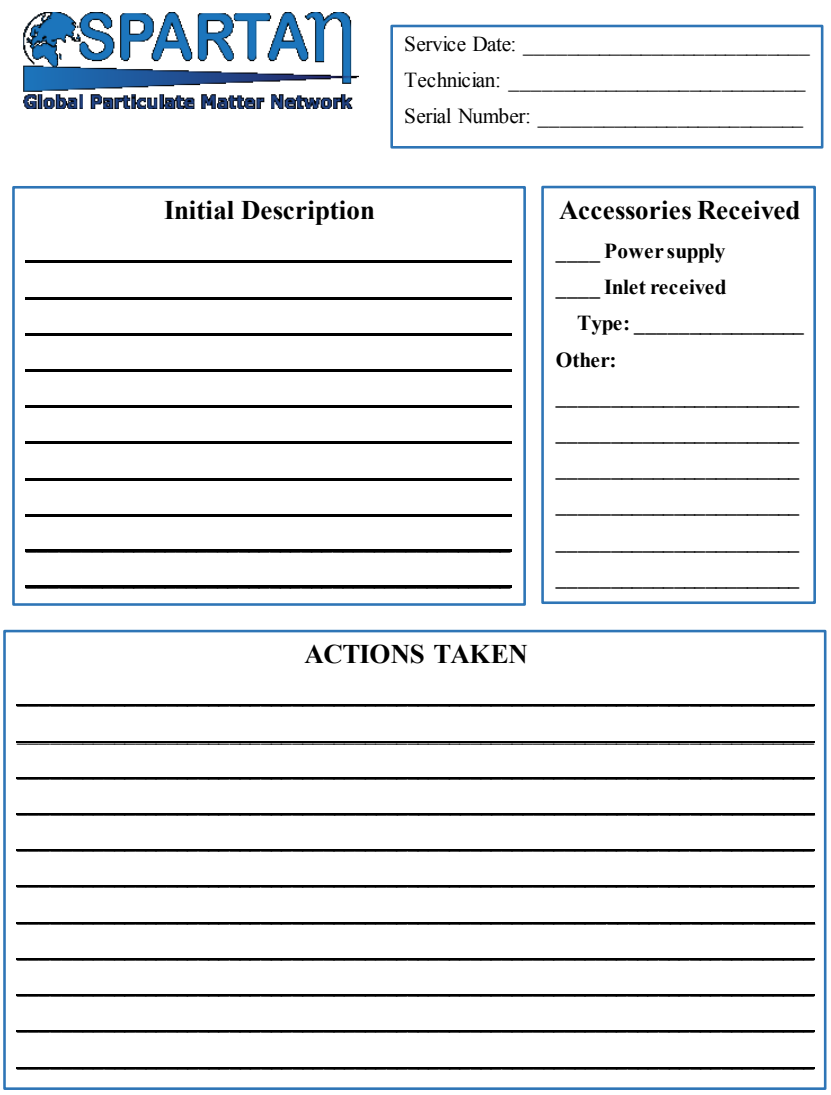
SPARTAN
Global Particulate Matter Network

Service Date: _____
Technician: _____
Serial Number: _____

Initial Description

Accessories Received

____ Power supply
____ Inlet received
Type: _____
Other:

ACTIONS TAKEN

Figure B.13: Blank SPARTAN Service Report to be completed upon receiving a nephelometer from the field

B7.0 AERONET sunphotometer data

B7.1 General Information

This section provides a brief explanation of AERONET aerosol optical depth data obtained from: https://aeronet.gsfc.nasa.gov/cgi-bin/webtool_opera_v2_new. For more detailed information on AERONET data please see: http://aeronet.gsfc.nasa.gov/new_web/data_description_AOD_V2.html

B7.2 Data Description

All SPARTAN analysis is completed using level 2.0 data when available, otherwise level 1.5 can be used. A description of the main difference between level 1.0, 1.5 and 2.0 data are shown in Table B.4. Data are downloaded for full years, even though the files may not be complete. All-point spectral deconvolution algorithm data are used. AOD at 550 nm is inferred from AOD retrieved at 500 nm and 675 nm using the angstrom exponent. All-point data are averaged into hourly means, and then into averages during satellite-overpass times (10:00 – 12:00 and 13:00 – 15:00 local time).

Table B.4. AERONET data description

Level	AERONET Quality- Assured?	Description
1.0	No	Unscreened and may not have final calibration applied
1.5	No	Automatically cloud cleared but may not have final calibration applied.
2.0	Yes	Pre- and post-field calibrated, automatically cloud cleared, and manually inspected.

B8.0 Site Selection, Installation, and Maintenance Procedures

B8.1 Purpose

The purpose of this Standard Operating procedure is to provide consistency for the selection and installation of all SPARTAN sampling sites. It will also provide instruction on the maintenance of the SPARTAN sampling site once installed.

B8.2 Site Selection

SPARTAN sites are to be collocated with CIMEL sunphotometers at existing AERONET sites when possible. However, the following variables must still be considered when selecting the specific location for the sampling station:

a. Representativeness of area-wide air quality
b. Security
c. Electrical Power

B8.2.1 Representative of Regional Air Quality

The site should be in a location that is representative of regional air quality. This means that the site should not be located within less than 2 km of a pollution point source that includes, but is not limited to, power plants and factories. As well, the site should not be within 500 meters of major roads/highways. Heavily used dirt roads that can produce dust unusual for the region should also be avoided.

The site should be at least 5 meters away from other structures or surfaces such that airflow is unimpeded from all directions. The top of such structures within 100 meters should not have any more than a 30º angle from the sampler inlet (see Figure B.14). Sites can be either located at ground level or on the rooftop of a building no more

than 5 stories (~15m) high. To remain representative, if a site is located on a rooftop it needs to be placed away from vents, cooling towers, and other ventilation equipment such as motors, and air intakes. Ultimately, the sampling stations are placed according to exposure to regional air quality.

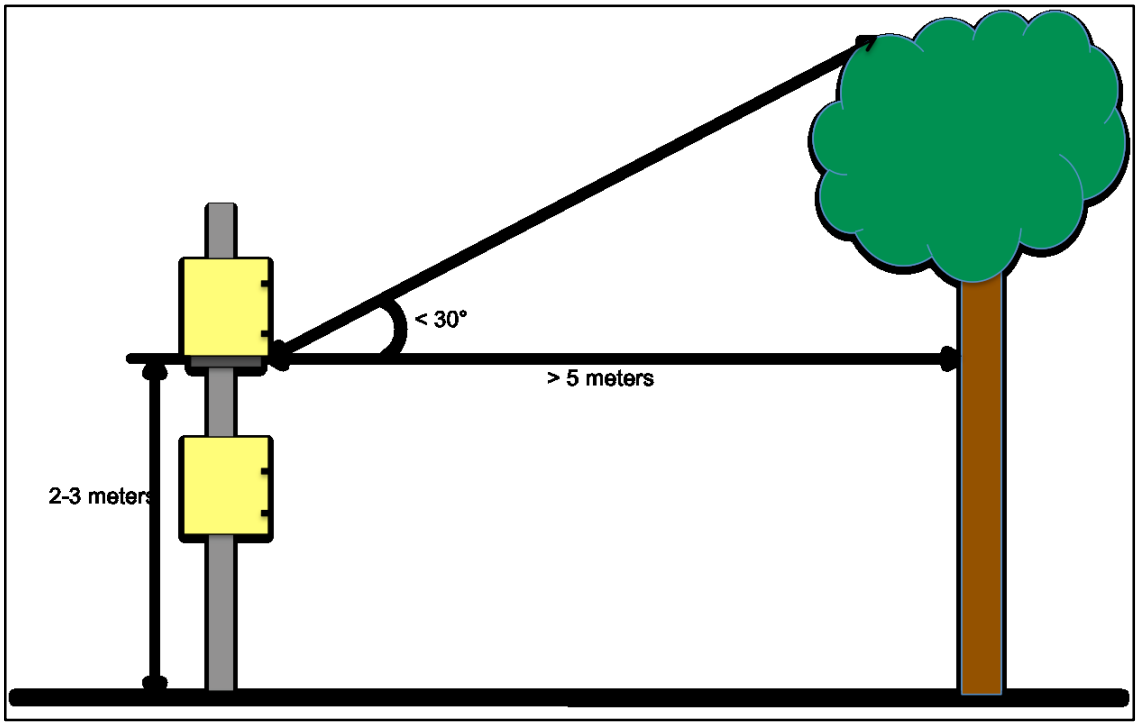

Figure B.14. Illustration of SPARTAN sampler set-up (tree is used as an example, this could be a wall or any other tall object).

B8.2.2 Security

It is critical that the sampling station is in a location such that unauthorized persons cannot get access to the instruments. If the sampling station is located next to an existing AERONET site security measures should have previously been implemented. If not, it is important to guarantee security before receiving the sampling instrumentation. This means that if the best location is found at ground level, appropriate security measures must be taken such as fencing, lights, etc. If the use of such security measures

is not feasible, the sampling station should be located on a low-rise rooftop that provides adequate security.

B8.2.3 Electrical Requirements

To guarantee that there is sufficient power at the site, there should be at least a 1.0 Amp, 220 (or 110) V line available on site. For sites where this is not possible, or are on intermittent power grids, it is necessary to have a back-up battery and solar panel available. For further information regarding the solar panel and battery backup please see section B8.4.3.

Note: these criteria are not absolute, a site location that falls slightly outside the criteria may be the best choice. Any significant variances from the criteria should be well documented and reviewed before site installation.

B8.3 Site Installation

The general approach employed is to minimize travel time as well as the cost of shipping equipment while increasing the efficiency of site installation. Therefore, it is important that the site is prepared for installation before the sampling equipment and site manager from Dalhousie is due to arrive.

B8.3.1 Equipment and Materials Required for Site Installation

- Pole 3 to 4 m in length and between 4 and 6 cm in diameter
- Extension cords (if necessary)
- Weather/radiation shield that is silver or white in color with dimensions of at least 6 cm deep x 8 cm wide x 14 cm long, such as an aluminum cover (or plastic container) shown in Figure B.15.

B8.3.2 Pre-Installation Activities

- Arrange appropriate site security if not already done so
- Ensure that electrical requirements of the site have been met
- Obtain supplies listed above
- Pole required for mounting the samplers must be secured and therefore should be stable to avoid vibration and shifting after installation. It should also be able to withstand extreme weather events.

B8.3.3 Instrumentation Checklist

Upon receiving SPARTAN instrumentation, it is important to make sure you have received all parts and accessories needed to proceed with installation of the sampling station. If you are missing any of the items on the following list, please contact the appropriate site manager at Dalhousie University.

- Sampling case 1 (electronics)
- Sampling case 2
- Sampling station pump and corresponding case (attached to the bottom of control box case)
- Nephelometer
- 3 pre-loaded cartridges
- External flow adapter
- External rotameter and tubing
- Vacuum grease
- 3 log sheets (one per cartridge)

- Kim-wipes (small)
- Power cables

B8.3.4 Installation of Filter-Based Sampler to Support Structure

The sampling case that contains the 8 sampling inlets must be positioned at least 2 meters above ground height. Even if the site is located on a rooftop the height requirement of 2 meters from the roof surface needs to be observed. This allows for proper mixing of air and reduces sampling of emissions directly from the roof/ground. Please refer back to Figure B.14 for an illustration.

The sampler has a metal bar attached to the back of each case; use this to attach the sampler to the pre-assembled pole with the provided hose clamps as shown in Figure B.16. It may also be effective to use a durable strap (e.g. cloth or zip-tie) to provide extra support for the sampler. Utilization of the strap may be especially important if a pole of appropriate diameter (Section B8.3.1) was unable to be located. After the samplers are secure attach the weather/radiation shields. Figure B.15 shows an example of the final set-up of the SPARTAN filter-based sampler.

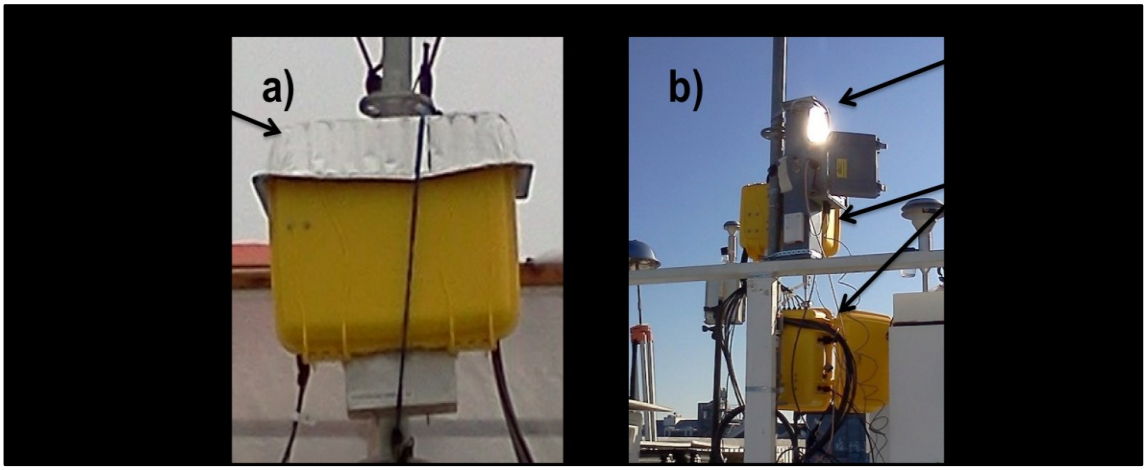

Figure B.15. a) Example of weather/radiation shield installed on the filter sampler, and b) Positioning of the filter sampler and nephelometer on the same pole.

B8.3.5 Installation of the Nephelometer to the Support Structure

The same height restrictions apply to the nephelometer as that for the filter-based sampling cases. The nephelometer can be bolted to a wooden platform or also attached to a pole using the provided hose clamps. It is important that the inlet and outlet are situated such that they cannot be blocked in the case of a snow, sand, or water. The nephelometer can be attached to the same pole as the filter-based sampler, however, it is important to ensure that the nephelometer outlet is situated away from the inlet valves of the filter-based sampler and vice versa. Please refer to Figure B.15 for an example illustration of the final set up of the SPARTAN filter-based sampler and nephelometer.

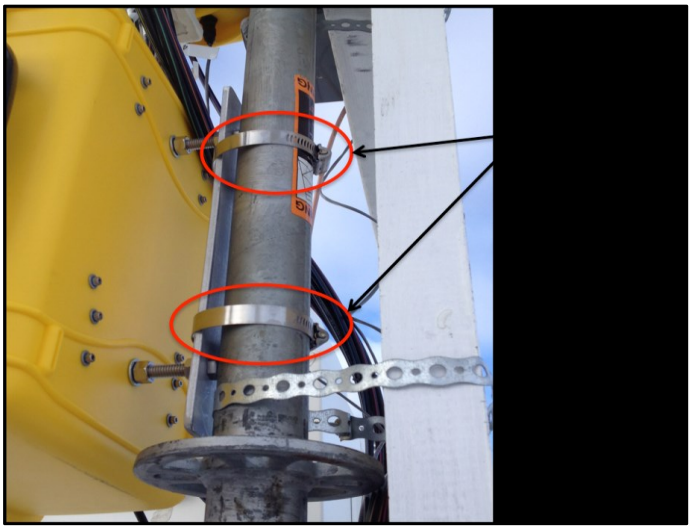

Figure B.16. Example of using the metal bar on the back of the sampler cases to attach to a preassembled pole using the provided hose clamps.

B8.4 Sampling Procedure

The filter cartridge to be inserted in the filter-based sampling case contains 8 filter slots, each of which contains a combination of a coarse particle Nuclepore filter and a fine particle Teflon filter. The first 7 of 8 filter combinations are sampled, and the 8th is a field blank.

At sites with an ambient coarse particulate matter (PM_{coarse}) concentration **less than 28 µg/m^3** each sampled filter combination actively samples for a total of 24 hours starting at 09:00 hours local time and with the following duty cycle:

- Day 1: 09:00 – 12:00 (e.g. July 1)
- Day 2: 12:00 – 15:00 (July 2)
- Day 3: 15:00 – 18:00 (July 3)
- Day 4: 18:00 – 21:00 (July 4)
- Day 5: 21:00 – 00:00 (July 5)
- Day 6: 00:00 – 00:00 (**July 6**)
- Day 7: 00:00 – 03:00 (**July 7**)
- Day 8: 03:00 – 06:00 (July 8)
- Day 9: 06:00 – 09:00 (July 9)

At sites with an ambient PM_{coarse} concentration **greater than 28 µg/m^3** a duty cycle framework will be used. This means that instead of sampling the full 3 hours the sampler will run for a fraction of this time that is calculated specifically for each site to avoid filter clogging. The fraction of time sampled within the framework stated above is inversely proportional to the mean annual $PM_{2.5}$ concentration at each site. In general, the number of minutes sampled within the framework (maximum being 160 minutes, minimum being 16 minutes) is calculated using Equation B1:

$$\%\ \text{Duty} \approx \begin{cases} 100\% & \langle PM_{coarse} \rangle \leq 28\ \mu g\ m^{-3} \\ \frac{160\ \mu g}{[\langle PM_{coarse} \rangle + 2\sigma] \cdot V_{samp}} \cdot 100\% & \langle PM_{coarse} \rangle > 28\ \mu g\ m^{-3} \end{cases} \quad \text{(B1)}$$

where $<PM_{coarse}> + 2\sigma$ is the upper limit coarse aerosol concentration for 95% of the 9-day sampling periods and V_{samp} is the volume of air passing through the filter in 24 hours (5.76 m^3 for 24 hours at 4 lpm).

After the number of minutes to be sampled is calculated, the appropriate duty cycle to be programmed into the instrument will be provided to each site upon start-up. Given the 9-day sampling procedure, each cartridge can remain and operate unattended in the field for a total of 63 days. The collocated nephelometer will remain in the field along with the filter-based sampler and sample for 24 hours a day, 7 days a week. For further information on programming the SPARTAN filter-based sampler and nephelometer please see sections B8.4.1 and B8.4.2, respectively.

Note: The % duty can be modified at any time if it is found that it is either too strict or too relaxed for the sampling sites. Site operators will be notified if a change is necessary.

B8.4.1 Programming the SPARTAN Filter-Based Sampler

Upon receiving and setting up the instrument it is important that the instruments are programmed correctly with local date/time, etc. To begin this programming please enter the "Menu" and select "Next" until the "System Settings" screen is displayed; press "Go". The time to be programmed is local date/time and is on a 24-hour clock.

After successfully programming the instrument with local settings, proceed with programming the sampling procedure (outlined by Dalhousie University site managers as this can vary from site to site). A quick description of the elements that contribute to programming the sampling procedure are listed below:

1. **Start Time** – local time when sampling will begin.

Note: Sampling will start the next time this hour occurs (e.g. If it is currently 13:00 on July 22 and the sampler is programmed to start at 09:00, it will start sampling at 09:00 on July 23. However, if it is 08:00 on July 22, the sampler will start at 09:00 on July 22)

2. **Period** – amount of time a particular filter will be used. At the beginning of each new period, a new filter will start sampling; this proceeds progressively from filter 1 through 7.
3. **Duration** – within a given period, the duration determines how long each filter will actively be sampled on (must be equal to or less than the Period).
4. **Duty Duration** – determines the duty cycle duration. For example, if the duty duration is set at one hour, the system will be 'on' for the **duty percentage** of time during that one hour and 'off' for the remainder of that hour.
5. **Duty Period** – percentage of time that the system is 'on' during the duty duration (must be equal to or less than Duty Duration).
6. **Short Duration** – duration within the duty duration
7. **Short Period** – period within the short duration

The following information is to be used specifically for sampling with the duty cycle stated in section B8.4 for sites with an ambient PM_{coarse} concentration **of 28 µg/m^3 or less**. The information below is to be programmed into the sampler exactly as shown below.

Start Time: 09:00

Period: 09/00:00:00 (9 days)

Duration: 09/00:00:00 (9 days)

Duty Period: 001/03:00:00 (1 day, 3 hours)

Duty Duration: 000/03:00:00 *

Short Period: 000/00:00:00

Short Duration: 000/00:00:00

For sites with an ambient PM_{coarse} concentration **greater than 28 µg/m^3** the start time, period, duration, duty period, and short period all remain the same as shown above. **The only element of the programmed information that changes is the duty duration.** Upon installation of a new site, the duty duration and short duration to be programed in the sampler will be provided by the SPARTAN site manager. Given that no problems arise, each cartridge will remain in the field for 63 days.

B8.4.2 Programming the SPARTAN Nephelometer

To start the nephelometer, flip the switch inside the attached case to the 'ON' position. Once the nephelometer is started it will run continuously and record both forward and back scattering data every 15 seconds for the following wavelengths: 455 nm (blue), 530 nm (green), and 630 nm (red). To stop sampling, simply flip the switch inside the attached case to the 'OFF' position.

B8.4.3 Solar Panel and Battery

For areas on an intermittent power grid or with no available power, a backup battery and solar panel (for charging) are essential for operation. The sampling station will run on AC power as long as it is available. If AC shuts off the sampler will automatically change to battery power given that it is connected and switched ON. There

is no specific programming necessary when the sampler is hooked up to battery power, only simple variations using the ON/OFF switches in the electronics case.

1. No battery/solar panel: “AC Mains” switch should be in the ‘ON’ position and the “Battery” switch in the ‘OFF’ position.
2. No available AC power: “AC Mains” switch should be in the ‘OFF’ position and the “Battery” switch in the ‘ON’ position.
3. AC available with battery backup: both switches need to be in the ‘ON’ position.

If your site requires battery backup further instruction regarding obtaining and installing the battery and solar panel will be provided.

B8.5 Installing and Changing Filter Cartridges

As stated in Section B8.4.1, each cartridge can remain in the field for 63 days, after such time the full cartridge will need to be replaced with a new one before the scheduled start time. Cleaning and greasing the impactor plates, as well as measuring start/end flows, are important factors in sampling. Instruction on how to clean and grease the impactor plates is outlined in section B8.5.1. Instruction on how to measure the start and end flows is outlined in section B8.5.2.

To install new cartridges (skip to step 6 for first cartridge install) or replace full cartridges, please follow the procedure outlined below:

1. Before removing the full cartridge, it is important to measure the end flows of each valve and record the values on the log sheet received with the cartridge.

2. After taking the end flows, clean and grease the impactor plates of all 8 valves.
3. Lift the two red clamps on either side of the cartridge slot and remove the full cartridge.
4. Place the full cartridge inside 3 sealed plastic bags and write “SAMPLED’ using a permanent marker on the outermost bag.
5. Remove the memory card for the full cartridge and place inside the bag containing the cartridge
6. Place the new cartridge in the cartridge slot under the valve inlets, making sure that the gaskets on either side are not impeding flow and are creating a seal.
7. Secure the cartridge into place by pushing the two red clamps on either side of the cartridge down tightly (Figure B.17).
8. Insert the memory card for the new cartridge in the memory card slot. Make sure that the cartridge and memory card numbers are the same (e.g. 5001). It is important to insert the memory cards while the sampling station is OFF.
9. Double check that the sampling settings are the same as those outlined in Section B8.4.1. Also double-check that the impactor plates have a thin layer of fresh grease.
10. Fill out the first page of log sheet for the new cartridge.
11. Measure the start flows for the new cartridge (adjust the external flow to 4.0 +/- 0.2 lpm using the flow control knob but adjust **valve 1 only**; however all valves 1 through 8 must have the flow measured) and record on the second page of the log sheet.

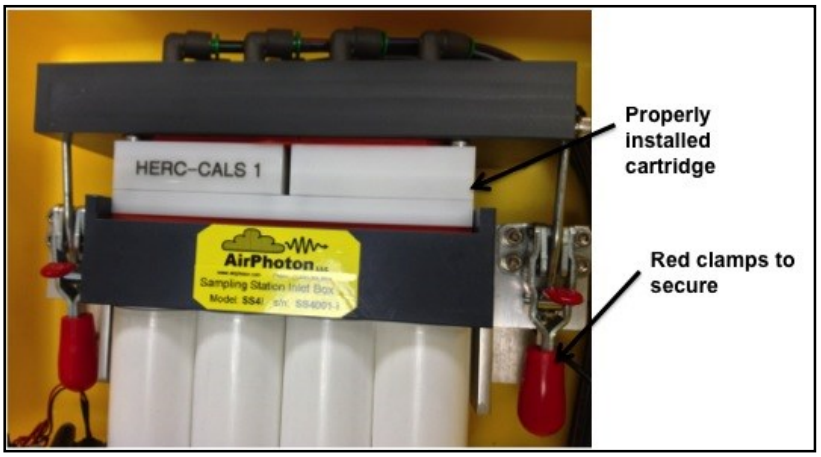

Figure B.17. Example of a properly installed cartridge.

B8.5.1 Cleaning and Greasing Impactor Plates

Every time the cartridge is changed, the impactor plates, shown in Figure 6a, need to be cleaned and re-greased. To clean the old grease off the impactor plates, shown in Figure B.18, use methanol if necessary (cold weather conditions) and a low-lint tissue wiper (e.g. Kim-wipe®) and simply wipe it off the plate. After the plates are clean, reapply a small amount of grease in a very thin layer. Make sure that there are no large deposits of grease, and that the grease is an even, uniform layer. Be sure that there is no grease on the walls of the valves.

B8.5.2 Measuring Flow Rates

Measuring the flow rates before and after sampling is a means of verifying the flow rates reported/recorded by the instrument. Figure B.18 shows how to properly install the flow adapter to measure external flow rates.

After inserting the new cartridge into the filter sampler, the start flows need to be measured and recorded on the log sheet as shown in Figure B.4.

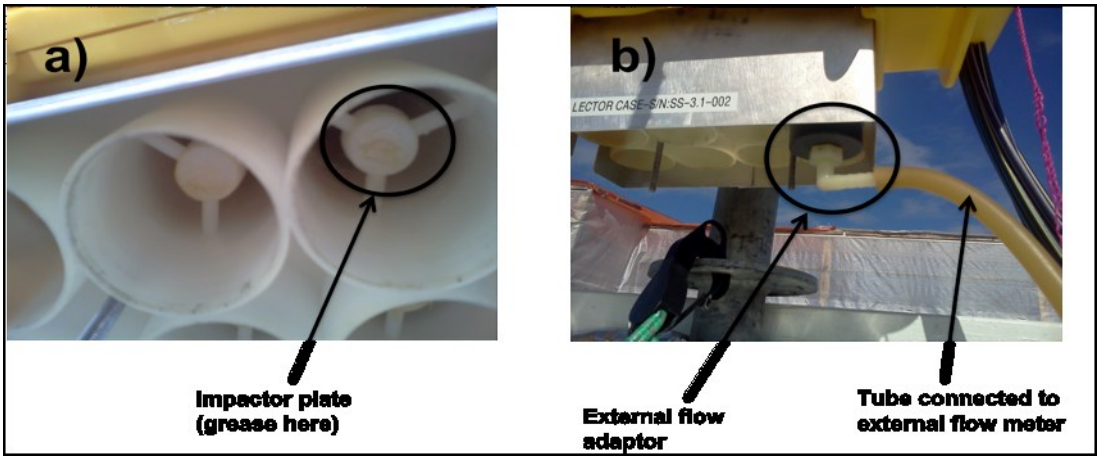

Figure B.18. a) Picture of where to place the vacuum grease on the impactor plates, and b) How to use the external flow adaptor to measure flow rates.

B8.6 Downloading Data and Recording information

B8.6.1 Downloading Data from Instruments

The nephelometer and the filter-based system use a memory card (found in the electronics case) to record data collected during sampling. These data are extremely important and must be handled with care.

At a minimum, the nephelometer data should be downloaded when a new cartridge is installed, when a full cartridge is removed, and at an approximate midpoint between cartridge installation and removal. However, downloading nephelometer data on a bi-weekly basis ensures that data can be sent to Dalhousie University easily. Be sure to turn off the nephelometer BEFORE removing the memory card and do not turn the nephelometer back on until the memory card has been reinserted. Download the data by inserting the memory card into the appropriate slot in a computer. To access the data, open the file that reads “INXXXX” (XXXX = sampling station number). The data will be in a CSV file (.csv format).

Data can be sent to the SPARTAN site manager by email or through a file sharing system such as Dropbox or Google Drive. The method of sharing data with the site manager is based on what works best for the on-site operators. Files larger than 25 MB are too large to send by email, and the nephelometer produces approximately 10 MB of data per week. Please keep this figure in mind when considering the method of file sharing as well as how often the site operators plan to download data.

After downloading the nephelometer data, place the memory card back in the appropriate slot and turn the nephelometer back on. Do not send the nephelometer memory card to Dalhousie University and do not clear the memory card until instructed by a site organizer from Dalhousie University.

As with the nephelometer, the memory cards remain with the sampling station until instructed by the site manager or the memory card is no longer usable. It is very important to turn off the sampling station before removing the memory card. Memory card data are shared with the site manager at the end of each sampled cartridge and can be erased from the memory card once it has been safely copied. When a cartridge is installed it is important to program the instrument with the memory card number found on the memory card itself, which is the same as the cartridge number. For example, if the cartridge is BDDU-005, program the memory card as “005”.

B8.6.2 Recording Log Sheet Information

Keeping accurate records of flow measurements, weather conditions, and programmed information for each cartridge is crucial to identifying potential issues in collected data. When a new pre-loaded cartridge is received a log sheet for that specific cartridge will accompany it. The log sheet will include the labels pertaining to the filters

inside the cartridge slots (1 through 8). When installing the cartridge all of the information on the first page (e.g. weather conditions, programmed information, etc.) as well as the start flows must be recorded. Before removing the cartridge after the sampling period, the end flows must be measured and recorded on the log sheet. The log sheet is then returned to Dalhousie University along with the sampled cartridge. Please make a copy for your own records. An example of a completed log sheet is shown in Figure B.4

B8.7 Storage and Shipment of Filter Cartridges

After a cartridge is finished sampling it is to be returned to Dalhousie University within three business days. While awaiting shipment the filter cartridge can be stored under ambient conditions; no cold storage is necessary. Methods of shipment vary from site to site and will be discussed/communicated with you upon site start-up by a site manager.

Appendix C Copyright Agreement Letters

Title: Global Estimates of Fine Particulate Matter using a Combined Geophysical-Statistical Method with Information from Satellites, Models, and Monitors

Author: Aaron van Donkelaar, Randall V. Martin, Michael Brauer, et al

Publication: Environmental Science & Technology

Publisher: American Chemical Society

Date: Apr 1, 2016

LOGIN

If you're a copyright.com user, you can login to RightsLink using your copyright.com credentials.

Already **a RightsLink user** or want to learn more?

PERMISSION/LICENSE IS GRANTED FOR YOUR ORDER AT NO CHARGE

This type of permission/license, instead of the standard Terms & Conditions, is sent to you because no fee is being charged for your order. Please note the following:

- Permission is granted for your request in both print and electronic formats, and translations.
- If figures and/or tables were requested, they may be adapted or used in part.
- Please print this page for your records and send a copy of it to your publisher/graduate school.
- Appropriate credit for the requested material should be given as follows: "Reprinted (adapted) with permission from (COMPLETE REFERENCE CITATION). Copyright (YEAR) American Chemical Society." Insert appropriate information in place of the capitalized words.
- One-time permission is granted only for the use specified in your request. No additional uses are granted (such as derivative works or other editions). For any other uses, please submit a new request.

If credit is given to another source for the material you requested, permission must be obtained from that source.

BACK CLOSE WINDOW